JPL Quarterly Technical Review

Volume 1 October 1971 Number 3

Papers on:

Computer Programs
Management Systems
Materials
Orbits and Trajectories
Photography
Power Sources
Propulsion
Telecommunications

Abstracts of:

Technical Reports
Technical Memorandums
JPL Quarterly Technical Review
Open Literature Reporting

Jet Propulsion Laboratory/California Institute of Technology

JPL Quarterly Technical Review
Volume 1, Number 3

Jet Propulsion Laboratory
California Institute of Technology
4800 Oak Grove Drive
Pasadena, California 91103

Prepared Under Contract NAS 7-100
National Aeronautics and Space Administration

JPL Quarterly Technical Review

Volume 1 October 1971 Number 3

Contents

Bibliography of Current Reporting

The Characterization of Facsimile Camera Systems for Lunar and Planetary Surface Exploration

A. Eisenman

Guidance and Control Division[1]

For imagery of lunar and planetary surfaces from stationary or stopped remotely controlled vehicles, facsimile camera systems offer unique advantages: better geometric fidelity than television systems, more picture elements per frame, ability to take single frame panoramic pictures, a very high contrast ratio within a picture, a choice of one or more narrow-band spectral responses over a wide possible range, image transmission over a low bit-rate communications channel without storage, very low power, small size, low weight, and ruggedizability to meet space flight requirements. Systems of this kind are under development for the 1975 Viking Martian lander, and have been used by the Soviets on Lunas and Lunokhod. JPL has recently completed laboratory and field evaluation of an existing facsimile camera system. The results of this test program are presented. The applicability of facsimile cameras to lunar and planetary rovers is demonstrated.

Introduction

In pursuit of NASA interests in electronic imaging for lunar and planetary automated rover applications (Reference 1), the Marshall Space Flight Center (MSFC) initiated a facsimile camera evaluation program in the winter of 1970. The program involved MSFC, the U.S. Geological Survey, and JPL, and consisted of laboratory and field evaluation of the one existing sample of the Philco Ford-designed and built Minifax television camera and its film reproducer. The camera is shown in Figure 1, and the specifications of the camera and reproducer are given in Tables 1 and 2, respectively. A sample Minifax panorama is shown in Figure 2.

[1] Work performed during prior assignment to the Space Sciences Division.

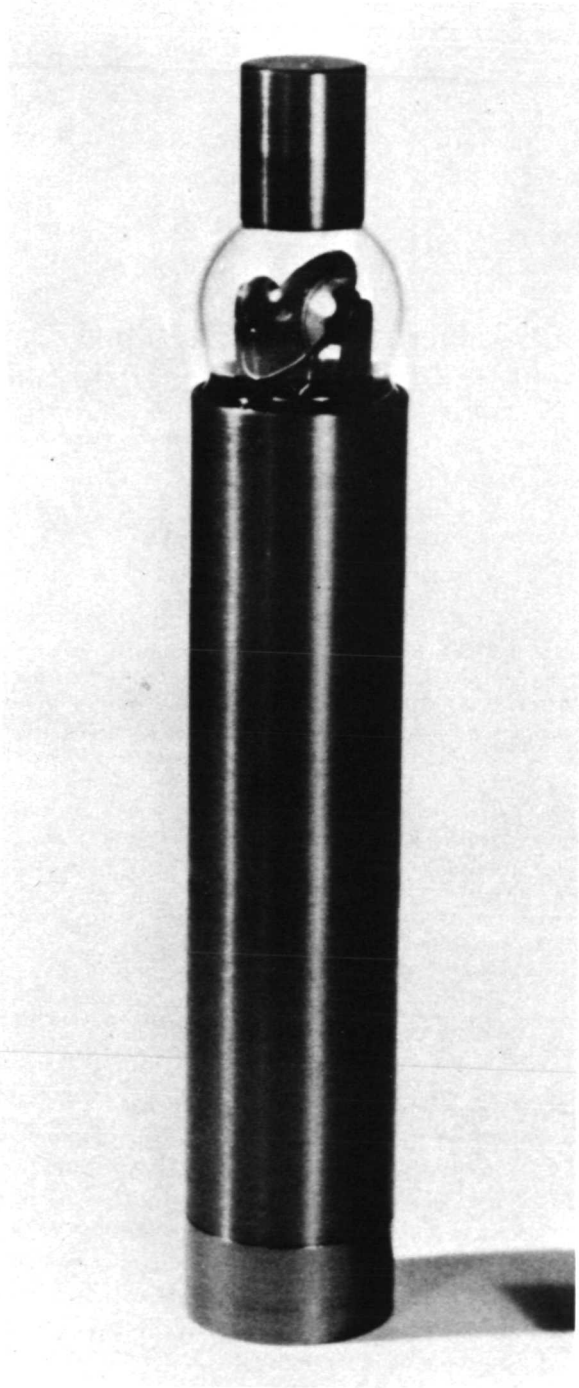

Figure 1. Minifax camera

Table 1. Minifax camera specifications after Philco Ford

Image field of view	+1.05, −0.525 × 2π rad
Scan format	900 horizontal lines
Image point spacing	1.74 mrad
Scan rate	30 lines/s
Data rate	108,000 image points/s
Frame time	30 s
Spectral response	Silicon, 0.4–1.0 μm
Noise equivalent brightness	86 cd/m^2 at 54 kHz
Dynamic range	86–34,300 cd/m^2
Data synchronization	Line and frame sync
Scan sync reference	6 kHz
Operating power	1.5 W at 14 Vdc
Video output	0–10 V
Size	2.5 cm diam × 15 cm long
Weight	260 g
Environment	1000-g delivery shock
	−23 to +72°C exposure, 1 yr

Table 2. Minifax recorder specifications after Philco Ford

Image size	11.4 × 45 cm
Record medium	Photographic film
Line spacing	0.0127 cm
Line-to-line correlation	0.0025 cm (0.35 mrad)
Recording dynamic range	200/1
Operating power	150 W at 110 V, 60 Hz
Size	23 × 36 × 36 cm
Weight	23 kg
Operating features	Gain and bias controls
	Daylight loading
	Real-time recording portable

Figure 2. Minifax field site panorama (Sun covered by shading disc)

The test program was intended to fill gaps in knowledge about functioning, flightworthy, mechanical scanning telephotometers. The first facsimile-equipped U.S. spacecraft flight will be the 1973 launching of the Radio Astronomy Explorer B whose cameras are to observe antenna deployment and dynamics. The first U.S. lander facsimile camera will be on the 1975 Viking to Mars which will carry two such devices, providing both stereo and color panoramic imaging. The present Minifax camera is descended from one developed for the Ranger Project in 1960–1964 but never flown to the Moon. The principle of building up and transmitting an image point-by-point has been demonstrated in space, for example, by the spin-scan cameras on the Applications Technology Satellites.

In spite of the present lack of U.S. flight experience, facsimile cameras are not strangers in space. The USSR has a long history of use covering lunar landers and the recent Lunokhod automated rover (Reference 1). Lunokhod carried four facsimile cameras, two on each side of the vehicle. One of each pair was mounted to take vertical panoramas, and one to take horizontal panoramas. A Lunokhod telephotometer panorama is shown in Figure 3. The time to take the picture was indicated to be 1800 s. Analysis of the print shows a vertical scan line orientation with a scan line spacing of approximately 1.3 mrad, and a field of view of approximately 4.7 rad horizontal by 0.61 rad vertical.

The justification for facsimile cameras instead of, or supplementing, vidicon types stems from certain basic problems to be solved by imaging on a remotely controlled lunar or planetary mobile vehicle. These problems are to see where the vehicle is located, to determine its relationship to the surrounding region, and to identify features of potential scientific interest for further exploration. The solution lies in obtaining an appropriate full-circle panorama from the rover. In the case of a stationary lander, this can be done by assembling many frames from a raster scan television camera together into a single, full-circle, panoramic mosaic, as was done for Surveyor. In the case of a roving vehicle, this is too time consuming and tedious to be performed at each site of interest, along an entire traverse, and suffers from other shortcomings. Of possible alternatives to vidicon camera mosaics, the most direct, optimum choice for the job is the photo facsimile television camera.

Facsimile Camera Functional Description

Basically, facsimile cameras consist of a telephotometer (a point detector with a lens) which is mechanically scanned across the image. A variety of implementations is possible, but the simplest, and most efficient, for most rover panorama purposes is a helical scanning camera, such as the Minifax with a scan that starts in the upper lefthand corner of the frame and ends in the lower righthand corner.

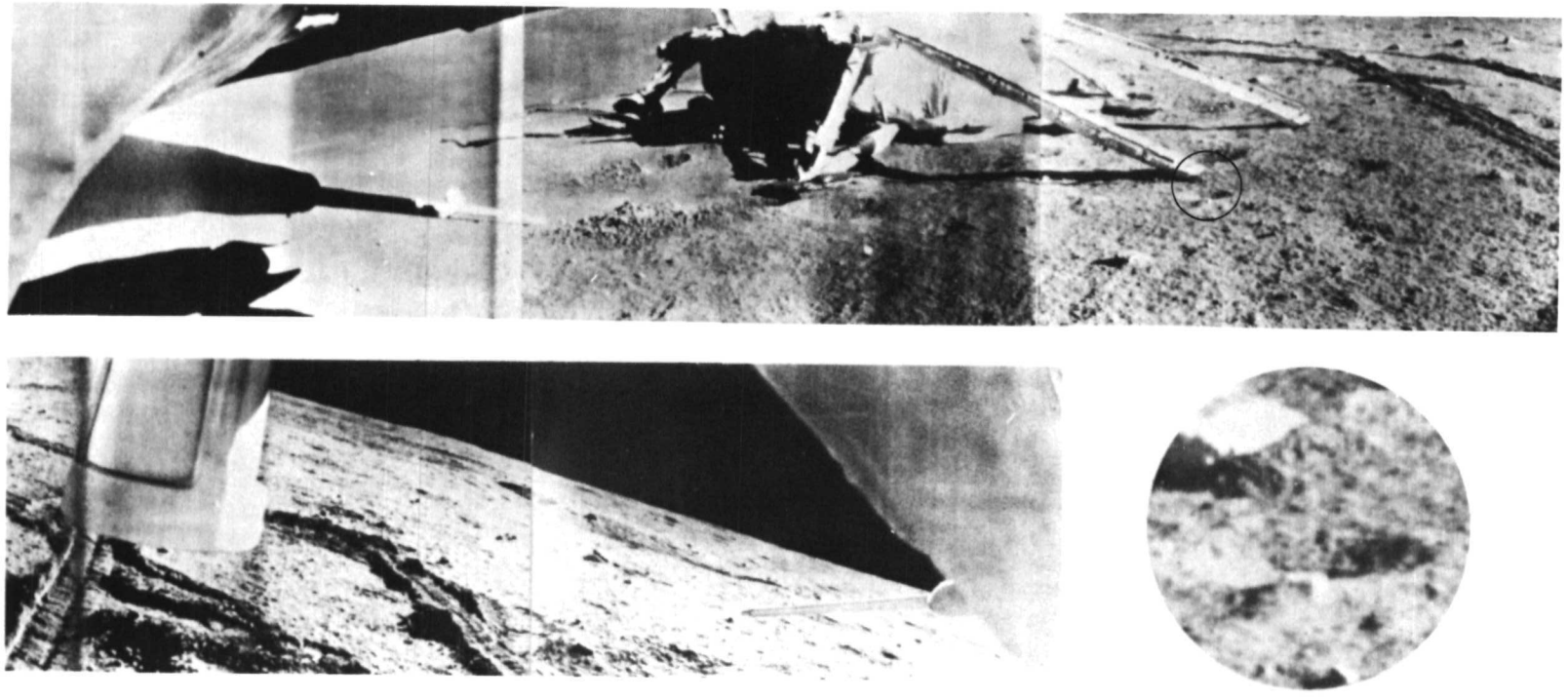

Figure 3. Lunar panorama from Lunokhod telephotometer showing landing platform and tracks of Lunokhod, Jan. 19, 1971 (courtesy of Dr. K. P. Florensky)

The advantages of a facsimile camera for this application are as follows:

(1) *High geometric accuracy.* This is a requirement for terrain navigation. Since the camera operates as a precision optical divider head, it may be designed to be calibrated to about one scanning line width of relative geometric accuracy over the entire frame. This is in contrast to the much larger geometric nonlinearities of electronically scanned cameras.

(2) *Panoramic capability.* There is no inherent restriction on the horizontal field of view. Therefore, full-circle coverage is possible without variations in response or shading. This large field of view, with its attendant large number of picture elements per frame, would be impossible in a single frame with a vidicon camera.

(3) *Large dynamic intensity range.* The point sensor of the camera can be operated linearly over an intensity range in excess of three decades starting with the preamplifier noise level and extending to the saturation point of the electronics. A range of this magnitude is generally impossible to achieve using other imaging techniques.

(4) *Direct solar imaging.* Direct solar imaging is possible without damage to the detector. Typical solar thermal loading of the detector is only 2 mW. This removes restrictions on solar pointing encountered with vidicon cameras. Rapid recovery from solar saturation to normal video levels within a few picture elements can also be incorporated in the design. Imaging the Sun would destroy many types of vidicon cameras, as happened during Apollo 12.

(5) *Wide spectral coverage.* The commonly used silicon phototransistor detector is usable over the entire visible spectrum, and beyond into the near infrared. With a trade-off between the total spectral coverage and sensitivity, narrow-band spectral filters may be introduced as required.

(6) *Low data rate matched to telemetry requirements.* There is no limitation on the minimum data rate of the camera. It may be operated at any rate below a maximum dictated by the threshold sensitivity. This then permits matching the generally low telemetry rates available from a rover without sensor or electronic storage, as required for other cameras.

(7) *Small size, low weight and power.* A facsimile camera simultaneously combines small physical volume, low weight, and low power consumption. Generally, at least an order of magnitude improvement in all of these parameters is realized compared to vidicon types.

(8) *Easily ruggedized.* The construction of the camera permits meeting shock loads to over 1000 *g*, thus meeting space flight launch and landing requirements with a large margin to spare.

JPL Test Program

The JPL test program was conducted in the two phases of laboratory tests and field tests, with emphasis on the laboratory effort. The work was done as part of the JPL Advanced Lunar Studies Program.

The purpose of the laboratory tests was to quantitatively characterize the performance of the camera in areas where this had not previously been done, and to isolate the limiting aspects of performance as they are pertinent to a lunar rover. The field pictures were taken to be used for scientific site evaluation, using previously obtained film panoramas of the sites as a reference. Additional horizontal and vertical stereo pairs were taken to judge the value of facsimile stereo and the relative merits of the two techniques.

The approach to the laboratory tests was to divide the measurements into the two groups of photometric and resolution related parameters. Additionally, an indirect test of azimuthal geometric accuracy was run, which isolated static and dynamic errors. Other parameters, such as solar flare and saturation recovery, were estimated from the field pictures.

Measurements and Summary of Results

An outline of the laboratory tests performed on the camera is given below.

(1) Photometric tests.

  (a) Photometric transfer response.

  (b) Preamplifier noise spectrum analysis at three light levels.

  (c) Relative spectral response.

(2) Horizontal resolution tests.

  (a) Modulation transfer function at a reference light level and at four lower levels.

  (b) Modulation transfer function (MTF) derived from constituent components of video frequency response, jitter MTF, and optical MTF.

A summary of the test results is given in Table 3. The projected requirements for a lunar rover camera are given in Table 4 (Reference 2).

Stereo Results

Vertical and horizontal stereo pairs were taken near JPL, at a site in the Arroyo Seco, for the purpose of determining the value of stereo in aiding terrain assessment. Two horizontal camera spacings of 2.2 and 5.5 m were

Table 3. Measured values of minifax parameters[a]

Parameter	Value
Light transfer independent linearity	±6% from 34 to 12,300 cd/m^2
Spectral response	370 to 970 nm (est) at 5% response
Peak spectral response	675 nm
Threshold sensitivity	58 cd/m^2 at 7.8 mrad per line pair resolution at 10% modulation
Preamplifier random noise equivalent brightness	21 cd/m^2 at unity S/N ratio
Horizontal resolution	1.9 mrad per line pair at 5% response at 1300 cd/m^2
System horizontal resolution	12 mrad per line pair at 5% response at 1300 cd/m^2
Repeatable geometric error	3.3 mrad peak to peak (approx)
Random geometrical error	0.23 mrad (rms approx)
Solar flare	600 cd/m^2 (est)
Solar saturation recover	150 picture elements (est)

[a] All specifications on camera only, except "system horizontal resolution."

Table 4. Lunar rover facsimile panorama requirements

Parameter	Value
Field of view	+0.26 rad, -0.52 rad vertical × 2π rad horizontal
Scan line resolution	0.87 mrad
Slant range	3 m to ∞
Frame scan time	60 s
Active scan lines	900
Video bandwidth	55 kHz
Threshold sensitivity	3.4 cd/m^2
Intensity dynamic range	2500:1
Geometric accuracy	1.74 mrad
Spectral coverage	Visual, monochromatic
Power	$<$8 W
Size	$<$170 cm^3
Weight	$<$900 g

used. Vertical spacings were 30 cm, 70 cm, and 1 m. The vertical stereo showed the expected benefit of radially uniform separation in the ground plane; however, interpretation of the 1-m pair by R. Choate (Reference 3) revealed the following unexpected dividend:

"Many terrain features of interest are large in two dimensions within the ground plane, but are small in the vertical dimension. Thus, when viewed from near ground plane elevations, such features appear as long linear elements. A common terrestrial example would be a terrace, which when viewed from near the ground is almost invisible, i.e., it appears as a horizontal thin line. Lunar examples are craters of all sizes and ejecta rims surrounding many of them. When viewed from near the ground, the only evidence indicating the presence of these two features would be the rim of ejecta which would look like a long low linear ridge.

"Therefore, from the reasoning above, it would be expected that vertical stereo pairs would enhance the presence of planar features by presenting views from different elevation angles to each eye. This was borne out by the pronounced appearance of terrace-like features in the vertical base Arroyo Seco pairs. This effect was lost in monocular pictures, and in horizontal stereo pairs. Also, the uniform, full-circle stereo of the vertical pair aided substantially in the identifications of rocks, holes, mounds, and other three-dimensional objects."

The conclusion, then, from the field stereo work is that facsimile stereo is a worthwhile adjunct to monocular facsimile imaging terrain assessment and that the preferred stereo mode is vertical.

Performance Results

The results of the test program are given here in the form of performance graphs encompassing specific photometric and resolution characteristics of the Minifax system.

The first graph is that of the light transfer curve for the camera (Figure 4). The curve was taken with the scanner stopped. The camera was pointing at a Mariner flight TV, flat field, xenon light cannon. The intensity range of the light cannon was extended downwards from its 160-cd/m^2 lower limit with a log 1.1 neutral density filter taped over the imaged spot. The camera's electrical output was filtered with a 1-s time constant, low-pass filter and monitored with a digital volt meter.

The resulting intensity curve exhibits good linearity (unity gamma) over its central portion from 70–7000 cd/m^2. The beginning of saturation is seen above 7000 cd/m^2, and nonlinearities due to the silicon phototransistor detector dominate the low end of the response. The latter effect is a correctable design defect.

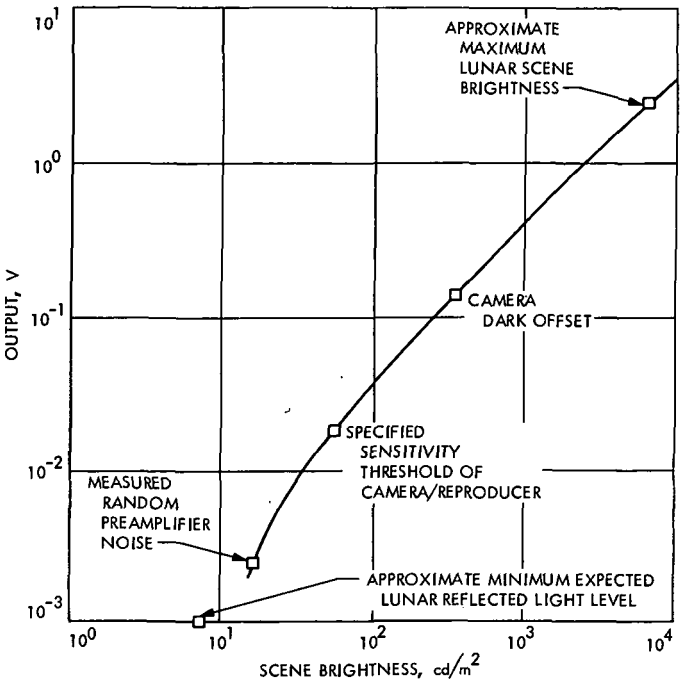

Figure 4. Camera light transfer

A spectrum analysis of the camera's preamplifier and detector noise is shown in Figure 5. The curves were taken with the scanner stopped, using a seven-cycle bandwidth analyzer. The curves are for zero, ½-scale, and full-scale light levels. Aspects of note are the lack of $1/f$ noise in the 100- to 1000-Hz range, the relatively flat nature of the noise, and the expected increase of noise as a function of light level.

The noise shown in Figure 5 is of interest in representing the limits of camera performance. Actual operating noise (with the scanner running) is much higher due to the pickup of interfering signals in the camera tested. Reduction of actual noise to approach the detector and preamplifier levels would be a requirement in a flight camera design. Low intensity photoelectron noise is not a limitation for the levels of interest which are above 3.4 cd/m^2.

Figure 6 covers the relative spectral response of the camera. The photopic response of the eye and the response of a Surveyor-type vidicon are shown for reference. The wide spectral response of the camera makes it possible to use narrow-band spectral filters to produce visual color, or to do near-IR studies, with a corresponding loss in sensitivity.

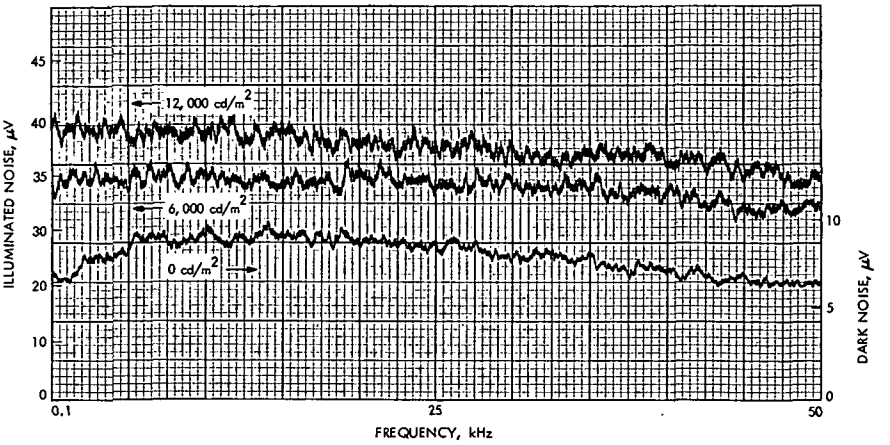

Figure 5. Camera noise spectrum at three light levels

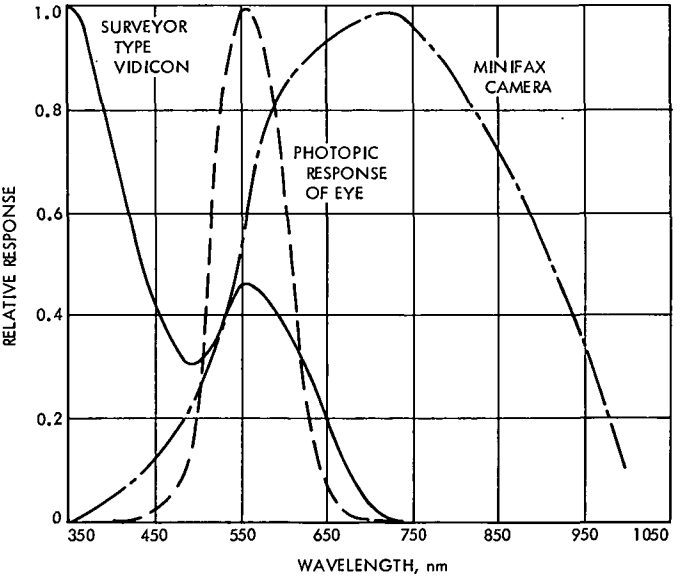

Figure 6. Camera relative spectral response

The next set of curves (Figure 7) covers camera and camera/reproducer resolution. They were made with the use of opaque high contrast U.S. Air Force and National Bureau of Standards bar charts. Resolution is presented in the form of modulation transfer function (MTF) curves which portray relative output (% modulation) as a function of spatial frequency, in units of cycles per radian. Here, a cycle is either one input optical square wave, or one input optical sine wave. Since the test charts are bar charts, creating input optical square waves, sine wave equivalent input curves were

calculated from the square wave data. Sine wave curves are essential where individual parameters are convolved together, as is done in Figure 7d.

Figure 7a shows the measured camera-only resolution at a light level of 1300 cd/m^2. The measurements were made using single lines of video scanning a selected bar group of a test chart. The video was recorded on photographic film from an oscilloscope presentation. Illumination light levels were obtained from the camera itself operating as a non-scanning telephotometer.

The response of the camera at the current line rate of 285 cycles/rad (equivalent to 1.75 mrad scanning line spacing) is seen to be 39%. The limiting resolution at 5% response is 475 cycles/rad, indicating the good potential for improving resolution to the desired value specified in Table 4 of 570 cycles/rad.

The effect of reduced light levels on resolution is illustrated in Figure 7b. Measurements were made at levels down to 58 cd/m^2.

Figure 7c demonstrates the loss in system resolution caused by the degradation of the film reproducer. In fact, this degradation is sufficient to mask any changes in camera focus resulting from changes in the target-to-camera distance at 2.6, 3.9, and 4.8 m. Line-to-line sync jitter appeared to be the principal factor in reproducer resolution losses.

The camera/reproducer measurements were made from the reproducer film, not from paper print copies. The film images were enlarged by a factor of ~5 on high resolution, unity gamma film, and then relative response measurements were made with a recording microdensitometer. Modulation was calculated from the microdensitometer values, including approximate corrections for the enlarging lens and the scanning slit MTFs.

The final curves are those of Figure 7d for the components of camera resolution, with the overall camera response obtained by convoluting the components together. The top curve of the set is the MTF equivalency of the video channel frequency response. This measurement was made by exciting the stopped camera with a sine wave modulated light source generated by a light emitting diode.

The second curve is that for the MTF loss caused by jitter in the motion of the mirror scanning mechanism. An approximate rms value of jitter was derived from the line-to-line phase error of the scanning motor control signal over a single frame composed of 900 scanning lines. The jitter was assumed to be random, and was then translated into an effective MTF curve based on the techniques of M. D. Rosenaue, Jr.

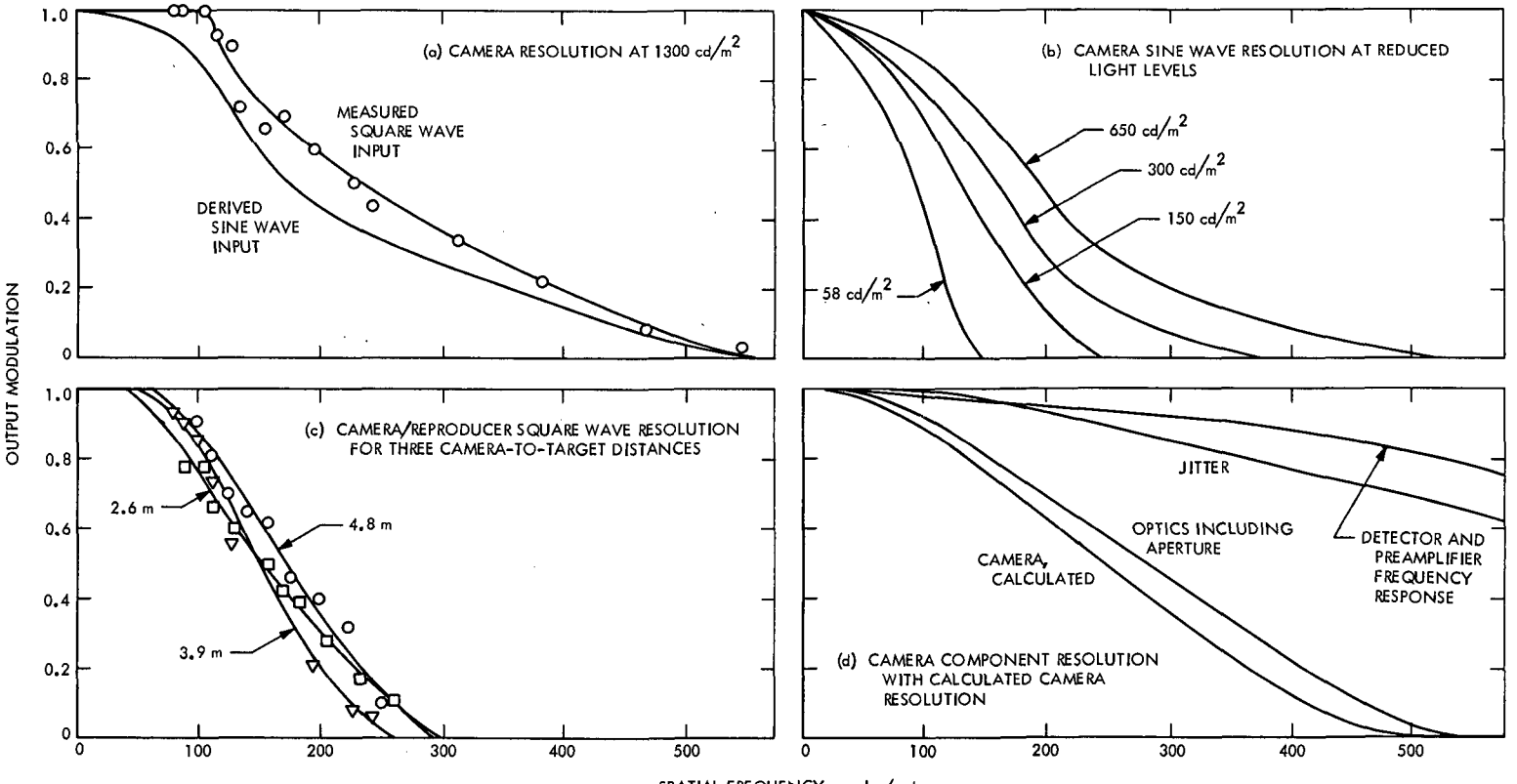

Figure 7. Minifax modulation transfer functions

The third curve is that of the camera's optical MTF, which was measured by driving the test targets at a constant slow rate past the beam of the non-scanning camera.

The components of camera MTF of frequency response, jitter, and optics were then multiplied together to obtain the camera resolution curve of Figure 7d. The results indicate a response about 40% better in the midspatial frequencies than the measured response of Figure 7a. The greater derived response is likely to be due to measurement errors (particularly jitter), and to the non-inclusion of potentially significant terms such as electrical motor sync signal noise. However, the derived curve does demonstrate that the principal determinant of resolution is the optics, and that the camera resolution could be significantly improved with an improvement in beam size and shape.

Conclusions and Recommendations

The results of the JPL Minifax test program can be summarized as follows:

(1) Helical scanning facsimile cameras can meet lunar rover panoramic imaging requirements for scientific and navigation purposes.

(2) The present Minifax camera design can be modified to do the above job.

(3) Facsimile camera vertical base stereo is a valuable aid in terrain assessment from a rover.

The evaluation of the Minifax camera system revealed that the following feasible modifications would be required in the camera design in order to fully meet present lunar rover requirements:

(1) Reduce line spacing by 2:1.

(2) Improve optical focus to 0.88 mrad.

(3) Reduce azimuth sweep rate by 4:1.

(4) Improve coherent noise ratio by 20:1.

(5) Improve random noise ratio by 3:1.

(6) Improve solar saturation recovery to less than 20 picture elements.

(7) Improve low level light transfer linearity to within 6% to 3.4 cd/m^2.

(8) Change vertical field of view to 0.26 rad, -0.52 rad, relative to the horizon.

References

1. Brereton, R. G., Burke, J. D., Coryell, R. B., and Jaffe, L. D., "Lunar Traverse Missions," in *JPL Quarterly Technical Review*, Vol. 1, No. 1, pp. 125–137. Jet Propulsion Laboratory, Pasadena, Calif., Apr. 1971.

2. Jaffe, L. D., Choate, R., Coryell, R. B., Eisenman, A., Hornbrook, G. K., and Strelitz, R. A., *Payload Requirements for Remotely Controlled Long Range Lunar Traverse Vehicles*, Document 760-62, Aug. 1971 (JPL internal document).

3. Choate, R., *The Value of Stereo Using the Minifax Camera*, July 1971 (JPL internal document).

Reliability Estimation Procedures and CARE: The Computer-Aided Reliability Estimation Program

F. P. Mathur

Astrionics Division

Ultrareliable fault-tolerant onboard digital systems for spacecraft intended for long mission life exploration of the outer planets are under development. The design of systems involving self-repair and fault-tolerance leads to the companion problem of quantifying and evaluating the survival probability of the system for the mission under consideration and the constraints imposed upon the system. Methods have been developed to (1) model self-repair and fault-tolerant organizations; (2) compute survival probability, mean life, and many other reliability predictive functions with respect to various systems and mission parameters; (3) perform sensitivity analysis of the system with respect to mission parameters; and (4) quantitatively compare competitive fault-tolerant systems—various measures of comparison are offered. To automate the procedures of reliability mathematical modeling and evaluation, the CARE (computer-aided reliability estimation) program was developed. CARE is an interactive program residing on the UNIVAC 1108 system, which makes the above calculations and facilitates report preparation by providing output in tabular form and graphical 2-dimensional plots and 3-dimensional projections. The reliability estimation of fault-tolerant organization by means of the CARE program is described in this article.

Introduction

The task of evaluating system performance of digital system architectures designed for long life or ultrareliability is a recurring one. The state-of-the-art of fault-tolerant computing makes available to the designer various models or schemes which by judiciously using protective redundancy impart greater system probability of survival than would be possible by the use of simplex technology alone. One or more of these fault-tolerant schemes—triple modular redundancy (TMR), *N*-tuple modular redundancy, TMR/simplex redundancy, component redundancy, standby replacement, *K*-out-of-*N* systems, hybrid redundancy, and hybrid/simplex redundancy (References 1–5)—in combination make the architecture of fault-tolerant organizations. The overall reliability model takes into consideration the effect of

variation in individual parameters of the basic schemes on the overall system reliability goals—this relationship being expressed as a mathematical function which is often referred to as the reliability mathematical model of the system. The reliability evaluation task, once the system reliability mathematical model is known, may be: (1) to evaluate the system reliability given the values of the model parameters, or (2) to optimize the reliability objective by selecting optimum values of the model parameters. Since the number of combinations of the basic schemes and the range of possible values that the system parameters may undertake are very large, the decision was taken to automate the reliability evaluation procedure which resulted in the development of a conversational computer program called CARE (computer-aided reliability estimation).

Functional Description of CARE

CARE's purpose is to serve as a computer-aided reliability design tool to designers of ultrareliable fault-tolerant systems by facilitating reliability computation, data generation, and comparative evaluation. CARE consists of 4150 Fortran V statements designed to be run on the UNIVAC 1108 under EXEC 8, version 11C (References 6 and 7). The results of the program are available in three forms: (1) as printouts, (2) as graphical 2-dimensional plots, and (3) as graphical 3-dimensional projections.

CARE has three modes of operation: (1) "conversational" or interactive mode, (2) batch mode, and (3) remote-started batch mode. In the "conversational" mode, CARE may be interactively accessed by users from remote teletypes or other communication consoles to perform reliability analysis in "real time." In the batch mode the job is submitted off-line and necessarily no dynamic changes to the user requirements can be made; this mode is expeditious when the user knows his needs exactly and hence need not spend time sitting at a console to input his queries. The remote-started batch mode is similar to the batch mode except that instead of submitting the job as a deck of punched cards the deck entry may be made via a console.

Essentially, CARE consists of a repository of mathematical equations defining the various basic redundancy schemes. These equations may then, under program control, be interrelated to generate the desired mathematical model to fit the architecture of the system under evaluation. The mathematical model may then be supplied with ground instances of its variables and then evaluated to yield values for the specified independent variable or the mathematical model may be further manipulated so as to yield other reliability theoretic results.

CARE's Repository of Equations

The equations residing in CARE model the following basic fault-tolerant organizations:

(1) *Hybrid-redundant (N,S) systems* (see References 1 and 2).

   (a) NMR (*N*,0) systems (see References 3 and 8).

   (b) TMR (3,0) systems (see Reference 3).

   (c) Cascaded or partitioned versions of the above systems.

   (d) Series string of the above systems.

(2) *Standby-sparing redundant (1,S) systems* (see References 3 and 4).

   (a) *K*-out-of-*N* systems (see Reference 4).

   (b) Simplex systems.

   (c) Series string and cascaded versions of the above.

(3) *TMR systems with probabilistic compensating failures* (see Reference 3).

   (a) Series string and cascaded versions of the above.

(4) *Hybrid/simplex redundant* $(3,S)_{sim}$ *systems* (see References 5 and 9).

   (a) TMR/simplex systems (see Reference 4).

   (b) Series string and cascaded versions of the above.

For the description of the above systems and their mathematical derivations, refer to the cited references. These equations are the most general representation of their systems parameterizing mission time, failure rates, dormancy factors, coverage, number of spares, number of multiplexed units, number of cascaded units, and number of identical systems in series. The definition of these parameters resides in CARE and may be optionally requested by the user (see Figure 1). More complex systems may be modeled by taking any of the above listed systems in series reliability with one another.

These reliability equations may be evaluated as a function of absolute mission time, normalized mission time, nonredundant system reliability, or any other system parameter that may be applicable. Among the various measures of reliability that the user may request for computation are: the system mean-life, the reliability at the mean-life, gain in reliability over a simplex system or some other competitive system, the reliability improvement factor, and the mission time availability for some minimum tolerable mission reliability.

Formulation of a Typical Problem for CARE

A typical problem submitted for CARE analysis may be the following: Given a simplex system with 8 equal modules which is made fault-tolerant by providing two standby spares for each module, where each module has a constant failure rate of 0.5 failures per year and where the spares have an

```
@XQT ATMAN.CARE
HELLO TERMINAL - I AM YOUR RELIABILITY ANALYST WITH THE
CARE (COMPUTER-AIDED RELIABILITY ESTIMATION) PACKAGE
DO YOU WISH TO HAVE YOUR ANSWERS TO THE QUESTIONS PRINTED BACK.
ANSWER YES OR NO
YES
DO YOU WISH TO KNOW THE DEFENITIONS OF RELIABILITY PARAMETERS AND TERMS.
ANSWER YES OR NO
YES
THE DEFENITIONS OF THE VARIOUS RELIABILITY PARAMETERS
AND TERMS ARE AS FOLLOWS.

 T = MISSION TIME.
 R = SYSTEM RELIABILITY.
 S = THE TOTAL NUMBER OF SPARES.
 N = THE NUMBER OF MULTIPLEXED UNITS.
 K = INVERSE DORMANCY FACTOR = (LAMBDA/MU).
 C = COVERAGE FACTOR.
   = CONDITIONAL PROBABILITY OF SYSTEM RECOVERING GIVEN A FAILURE OCCURANCE.
 Q = QUOTA, NUMBER OF IDENTICAL UNITS IN A SIMPLEX SYSTEM.
 W = NUMBER OF CASCADED UNITS.
 Z = NUMBER OF IDENTICAL SYSTEMS IN SERIES.
 P = PROBABILITY OF A UNIT FAILING TO A LOGIC ZERO.
 RV= RELIABILITY OF THE RESTORING ORGAN.
 MU= UNPOWERED FAILURE RATE OF A SIMPLEX SYSTEM = K/LAMBDA.
 LAMBDA = POWERED FAILURE RATE OF A SIMPLEX SYSTEM = K*MU.

 LAMT = NORMALISED TIME = LAMBDA*MISSION TIME.
 ELAMT = EXP(-LAMT).
 REL = SYSTEM RELIABILITY.
 UNREL = SYSTEM UNRELIABILITY = (1 - REL).
 SIMREL = SIMPLEX RELIABILITY = ELAMT.
 SIMGAIN = GAIN IN RELIABILITY WITH REFERENCE TO A SIMPLEX SYSTEM .
         = REL/SIMREL.
 SIMRIF = RELIABILITY IMPROVEMENT FACTOR WITH REFERENCE TO A SIMPLEX SYSTEM.
        = (1 - SIMREL)/(1 - REL).

DO YOU NEED INSTRUCTIONS FOR RUNNING THE CARE PROGRAM
ANSWER YES OR NO
YES
SHORTCOMMENT - THE CARE PROGRAM COMPUTES, WITH RESPECT TO THE
SELECTED EQUATIONS AND PARAMETERS THE FOLLOWING RELIABILITY
FUNCTIONS - THE RELIABILITY (REL), UNRELIABILITY (UNREL),
SIMPLEX RELIABILITY (SIMREL), SIMPLE GAIN (SIMGAIN), SIMPLE
RELIABILITY IMPROVEMENT FACTOR (SIMRIF), MEAN TIME TO FAILURE
(MTF), RELIABILITY AT THE MTF, RELIABILITY DIFFERENCE (DIFF),
RELIABILITY GAIN (GAIN), RELIABILITY IMPROVEMENT FACTOR (RIF),
SIMPLE MAXIMUM MISSION TIME (SIMTMAX), MAXIMUM MISSION TIME (TMAX),
SIMPLE TIME IMPROVEMENT FACTOR (SIMTIF), AND THE RATIO OF
TIME IMPROVEMENT FACTORS (RATIF).

2D AND SOME 3D PLOTS CAN BE OBTAINED FOR THE ABOVE COMPUTATIONS.
VARIOUS PLOTTING OPTIONS TO SPECIFY THE ABSCISSA, THE RANGE
OF ABSCISSA AND ORDINATE VALUES ARE AVAILABLE.ABILITY TO PLOT 3D
INTERSECTIONS OF 3D PROJECTIONS WITH 2D PLANES IS ALSO AVAILABLE.
```

Figure 1. A sample of CARE's question/answer capability

```
 THE CARE PROGRAM ALSO EVALUATES COMPLEX RELIABILITY FUNCTIONS
 FORMED BY TAKING PRODUCTS OF THE BASIC RELIABILITY EQUATIONS.

 CARE HAS A MAXIMUM OF 10 DIFFERENT RELIABILITY EQUATIONS
 THESE ARE TABULATED BELOW.
 1. R(N,S) = F(T,LAMBDA,MU,S,N,K,RV,Z,W)
    THIS IS THE GENERAL RELIABILITY EQUATION OF AN HYBRID-
    REDUNDANT SYSTEM.
 2. R(Q,S) = F(T,LAMBDA,MU,S,K,Q,C,Z,W)
    THIS IS THE GENERAL RELIABILITY EQUATION OF A STANDBY-
    REPLACEMENT SYSTEM.
 3. VOID
 4. VOID
 5. R(3,0) = F(T,LAMBDA,RV,Z,W,P)
    THIS IS THE EQUATION FOR A TMR SYSTEM WHERE THE PROBABILITY
    OF A UNIT FAILING TO LOGICAL ONE OR ZERO IS PARAMETERISED.
 6. R(1,0) = (EXP(-LAMBDA*T))**(Z/W)
    THIS IS A GENERAL EQUATION FOR A SIMPLEX SYSTEM.
 7. DUMMY
 THIS IS A DUMMY EQUATION WHICH IS ALL SET UP TO RECEIVE A NEW EQUATION.
 8. BLANK
 9. BLANK
 10.BLANK

 INSTRUCTIONS WILL BE GIVEN FOR ENTERING INPUT DATA
 AT THE TIME THE INPUT DATA IS NEEDED BY THE PROGRAM.

 DO YOU WISH TO FORM A PRODUCT OF RELIABILITIES
 ANSWER YES OR NO
 NO
 TYPE IN COLUMN 1 THE NUMBER OF THE RELIABILITY EQUATION
 TO BE USED - 1 THRU 7

 1
 INPUT VARIABLES FOR EQUATION  1
 T, LAMT, OR ELAMT MUST BE SPECIFIED AND ITS VALUE
 IS THE MAXIMUM VALUE FOR THAT VARIABLE.  MIN IS THE MINIMUM
 AND STEP IS THE INCREMENT FOR T, LAMT, OR ELAMT.
    SOME VARIABLES THAT ARE NEEDED BY THE EQUATIONS ARE SET
 EQUAL TO A DEFAULT VALUE IF THEY ARE NOT INPUTED.  THESE
 VARIABLES AND THEIR DEFAULT VALUES ARE: S=1, N=1, Z=1, W=1
 Q=1.0D0, C=.999..D0, P=1.0D0, MIN=0.0D0,
 STEP=1.0D0, AND ELAMT=1.0D0.
    IF B IS INPUTED, THEN THIS VALUE IS USED AS THE FIRST
 GUESS FOR THE UPPER LIMIT OF INTEGRATION IN THE CALCULATION
 OF MTF.
    IF OPTION=1, THEN DIFF, RIF, AND GAIN ARE CALCULATED FOR
 ALL POSSIBLE COMBINATIONS OF THE PARAMETER.  IF OPTION=2,
 THEN DIFF, RIF, AND GAIN ARE CALCULATED FOR THE LAST TWO
 PARAMETER VALUES.  IF OPTION=0 OR IS NOT INPUTED, THEN THE
 PROGRAM WILL ASK  THE USER AS TO WHICH PARAMETER VALUES
 DIFF, RIF, AND GAIN ARE TO BE CALCULATED.
 NOTE: DIFF, RIF, AND GAIN ARE NOT COMPUTED IF THE USER IS
 CALCULATING THE PRODUCT OF RELIABILITIES OR PLOTTING 3-D.
```

Figure 1 (contd)

```
THE VARIABLES FOR EQUATION  1 ARE INPUTED USING
VAR AS THE NAMELIST NAME.  A SAMPLE INPUT FOR EQUATION 5 FOLLOWS:
 $VAR
 T=12.0D0,
 LAMBDA=1.0D0,1.5D0,2.0D0,
 RV=1.0D0,
 Z=1,
 W=1,6,
 OPTION=2
 B=10.0D0
 $END
NOTE: NAMELIST INPUT IGNORES COLUMN 1
THE INPUT VARIABLES ARE TYPED AS FOLLOWS
   DOUBLE PRECISION: T, LAMT, ELAMT, MUT, LAMBDA, MU,
     K, RV, Q, C, P, MIN, STEP, AND B
   INTEGER: S, N, W, Z, AND OPTION
INPUT VARIABLES NOW
DO YOU WISH TO MAKE ALTERATIONS TO THE $VAR LIST
ANSWER YES OR NO
NO
DO YOU WISH TO HAVE 2-D RELIABILITY PLOTS - ANSWER YES OR NO
 YES
INPUT A 1 IN THE COLUMN SPECIFIED BELOW IF YOU WISH
THE CORRESPONDING PLOT OPTION, OTHERWISE INPUT 0.
NOTE: WHEN PERFORMING PRODUCT OF RELIABILITIES, NO OTHER
PLOT OPTION BESIDES PRODUCT OF RELIABILITIES MAY BE SPECIFIED.
COLUMN 1 - PLOTS PRODUCT OF RELIABILITIES
COLUMN 2 - PLOTS RELIABILITY
COLUMN 3 - PLOTS DIFF, RIE, AND GAIN
COLUMN 4 - PLOTS MTF AND RELIABILITY AT MTF
COLUMN 5 - PLOTS UNRELIABILITY
01100
FOR ABSCISSA, INPUT 1 IN COLUMN 1 IF ABSCISSA IS T,
 1 IN COLUMN 2 IF ABSCISSA IS LOG(T) - BASE 10,
 1 IN COLUMN 3 IF ABSCISSA IS LAMT,
 1 IN COLUMN 4 IF ABSCISSA IS LOG(LAMT) - BASE 10,
 1 IN COLUMN 5 IF ABSCISSA IS EXP(-LAMBDA*T),
 1 IN COLUMN 6 IF ABSCISSA IS LOG(EXP(-LAMT)) - BASE 10.
 **1***
IF YOU WISH TO PLOT A CERTAIN RANGE OF X-AXIS VALUES
FOR THE 2-D PLOTS, ENTER LEFT-END POINT IN COLUMNS 1-8 WITH
FORMAT F8.0 AND RIGHT-END POINT IN COLUMNS 9-16 WITH FORMAT F8.0;
OTHERWISE INPUT NO
NO
IF YOU WISH TO PLOT A CERTAIN RANGE OF Y-AXIS VALUES
FOR THE 2-D PLOTS, ENTER LEFT-END POINT IN COLUMNS 1-8 WITH
FORMAT F8.0 AND RIGHT-END POINT IN COLUMNS 9-16 WITH FORMAT F8.0;
OTHERWISE INPUT NO
NO
DO YOU WISH TO PLOT THE LOCUS OF RV SUCH THAT THE
SYSTEM RELIABILITY EQUALS THE UNIT RELIABILITY.
ANSWER YES OR NO
NO
DO YOU WISH TO HAVE 3-D RELIABILITY PLOTS - ANSWER YES OR NO
NO
DO YOU WISH TO CALCULATE MAXIMUM MISSION TIME AND SIMPLE TIME
FOR GIVEN RELIABILITY - ANSWER YES OR NO
```

Figure 1 (contd)

```
YES
DO YOU WANT PLOTS FOR THESE CALCULATIONS - ANSWER YES OR NO
YES
DO YOU WISH TO CALCULATE MAXIMUM MISSION TIME FOR
GIVEN RELIABILITY AND COMPARE IT AGAINST OTHER PARAMETERS.
ANSWER YES OR NO
YES
INPUT IN COLUMN 1 ONE OF THE FOLLOWING THREE OPTIONS:
1. MAXIMUM MISSION TIME IS COMPARED AGAINST ALL POSSIBLE
COMBINATIONS OF THE PARAMETER,
2. MAXIMUM MISSION TIME IS COMPARED AGAINST THE LAST TWO
PARAMETER VALUES,
3. THE PROGRAM ASKS THE USER AS TO WHICH PARAMETER VALUES
MAXIMUM MISSION TIME IS TO BE COMPARED.
1
DO YOU WANT PLOTS FOR THESE CALCULATIONS - ANSWER YES OR NO
NOTE: WHEN EXERCISING OPTION 1, THE PROGRAM PLOTS
ONLY THE FIRST 15 PARAMETER COMPARISONS
YES
INPUT THE FOLLOWING 4 VARIABLES EACH WITH FORMAT F8.0
COLUMNS 1-8 - REFERENCE RELIABILITY R2
COLUMNS 9-16 - MINIMUM RELIABILITY R1
COLUMNS 17-24 - MAXIMUM RELIABILITY R1
COLUMNS 25-32 - RELIABILITY R1 STEP SIZE
   1.000    .000   1.000    .100
DO YOU WISH TO HAVE PRINTED TABLE OF RELIABILITY RESULTS
ANSWER YES OR NO
YES
DO YOU WISH TO HAVE PRINTED TABLE OF DIFF, RIF,
AND GAIN RESULTS - ANSWER YES OR NO
YES
DO YOU WISH MTF AND RELIABILITY AT MTF RESULTS PRINTED
ANSWER YES OR NO
YES
DO YOU WANT PRINTED RESULTS OF THE MAXIMUM MISSION
TIME CALCULATIONS - ANSWER YES OR NO
YES
TYPE IN THE VARIABLE THAT IS TO BE USED
FOR THE FAMILY OF PARAMETERS - MUST BE SPECIFIED
K

      CALCULATIONS FOR EQUATION  1A      (NI MEANS NOT INPUTED)
                          PARAMETER IS K

 LAMBDA          MU          S    N          K          Q
    NI      .0000000         1    1    .1000000+01      NI

    C          RV           Z    W          P         MUT
   NI    .1000000+01         1    1    .1000000+01      NI

 LAMT       REL          UNREL        SIMREL       SIMGAIN       SIMRIF
 .000   1.0000000     .0000000   1.0000000    .1000000+01   .1000000+36
 .100    .9967989     .0032011    .9948374    .1101633+01   .2972798+02
 .200    .9794141     .0205859    .8187307    .1196259+01   .8805495+01

ETC...
```

Figure 1 (contd)

inverse dormancy factor of 10 and the applicable coverage factor being 0.99, it is required to evaluate the system survival probability in steps of 1/10 of a year for a maximum mission duration of 12 years. It is required that the system reliability be compared against the simplex or nonredundant system and that all these results be tabulated and also plotted. It is further required that the mean-life of the system as well as the reliability at the mean-life be computed. It is of interest to know the maximum mission duration that is possible while sustaining some fixed system reliability objective and to display the sensitivity of this mission duration with respect to variations in the tolerable mission reliability.

It is also required that the above analysis be carried out for the case where three standby spares are provided and these configurations of three and two spares be compared and the various comparative measures of reliability be evaluated and displayed.

The above problem formulation is entered into CARE by stating that Equation 2 (which models standby spare systems) is required and the pertinent data (S = 2, 3; Z = 8; K = 10; T = 12.0; LAMBDA = 0.5; C = 0.99; STEP= 0.1; option = 2) is inserted into CARE between the delimiters \$VAR. . .\$END using the VAR namelist.

The above example illustrates the complexity of problems that may be posed to CARE, and the simplicity with which the specifications are entered. The reliability theoretic functions to be performed on the above specified system are acknowledged interactively by responding a YES or NO on the demand terminal to CARE's questions at the time it so requests. A

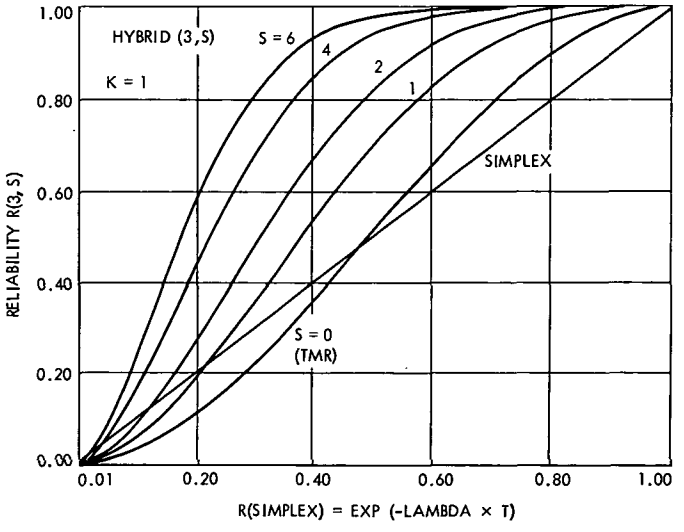

Figure 2. A sample plot by CARE

partial sample run illustrating the question/answer segment of CARE is shown in Figure 1. A sample reliability plot generated by CARE for the hybrid (3,S) system for $S = 6, 4, 2$, and 1 at $K = 1$ is given in Figure 2.

Acknowledgment

The author wishes to acknowledge the support of Mr. G. L. Winje of the Data Systems Division of JPL for much of the programming required in the implementation of the CARE subroutines.

References

1. Mathur, F. P., "Reliability Modeling and Analysis of a Dynamic TMR System Utilizing Standby Spares," *Proceedings of the Seventh Annual Allerton Conference on Circuit and System Theory, University of Illinois, Urbana, October 8–10, 1969*, pp. 243–252.

2. Mathur, F. P., and Avizienis, A., "Reliability Analysis and Architecture of a Hybrid Redundant Digital System: Generalized Triple Modular Redundancy with Self-Repair," *AFIPS Conference Proceedings (Spring Joint Computer Conference), Vol. 36, Atlantic City, May 5–7, 1970.*

3. Mathur, F. P., *Reliability Modeling and Architecture of Ultra-Reliable Fault-Tolerant Digital Computers*, Ph.D. Thesis, University of California at Los Angeles, Computer Sciences Dept., June 1970. University Microfilms, Inc., Ann Arbor, Mich., Reorder No. 71-662.

4. Roth, J. P., Bouricius, W. G., Carter, W. C., and Schneider, P. R., *Phase II of an Architectural Study for a Self-Repairing Computer*, Report SAMSO TR-67-106. International Business Machines Corp., Nov. 1967.

5. Mathur, F. P., "On Reliability Modeling and Analysis of Ultrareliable Fault-Tolerant Digital Systems," to be published in the Special Fault-Tolerant Computing issue of the *IEEE Transaction on Computers*, Vol. C-20, No. 10, Nov. 1971.

6. *Univac 1108 Multi-Processor System: System Description*, Form UP-4046, Rev. 2. Sperry Rand Corp., 1968.

7. *Univac 1108 Multi-Processor System: Fortran V Programmer's Reference Manual*, Form UP-4060, Rev. 1. Sperry Rand Corp., 1969.

8. Mathur, F. P., "Reliability Study of Fault-Tolerant Computers," in *Supporting Research and Advanced Development*, Space Programs Summary 37-58, Vol. III, pp. 106–113. Jet Propulsion Laboratory, Pasadena, Calif., Aug. 31, 1969.

9. Mathur, F. P., "Reliability Modeling, Analysis and Prediction of Ultrareliable Fault-Tolerant Digital Systems," *Digest of the 1971 International Symposium on Fault-Tolerant Computing, Pasadena, California, March 1–3, 1971*, pp. 79–82.

Computer Program for the Automated Attendance Accounting System

P. Poulson and C. Rasmusson

Data Systems Division

The Automated Attendance Accounting System (AAAS) was developed under the auspices of the Space Technology Applications Office at JPL. The task is basically the adaptation of a small digital computer, coupled with specially developed pushbutton terminals located in school classrooms and offices for the purpose of taking daily attendance, maintaining complete attendance records, and producing partial and summary reports. Especially intended for high schools, the system will relieve both teachers and office personnel from the time-consuming and dreary task of recording and analyzing the myriad classroom attendance data collected throughout the semester. In addition, since many school district budgets are related to student attendance, the increase in accounting accuracy is expected to augment district income. A major component of this system is the real-time AAAS software system, which is described in this article.

Introduction

The Automated Attendance Accounting System (AAAS) provides the capability to report, maintain, and interrogate attendance data automatically rather than manually. Its use is intended for junior and senior high schools where a period-by-period accounting of students is desired. The system is composed of a Varian 620i mini-computer with a 4096-word (16 bits/word) memory, a Vermont drum memory with 96 tracks (184,000 words), a teletype, 96 keyboard entry terminals, multiplexer and data buffer interface assembly, and the AAAS software. The 96 keyboard entry terminals are located in the classrooms, attendance office, and certain administrative offices. Each of these terminals has keys numbered 0 to 9 to record student numbers, plus buttons to signal absentees, tardinesses, error corrections, and emergency calls. Each student is assigned a unique four-digit identification number and is allocated a vital statistic and data file on a quick retrieval memory device. In this way, an up-to-date and recallable record of each student is available, as well as class rosters, class reports, and daily and monthly summaries.

The software capabilities fall into four general categories: interrupt processing, period processing, daily processing, and request processing. The program consists of approximately 8000 instructions with the interrupt processors and period processors residing in core continuously. The daily processors and request processors reside on drum and are loaded into core when needed by a set of overlay programs. This overlay procedure enables the program to greatly exceed available primary computer memory.

Attendance reporting is done by the teacher on a terminal in the classroom. This information is sent to the computer from the terminal. The data is then processed, stored on the drum, and displayed on the printer to be used by the attendance accounting office and the school administration.

Interrupt Processing

Interrupt processing refers to a hardware mechanism that temporarily suspends computational activity by the computer in order to receive and process events externally generated. Usually such interrupts are short in nature, and the system is designed to minimize the extent of computational perturbation. The clock, teletype operation, and classroom terminal inputs are processed on an interrupt basis. The clock interrupts are used to maintain the time of day in 4-s increments. Both the input and the output on the teletype are processed by interrupts. Once an output line is started, the computer resumes normal processing with the output being typed as the teletype is available. Classroom inputs consist of an event key generally preceded by a four-digit (student or teacher) identifier. The interrupt processor stores the classroom inputs into tables ordered by device number. One table holds the event input while a parallel table holds the four identifier digits (if more than four digits are input, only the last four are retained). The tables are processed in normal, non-interruptive, computational manner. If the input was acceptable, the feedback light is turned on for the terminal from which the input came. The response time is normally less than 1 s, but in extreme cases it could be as high as 3 s. The one exception to this processing is the emergency event. As soon as an emergency event is input, a message giving the location of the terminal is immediately output at the teletype.

Period Processing

During each period of the day, the software will accept attendance reporting from any terminal which has been activated by the input of a legitimate teacher key. Attendance input consists of a four-digit student identifier followed by an absence, tardy, or error event. The software updates the student master file from these inputs and produces the following output.

(1) At 8 min after period start time: an alphabetized list of absent students and an alphabetized list of tardy students.

(2) At 30 min after period start time: a list of returnees (except first period) and a list of returnees on probation (first period only).

(3) At 45 min after period start time: an alphabetized list of absent students that have been reported since the first listing was made, followed by an alphabetized list of tardy students that have been reported since the first listing was produced.

Terminals in the counselor's office may override any classroom absent input with a "student present this period" input. This provides for a student that is absent from class but is in the counselor's office. The attendance office terminals may be used to re-admit students with the proper reason (unexcused, excused, or other) and to declare a student absent all day.

Daily Processing

After the end of the last period, an end-of-day report is generated. This report shows the attendance (by period) for every student that was reported absent one or more periods during the day. Included in this list are indicators showing students on probation, students with excessive absences, students with excessive tardinesses, and problem students. In addition to the above output, a list is made of all students on probation that returned to class without re-admitting through the attendance office. The program also does a daily drum update. This processor takes the daily absence information and makes it part of the permanent file. This operation is either done on request (after the end-of-day list) or, if not requested, at 9:30 p.m.

Request Processing

The request processing capability of the AAAS provides the means of communication between the operator and the computer. Whenever possible, the computer will enter the request mode and the teletype will print, DEMAND, MODE: TYPE REQUEST PLEASE. This typeout indicates that the machine is available for communication. A request may be made using any one of the following teletype keys:

A — *Add a student record*
This allows the user to add a student to the master file. The student will be inserted alphabetically in the threaded file of students, and the computer will assign the student's identification number.

C — *Change a student record*
This allows the user to change any part of a student's master file except his student number and name.

D — *Delete a student record*
This allows any student record to be deleted from the master file.

I — *Interrogate a student record*
This allows any student record to be displayed given the student number.

K — *Update teacher keys*
This allows the user to change, add, or delete any teacher key.

R — *Prepare a special report*

(1) Print a class roster: a class roster for any good teacher key will be printed out for all periods.

(2) Produce an ADA monthly report: the information necessary to prepare the attendance report for state funding is printed.

(3) List students with excessive absences: students that have been flagged as having excessive absences are printed in an alphabetical list.

(4) List students on probation: students that have been flagged as probationary are listed alphabetically.

S — *Update period schedule*
The start and end times of any period can be changed. A free period may be created as desired.

T — *Initialize a time and school day number*
At the beginning of each day, the time must be input to synchronize the computer clock and the wall clock. The time may be set any time during the day if desired.

TAPE — *Dump allocated drum to tape*
All the information stored on the drum is punched on paper tape.

(NOT TAPE) — *Dump selected drum to tape*
All the volatile fields of the student records are punched on paper tape.

U — *Update drum*
All information contained in the daily attendance data portion of the master file is moved to the permanent portion of the student file.

/ — *Cancel current input*
This allows the requested input that is currently being typed to be aborted and processing to restart at the prior requested input.

RUBOUT *Cancel prior request*
The last request will be aborted and the program will await the next request (*demand mode*).

Additional input and/or output may be required depending upon the request processor selected.

If during the operation of a request processor it becomes time to do the period processing, the request processor is aborted and must be restarted when the program returns to *demand mode.*

The AAAS has hardware and software power fail capability. If power falls below a threshhold level, the program will be interrupted, registers saved, and automatically restarted when power is restored. If the power has been off for any length of time, then the time of day must be updated.

Conclusions

The Automated Attendance Accounting System has been in operation at the John F. Kennedy High School in Sacramento since February 1971. One of the more important and interesting aspects of the task is the application of this type of technology and fabrication totally outside the aerospace industry. Here was an opportunity to conceive, design, and install a system for use by individuals totally unfamiliar with computers and their possible applications. The outstanding problem was in the articulation of just exactly what type of system was needed, or, indeed, even wanted. It was illuminating to discover the difficulties in communication between people of diverse and dissimilar disciplines, further complicated by a kaleidoscope of opinions and pre-conceived ideas. The faculty especially presented a range of mixed feelings. The operational test period has shown that there is some need for enhancement in both the software and hardware, but that the system does work and is capable of doing automatic attendance accounting. During this period, it was noted that the teacher input for all periods was less than desired. After the initial learning period was over, the percentage of all day absent students that were counted absent all periods was between 40 and 70%. The correct input of re-admits, when the student returns to class, will override this lack of integrity of absent data as far as the average daily attendance (ADA) reporting to the state is concerned; however, the individual student's absent record for each period is still in error. During the next operational test, an attempt will be made to increase the teacher input.

The AAAS will provide school officials with rapid, continuous attendance information which will satisfy the state requirements for attendance (ADA) accounting information, and, at the same time, fulfill the need for improved saving of valuable teacher time, which was previously devoted to the attendance accounting function. The system will allow the attendance officer more time for individual student attendance problems by eliminating most of the manual processing of attendance data, and by generating most of the

attendance reports automatically. The real-time accountability of each student for each period will be a valuable asset to the school administration in the smooth and tranquil operation of the school. An indirect advantage of the system is that it makes possible the implementation of a student attendance honor system. This system is desirable from the administration standpoint in that it reduces congestion at the re-admit windows, and, from the student standpoint, it gives them an added responsibility.

Onset of Superconductivity in Sodium and Potassium Intercalated Molybdenum Disulphide

R. B. Somoano and A. Rembaum

Propulsion Division

Molybdenum disulfide in the form of natural crystals or powder has been intercalated at -65 to -70°C with sodium and potassium using the liquid ammonia technique. All intercalated samples were found to show a superconducting transition. A plot of the percent of diamagnetic throw versus temperature indicates the possible existence of two phases in the potassium intercalated molybdenum disulfide. The onset of superconductivity in potassium and sodium intercalated molybdenite powder was found to be ≅6.2 and ≅4.5 K, respectively. The observed superconductivity is believed to be due to an increase in electron density as a result of intercalation.

There is considerable interest at present in one- and two-dimensional superconducting systems (References 1, 2, and 3). In an attempt to investigate superconductors which are two dimensional in nature, we have introduced metallic sodium and potassium into the layered structure of molybdenum disulphide (MoS_2). In the present communication we report preliminary data which indicate that MoS_2 intercalated with sodium or potassium is superconducting.

MoS_2 has been extensively studied (Reference 4) and its electrical, magnetic, optical, and structural properties are well known. It has a layered structure, characterized by a high degree of anisotropy as shown in Figure 1. Within each layer there exists trigonal prismatic coordination between the Mo and S atoms, and the bonding in the layer is primarily covalent. Variations in the stacking sequence of the layers result in the formation of two polytypes (Reference 5). These are the 2H (H denoting the hexagonal unit cell) and the 3R (rhombohedral) polytypes. The layers are held together by weak Van der Waals forces. The result of this weak binding is that the interlayer gap may easily be increased to accept alkali metal atoms or ions from an alkali metal-ammonia solution. Chemical and X-ray data for the alkali metal intercalates of MoS_2 have been obtained by Rudorff (Reference 6). The optical spectrum of MoS_2 contains two excitonic absorption bands,

of hydrogenic nature (Reference 7), which results from transitions from a spin orbit split valence band (Reference 4). MoS_2 is not superconducting down to 1.28 K (Reference 8).

The MoS_2 samples used in the present investigation were crystals of high purity grown by chemical vapor transport,[1] crystals cleaved from a large natural crystal of molybdenite,[2] and purified natural ore.[3] X-ray powder diffraction data indicated that all types of samples were of the 2H polytype. An emission spectrographic analysis of the impurities is shown in Table 1. The MoS_2 samples were tested for superconductivity prior to intercalation using a self-inductance technique (Reference 9), and none of the samples were found to be superconducting. The samples were intercalated by placing them in a blue sodium-ammonia or potassium-ammonia solution (concentration ~0.1 mole percent metal) for ~72 h. This was followed by rinsing with liquid ammonia until all traces of excess metal had been removed from the surface, and, finally, by outgassing for 24 h to remove traces of ammonia. All operations were carried out in a high-vacuum system in absence of air.

[1] The authors are indebted to Dr. Fred Gamble of Synvar Associates, Palo Alto, Calif., for supplying the synthetic crystals.

[2] Molybdenite samples obtained from Ward's Natural Science Establishment, Rochester, N.Y.

[3] From Climax Molybdenum Co., Ann Arbor, Mich.

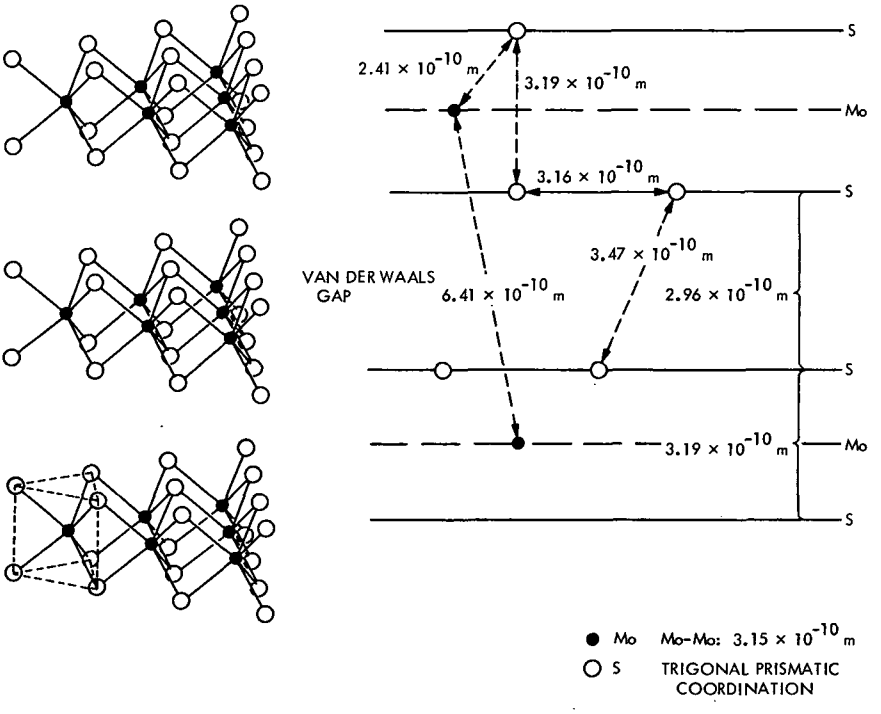

Figure 1. The structure of MoS_2

The determination of sodium or potassium by means of atomic absorption and chemical analysis showed that the crystals were only partially intercalated and their composition could be represented by M_xMoS_2 ($0.1 \leq x \leq 0.5$), where M is sodium or potassium. Therefore, the amount of metal was less than in the specimens prepared by Rudorff (Reference 6), and this result could be attributed to insufficient intercalation time. The fact that the intercalations were not complete was confirmed by X-ray analysis of the sodium or potassium intercalates carried out in absence of air. The X-ray results indicated the presence of both unintercalated as well as intercalated MoS_2.

In addition, the C_0 dimension of sodium and potassium intercalated samples expanded by 1.5×10^{-10} and 4.07×10^{-10} m (1.5 and 4.07Å), respectively. The expansion of the C_0 dimension of the sodium intercalated molybdenite crystal is approximately half that found by Rudorff. This is probably due to the sodium ions occupying the octahedral holes in only one of the two Van der Waals gaps in the unit cell, and would imply a stage two-type intercalation.

Table 1. Emission spectographic analysis of impurities in MoS_2

Component	Molybdenite (natural crystals),[a] ppm	Synthetic crystals,[b] ppm	Molybdenite purified natural ore,[c] ppm
Si	1200	<100 (not detected)	
Fe	870	230	590
Cu		17	
Ca	550	<10 (not detected)	
Mg	10	6.5	
C	900		2000
MoO_3			140
Oil			240
H_2O			350
Acid insoluble			220

[a] Purity = 99.6%.

[b] Purity = 99.97%.

[c] Purity = 99.65%.

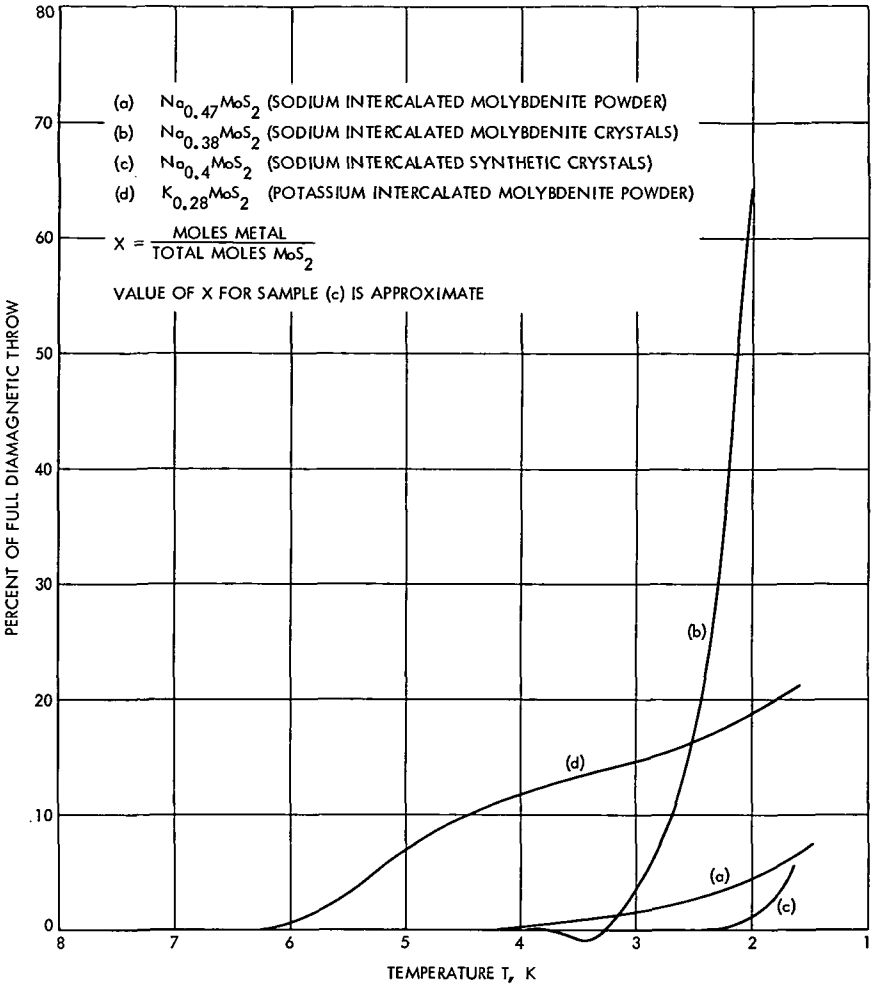

Figure 2. Onset of the superconducting transition in intercalated samples

All intercalated samples exhibited a superconducting transition (Figure 2). In Figure 2, the percent of the full diamagnetic throw is plotted against absolute temperature for potassium and sodium intercalated samples. The percent of the full diamagnetic throw observed in the samples studied was determined by calibration runs using several volumes of either lead or niobium. The sodium intercalated molybdenite powder (curve a) exhibits a wider transition than that observed for sodium intercalated molybdenite crystals (curve b). A sharper transition is found as expected in pure synthetic crystals (curve c). The onset of superconductivity in the potassium intercalated molybdenite powder (curve d) is approximately 2.3 deg higher than the sodium intercalated powder (curve a). At the present stage of investigations, the differences in the onset of the superconducting transitions shown by different alkali metals are not well understood. The shape of curve d indicates the possible existence of a second phase in the potassium

intercalated molybdenite powder. This could be due to two different coordinations of the potassium atoms in the Van der Waals gap or to two different stages of intercalation. Preliminary X-ray powder diffraction data seem to corroborate the existence of two phases (the 002 line is unusually broad). It is hoped that X-ray examination of intercalated single crystals might yield a definite answer to this question.

Superconductivity in these intercalates of MoS_2 is believed to be due to electrons from the alkali metal going into the unfilled d-band of MoS_2. The increase in free electron charge density increases the transition temperature of MoS_2 to the measurable values found in this investigation. This process utilizes the proposed band structure (Reference 10) and has been suggested previously in the interpretation of optical data on Na_xMoS_2 (Reference 11). Work is presently underway to determine the mechanism of the observed superconductivity, the effects of different alkali metals, and the effect of crystal orientation on the superconducting transition.

Acknowledgment

The authors express their appreciation to Dr. J. Mercereau for the superconductivity test down to 1.3 K and to Drs. A. Hermann, V. Hadek, and S. P. S. Yen for experimental help and useful discussions.

References

1. Hannay, N. B., Geballe, T. H., Matthias, B. T., Andres, K., Schmidt, P., and MacNair, D., *Phys. Rev. Lett.*, Vol. 14, p. 225, 1965.
2. Salzano, F. J., and Strongin, M., *Phys. Rev.*, Vol. 153, p. 533, 1967.
3. Gamble, F. R., Di Salvo, F. J., Klemm, R. A., and Geballe, T. H., *Science*, Vol. 168, p. 568, 1970.
4. Wilson, J. A., and Yoffe, A. D., *Advan. Phys.*, Vol. 18, p. 193, 1960.
5. Jellinek, F., Brauer, G., and Mueller, H., *Nature*, Vol. 185, p. 376, 1960.
6. Rudorff, W., *Chimia*, Vol. 19, p. 489, 1965.
7. Evans, B. L., and Young, P. A., *Proc. Roy. Soc. London, Ser. A*, Vol. 284, p. 402, 1965.
8. Matthias, B. T., and Hulm, J. K., *Phys. Rev.*, Vol. 87, p. 799, 1952.
9. Schawlow, A. L., and Delvin, G. E., *Phys. Rev.*, Vol. 113, p. 120, 1959.
10. Connell, G. A. N., Wilson, J. A., and Ioffe, A. D., *J. Phys. Chem. Solids*, Vol. 30, p. 287, 1969.
11. Acrivos, J. V., Liang, W. Y., Wilson, J. A., and Yoffee, A. D., *J. Phys., Sec. C*, Vol. 4, p. 118, 1971.

Long-Term Aging of Elastomers: Chemical Stress Relaxation of Fluorosilicone Rubber and Other Studies

S. H. Kalfayan, A. A. Mazzeo, and R. H. Silver

Propulsion Division

Elastomers have varied aerospace applications, including: propellant binders, bladder materials for liquid propellant expulsion systems, and fuel tank sealants, particularly for high-speed aircraft. Predicting the long-term behavior of these materials is of paramount importance. A comprehensive molecular theory for mechanical properties has been developed at JPL. It has only been tested experimentally in cases where chemical degradation processes are excluded. Hence, a study is underway to ascertain the nature, extent, and rate of chemical changes that take place in some elastomers of interest. The results can then be incorporated in the theoretical framework. This article reports progress on the investigations of chemical changes that may take place in the fluorosilicone elastomer, LS 420, which is regarded as a fuel and high-temperature-resistant rubber. The kinetic analysis of the chemical stress relaxation and gel permeation chromatography studies comprise the major portion of this article.

Introduction

The nature and extent of chemical changes that take place in a number of selected elastomers at long times is under study. Previously, investigation of the chemical degradation of styrene-butadiene rubber (SBR) was reported (References 1, 2, and 3). Presently, the fluorosilicone gum rubber LS 420 and its peroxide vulcanizate is under examination. The structure of this elastomer is represented as follows:

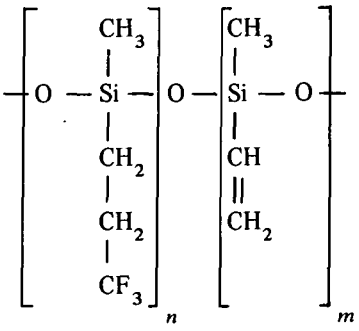

$n > 99.5\%$

Silicones are noted for their resistance to extremes of temperature, but they lack resistance to hydrocarbon-based fuels and lubricating oils used in aircraft. The introduction of fluorine atoms imparts resistance to non-polar fluids. The vinyl groups in the fluorosilicone chain provide sites for crosslinking (curing). Their concentration is less than 0.2% by weight. LS 420 was selected because it represented a suitable test material to support the theoretical developments for viscoelastic behavior generated at JPL (Reference 4), and also because it related this study to the advanced sealants, particularly the fuel tank sealants program at the Marshall Space Flight Center.

Four different methods were applied to determine the network changes that take place when the fluorosilicone elastomer is heat-aged. These were: (1) infrared spectroscopy, (2) gel permeation chromatography (GPC), (3) thermogravimetric analysis or weight-loss measurements, and (4) stress-relaxation measurements. This article discusses the results of these measurements.

Results and Discussion

IR Studies

The residues of the samples of LS 420 gum heated in air from 180 to 315°C showed no changes in the IR spectra, although degradation, particularly at the higher temperatures, was severe as evidenced by the high weight losses and the change in the physical condition of the samples. This indicates that possible alterations in the structure of the repeating unit of the elastomer must be less than 4–5%, i.e., the sensitivity limit for IR. Elemental analyses of the degraded and undegraded polymer showed no significant change in composition, indicating the absence of new functional groups, such as —OH, —OOH or >C=O. These results are unlike those obtained for the hydrocarbon rubber, SBR, which on oxidation showed the presence of —OH and >C=O groups in the polymer network (Reference 3).

LS 420 was also subjected to oxygen plasma at 20 N/m^2 (0.15 mm of Hg).[1] Changes in the IR spectra were not observable, although the samples showed some crazing and hardening.

Gel Permeation Chromatography

The GPC chromatogram of the unheated LS 420 gum showed two peaks, the larger representing a compound of molecular weight 450,000 (polystyrene calibration) and the smaller representing a compound of molecular weight 630 (polypropylene glycol calibration). Peak area measurements indicated 93–95% high molecular weight species and 5–7% low molecular weight compound. A molecular weight of 624 corresponds to a tetramer of γ, γ', γ''-trifluoropropyl methyl siloxane, the principal repeating unit of LS 420. The tetramer most probably is cyclic, because that represents the most stable configuration (actually the polymer is made from the cyclic tetramer), and because no end-groups such as —OH, —OR were detected by IR or wet chemical analysis. As heat aging of the fluorosilicone progressed, GPC analysis showed a gradual increase in the concentration (increase in the peak area) of the 630 molecular weight compound, and a gradual decrease in the concentration of the high molecular weight compound, indicating the possibility of using GPC for degradation rate studies. But this intent was complicated by the finding that THF, the solvent used in analysis, degrades the polymer even at room temperature. This was proved by viscosity and molecular weight measurements of THF solutions of the polymer. Reduction in both viscosity and molecular weight was observed. Moreover, the degradation was enhanced when the THF solution was filtered through an asbestos filter prior to GPC analysis. No acceleration was noticed when the solution was filtered through fritted glass. The pH of the asbestos is the suspected cause of this phenomenon.

Other solvents that attacked LS 420 chemically were acetone and MIBK, both of which, like THF, are mildly nucleophilic and could attack the slightly positive silicone atom in the fluoropropyl siloxane chain.

The GPC chromatograms also indicated that degradation or scission of the siloxane chain is most probably random as opposed to the ordered unzipping of the repeating unit, because molecular weight decrease was very rapid.

Weight-Loss Studies

The weight loss versus time studies were made in air at temperatures from 240 to 315°C. The data obtained fitted a first-order rate equation. The Arrhenius plot yielded an activation energy, ΔE, of 1.037×10^5 J/mole (24.7 kcal/mole) (Figure 1).

[1] Values in customary units are included in parentheses after values in SI (International System) units if the customary units were used in the measurements or calculations.

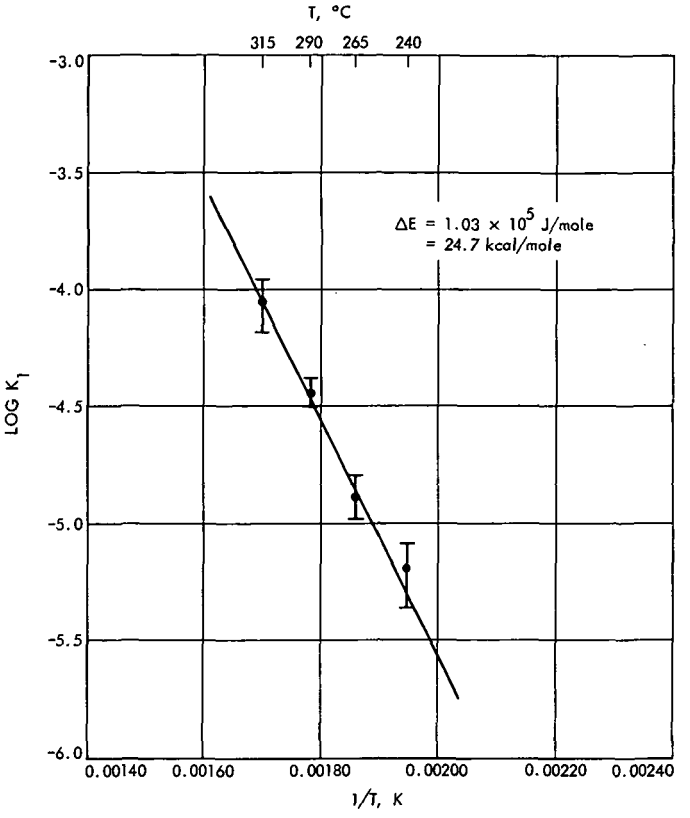

Figure 1. Temperature dependence of rate constants obtained from weight-loss measurements for LS 420 fluorosilicone rubber

Stress-Relaxation Measurements

Stress relaxation is a valuable technique to obtain data of fundamental significance concerning the aging or the chemical degradation of elastomers. It was developed by Tobolsky and others in the early 1940's (Reference 5). The stress-relaxation experiments were carried out with dicumyl peroxide (Di-cup)-vulcanized LS 420 in air, in nitrogen, and in JP-4 fuel. A specially constructed relaxometer capable of measurements at high temperatures, i.e., up to 260°C, and in fuel, was used. Some of the results shown in Figure 2 are plots of the logarithms of relative stress-relaxation f_t/f_0 versus time, where f_t and f_0 are the tensile force at time t and t_0, respectively.

Energy of activation values were obtained from Arrhenius plots (Figure 3) by using two sets of data obtained from the stress-relaxation experiments carried out in air: (1) half-times, and (2) shift factors, log K_t along the time

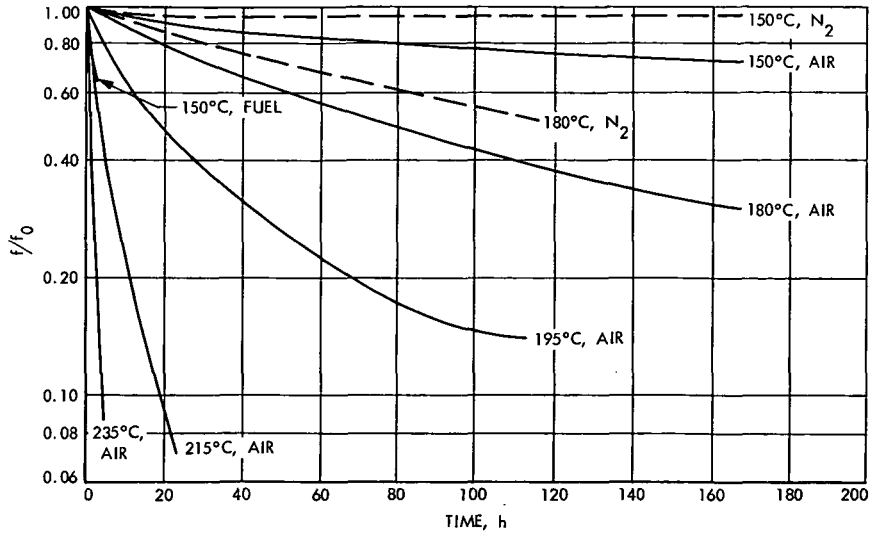

Figure 2. Effect of temperature on stress relaxation of peroxide-cured LS 420 fluorosilicone rubber

axis. The shift factors were obtained by superposition of f_t/f_0 versus log t curves at various temperatures over the curve obtained at 215°C, the reference temperature. Half-times refer to the time it takes for the initial stress to decay 50%. Activation energies, ΔE, were as follows:

(1) 1.52×10^5 J/mole (36.3 kcal/mole) from half-time data.

(2) 1.58×10^5 J/mole (37.7 kcal/mole) from shift factors.

These values are in good agreement. However, ΔE obtained from weight-loss measurements is much lower. The two processes, chemical stress relaxation and thermal degradation, are most probably due to different reaction mechanisms.

Continuous and intermittent stress-relaxation measurements enable the determination of the number of network chains, ν_e, formed during aging. Intermittent relaxation measures the net result of both scission and crosslinking during network breakdown. Continuous relaxation measurements cannot distinguish between new network chains formed by crosslinking from the original chains. If at anytime during the intermittent relaxation experiment the stress is larger than during the continuous relaxation experiment, the difference represents the contribution of the crosslinking

reaction (Reference 6). The number of new network chains, or the number of crosslinks formed, ν_e, can be calculated from the following equation:

$$\nu_e = \frac{1}{RT\left(\lambda - \frac{1}{\lambda^2}\right)}\left[\frac{\left(\frac{f_t}{f_0}\right)^i (f_0)^i}{A^i} - \frac{\left(\frac{f_t}{f_0}\right)^c (f_0)^c}{A^c}\right]$$

where

λ = the extension ratio

A = the cross-sectional area of specimen

f_t, f_0 = stresses at time t and t_0

R and T have their usual meanings. The superscripts i and c denote intermittent and continuous stress relaxation.

Examination of the intermittent and continuous stress-relaxation curves (Figure 4) shows that vulcanized LS 420 undergoes crosslinking during thermal aging in air at 195 and 215°C, the two temperatures at which intermittent runs have been made so far. Plots of ν_e versus time (Figure 5) show that crosslinking first increases with time and then decreases for experiments carried out in air. The experiment performed in nitrogen at 180°C (Figure 5) was discontinued after 50 h because of specimen failure. It is probable that this curve would also slope downwards after reaching a maximum, as in the case of the two other curves in the same figure.

Stress-relaxation curves obtained for runs carried out in pure nitrogen at 150 and 180°C lie above those carried out in air at the same temperatures (Figure 2), indicating that relaxation due to chemical changes is caused more by atmospheric oxygen than by thermal effects at the temperatures used. Values of stress decay in air and nitrogen are given in Table 1.

It is of interest to know whether scission takes place randomly along the polymer chain, or at the crosslink sites. The crosslink site in LS 420 is

probably as follows (Reference 7), formed from the vinyl-free radical of one chain and the $-CH_3$ of another chain:

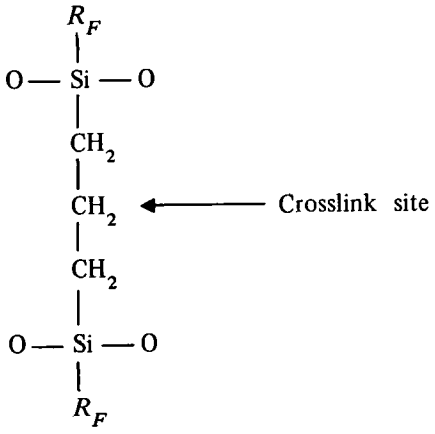

where R_F represents $-CH_2-CH_2-CF_3$.

It has been stated that random scission along the polymer chain is indicated when the rate of relaxation is found to be inversely proportional to the crosslink density, and scission at the crosslink is indicated when the rate of relaxation is independent of crosslink density (Reference 6). The stress-relaxation rate of an LS 420 specimen cured with 0.05% Di-cup, yielding a rubber of lower crosslink density than those used in this study, was much higher, indicating that random scission along the polymer chain predominates.

Table 1. Values of stress decay in air and nitrogen

Test condition	Decay of tensile force, %	
	150°C	180°C
Air		
After 14 h	14	22
After 168 h	30	70
Nitrogen		
After 14 h	4	12
After 168 h	5	40

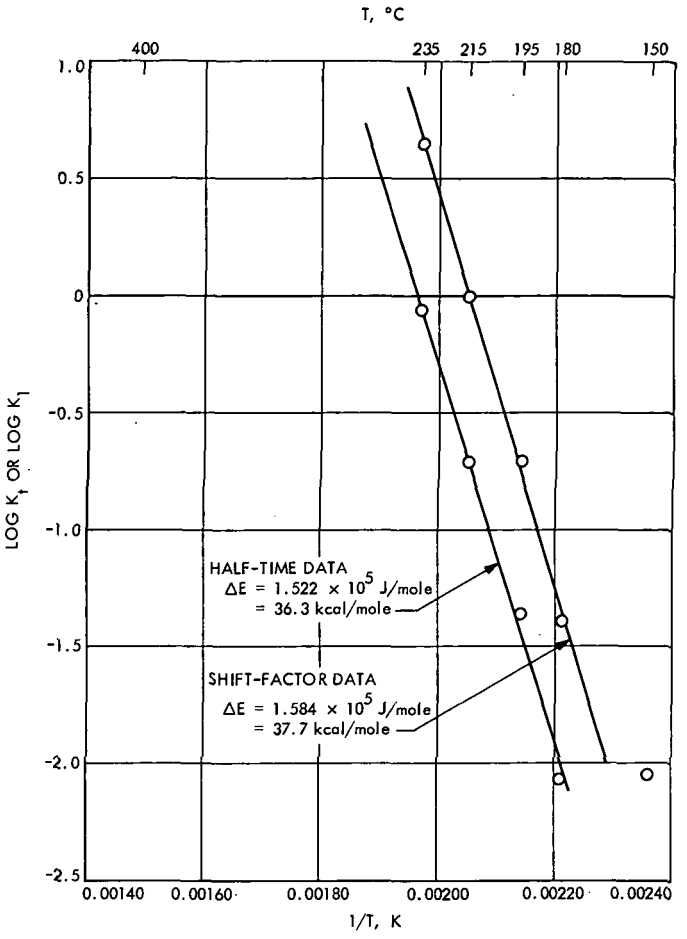

Figure 3. Temperature dependence of shift factors and half-time data obtained from stress-relaxation measurements

Conclusions

Results of these experiments indicate that:

(1) Some crosslinking takes place when the fluorosilicone rubber, LS 420, is heated in air, but scission predominates.

(2) Scission takes place randomly along the chain, rather than by an orderly unzipping of monomer units from the polymer molecule.

(3) Chain scission rather than scission at the crosslink sites predominate. [The former involve the breaking of siloxane bonds, i.e., —Si–O—Si— (bond energy 88.2 kcal/mole). Scission at crosslinks involves the breaking of Si—C or C—C bonds (bond energies 69.3 and 83.1 kcal/mole, respectively). Although the siloxane bond is the strongest, its

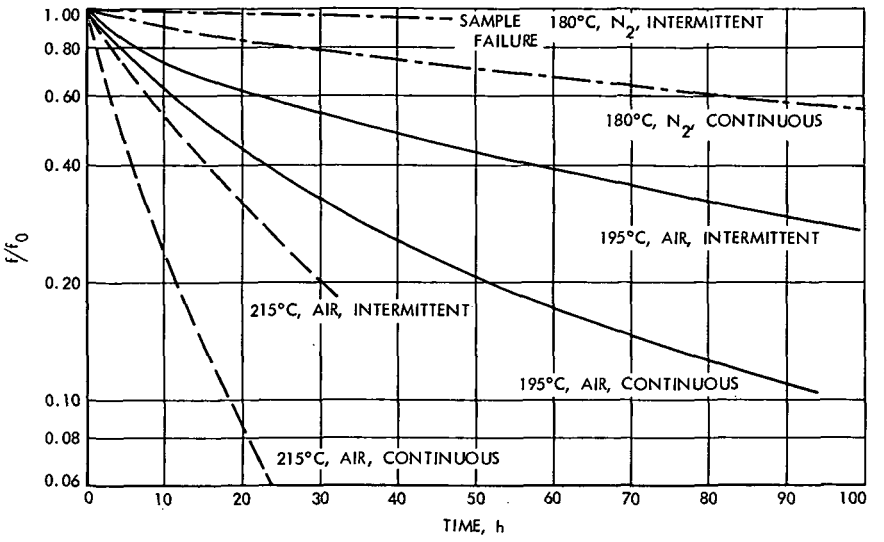

Figure 4. Continuous and intermittent stress relaxation in LS 420 at various temperatures in air and nitrogen

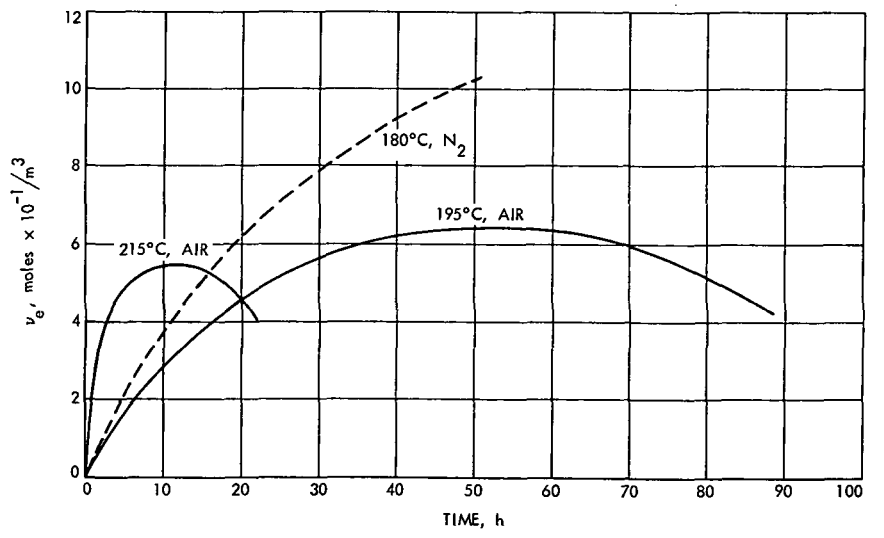

Figure 5. Additional network chains formed in LS 420

51% ionic character makes it susceptible to nucleophilic and electrophilic attack. Thus, basic and acidic impurities found in the rubber (such as polymerization catalysts) will enhance the scission of the relatively strong Si—O bond at elevated temperatures.]

(4) Analysis of the kinetic data obtained indicate that at room temperatures (20 to 25°C) the fluorosilicone rubber will show negligible chemical degradation for very, very long times, i.e., several decades.

References

1. Kalfayan, S. H., Rakutis, R., and Silver, R. H., "Long-Term Aging of Elastomers: Chemical Stress Relaxation Studies of Peroxide-Cured Styrene-Butadiene Rubber," in *Supporting Research and Advanced Development*, Space Programs Summary 37-59, Vol. III, pp. 194–198. Jet Propulsion Laboratory, Pasadena, Calif., Oct. 31, 1969.

2. Rakutis, R., and Kalfayan, S. H., "Long-Term Aging of Elastomers: Stress Relaxation of SBR With Thiophenol," in *Supporting Research and Advanced Development*, Space Programs Summary 37-62, Vol. III, pp. 242–244. Jet Propulsion Laboratory, Pasadena, Calif., Apr. 30, 1970.

3. Rakutis, R., Silver, R. H., and Kalfayan, S. H., "Long-Term Aging of Elastomers: Kinetics of Oxidation of SBR by Infrared Spectroscopy," in *Supporting Research and Advanced Development*, Space Programs Summary 37-64, Vol. III, pp. 125–130. Jet Propulsion Laboratory, Pasadena, Calif., Aug. 31, 1970.

4. Moacanin, J., and Aklonis, J. J., "Viscoelastic Behavior of Elastomers Undergoing Crosslinking Reactions," in *Supporting Research and Advanced Development*, Space Programs Summary 37-66, Vol. III, pp. 187–189. Jet Propulsion Laboratory, Pasadena, Calif., Dec. 31, 1970.

5. Tobolsky, A. V., Prettyman, I. B., and Dillon, J. H., *J. Appl. Phys.*, Vol. 15, p. 309, 1944.

6. Tobolsky, A. V., *Properties and Structure of Polymers*, p. 223. John Wiley & Sons, Inc., New York, 1960.

7. Thomas, D. K., *Heat Stability in Fluorosilicones*, Technical Report 68234. Royal Aircraft Establishment, Farnborough, England, Sept. 1968.

TOPS Attitude Propulsion Subsystem Technology

P. I. Moynihan

Propulsion Division

This article summarizes the JPL Thermoelectric Outer-Planet Spacecraft (TOPS) Attitude Propulsion Subsystem effort through the end of fiscal year 1971. It includes the tradeoff rationale that went into the selection of anhydrous hydrazine as the propellant, followed by a brief description of three types of 0.445-N (100-mlbf)[1] thrusters that were purchased for in-house evaluation. A discussion is also included of the 0.2224-N (50-mlbf) JPL-developed thrusters and their integration with a portable, completely enclosed, propulsion module that was designed and developed to support the TOPS single-axis attitude control tests in the JPL Celestarium. The article concludes with a synopsis of further work which will be accomplished prior to the onset of an outer-planet mission.

Function and Description

The Thermoelectric Outer-Planet Spacecraft (TOPS) is a three-axis stabilized vehicle for which the primary attitude control and stabilization is performed by three mutually perpendicular momentum wheel sets. The wheels in each axis have been implemented as redundant pairs to increase the mission probability of success. The primary requirement of the Attitude Propulsion Subsystem (APS) is to function in support of the Attitude Control Subsystem.

The APS is required to: (1) perform tipoff rate reduction and acquisition maneuvers immediately after launch; (2) perform approximately 2500 momentum wheel unloadings in the yaw axis (less in the pitch and roll axes); (3) perform commanded turns, which consist of nine positioning maneuvers throughout the 10-yr mission to orient the spacecraft for trajectory correction, of rolling the spacecraft 60 times (once every half AU) and yawing 30 times (once every AU) for calibration of science instruments, and of performing up to 20 re-acquisitions in the event of transient excursions

[1] Values in customary units are included in parentheses after values in SI (International System) units if the customary units were used in the measurements or calculations.

outside the sensor deadband; and (4) perform backup limit cycle control in the event that 2 wheels fail in a single axis. These functions, with the exception of item (4), are summarized in Table 1 in terms of the required torque impulse. If backup limit cycle is required, the necessary propellant will be derived from the Trajectory Correction Propulsion Subsystem (TCPS) allocation. A spacecraft system-level tradeoff has determined that a net mass saving can be realized if the momentum wheel mass is reduced by transferring the functions of performing the various commanded turns to the APS.

The TOPS APS baseline configuration is integral with the TCPS, thus comprising the TOPS propulsion module. The TCPS and the APS share a common propellant supply of liquid anhydrous hydrazine, which is sized primarily by the TCPS design requirements. The APS propellant lines extend from the supply tank to the thruster/valve assemblies located in the propulsion bay and protrude through the thermal blanket. The present configuration of the TOPS propulsion module is depicted in Figure 1. The locations of the roll, pitch, and yaw thruster/valve assemblies, along with the related components, are indicated.

Table 1. TOPS APS torque impulse requirements[a]

Function	Pitch		Yaw		Roll	
	m-N-s	(ft-lbf-s)	m-N-s	(ft-lbf-s)	m-N-s	(ft-lbf-s)
Rate reduction (54 mrad/s)	21.76	(16)	110.2	(81)	110.2	(81)
Commanded turns (3 mrad/s)						
Positioning for trajectory correction (9)	—	—	220.3	(162)	220.3	(162)
Science maneuvers (60 roll, 30 yaw)	—	—	734.4	(540)	734.4	(540)
Re-acquisitions (2/yr)	48.96	(36)	244.8	(180)	244.8	(180)
Wheel unloadings						
Solar torques	122.4	(90)	613.4	(451)	97.9	(72)
Micrometeoroid	68.0	(50)	68.0	(50)	68.0	(50)
Contingency	78.9	(58)	171.2	(126)	224.5	(165)
Totals	340.0	(250)	2162.3	(1590)	1700.1	(1250)

[a] Required total impulse (based on nominal moment arms for the 3 axes) = 10,200 N-s /2295 lbf-s).

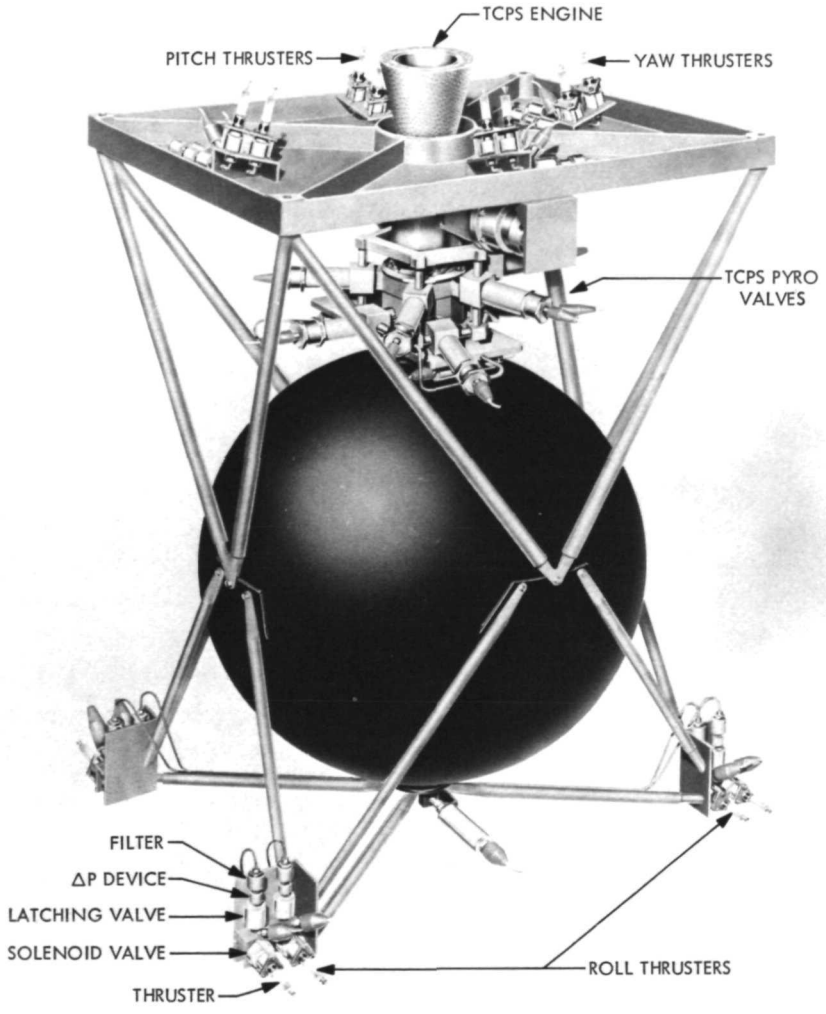

Figure 1. TOPS propulsion module configuration 12L/A

The APS consists of 16 thruster/valve assemblies, of which 8 will be active and 8 will be standby redundant. In the event of a single thruster/valve failure, the function of the failed unit will be transferred to the standby unit on a one-for-one basis. The requirement for 8 active thrusters rather than 6 is derived from the fact that the roll thrusters are implemented as a couple, while those for pitch and yaw are non-coupled. The nominal beginning-of-mission torque level requirements are 0.136 N-m (0.1 ft-lbf) in pitch and 0.27 N-m (0.2 ft-lbf) in roll and yaw. Each thruster is designed for a nominal 0.4448-N (0.1-lbf) thrust.

The single-propellant tank operates in a blowdown mode (rather than being pressure-regulated) to improve subsystem reliability. The tank pressure blows down from 2.76×10^6 to 1.38×10^6 N/m^2 (400 to 200 psia) as dictated by TCPS requirements. The APS thrusters operate at a lower inlet pressure than does the TCPS thruster, and, therefore, each APS thruster/valve combination incorporates a pressure-dropping device. The baseline device is a coiled section of small diameter tubing [approximately 0.381 m (15 in.) long by 2.54×10^{-4} m (0.01 in.) internal diameter]; however, a smaller fluid resistance device that is less susceptible to contamination is also being tested. The pressure-dropping device also serves as a means of metering the very low liquid flowrates [approximately 2.268×10^{-4} kg/s (5×10^{-4} lbm/s)].

Each APS thruster/valve assembly consists of a thruster, a thermal isolation structure and injector tube, a normally closed solenoid valve, a latching solenoid valve, the pressure-dropping/flow-metering device, and a filter. Each active thruster is injected with liquid anhydrous hydrazine, which is decomposed through a 20–30-mesh Shell 405 catalyst bed to generate hot gases that are expelled through a high-expansion-ratio nozzle. Each thruster is coupled to its solenoid valve through the thermal isolation structure to minimize heat soakback into the valve seat area.

The baseline filter is a 1-μm (absolute), stacked disc labyrinth filter. This unit, which incorporates a JPL etched disc design, was designed and fabricated by a contractor who has assembled and acceptance-tested five units. These have been delivered to JPL for further evaluation.

The baseline normally closed solenoid valve incorporates an internally actuated, in-line poppet to take advantage of the smaller mass and envelope. However, studies of the externally actuated (torque motor) concept are also being conducted. The valves incorporate a soft seat sealing configuration,and studies to determine the optimum seat design and material are being conducted.

The latching solenoid valve is similar to the normally closed solenoid valve but possesses a bi-stable actuator that enables the valve to be positioned in either an open or closed condition. The valve repositioning is executed by a short-duration electrical pulse, after which no further holding power is required.

Tradeoff Rationale

At the time when a liquid hydrazine Attitude Propulsion Subsystem was first considered for TOPS, the baseline mass expulsion system was the traditional cold gas nitrogen with 0.04448-N (0.01-lbf) thrusters located at the end of 3.048-m (10-ft) lever arms. The higher performance (I_{sp}) of a

hydrazine system enabled the thrusters to be relocated within the propulsion bay. This option eliminated the requirement for thermal control of the long feed lines. It also eliminated the need for line flexures and the impact on other subsystems from thruster feed lines being threaded through them. Having the propellant source common with the TCPS supply permits increased APS reserves, and eliminates the requirement for high-pressure tankage. The combination of high system performance and the storage of a low-pressure liquid (instead of high-pressure gas) propellant resulted in a reduced subsystem mass with equivalent reliability.

Experimental Thrusters

Late in fiscal year 1970, JPL purchased 0.4448-N (0.1-lbf) thrusters from Hamilton-Standard, Marquardt, and Rocket Research for in-house evaluation. These thrusters, although similar in physical size (Figure 2), are of three different internal designs. The thrusters are currently being evaluated for a TOPS duty cycle.

In support of the TOPS single-axis attitude control validation tests in the JPL Celestarium (a stellar simulation facility), a nominal 0.2224-N (0.05-lbf) catalytic thruster was designed, fabricated, and tested in-house. Since the tests in the Celestarium were to be performed on an air-bearing table at atmospheric pressures, the thruster was designed with an expansion area ratio of 1.5. The steady-state chamber pressure is nominally 4.5×10^5 N/m^2 (65 psia). A sea-level I_{sp} of approximately 1225.7 N-s/kg (125 lbf-s/lbm) was obtained, which translates to a vacuum I_{sp} of approximately 2010.2 N-s/kg (205 lbf-s/lbm) for a nozzle with a 40:1 expansion ratio. The steady-state c^* is nominally 1188.7 m/s (3900 ft/s). A conceptual view of this thruster is presented as Figure 3.

Two of these thrusters were then integrated into a self-contained, completely enclosed, portable propulsion module (shown in Figure 4), which was tested in the Celestarium. The module is composed of a 0.3048- × 0.1524- × 0.3302-m (12- × 6- × 13-in.) sheet metal enclosure for the feed system and a 0.2286- × 0.1016- × 0.076-m (9- × 4- × 3-in.) container for the solenoid valves, capillary tubes, and thruster supports. These all-aluminum enclosures are joined by a 0.457- by 0.0381-m (18 by 1½-in.)-diameter tube which functions both as a support member and as an enclosure for the propellant feed tube. All surfaces have been black anodized for minimum light reflection during Sun sensing operations. The larger section in the figure encloses the feed system, which consists of a propellant tank containing 500 cm^3 (½ liter) of hydrazine, a 5-μm (absolute) filter, a hand-operated shutoff valve (shown between the liquid and gaseous nitrogen fill valves), and the related tubing. The smaller enclosure contains two opposing thrusters (shown protruding from each end), the solenoid valves, and the pressure-dropping/flow-metering capillary tubes. The thrusters are insulated for better performance in the atmosphere. The propulsion module is

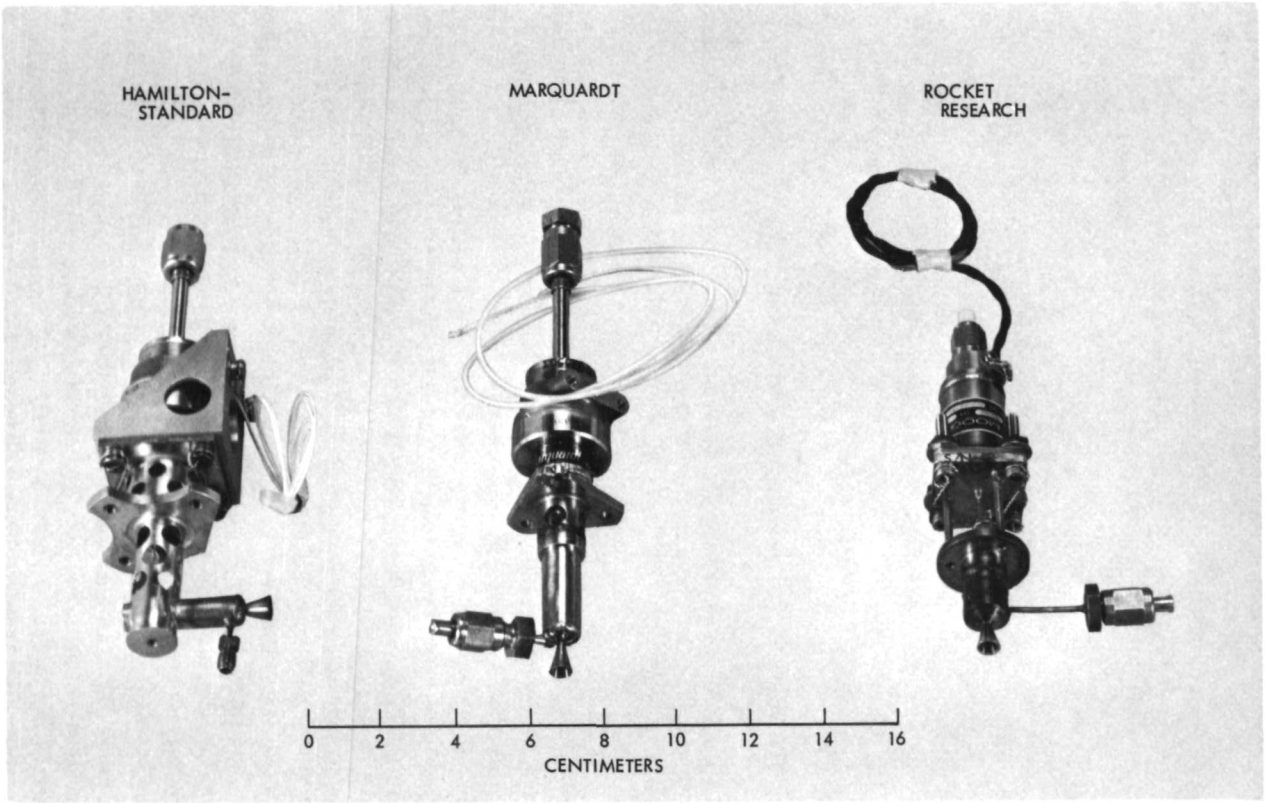

Figure 2. 0.4448-N hydrazine thrusters purchased for evaluation

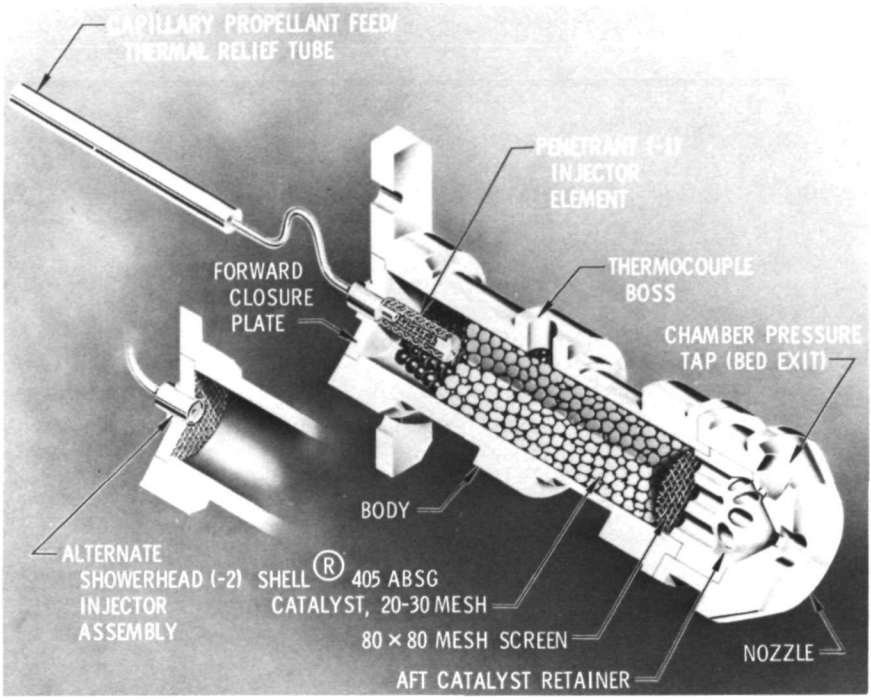

Figure 3. In-house 0.22-N (0.05-lbf) thruster design

shown assembled on the air-bearing table in the insert of Figure 4 and has been photo retouched (lightened in color) for clarity.

The feed system was assembled from components designed to sustain very high pressures. The supply tank, one of the weaker components, has been coded for a 2.758×10^7 N/m^2 (4000 psig) working pressure with a 4:1 safety factor and has been proof-tested to 4.137×10^7 N/m^2 (6000 psig). The maximum pressure to be experienced during air-bearing table tests is 2.758×10^6 N/m^2 (400 psig). This ample margin of safety, combined with a history of safe operation and nominally low chamber pressures, was instrumental in obtaining a "man rating" for the module so that it could be operated in the presence of personnel. This action greatly facilitated the checkouts and demonstrations of the air-bearing table.

For comparison, an additional 0.2224-N (0.05-lbf) thruster was fabricated with a shorter (0.0128-m) catalyst bed for less ammonia dissociation (55% instead of 72%) and loaded with 20–30 mesh, 90% attrited Shell 405 catalyst (nearly spherical granules). This thruster has been subjected to a series of 1532 "cold" starts [thruster and propellant temperature at a nominal 20°C (68°F) prior to each ignition]. The steady-state on-time for each cold start was approximately 10 s to allow the catalyst bed temperature to approach thermal equilibrium. This test series precipitated from the consideration

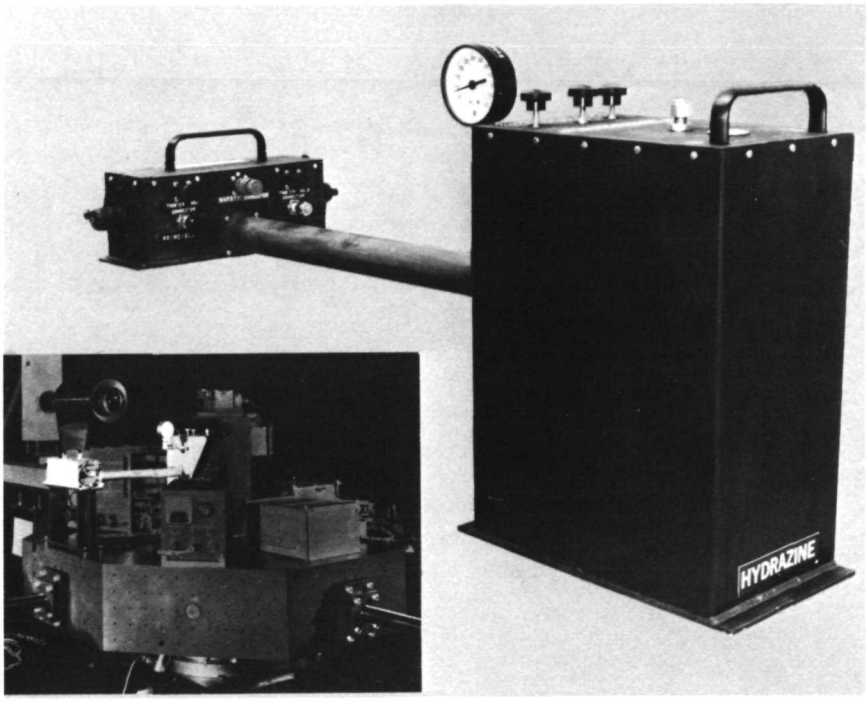

Figure 4. Celestarium propulsion module

that the propulsion bay of an outer-planet mission spacecraft would be thermally controlled between 4.45 and 32.2°C (40 and 90°F) at a nominal 20.1°C (70°F), and from the original requirement that there would be approximately 1100 starts per thruster with the thruster initially in thermal equilibrium with the propulsion bay. The number 1500 was chosen as having sufficient margin to demonstrate feasibility. The 90% attrited catalyst was chosen from data that tended to indicate that it may have the highest cold-start survival probability. (However, more recent findings indicate that, in reality, the non-attrited granules may be superior.) Since the time these tests were performed, the requirements for maximum number of starts in any one axis have increased from 1100 to approximately 2500 in yaw.

Concluding Remarks

It has been demonstrated that a liquid hydrazine Attitude Propulsion Subsystem can meet the primary TOPS mission requirements. The capability of the system to survive the life (duty cycle) requirement has been verified by vacuum chamber tests, and the system compatibility with the spacecraft dynamics has been demonstrated by the air-bearing table tests in the Celestarium.

Future Effort

The remaining TOPS APS effort will be to complete the evaluation of the purchased catalytic thrusters for a TOPS duty cycle and to publish a detailed final report on the overall APS activity. This effort is scheduled for completion by the end of 1971. An effort is underway to obtain and evaluate at least one electrothermal thruster in parallel with the TOPS effort for possible application on an outer-planet mission spacecraft. An electrothermal thruster operates on the principle that the monopropellant decomposition is initiated by an electrically induced heat source and sustains itself thereafter with no further power input.

More extensive work in the APS valve area is required and will be conducted with specific emphasis on extended life expectancy, seat design, power and envelope tradeoffs, and magnetic field definition.

The filtration requirements will be re-evaluated to ascertain an acceptable flight minimum. Further evaluation of the 1-μm (absolute) filter will be conducted to specifically address the question of the ultra-fine filtration limitations and operating problems. This effort will aid in defining realistic requirements related very closely to the propellant cleanliness definition and valve seat particle absorption capability.

Long-Duration Firings of a Mariner Mars 1969 Catalytic Reactor

T. W. Price

Propulsion Division

Two long-duration tests were conducted with a surplus Mariner Mars 1969 monopropellant hydrazine reactor in an attempt to induce the "washout" phenomenon. The Mariner Mars 1969 reactor was chosen because it has a long development history and thus is well characterized. No "washout" occurred during either of the two 1000-s tests, although slow transients were observed in the reactor operation during what were nominally steady-state conditions. The 2000 s of operating time represents nearly an order of magnitude increase over the rated life of the engine.

Introduction

In recent years, a phenomenon termed "washout" has been observed in hydrazine monopropellant reactors. This "washout" is characterized by a rather slow but significant decrease in reactor performance (i.e., chamber pressure and thrust decrease while the fuel mass flowrate increases) during what is otherwise steady-state operation. Most significantly, this performance decrease first occurs *after* the reactor has reached thermal equilibrium. If allowed to proceed, the rate of the performance degradation increases and can eventually result in a complete cessation of hydrazine decomposition. Only partially reacted fuel then flows through the catalyst bed. One of the more interesting aspects of this phenomenon is that, if fuel flow is completely stopped after "washout" and is restarted after a delay as short as 1 s, the reactor again operates in a normal manner. However, "washout" will re-occur and the succeeding time interval before the next occurrence is always shorter. The "washout"–normal behavior–"washout" cycle can be repeated many times. The time until "washout" occurs is apparently affected by the previous history of the catalyst (both the operation time and the number of ambient temperature starts), by the bulk temperature of the liquid hydrazine, and by the amount of water (mil-spec hydrazine can contain up to 1.5%) in the hydrazine. Subsequent to the tests described here, "washout" has been observed at JPL, but not with the Mariner Mars 1969 reactor. These tests, described in Reference 1, identified the catalyst surface

area per unit chamber volume as an additional variable significant in the "washout" process.

An attempt has been made to induce "washout" in the well-characterized reactor used in the Mariner Mars 1969 propulsion system and the results of these tests are the subject of this article. The primary purpose of these tests was to gain some insight into questions such as: Is "washout" a fundamental, but heretofore unobserved, characteristic of the Shell 405 catalyst? Is "washout" a characteristic of all monopropellant hydrazine catalytic reactors? Is "washout" hardware related (e.g., injection technique)?

Apparatus and Procedures

For the "washout" tests a surplus Mariner Mars 1969 reactor (see Figure 1), serial number S/N 008, was modified slightly from the basic design. The modifications consisted of the addition of a 10-mesh screen, made of L-605 alloy, just below the 20–30-mesh catalyst, the addition of a pressure tap to measure the reactor chamber pressure upstream of the catalyst bed and thus permit a determination of the pressure drop across the bed, and the addition of four fittings to allow the insertion of thermocouples within the lower catalyst bed to obtain direct measurements of the gas temperature.

In addition to the modifications described above, the catalyst used for these tests differed slightly from the Mariner Mars 1969 design. First, the engine was packed with used catalyst (exact history unknown) since prior use of the catalyst had been observed to promote "washout." Second, the lower bed of the engine (see Figure 1) was packed with 100% Shell 405 catalyst in place of the 75% Shell 405/25% HA-3 mixture used in the basic Mariner Mars 1969 engine. Since this mixture is peculiar to JPL and has not been widely used elsewhere, it was felt that this substitution would simplify comparisons with outside tests. Also, in an attempt to promote the "washout," the hydrazine used for these tests was cooled to approximately 280 K (45°F)[1] for both of the long-duration tests conducted.

Results and Discussion

Two tests, each nominally 1000 s in duration, were completed. No "washout" occurred during either test, although a change occurred in the engine characteristics about midway through the first test that might be interpreted as incipient "washout." This condition spontaneously disappeared and the test was completed without further incident. Reactor performance, as measured by the characteristic velocity (c^*), remained relatively constant during both tests. During the anomaly noted above, the

[1] Values in customary units are included in parentheses after values in SI (International System) units if the customary units were used in the measurements or calculations.

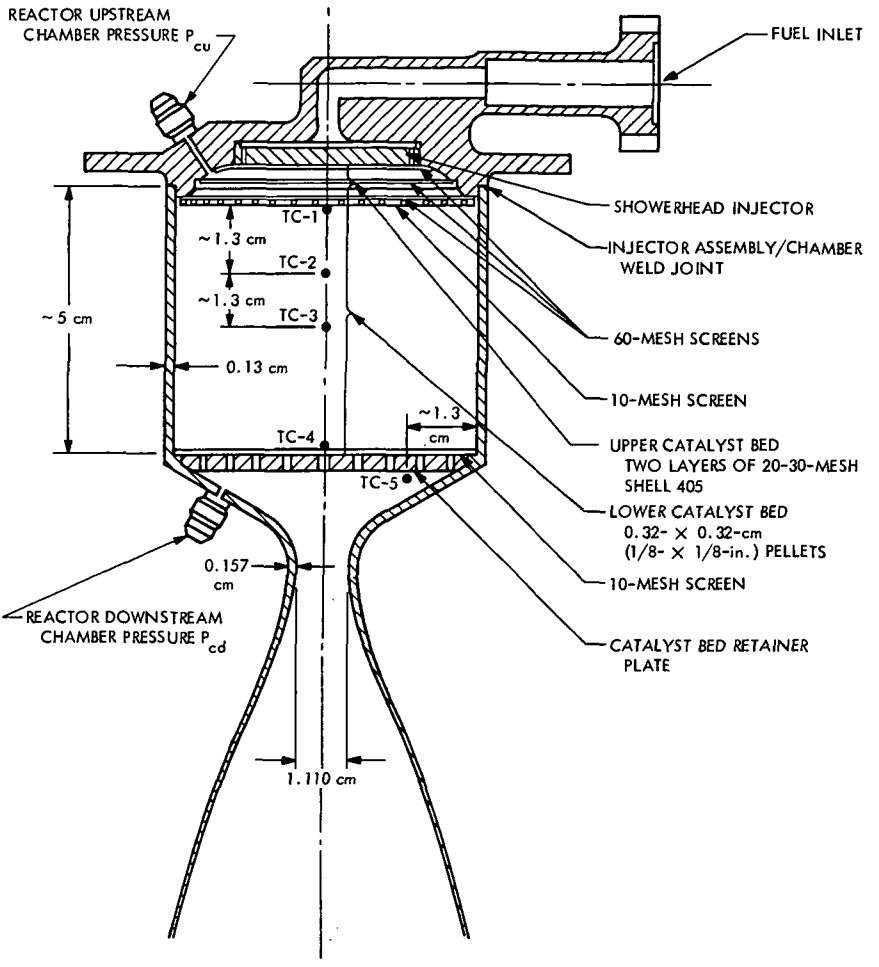

Figure 1. Internal configuration of Mariner Mars 1969 engine including modifications for "washout" tests

c^* decreased about 61 m/s (200 ft/s) but the c^* values were never below 1250 m/s (4100 ft/s). The measured value for this engine during flight acceptance testing was 1320 m/s (4320 ft/s). More significantly, there were no periods of rapid, sustained c^* decrease as is usual in "washout."

Although no "washout" was observed, the tests are of interest for several reasons. The 2000 s of operation with the same catalyst bed represents an order of magnitude increase in operation time over the nominal life of the Mariner Mars 1969 reactor. Of particular interest is the slow transient processes observed which occurred during what was nominally a steady-state operation.

A primary factor in the achievement of nearly 2000 s of test time on a single catalyst bed without excessive loss of catalyst is believed to be the 10-mesh screen (see Figure 1) added specifically for these tests. This screen provides structural rigidity for the 60-mesh screens, which in turn retain the 20–30-mesh catalyst. If the fine mesh screens do distort, a void is created in the upper catalyst bed. The catalyst particles can then move relative to one another and the upper bed can abrade itself into particles small enough to pass through a 60-mesh screen and hence out of the reactor. While the original screen design is adequate for the Mariner requirements, nominally 200 s of firing time, it is probably inadequate for the 2000 s of testing completed here. All screens were intact after the tests and only 5% of the catalyst from the upper bed was lost. The loss from the lower bed was about 1%. These are acceptable attrition rates.

The quality of a catalytic hydrazine reactor's performance is generally judged by three parameters: the characteristic velocity c^*, the "roughness" (as measured by the chamber pressure variations about the nominal steady-state pressure), and the pressure drop across the catalyst bed ($\Delta P_{bed} \equiv P_{cu} - P_{cd}$). These parameters, along with others of interest, are shown in Figures 2 and 3 as a function of time.

The plotted points of Figures 2 and 3 are taken from the data recorded by a high-speed digital recording system. Each parameter was sampled every 0.042 s. Only a few of these data are shown in Figures 2 and 3, but the long-term trends are reproduced there. Among the parameters not displayed are the fuel supply tank pressure, the fuel supply line pressure at the entrance to the reactor injector, and the fuel temperature at the injector entrance. (Note that the difference between the upstream and downstream chamber pressures (P_{cu} and P_{cd}) is plotted rather than P_{cu} itself.) The supply tank pressure was essentially constant during both tests. The injector pressure varied during the tests but the pressure drop across the injector varied directly with the fuel flowrate and agreed with the pre-test water flow calibration of the injector, and this would indicate that at no time were the injector orifices plugged. During both tests the fuel temperature increased slightly but continuously throughout the tests. The initial and final values for the first test were 282 K (48°F) and 285 K (53°F), respectively. The corresponding values for the second test were 279 K (42°F) and 280 K (45°F). The behavior of these parameters then leads to the conclusion that the variations in other measurements resulted from changes within the reactor itself and did not occur because of non-constant inlet conditions.

For a given reactor design, roughness generally increases as operating time is accumulated and is often the parameter used to define the useful life of a catalyst bed. Measured roughness for the engine during its flight acceptance testing was 3.45×10^4 N/m^2 (5 psi) as measured peak to peak. At the beginning of the first 1000-s test, the roughness level was the same as measured during acceptance testing. This relatively low level was somewhat surprising since tests early in the Mariner Mars 1969 development had

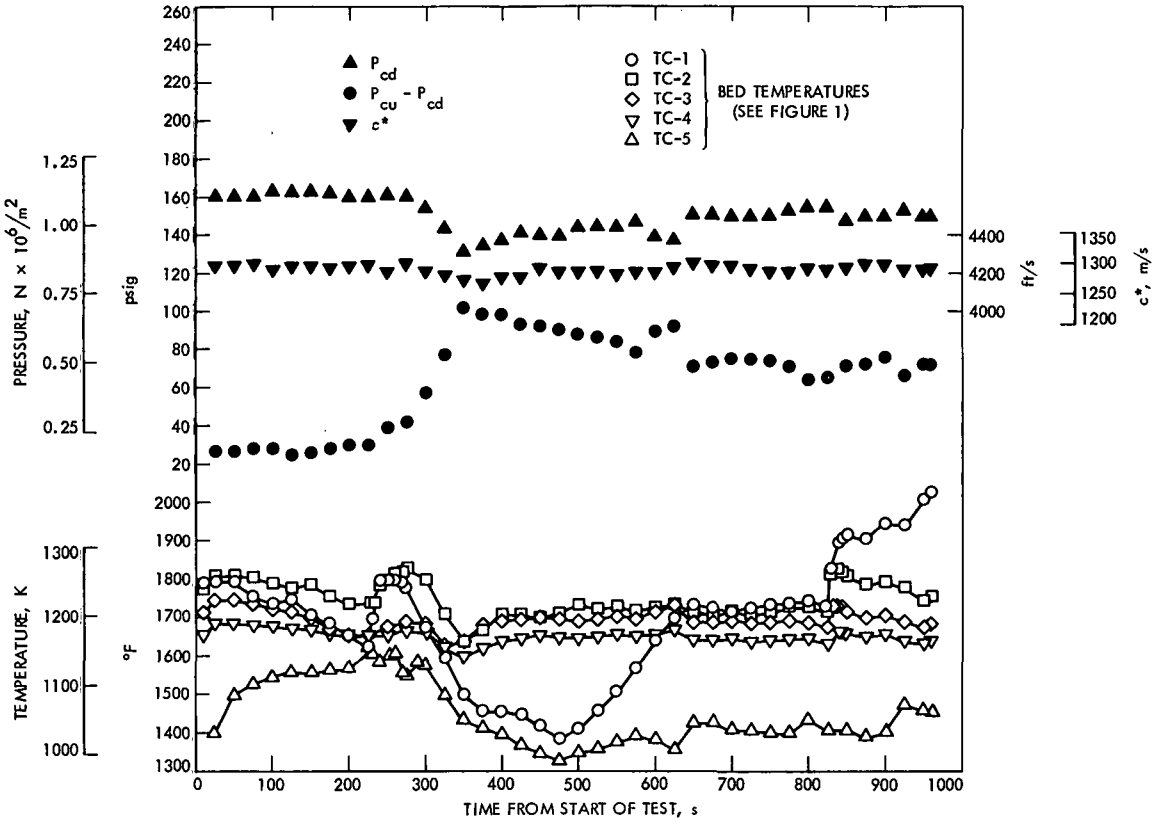

Figure 2. Results of test 1

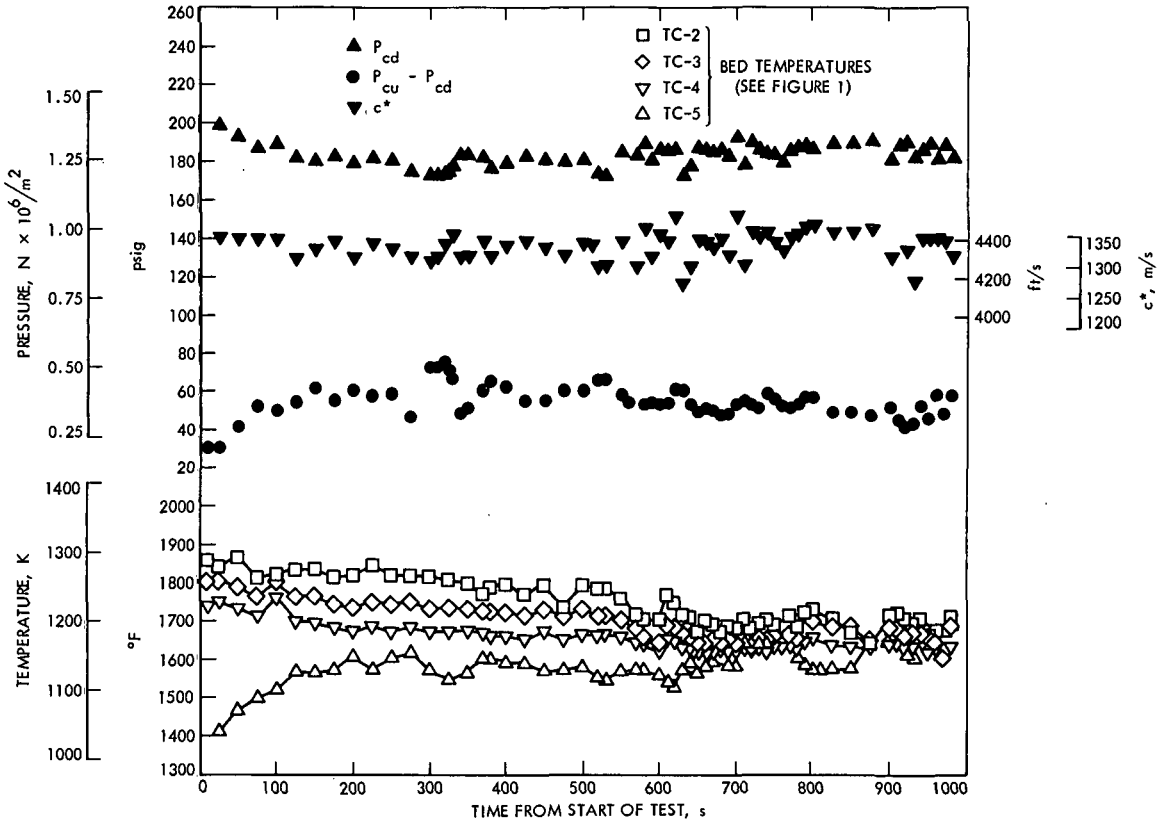

Figure 3. Results of test 2

shown that a lower bed composed of 100% Shell 405 pellets resulted in rougher operation than the mixture finally selected for the flight engines. During the first 400 s of operation, the roughness increased gradually to 4.14 $\times 10^5$ N/m^2 (60 psi) peak to peak.

The usual form of the roughness associated with monopropellant reactors is a continuous, random fluctuation in chamber pressure. During both tests the reactor roughness was noticeably different and could best be described as smooth [i.e., roughness levels of 3.45 $\times 10^4$ N/m^2 (5 psi) peak to peak], but interspersed with short-duration pressure pulses characterized by a rapid increase in the chamber pressure. As the roughness level increased, the time between pulses decreased. A section of an oscillogram from the first test is reproduced in Figure 4 and shows the type of chamber pressure disturbances observed. This type of pressure disturbance is generally attributed to small amounts of liquid hydrazine accumulating within the reactor which rapidly decompose after being heated enough to spontaneously react. The added catalyst retention screens could provide a place for such accumulation to occur.

Somewhat surprisingly, after the initial period of increasing roughness, the reactor operation gradually became smoother until after about 600 s when the pressure excursions were just under 1.38 $\times 10^5$ N/m^2 (20 psi) peak to peak. Except for several pressure disturbances as large as 2.76 $\times 10^5$ N/m^2 (40 psi) peak to peak, the roughness remained slightly under 1.38 $\times 10^5$ N/m^2 (20 psi) for the remainder of the test.

During the second test the roughness began increasing from shortly after ignition and increased fairly rapidly to 1.38 $\times 10^5$ N/m^2 (20 psi) peak to peak and generally remained at that level throughout the test. Again, there were several periods during which larger pressure excursions occurred but none that approached the 4.14 $\times 10^5$ -N/m^2 (60-psi) level observed during the first test.

As can be seen from Figures 2 and 3, the catalyst bed pressure drop ΔP_{bed}, varied noticeably during these tests. An increase in ΔP_{bed} as a function of operating time is commonly observed in hydrazine reactors. Since a pressure differential of ~6.9 $\times 10^5$ N/m^2 (100 psi) may result in the physical crushing of the catalyst, this valve is often used as an indication of when the bed life has been expended. This level was reached during the first test (see Figure 2), but surprisingly the ΔP_{bed} then decreased during later stages of the test and remained relatively constant during the entire second test (see Figure 3).

During both tests, but most noticeably during the first, there were apparent slow movements of the primary reaction zone or "flame front" within the catalyst bed. This was detected both by visual observation of the reactor exterior and by the temperature measurements taken within the bed itself. As is usual in experimental reactor tests, where attainment of maximum performance is not a major goal, the flight insulation was removed from the

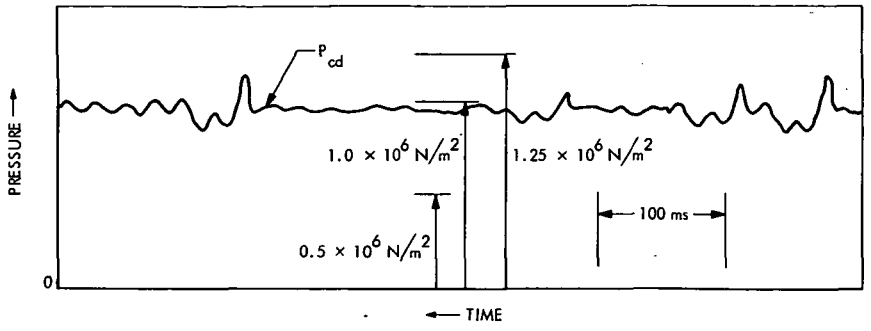

Figure 4. Typical oscillogram record

reactor walls. This allows a more convenient test stand installation, additional instrumentation, and visual observation of the reactor. Since there is no cooling other than radiation and natural convection, the reactor wall temperature is very nearly that of the reaction products, between 1100 K (~1500°F) and 1500 K (~2200°F). The chamber becomes incandescent during operation, and there is an axial temperature gradient in the catalyst bed. Thus, the color of the wall varies from a light, bright orange near the injector to a dull red at the bed exit.

During the first test, the axial location of the highest temperature (light orange) region moved slowly toward the exit of the catalyst bed and then back to its original location. The total movement was on the order of 1.27 cm (½ in.). In addition, a circular region, about 1.9 cm (¾ in.) in diameter, of low temperature developed about halfway down the chamber. This "cool" spot was observed to move slowly both axially and circumferentially. No such phenomena were observed during the second test of this series.

The description of the reactor exterior given above is of necessity general and qualitative since it is the result of visual observations by the test personnel and no photographic records were made. Definitive temperature measurements were made within the catalyst bed at the locations shown in Figure 1. The bare junction thermocouples used were similar to those described in Reference 2 except that the wire guards were not used. The data from these thermocouples are shown in Figures 2 and 3. They also indicate an apparent movement of the reaction zones during the first test and little or no movement during the second.

For a given reactor, i.e., one for which the catalyst size, the catalyst bed diameter, and catalyst bed length are fixed, the pressure drop across the bed can be correlated by means of two additional parameters. These are the propellant mass flowrate per unit cross-sectional area of the bed, G, and the catalyst bed porosity, ϵ, which is a measure of how tightly the catalyst particles are packed together. Implicit in the above statement is the assumption that the "flame front" occupies a unique axial position in the bed

for each combination of ϵ and G. This is so because the pressure drop results primarily from the flow of the low-density, high-velocity gases downstream of the "flame front." Thus, any change in the position of the "flame front" would alter the length of the gas flow path and hence the pressure drop.

The possibility of the "flame front" movements resulting from changes in the degree of particle packing (i.e., porosity) was investigated.[2] This was done utilizing the computer programs described in Reference 3. The results were negative in that while reasonable changes in ϵ produced changes in ΔP_{bed} of the magnitude observed experimentally, there was virtually no change in the predicted axial temperature gradient. Thus, the conclusion must be that the experimentally observed phenomenon results from variations in some reactor property not considered in the models of Reference 3. It may be conjectured, based on the continuing work of Reference 4, that this property is the catalyst activity. The catalyst activity could vary because of adsorption of the decomposition products on the active catalytic sites. This "poisoning" might progress axially in the bed and would be expected to be reversible if the inactive catalyst were heated. Note that this could explain "washout" as well as the phenomenon described above, but it must be emphasized that this explanation is preliminary and conjectural, and is yet to be proven by experiment.

Conclusions and Recommendations

Based on the results of the two 1000-s tests described above, the following conclusions concerning "washout" and catalytic reactors in general have been reached:

(1) Our understanding of the "washout" phenomenon is only superficial. While many of the factors which play a role have been identified, the underlying processes remain virtually unknown.

(2) The Mariner Mars 1969 reactor is resistant to "washout," although our understanding of why this should be is incomplete. As a corollary, the Mariner Mars 1969 reactor also appears to be capable of a much longer operating time than rated, after minor internal modifications.

(3) Our knowledge of the basic processes taking place within a catalyst bed in general is only partially complete. The work of Kesten and coworkers has shed much light on this subject, but as yet the slow thermal transients observed cannot be explained except by conjecture.

---

[2] Variations in G were eliminated as the source since the magnitude of the ΔP_{bed} and G changes are not compatible with any existing correlations. Rather the G variations must be merely a result of changes in ϵ.

(4) Further study of the fundamental processes that occur within a catalyst bed, and even within a catalyst particle itself, is recommended. In particular the phenomenon of "washout" is the subject of an ongoing JPL program for fiscal year 1972.

References

1. Heidenreich, A., "TOPS Trajectory Correction Engine," in *Supporting Research and Advanced Development,* Space Programs Summary 37-63, Vol. III, pp. 227–235. Jet Propulsion Laboratory, Pasadena, Calif., June 30, 1970.

2. Kesten, A. S., and Price, T. W., "Analytical and Experimental Studies of the Transient Behavior of Catalytic Reactors for Hydrazine Decomposition," presented at the 10th Liquid Propulsion Symposium, Las Vegas, Nev., Nov. 19–21, 1968.

3. Smith, E. J., Smith, D. B., and Kesten, A. S., *Computer Programs Manual for One- and Two-Dimensional Steady-State Programs—An Analytical Study of Catalytic Reactors for Hydrazine Decomposition,* Report UACRL.C910461. United Aircraft Research Laboratories, E. Hartford, Conn., Aug. 1968.

4. Sangiovanni, J. J., and Kesten, A. S., *First Annual Progress Report—Study of Hydrazine Reactor Vacuum Start Characteristics,* Report UARL H910758. United Aircraft Research Laboratories, E. Hartford, Conn., Dec. 1969.

Simulation of Mariner Mars 1971 Spacecraft

N. E. Ausman, Jr., N. K. Simon, and C. F. Rodriguez

Project Engineering Division

In preparation for the Mariner Mars 1971 mission, operations personnel took part in an extensive training program during which the primary source of spacecraft data was a computer program simulating the spacecraft. The objectives of a simulation model for training purposes differ from objectives appropriate to a design or analysis model. Model subsystems were designed to provide realistic telemetry data reflecting changes due both to commands and environmental parameters affecting the spacecraft at various times during the mission.

The spacecraft is modeled along two separate functional lines. Boolean operations are concentrated in the spacecraft logic model, which determines the spacecraft state or mode, while mathematical operations or algorithms are executed in computational subsystem models. Although logic parameters are interrogated as a part of each computational pass, actual logic model processing occurs only when a change-of-state input is generated by the operations organization. This article discusses the program design, some of the special characteristics of each of the modeled subsystems, and how the model was used in support of mission operations training.

Introduction

In the spring of 1971 the launch of two Mariner spacecraft (Figure 1) planned to orbit the planet Mars culminated nearly three years of preparation for Mariner Mars 1971 space flight operations at the Jet Propulsion Laboratory.

Just as the spacecraft and the launch vehicle must undergo a series of tests to verify readiness for launch, so must the Mission Operations Complex (MOC) be tested. Consisting of a Ground Data System, a Mission Operations Organization, and an Operations Plan, the MOC is required in the conduct of flight operations. Testing of the MOC is one of the last of the prelaunch preparatory activities directed by the Project. Basically, two classes of tests are involved:

(1) Ground Data System testing.

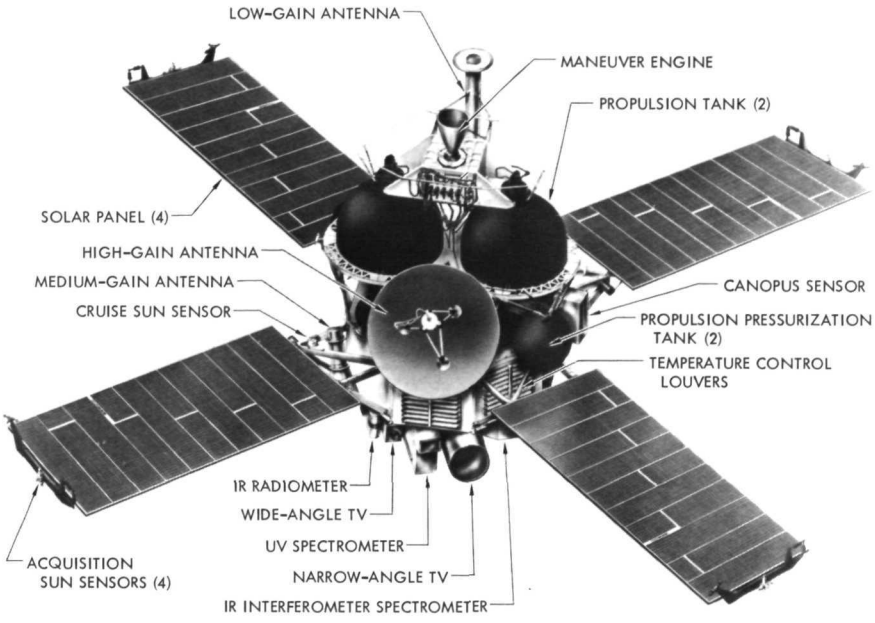

PROPULSION MODULE AND SCAN PLATFORM INSULATION BLANKETS NOT SHOWN

Figure 1. Mariner Mars 1971 spacecraft

(2) Organizational training.

Ground Data System testing verifies that the combination of hardware and software required to present spacecraft telemetry in a useful form and to generate commands which will control the spacecraft is, in fact, able to accomplish these functions. This class of test requires a data source capable of generating a known and relatively static input which can be compared against the output of the Ground Data System.

Organizational training presumes a checked out Ground Data System and verifies the ability of the organization to:

(1) Use the Ground Data System effectively.

(2) Understand the mission operations plan.

(3) Analyze spacecraft data properly and determine appropriate actions in nonstandard performance situations.

(4) Function efficiently as a team.

Organizational training requires a data source which accurately reflects a realistic mission environment and correctly responds to commands which change the operation of the data source.

The Mariner Mars 1971 Simulation System was designed to satisfy all of the foregoing requirements. The spacecraft model, as a part of the Mariner Mars 1971 Simulation System, was developed expressly as a data source for organizational training. It is this phase of the Mariner Mars 1971 simulation effort which will receive the greatest emphasis in this article.

The Mariner Mars 1971 Simulation System will be discussed in general so that the role of the spacecraft model is understood in its proper context. The spacecraft model, specifically the logic model and the computational model and their integration, will be discussed in detail.

Simulation System

The Mariner Mars 1971 Simulation System uses current computer and electronic technology to generate a realistic mission environment. The Simulation System consists of two major elements: the multi-mission element provided by the Tracking and Data Acquisition System (TDS) and the mission-dependent element provided by the Mission Operations System (MOS). The TDS provides tracking (metric), station (command response and monitor), and telemetry (calibration) data types, while the MOS provides the command responsive spacecraft model which generates realistic spacecraft telemetry data. In combination, all data types used either for operations control or analytic purposes during a mission are generated by the Simulation System.

The various elements of the Simulation System are shown in Figure 2.

The Simulation System can operate in either a short-loop mode during which data is delivered directly to the Space Flight Operations Facility (SFOF) as though it had been processed by a Deep Space Station, or it can operate in a long-loop mode during which data is delivered to the Deep Space Station, such as Goldstone Tracking Station in the Mojave Desert, as though it had been generated by the spacecraft.

The Simulation System consists of one or more software programs for each data type to be generated. These programs operate in a combination of computers located in the Space Flight Operations Facility (Building 230) at Pasadena and at tracking stations around the world.

The SCF Univac 1108 computer is used in non-real time to prepare trajectory tapes and in real time to operate the spacecraft mathematical models. The SFOF IBM 360/75 computer is used to convert trajectory information into tracking station predicts. The Simulation Center Electro-Mechanical Research (EMR) 6050 computer is used for overall simulation system control, conversion of predicts into simulated tracking data, and the generation of tracking station command and status data. The DSIF Xerox Data System (XDS) 910 computer at the tracking station is used to convert

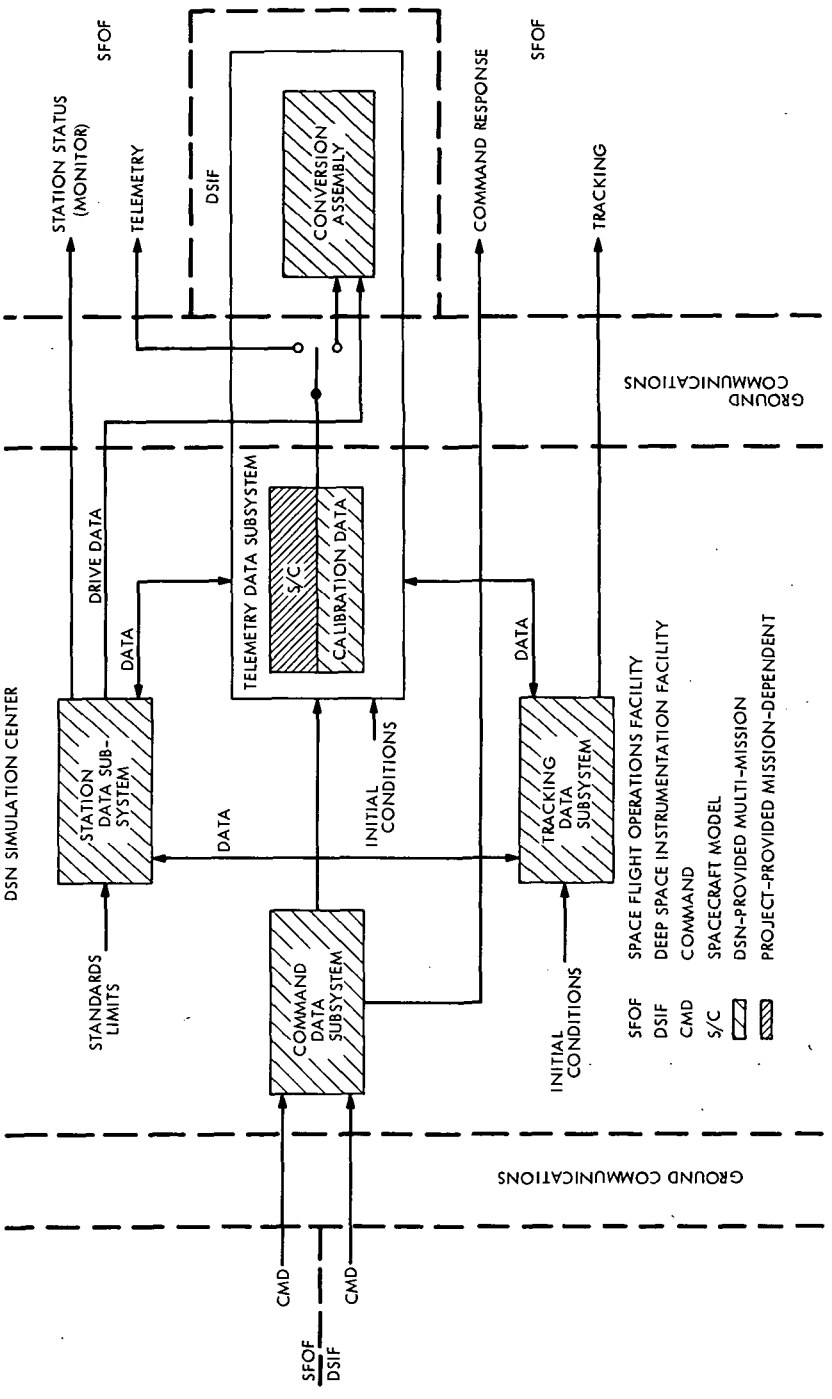

Figure 2. Simulation System

simulated telemetry data into a form appropriate for modulation on an RF carrier.

Elements of the Simulation System necessary to generate telemetry data are shown in Figure 3. Specifically, the telemetry subsystem is depicted as required to support long-loop training exercises.

Although it is important to understand the operations of the entire Simulation System, this article will concentrate on the spacecraft telemetry simulation.

The Spacecraft Model

The Mariner Mars 1971 spacecraft is modeled along two separate functional lines. All Boolean operations are performed in the spacecraft logic model which determines the spacecraft state or mode, while mathematical operations or algorithms are executed in a computational model. Although logic parameters are interrogated as an integral part of each computational pass, actual logic model processing occurs only when a change-of-state input is generated. There are several sources of change-of-state inputs, one of which is commands received and processed by the model in real time so that the telemetry stream reflects the changes in the spacecraft initiated by the operations organization. The logic and computational models will be discussed in subsequent paragraphs.

The Logic Model

Since the spacecraft state is essentially logically determined by relays and electronic switches, separating the logical program operations from the mathematical program operations within the model was a natural result of the spacecraft design.

The logical operation of each of the various spacecraft subsystems is described by a logic diagram. For example, the scan platform logic is portrayed in Figure 4. The diagram was developed from the spacecraft design specification for the scan platform subsystem which is a two-degree of freedom motorized platform for mounting and pointing the science instruments.

The motor, which can be turned on or off by command, is inhibited during launch. This is represented logically on the upper portion of Figure 4. The lower portion of the figure shows that the platform can be operated in three different modes:

(1) Fixed (both cone and clock are in stow position).

(2) Fixed cone (clock position is variable).

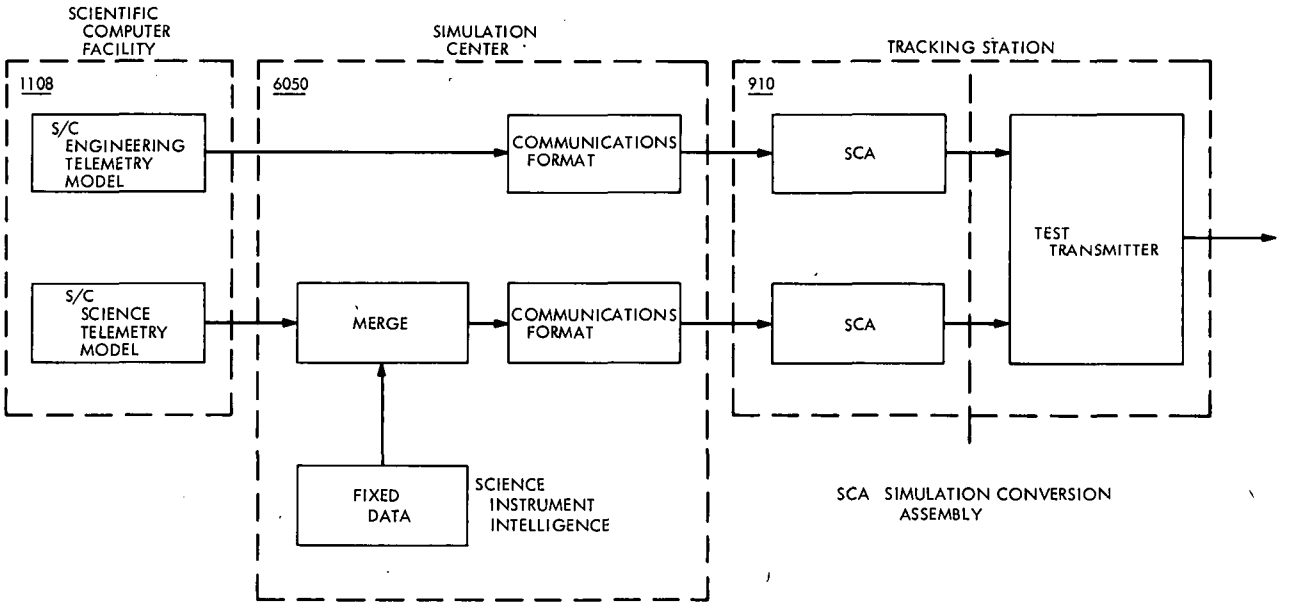

Figure 3. Simulation telemetry data subsystem (long-loop mode)

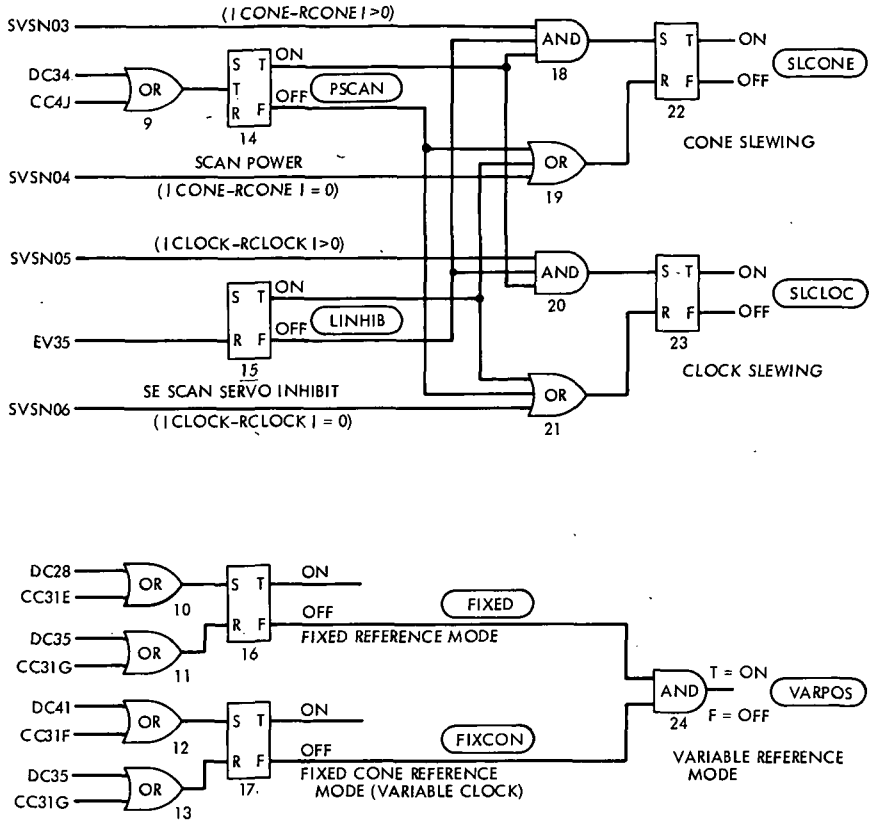

Figure 4. Scan logic

(3) Variable (both cone and clock positions are variable).

Shown at the far left of the diagram is the complete set of commands and events that can affect the state of the scan platform subsystem. The circled parameters are subsystem outputs which are either telemetered to the ground or used internally to describe the current state of the subsystem. Similar logic diagrams were developed and programmed for every subsystem on the spacecraft.

The programming technique used to implement the logic model is illustrated in Figure 5. Algorithms were developed for three logic elements: *and* gates, *or* gates, and flip flops. All change-of-state inputs (external stimuli) were collected and cards prepared which rename the input in program language. Three classes of stimuli are shown on the left-hand side of Figure 5. Cards were prepared which establish the relationship between the logic elements for each input. Finally, the logic model outputs were collected and cards prepared which convert program language logic states to a readable form. A logic state as used here describes the operating condition of an element of spacecraft hardware. As coded, the logic model

accepts stimuli changes and prints out the new model state. The resulting program can be operated either by itself to verify the spacecraft status during ground checkout or in conjunction with the computational model of the spacecraft.

The Computational Model

The spacecraft generates two telemetry streams: (1) science data, and (2) engineering data. Science data includes instrument housekeeping or status information in addition to instrument measurement data. Measurement data is defined as the actual science intelligence generated by the instrument. Science data simulation by computer model for Mariner Mars 1971 was limited to instrument status information. (Attempts to merge measurement data previously recorded on magnetic tape with the modeled instrument status data were abandoned, since the difficulty of developing this capability was not considered cost effective.) Fixed computer-generated measurement data was ultimately used instead. This data did not in any way approximate Mars data but was of use in testing and evaluating operational sequences. Science simulation is mentioned here only for the sake of completeness and will not be discussed further.

Engineering data includes all spacecraft state and housekeeping or status information. Spacecraft engineering data simulation was developed on a subsystem basis paralleling the organization and development of the flight spacecraft. In some cases, however, several spacecraft subsystems were combined. For example, the pyro, mechanical devices, and propulsion subsystems were combined in the model and designated as the propulsion model. The subsystem design approach was selected because it allows comparatively easy updating of the simulation model from project to project. The Mariner Venus–Mercury central computer and sequencer

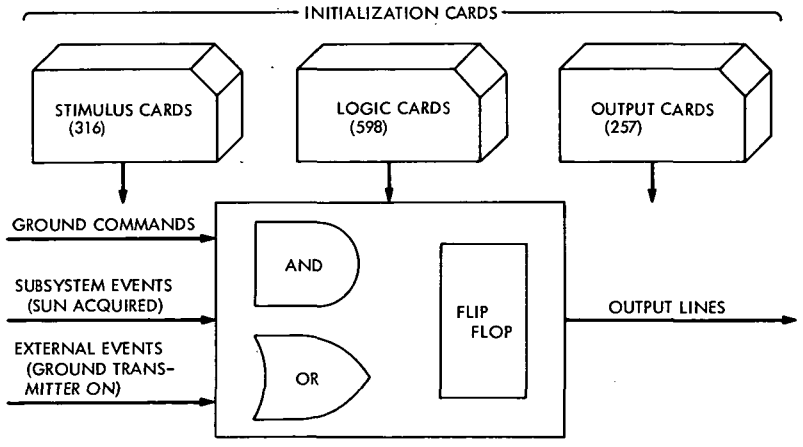

Figure 5. Logic program

(CC&S) is the same as the Mariner Mars 1971 CC&S. The Mariner Mars 1971 CC&S model will be usable in the Mariner Venus-Mercury 1973 model almost as is.

Information required to model each subsystem was provided by the engineers who were responsible for the design of the spacecraft. The simulation group translated the designer's knowledge into a software model that behaves in a manner similar to the actual spacecraft.

Subsystems modeled separately include the temperature (TMP), central computer and sequencer (CC&S), attitude control (AC), power (PWR), radio (RF), propulsion (PRP), data storage (DSS), scan platform (SCN), and flight telemetry (FLT). Each of these models will be described in subsequent paragraphs.

TMP. The temperature model computes all telemetered spacecraft engineering temperatures (28), including propulsion tank temperatures, electronic bay temperatures, solar panel temperatures, and science instrument temperatures. Twenty-seven other temperature calculations are computed for use by other subsystem models. Temperatures generally vary exponentially as a result of logic state or environmental changes. The environmental changes most affecting spacecraft temperatures are Sun and Mars radiation effects.

CC&S. The central computer is a general purpose, internally stored program digital computer with a 512-word memory. It is also a serial computer in that each memory access time (417 μs) obtains only one bit of the addressed memory location. A fixed sequencer is used to provide redundancy to the central computer during maneuvers.

The CC&S model provides a complete and exact map of the computer memory, issues 86 computer commands and 5 sequencer commands used by the other subsystem models, and generates data for 3 separate telemetry channels. In addition all CC&S maneuver states (tandem, parallel, computer, and sequencer) are modeled. Modeling of a serial computer on a parallel computer required the reversing of all computer words since the least significant bit of each CC&S word is located at the left end of each word. The computer clock is controllable so that it can be synchronized to simulation time. The CC&S model can be fast stepped either to speed up the check out of other mathematical model subsystems or to skip over programmed sequences not required during a particular test profile.

AC. The attitude control model provides dynamic simulation of the star (Canopus) sensor, Sun sensors, gyros, switching amplifiers, gas jets, autopilot, gimballed engine, spacecraft orientation, internal power consumption, and telemetry channel switching. A total of 17 telemetry measurements are simulated by the AC model in addition to event counter inputs.

The AC model computes the spacecraft orientation relative to the Sun–Canopus coordinate system using one of two separate star tables. The model automatically turns on the roll gyro if the reference star is lost and reacquires an appropriate reference star as does the actual spacecraft. The spacecraft Sun angle is calculated and used by the temperature and power models. Limit cycling about the celestial reference is also simulated.

Overall, attitude control was probably the most complex model to simulate since it was three dimensional and quite dynamic. Simplification, commensurate with the objective of accurately simulating telemetry data, was introduced where possible.

PWR. The spacecraft operates with energy from four solar panels backed up by a nickel–cadmium battery. The power model provides a total of 20 telemetered measurements. In addition to the solar panels and the battery, the PWR model simulates the battery charger, boost regulator, and inverter input/output. The model calculates the total spacecraft power load using information provided by other subsystem models and then determines the power source simulating either panel only, battery only, or shared modes of operations.

The Sun angle calculated by the AC model is used by the PWR model to determine the solar panel shadowing effect during maneuver.

RF. The radio frequency model computes 10 telemetry measurements, including high- and low-gain antenna drive and spacecraft receiver automatic gain control (AGC) and static phase error (SPE). In addition the model calculates the RF power radiated toward Earth, a function of antenna drive, spacecraft attitude, and ranging modulation. This calculation allows the accurate simulation of ground receiver AGC from launch through Mars orbit.

PRP. The propulsion model combines the functions of three spacecraft subsystems: propulsion, pyrotechnic, and mechanical devices subsystems. Propulsion subsystem pressures are computed as a function of temperature. During a motor burn, the spacecraft PRP model computes nitrogen pressure decay, engine mixture ratio, chamber pressure, and spacecraft acceleration. Propellant tank pressure decreases due to nitrogen gas/propellant saturation are also modeled. A total of nine telemetry measurements in addition to event counter inputs are calculated by the PRP model.

DSS. The tape recorder aboard the spacecraft records science data for subsequent playback when the spacecraft is being tracked by the Goldstone Tracking Station. The DSS model computes tape recorder start up and shut down characteristics, tape position, tape mode, and buffer loading. Power loads for each of the various modes are computed and sent to the PWR model. In addition to event counter inputs, three telemetry measurements are computed by the DSS model.

SCN. The scan model simulates the platform upon which the science instruments are mounted. The reference positions of the scan platform are updated by ground command. When the scan platform is enabled, the model will move to the newly commanded position. Four telemetry measurements are calculated by the SCN model.

FLT. The flight telemetry model simulates analog-to-digital conversion of spacecraft data, telemetry commutation, digital data conditioning, and command decoding. This model also converts the engineering units computed by each of the subsystem models into data numbers which are the integer equivalents of the binary bit stream telemetered to the ground stations.

System Integration

The logic model was programmed and checked out first. The separate subsystem models discussed above were programmed as separate entities and then checked out in conjunction with the logic model. As each subsystem model was delivered, it was integrated with the logic model and its subsystem predecessors to ensure the compatibility of data transferred between the subsystem models. The last model to be integrated was the AC model. Once the model integration was complete, system integration was accomplished. This building block technique of development and integration proved very effective, thus, minimizing integration problems.

The model can be operated in either a stand-alone mode (this is the way in which the program was originally checked out) or in a real-time operation mode as illustrated in Figure 6. Dual spacecraft simulation is achieved by time-sharing the model with all calculations based upon a spacecraft-peculiar set of constants. Thus, it is possible, for example, to simulate one spacecraft in a cruise state and another in a launch state.

The model resides in the Univac 1108. Stand-alone input is via demand terminal or cards. Real-time input is via an interface with the EMR 6050 computer which formats input instructions. The model uses approximately sixty thousand 36-bit words of the 1108 core and approximately 5% of the 1108 computing time for each simulated spacecraft. Other programs may operate at the same time in a time-sharing mode.

Concluding Remarks

Thus far the Mariner Mars 1971 spacecraft model has been used a total of 330 h in support of organizational training. The data generated by the spacecraft model compares favorably with the actual data streams generated by the flight spacecraft. Although problems with the Simulation System, primarily the EMR 6050, have detracted from the effectiveness of the training, it is apparent that the elements of the mission operations

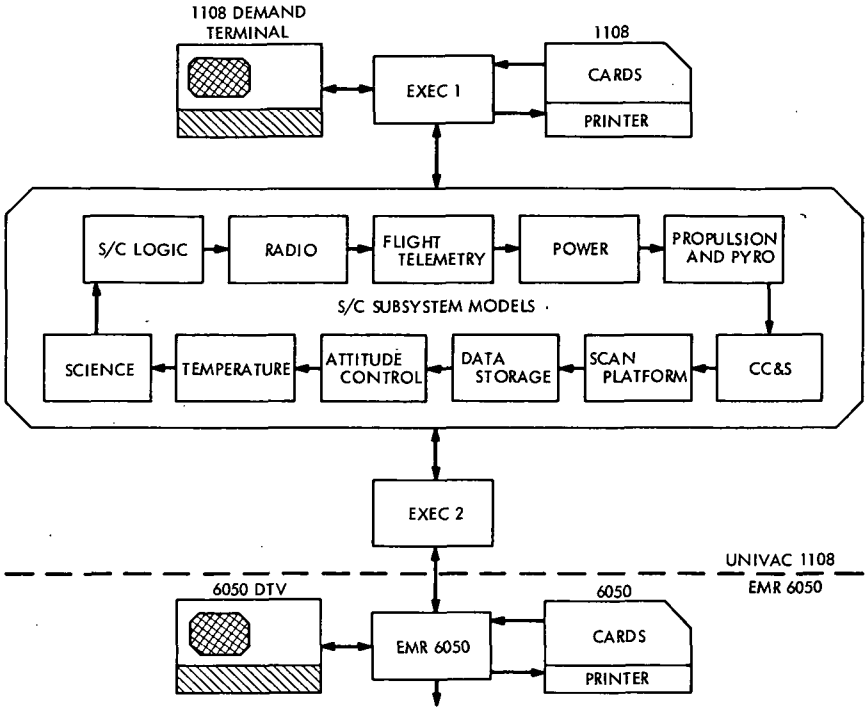

Figure 6. Spacecraft model processing

organization benefited significantly from the test program. The heart of this program was the ability to generate a realistic mission environment and to respond correctly to changes in that environment caused by the trainees. Such a response is only possible with a precision, operationally simple, software model. The Mariner Mars 1971 spacecraft model with its modular design is being used to support orbital training and in the future will be revised as necessary to meet the requirements of the Mariner Venus-Mercury Project.

Minicomputer-Controlled Programmed Oscillator

R. Winkelstein

Telecommunications Division

The programmed oscillator is a telecommunications receiver or transmitter subsystem which compensates for the known doppler frequency effect produced by the relative motion between a spacecraft and a tracking station. Two such programmed oscillators have been constructed, each using a low-cost minicomputer for the calculation and control functions, and each contained in a single rack of equipment. They are capable of operation in a phase-tracking mode as well as a frequency-tracking mode. When given an ephemeris suitable for the planet Venus, these units maintained phase coherence of better than 5 deg rms at 2388 MHz.

Introduction

A new design of the programmed oscillator has been developed and two units have been constructed and installed in the field. The programmed oscillator is an electronic frequency generation system that automatically produces a changing frequency as a precalculated function of time. This is accomplished currently by remote control of the search oscillator in a frequency synthesizer.

The programmed oscillator has been used as a receiver local oscillator subsystem for use in planetary radar (Reference 1) and to reduce the loop stress in phase-locked reception of spacecraft signals (Reference 2). As a transmitter exciter subsystem, the programmed oscillator has been used to reduce the stress in the spacecraft receiver loop (Reference 2) and to sweep the transmitter frequency in the Moon bounce time synchronization program (Reference 3).

Stimulus for this programmed oscillator development was the requirement for simultaneous coherent phase reception of signals at two Deep Space Network stations in an interferometer mode of operation. Phase stability needed for interferometric signal processing is less than 10 deg drift per minute and less than 5 deg rms phase noise at the S-band operating

frequency of 2388 MHz. Such accuracy is consistent with the development of the Hydrogen Maser Frequency Standard.

Additional objectives of the development were the utilization of a frequency synthesizer with a symmetrical search oscillator and the substitution of a minicomputer for the previously used medium-scale second-generation computer. The symmetrical search oscillator permits the midpoint of the search oscillator range to be set at any desired frequency resulting in fewer range crossovers with attendant loss of phase coherence than in the previous system which permitted ranges only at integral decade frequency points. Use of the minicomputer permits reduction of the equipment size from five racks of equipment to only one self-contained rack for the entire programmed oscillator system.

System Configuration

The programmed oscillator contains a modified commercial frequency synthesizer (Fluke 644A) controlled by a minicomputer (Lockheed MAC-16). A block diagram of the system is shown in Figure 1. At the beginning of a day's operation, station time and precalculated ephemeris polynomial constants are input to the computer. After the initial solution of the polynomial equations, the computer sets the range center frequency on the synthesizer through the decade control logic. The search oscillator range at the synthesizer output is 200 Hz. When multiplied by 64 in a receiver local oscillator chain, this range is equivalent to 12.8 kHz at an S-band frequency of 2388 MHz.[1] Frequencies within the selected 200-Hz range are obtained by controlling the search oscillator in a sampled data feedback control loop. The computer forms error numbers by differencing the desired phase calculated from the polynomial and the phase obtained from the counter. These error numbers are digitally filtered by the computer and output to the digital-to-analog (D/A) converter.

The D/A converter has 15 bits plus sign, thus accommodating a complete minicomputer word of 16 bits. An output of up to ±10 V may be obtained from the converter with a resolution of 305 μV. This voltage is fed to the integrator with a gain of 0.2155/second. The integrator has a linear output range of ±10 V which matches the remote control specification of the synthesizer search oscillator.

The search oscillator is a voltage-controlled oscillator subassembly within the synthesizer used normally to obtain smooth but noncoherent frequency offsets from the coherent frequency selected by the synthesizer decades. For the two programmed oscillators constructed, the search oscillator subassemblies have been screened for low noise characteristics (Reference 4). In

[1] Spacecraft missions requiring larger frequency swings with phase coherence may require alternate techniques.

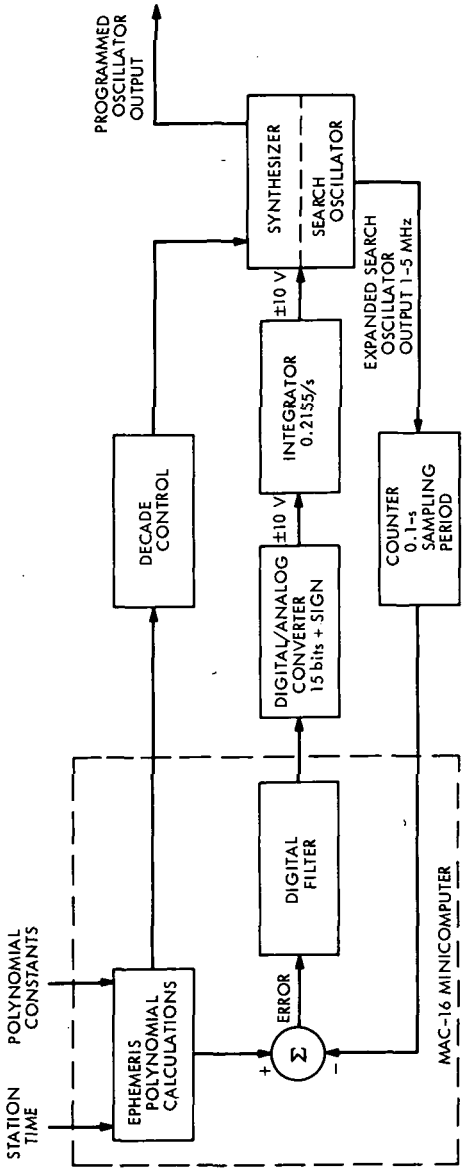

Figure 1. Programmed oscillator block diagram

addition to containing specially selected search oscillators, the synthesizers have been modified to provide a multiplied and frequency translated function of the search oscillator on a separate output connector. This expanded search oscillator output has a range from 1 to 5 MHz for the input control range of ±10 V, and is required to obtain the resolution needed for loop operation.

A 32-bit counter counts the expanded output of the search oscillator. Counting is continuous with the counter automatically recycling to zero when a full count is reached. Every tenth second to the nearest microsecond the count is dumped into a buffer register and then input to the computer without disturbing the counting process. Two computer words are needed to hold the count information with the least significant bit of the least significant word equal to one count cycle. Each count cycle is equivalent to 1.15 deg of phase at S-band. A picture of the assembled programmed oscillator is shown in Figure 2.

Control Loop Design

Figure 3 is a mathematical representation of the search oscillator control loop. In the figure s is the Laplace complex frequency, z is equal to e^{sT}, e is the Naperian logarithmic base, and T is the sampling time of 0.1 second. Shown also are the noise sources which limit the obtainable system accuracy. N_s is the search oscillator internal phase noise, and N_c is the counter resolution noise distributed between ±0.5 cycle at the counter output. Using the z-transform method of analysis, the open-loop transfer function G_0 is as shown in Figure 4. The digital filter equation has been chosen to cluster the poles of the closed-loop error transfer function G_c at z equal to 0.2, where (Reference 5)

$$G_c = \frac{1}{1 + G_0}$$

This cluster point represents a good compromise between the minimum transient response time which requires the poles to be clustered at z equal to 0 and the design of system response to internal noise sources which decreases as the cluster point is moved toward the unit circle.

As the gains of the loop components differ from their nominal values, the closed-loop poles will disperse from the design value of 0.2 as shown in the root locus diagram of Figure 4. Only the upper half plane is shown since the lower half plane is symmetric to the upper half plane about the real axis. K_n is an open-loop normalized gain constant which at unity places the closed-loop poles exactly at 0.2. Significant dispersion takes place for gain

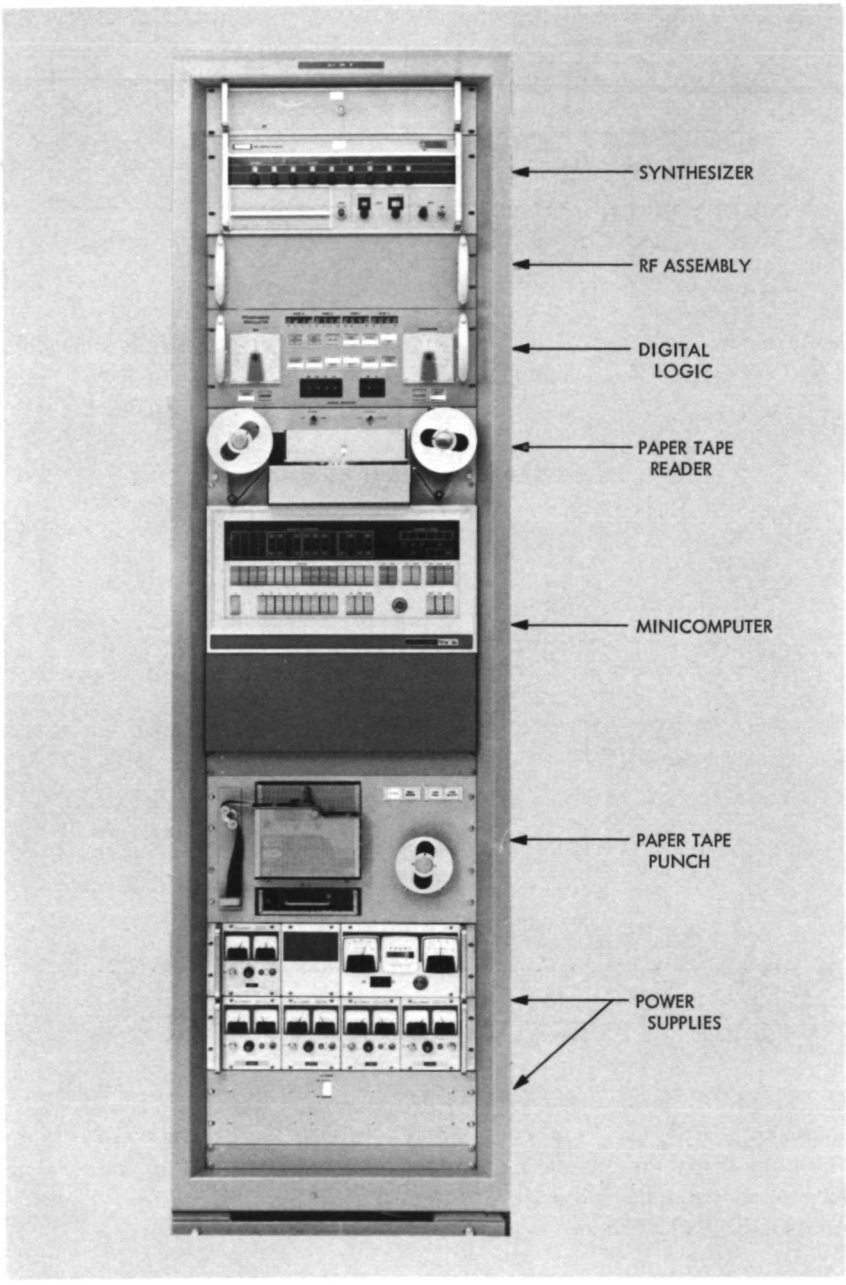

Figure 2. Programmed oscillator assembly

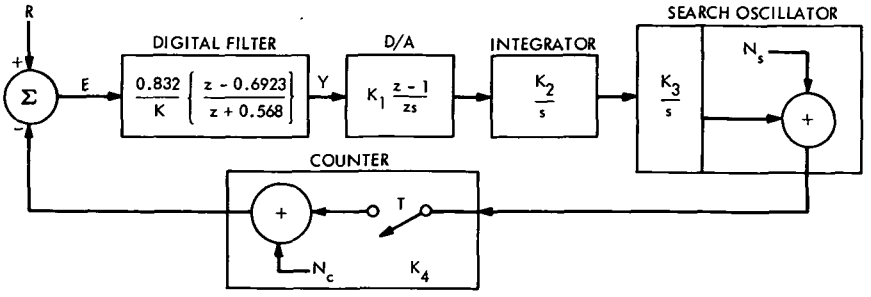

$T = 0.1$ second

$K_1 = 10 + 2^{15} = 0.305 \cdot 10^{-3}$ volt/computer integer

$K_2 = 0.2155$/second

$K_3 = 4 \cdot 10^6 + 20 = 2 \cdot 10^5$ cycles/volt-second

$K_4 = 1$ computer integer/cycle

$K = \frac{T^2}{2} K_1 K_2 K_3 K_4 = 0.06577$

Figure 3. Search oscillator control loop

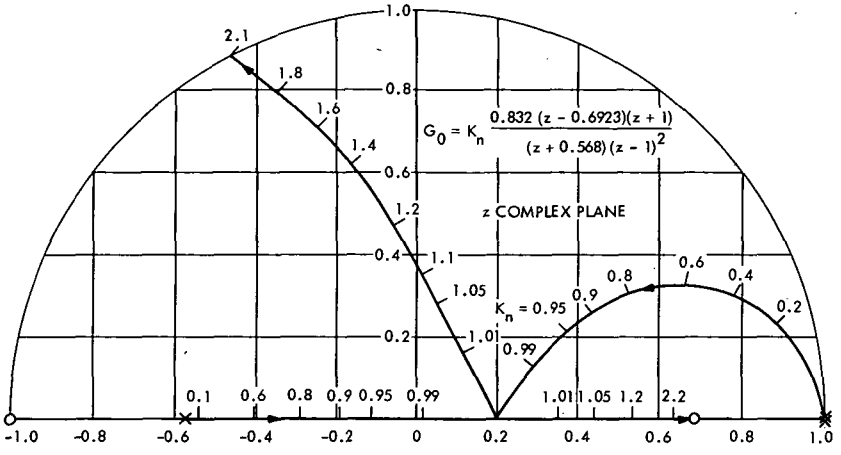

Figure 4. Closed-loop root locus

variations as little as 1% although the system is stable as long as the closed-loop poles remain within the unit circle. Tests on the operating system show that actual gains have remained within 5% of assumed values which still results in highly satisfactory operation.

Minicomputer

The MAC-16 minicomputer configuration used in the program oscillators includes a core memory of 8000 16-bit words, 7500 of which are used in the operational program. Other options included are hardware multiply/divide, direct memory access, power fail/auto restart, eight levels of priority interrupt, and a diode bootstrap loader. The peripherals used are an ASR-33

teletypewriter, a high-speed paper tape reader (300 characters per second), and a high-speed paper tape punch (60 characters per second). The reader is used to enter the program and the day's polynomial constants, and the punch is used to prepare the polynomial constant tape and for program development to meet revised requirements.

The primary function of the computer program is to compute the desired phase from the ephemeris polynomial equation versus time and using these values operate the search oscillator loop in a stable low-noise manner. The ephemeris polynomial is a 15th degree Chebyshev polynomial whose constants have been precalculated from orbit determination and curve fitting programs. Quadruple precision is used within the minicomputer to evaluate the polynomial every 32 seconds. The tenth-second phase numbers are obtained from a second-order interpolation of the frequency values obtained from the polynomial calculation. The calculation for the digital filter is determined directly from its mathematical expression in Figure 3 and is given by

$$Y_n = 12.65(E_n - 0.6923E_{n-1}) - 0.568Y_{n-1}$$

where Y_n is the present output to the D/A converter, Y_{n-1} is the previous output, E_n is the present error number, and E_{n-1} is the previous error number.

In addition to the above functions, the program is responsible for certain initialization and auxiliary functions. At the beginning of a day's operation, the program inputs station time and date and then synchronizes the timing logic to the station second tick signal with an accuracy of ± 1 μs. The program then reads in the correct day's ephemeris constants from a paper tape containing daily constants for the entire month. Power fail/auto restart and equipment configuration control are also program functions. During normal operation the program is responsible for operating the numeric display and for maintaining communication between the program and teletypewriter in a real-time mode. This real-time feature permits program alteration and control while the computer is actually controlling the synthesizer and is highly useful for program development and debugging.

Conclusion

Specifications of these newly constructed low phase noise programmed oscillators are outlined in Table 1. The controllability data is derived from the physical design constants, and the performance data is obtained from comparative measurements between the two units. Two columns of data are listed, one for values at the output of the synthesizer and the other for the

Table 1. Programmed oscillator specifications

Parameter	Synthesizer output	S-band × 64
Controllability		
Output range	200 Hz	12.8 kHz
Least increment of phase control	0.018 deg	1.15 deg
Maximum rate of frequency change	21.55 Hz/s	1379 Hz/s
Performance		
Jitter	0.02 deg p-p	1.28 deg p-p
Drift	0.03 deg/min	1.92 deg/min

equivalent values at an S-band frequency of 2388 MHz when the programmed oscillator is used as a receiver local oscillator with a times 64 multiplier. The output range of 200 Hz has been selected to permit maximum resolution while avoiding a range crossover which would interrupt the coherency of phase operation. The least increment of phase control is equivalent to one count of the counter and the maximum rate of change occurs when a full 10 V is fed from the D/A converter to the integrator. The performance figures show that the phase jitter and drift are well within the design goals of 5 deg rms and 10 deg/min.

One programmed oscillator is located at DSS 14 Mars site and the other located at DSS 13 Venus site, where they are currently being successfully used in the Planetary Radar Mapping programs.

References

1. Emerson, R., Fábián, E. S., and Thompson, G., "Digital Development: Mod V Programmed Oscillator," in *The Deep Space Network*, Space Programs Summary 37-39, Vol. III, pp. 71–77. Jet Propulsion Laboratory, Pasadena, Calif., May 31, 1966.

2. Goldstein, R. M., et al., "Loop Stress Diminution," in *The Deep Space Network*, Space Programs Summary 37-64, Vol. II, pp. 61–67. Jet Propulsion Laboratory, Pasadena, Calif., Aug. 31, 1970.

3. Baumgartner, W. S., "Time-Synchronization System," in *The Deep Space Network*, Space Programs Summary 37-43, Vol. III, pp. 92–106. Jet Propulsion Laboratory, Pasadena, Calif., Jan. 31, 1967.

4. Winkelstein, R., "Digital Devices Development: Screening Test Method for Low-Noise Voltage-Controlled Oscillators," in *The Deep Space Network*, Space Programs Summary 37-60, Vol. II, pp. 17–19. Jet Propulsion Laboratory, Pasadena, Calif., Nov. 30, 1969.

5. "Control System Synthesis for Programmed Exciter," in *The Deep Space Network*, Space Programs Summary 37-32, Vol. III, pp. 38–44. Jet Propulsion Laboratory, Pasadena, Calif., Mar. 31, 1965.

A Multiple-Beam Spherical Reflector Antenna

R. Woo

Telecommunications Division

A spherical reflector with multiple feeds is an attractive possibility for application in future communications satellite systems. Data are presented which show that spherical reflectors possessing relatively high gain (40 dB) and very small phase path error ($<\lambda/32$) are feasible. A design of a spherical reflector utilizing corrugated horn feeds is considered. Radiation patterns are computed using the physical-optics technique. The designed antenna is approximately 60λ in diameter. Calculations performed for this antenna with three beams indicate that each beam has a gain of about 42 dB, a beamwidth of 1.4 deg, and sidelobes that can be expected to be at least 28 dB down. These results indicate that the feature of low sidelobes makes the spherical reflector a promising candidate for a multiple-beam communications satellite antenna.

Introduction

Advanced communications satellite technology will be applied to future information transfer systems such as biomedical data nets, law enforcement networks, adult education, etc. The communications satellite will be in synchronous equatorial orbit and will provide a wideband point-to-point communication capability between any two points within the continental United States. This capability will be achieved by developing a multiplicity of satellite antenna beams which cover the region and operate in conjunction with a series of small ground terminals. The multiple-beam satellite antenna is required to have a field of view of 7 deg for complete coverage. Another critical requirement is that the satellite antenna must possess low sidelobe levels to reduce interference with adjacent beams. A spherical reflector with multiple feeds appears to be an attractive possibility and represents the subject of this study.

The Spherical Reflector Antenna

The spherical reflector antenna has been studied extensively (References 1 and 2) because of its wide scanning capability (i.e., movement of the beam by movement of the feed). Spherical reflector antennas may generally be separated into two types: (1) those representing a large portion, and (2) those representing a small portion of a sphere. In the first type, the spherical reflector deviates substantially from a paraboloidal reflector and large amounts of spherical aberration are introduced. This spherical aberration can be corrected by using phased line-source feeds, auxiliary reflectors, multiple-source feeds or correcting lenses (References 1 and 2). Aside from the complexity in feed design, these antennas are generally narrow band and some suffer from high sidelobes. In the second type, the spherical reflector deviates very little from a paraboloidal reflector and spherical aberration is consequently minimal. For such a reflector, a single-point source feed can be used and the feed design is a relatively simple one. Ashmead and Pippard (Reference 3) and Li (Reference 4) have studied this antenna for wide-angle scanning. Sidelobe levels of 20 dB were obtained. The communications satellite multiple-beam antenna is essentially a narrow-angle scanning antenna. For narrow-angle scanning the sidelobes of the feed do not illuminate the reflector and an improvement in sidelobe levels can be expected.

The purpose of this study is to determine the feasibility of using a spherical reflector representing a small portion of a sphere as a communications satellite multiple-beam antenna and to calculate typical sidelobe levels for such an antenna. Several feeds placed at various scan angles provide the multiple beams required.

Phase Path Error

By comparing a parabola and a sphere, Ashmead and Pippard (Reference 3) and Li (Reference 4) have shown that the phase path error $\Delta\ell$ in a spherical reflector is given by

$$\Delta\ell = \frac{D^4}{2048f^3} \tag{1}$$

where $\Delta\ell$ is the phase path error, D is the reflector diameter, and f is the focal length. (f and D are shown in Figure 1. The dimensions given in Figure

1 are referred to in the next section.) Equation 1 may be expressed in a more useful form:

$$\frac{\Delta \ell}{\lambda} = \frac{1}{2048} \frac{D}{\lambda} \frac{1}{\left(\frac{f}{D}\right)^3} \tag{2}$$

where λ is the wavelength. The focal length f is defined as

$$f = \frac{1}{4}\left[R + \sqrt{R^2 - \left(\frac{D}{2}\right)^2}\right] \tag{3}$$

where R is the radius of the sphere (Figure 1). Equations 1–3 were derived under the approximation that the spherical reflector represented a small portion of a sphere. This requirement means that f/D should generally be greater than 0.5. Under these conditions, $D/2$ is smaller than R and Equation 3 approaches $R/2$, which is known as the paraxial focus of the spherical reflector.

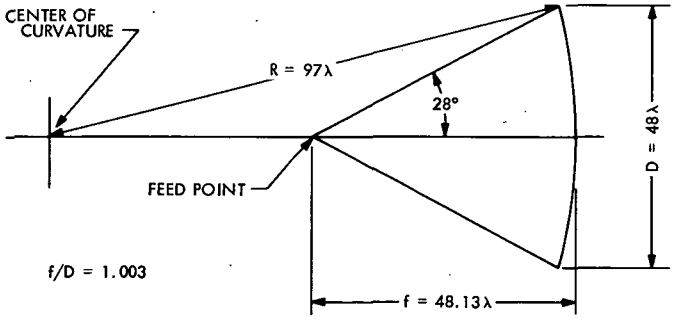

Figure 1. Spherical reflector geometry

The focal length given by Equation 3 is the focal length for which the total phase error is least over the aperture. For non-uniform illumination, this focal length does not necessarily yield the best radiation pattern. The optimum focal length for non-uniform illumination can be determined by a series of computations involving slight deviations from the value of f given by Equation 3.

Spencer (Reference 5) studied the degradation in antenna gain for uniform illumination in the spherical reflector caused by spherical aberration and found that

$$\frac{\Delta G}{G} = 3.5092 \left(\frac{\Delta \ell}{\lambda}\right)^2 \tag{4}$$

where G is the antenna gain.

The information contained in Equations 2 and 4 is shown in Figure 2. Corresponding values of gain for a paraboloid with uniform illumination are also shown. For a given spherical reflector, the phase path error and net antenna gain for uniform illumination can easily be obtained. For a fixed diameter reflector it is seen that the phase path error decreases rapidly with increasing f/D. Even for relatively large reflectors, phase path errors less than $\lambda/32$ are still practical. However, it must be kept in mind that for increasing values of f/D the illumination angle decreases. Consequently, higher gain feeds are needed and aperture blocking effects become significant. Another point worth mentioning is that for large values of f/D, the phase path errors may be smaller than the fabrication tolerances and the question of whether the reflector is a sphere or a paraboloid is merely an academic one. However, as will be seen in the next section, the reflector must be conceived as a spherical reflector and designed as such lest the virtues of a spherical reflector be lost.

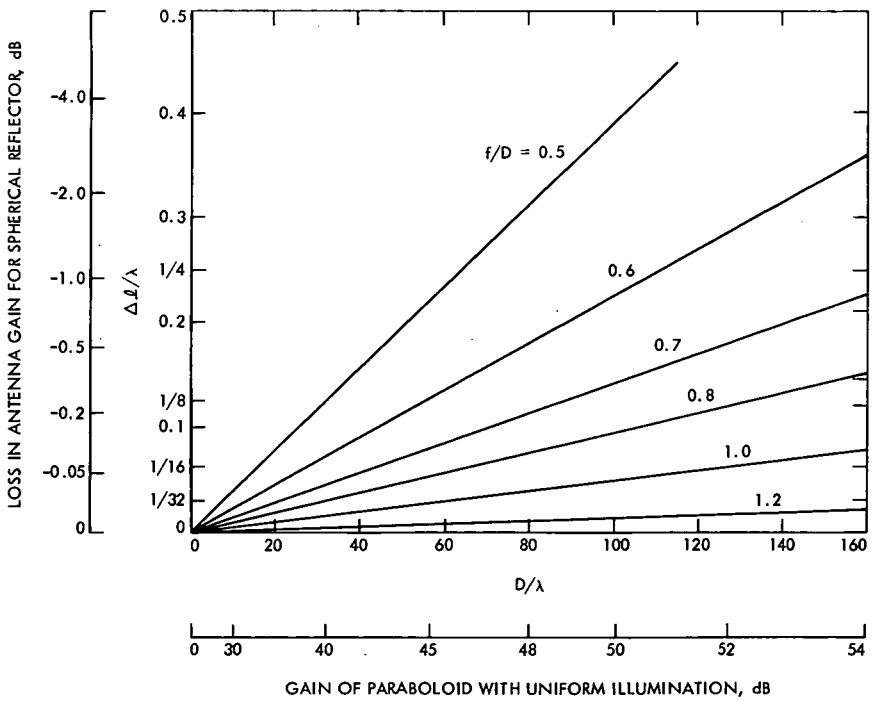

Figure 2. Phase path error of spherical reflectors

Antenna Requirements and a Multiple-Beam Antenna Design

A system study for the 12-GHz band (11.7 to 12.2 GHz) has suggested the use of four reflector antennas to cover the continental United States (Reference 6). Each reflector would have the following characteristics:

(1) Gain: ~40 dB.

(2) Beamwidth: ~1.4 deg.

(3) Number of beams: 3.

(4) Sidelobe isolation: >23 dB.

(5) Beam separation: up to 5–6 beamwidths.

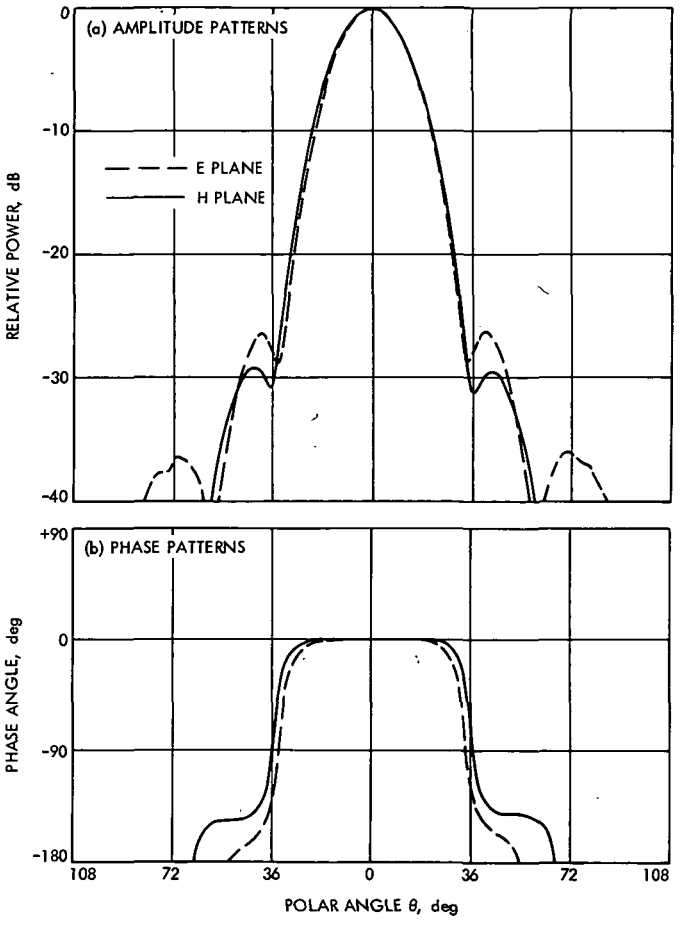

Figure 3. Measured corrugated horn feed patterns

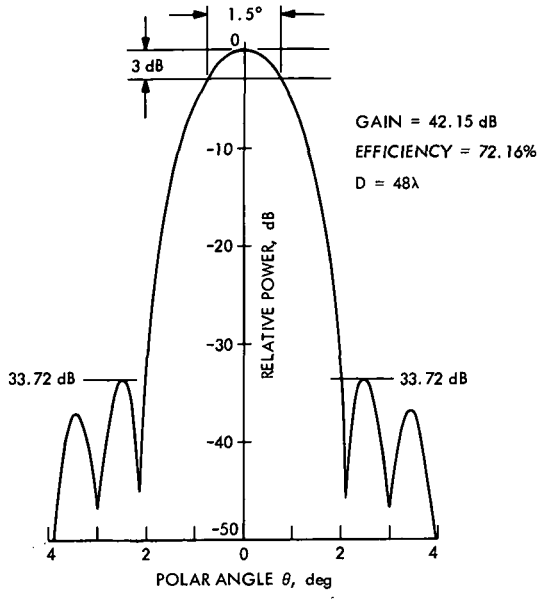

Figure 4. E-plane pattern for feed located on-axis

A spherical reflector offering these approximate characteristics has been designed and its radiation patterns obtained using the physical-optics technique (Reference 7). Efficiency is computed numerically and the results include the effects of both non-uniform illumination and spillover, but not blockage.

To achieve low sidelobes, (1) spherical aberration must be minimized, and (2) an illumination that is non-uniform and tapers toward the reflector edge must be employed. An aperture diameter of 48λ was chosen for the proper gain and beamwidth. (See Figure 1 for other antenna dimensions.) The f/D ratio is 1.003 and, according to Figure 2, the phase path error is less than λ/32. An edge taper of 18–19 dB results when the reflector is fed with a corrugated horn whose measured patterns are shown in Figure 3. Similar feed patterns with varying edge tapers were tried and it was found that the feed pattern in Figure 3 yielded the best results. The calculated radiation patterns are shown in Figure 4. Aperture blocking has been neglected. As can be seen, the sidelobes are at least 33.72 dB down. The antenna gain is 42.15 dB, while the antenna efficiency is 72.16%.

The spherical reflector must be made oversized if the sidelobes are to remain low for the two off-axis feeds. As seen in Figure 5, the reflector diameter must be increased to 60.14λ to ensure a phase path error less than λ/32 and an edge taper of at least 18 dB over a 4-deg scan. Typical radiation patterns are shown in Figure 6. Again, aperture blocking has been neglected. For a scan of over ±2 beamwidths, the patterns are essentially similar with the sidelobes remaining at least 34.9 dB down. It should be pointed out that

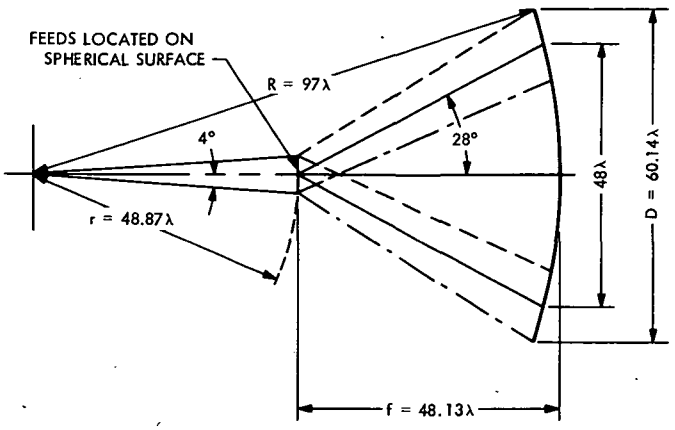

Figure 5. Multiple-beam spherical reflector

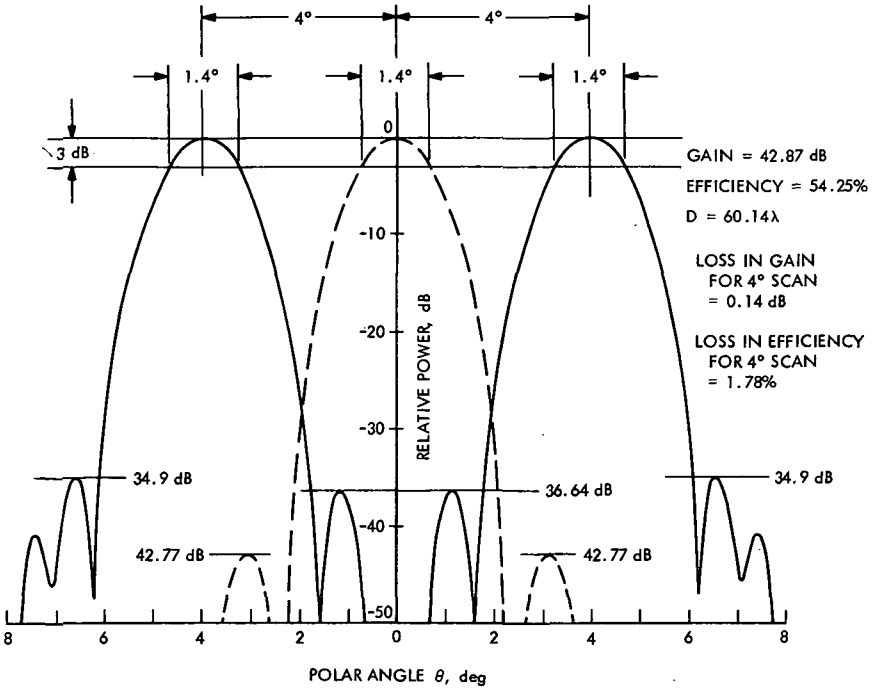

Figure 6. E-plane patterns for feed located 4 deg off-axis in the E-plane

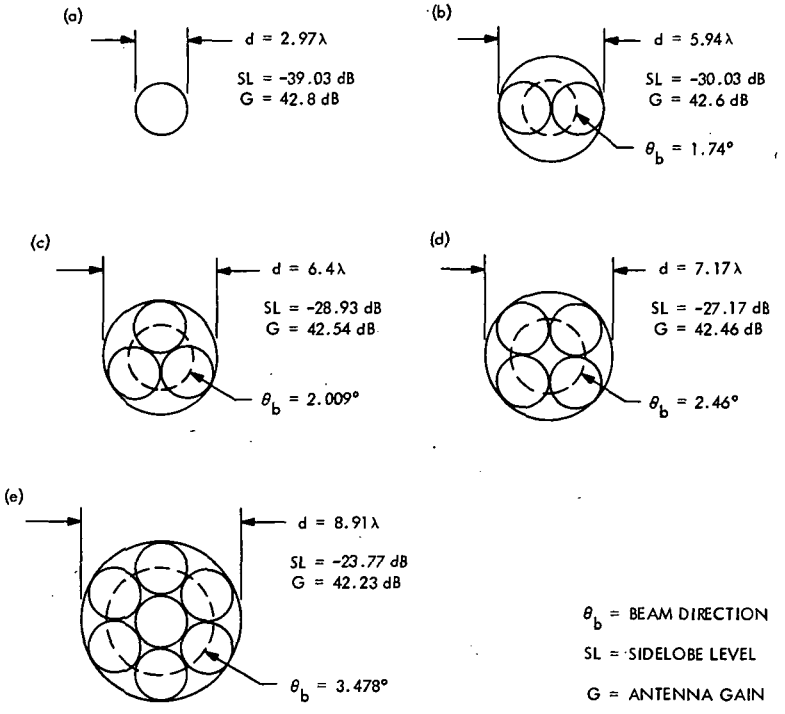

Figure 7. Circular blockage regions used for: (a) 1 horn, (b) 2 horns, (c) 3 horns, (d) 4 horns, and (e) 7 horns

these low sidelobes are obtained at the expense of antenna efficiency. Thus, to maintain the specified gain, a somewhat larger reflector is needed.

So far, aperture blocking effects have been neglected. For large values of f/D, these effects are important since the percentage of blocked area becomes significant. An exact analysis of aperture blocking is very difficult. Nevertheless, an indication of their effects can be obtained by omitting the current distribution over a blocked area which is the projection of the feed on the reflector. This has been carried out for circular blocked regions with diameters varying between 2.97λ and 8.91λ. The correspondence between the number of feeds and the circular blocked regions is illustrated in Figure 7. In all cases, the feed is located on the axis of the reflector. The calculated antenna gain and sidelobe level results are summarized in Figure 7. These calculations are approximate, but they do serve to indicate that even with three beams, sidelobe levels better than 28 dB can be expected. The exact sidelobe levels must, of course, be determined by constructing and testing an experimental model. The effects of mutual coupling between adjacent feeds are expected to be small but these must also be determined experimentally. Note, also from Figure 7, that as many as seven beams may be utilized within a field of view of 7 deg. The sidelobe levels are raised substantially but they are still better than 23 dB.

It was mentioned in the previous section that with the phase path error less than $\lambda/32$, the spherical reflector is very nearly a paraboloidal reflector. It is, however, important that the reflector be conceived and designed as a spherical reflector, otherwise the virtues of a spherical reflector would be lost. To illustrate this point, if the orientation of the two off-axis feeds in Figure 6 is changed so that they point to the center of the reflector, then the spherical symmetry is lost and, although the antenna is more efficient (an increase in efficiency of 0.88%), the sidelobes are substantially higher (an increase of 6.5 dB).

Concluding Remarks

Data have been presented to show that the feature of low sidelobes makes the spherical reflector a promising candidate for a multiple-beam communications satellite antenna. These low sidelobes are achieved at the expense of antenna efficiency. Sidelobe levels are very sensitive to aperture blocking and, although an estimate of these effects was obtained, the calculations were very crude. The exact sidelobes must be determined experimentally.

References

1. Hansen, R. C., *Microwave Scanning Antennas*, Vol. 1, pp. 236-238. Academic Press, Inc., New York, 1964.

2. Collin, R. E., *Antenna Theory*, Part 2, pp. 69-83. McGraw-Hill Book Co., Inc., New York, 1969.

3. Ashmead, J., and Pippard, A. B., "The Use of Spherical Reflectors as Microwave Scanning Aerials," *J. Inst. Elec. Eng. (London)*, Vol. 93, Part IIIA, pp. 627-632, 1946.

4. Li, T., "A Study of Spherical Reflectors as Wide-Angle Scanning Antennas," *IRF Trans. Antennas and Propagation*, Vol. 7, pp. 223-226, 1959.

5. Spencer, R. C., *Theoretical Analysis of the Effect of Spherical Aberration on Gain*, Technical Report E5082. USAF Cambridge Research Center, Cambridge, Mass., Dec. 1951.

6. Williams, W. F., *Final Report on Spacecraft Communications Satellite Antennas FY'71*, 1971 (JPL internal document).

7. Ludwig, A. C., *Calculation of Scattered Patterns From Asymmetrical Reflectors*, Technical Report 32-1430. Jet Propulsion Laboratory, Pasadena, Calif., Feb. 15, 1970.

Measurements of Plasma Parameters in a Simulated Thermionic Converter

K. Shimada

Guidance and Control Division

Cesium-filled thermionic energy converters are being considered as candidate electrical energy sources in future spacecraft requiring tens to hundreds of kilowatts of electric power. The high operating temperatures necessary for a large specific power and high efficiency inevitably impose stringent constraints on the converter fabrication to achieve the desired reliability of the power system. The converter physics for reducing operating temperatures and cesium plasma losses are being studied to achieve high reliability without sacrificing the power performance of the converters. Various cesium parameters which affect the converter performance are: (1) electron temperatures, (2) plasma ion densities, and (3) electric potential profiles. These were investigated using a Langmuir probe in a simulated converter. The parameters were measured in different cesium discharge modes.

Introduction

Cesium-filled thermionic energy converters are being considered as candidate electrical energy sources in future spacecraft requiring tens to hundreds of kilowatts of electric power. The advantage of the thermionic converter over other direct energy conversion devices is its high conversion efficiency, which in turn reduces the required fuel inventory. The conversion efficiency, which is typically larger than 15%, stems mainly from an operating temperature of nearly 2000 K at an emitter electrode where the primary heat is received. The high operating temperature also results in a reduced radiator area for heat rejection, which is an additional advantage. Conversely, the requirements for high temperatures add stringent constraints to the materials and the fabrications of these converters which must have high reliability.

To increase the reliability and to relax the engineering constraints so that the practical converters can be more readily fabricated, a reduction of operating temperatures is being considered. An investigation of a new mode of operation or a new improved converter design is essential to meet the

high reliability and performance of a low-temperature converter. To achieve this goal the converter physics must be re-examined in two areas: electrode surface physics and plasma physics.

In this article results of recent investigations of a cesium plasma using a Langmuir probe in a simulated thermionic converter are presented. The results include: (1) electron temperatures, (2) plasma ion densities, and (3) electric potential profiles in various discharge modes.

Test Vehicle

The diode used for probing the cesium plasma is a simulated thermionic energy converter with parallel plane electrode geometry. This device differs from a practical converter in that it has: (1) a sapphire window, (2) a large interelectrode distance (≅5.2 mm), and (3) a movable Langmuir probe. The 1-mm-diam probe wire, similar to that of Bullis (Reference 1), protrudes through a hole in the collector at its center. A micrometer mechanism makes it possible to move the probe across the entire interelectrode spacing between the collector and the emitter. The active area of the probe (0.0078 cm^2) is parallel to the collector. The active area of the collector is 1.27 cm^2; hence, the probe occupies 1/163 of the current-collecting area of the diode. The probe area is the exposed cross section of a tantalum wire. The cylindrical side of the probe is insulated by tantalum oxide, 0.005 cm thick, formed directly on the wire by a thermal oxidation process. The probe assembly is attached to the tube envelope through stainless steel bellows. The probe may be moved by a micrometer screw with respect to the tube envelope where the collector is mounted.

During the measurements, the diode envelope was heated by electric heating tapes. The cesium reservoir was kept at least 50°C below the tube envelope temperature so that the cesium pressure could be determined by the cesium reservoir temperature.

Measurements

The plasma parameters were measured with a circuit (Figure 1) consisting of: (1) the diode loop for driving it as a cesium gas discharge tube, and (2) the probe loop for measuring the probe current flowing in the probe–collector circuit through a variable probe bias. The probe characteristics were displayed on an X–Y recorder as the probe potential was swept between –6 V and +1 V with respect to the collector. A family of characteristic curves was obtained for different locations of the probe, and each family was taken for different discharge modes of the diode. Depending upon the diode current, the conduction occurred in four different modes of cesium discharge: (1) extinguished mode, (2) anode glow mode, (3) ball-of-fire mode, and (4) plasma mode. The first two modes occur at low currents before the

cesium vapor breaks down and the remaining modes, which are accompanied by the characteristic plasma column in the interelectrode space, occur thereafter. The diode operations were further defined by measuring the emitter temperature T_E and the cesium reservoir temperature T_R. The emitter temperature was measured through a sapphire window using an optical pyrometer at the blackbody hole in the emitter.

The location of the probe tip was measured from the plane of the collector by noting the turns of the micrometer screw required to protrude the probe into the interelectrode space. Thus, the probe tip is flush with the collector surface, showing no protrusion, when $d = 0$, and the tip is 1.04 mm from the collector when $d = 1$; at $d \cong 5$ the tip comes in contact with the emitter. From the measured probe characteristics, the temperatures of electrons, plasma ion densities, and the potential profiles in the interelectrode gap were determined.

Also, the visual observations of the cesium discharge are incorporated with the analysis to obtain comprehensive interpretations of these results.

Results

Diode Volt-Ampere Curves

To investigate various modes of cesium discharge, the diode was operated at relatively low temperatures at which the diode exhibits all modes, depending upon the magnitude of current. A volt-ampere curve shown in Figure 2 was obtained with $T_E = 1173$ K and $T_R = 404$ K. This curve exhibits a break at a voltage where the cesium vapor ignites. The volt-ampere curve is divided into two regions: the lower-current unignited region, and the higher-current ignited region. Within the unignited region, the cesium discharge occurs in two modes, i.e., the extinguished mode and the anode glow mode, depending upon the diode current. The anode glow

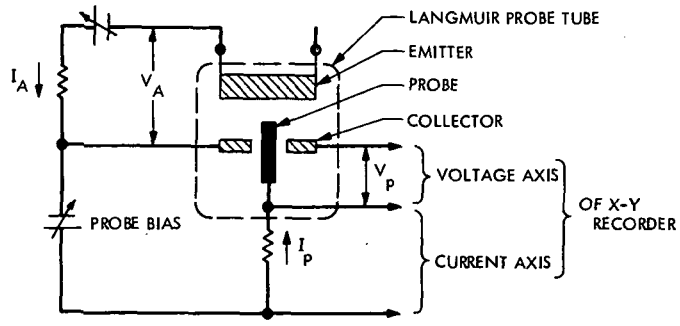

Figure 1. Schematic circuit diagram

mode is accompanied by a rapid increase of the diode current as a result of an increased electron-space-charge neutralization by those ions generated in the anode glow. As the applied voltage increases, the energy supplied to the stream of electrons becomes sufficiently large to cause a propagation of visible glow (ionized zone) toward the emitter which in turn results in the cesium ignition.

In an ignited condition the voltage drop in the plasma, which is in contact with the collector, becomes small since the plasma has nearly zero space charge. Consequently, the diode becomes equivalent to a diode having its virtual collector at the edge of the ball-shaped plasma. The emitter and plasma are separated by a thin dark space. Current conduction occurs with the interelectrode gap partially filled with a ball-of-fire plasma (Reference 2) at the magnitude of current shown at (3) in Figure 2. As the current

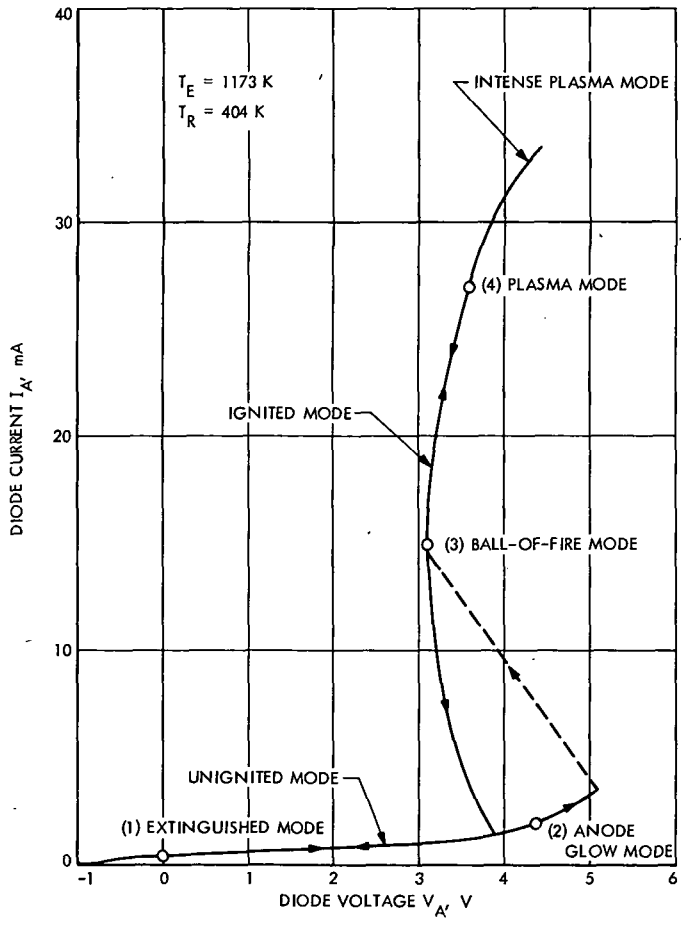

Figure 2. Diode volt-ampere curve

increases further, the plasma merely spreads to a larger area, maintaining the current density constant. The voltage across the diode remains practically constant between point (3) and (4) in the volt-ampere curve. This region is, therefore, similar to that in a normal glow discharge (Reference 3) in inert gases at low pressures. Further increase of diode current requires an increase in the diode voltage to produce an intense plasma. The plasma mode, which occurs between the ball-of-fire mode and an intense-plasma mode, is identified as the maximum power point in practical converters. Similar observations were made by Hansen (Reference 4) in a thermionic converter having an interelectrode spacing of approximately 1 mm.

The probe characteristics, showing the functional dependence of probe current on the probe voltage with respect to the collector, were also measured at four different operating points associated with four different discharge modes. A typical result is shown in Figure 3, where the positive current indicates that the net current to the probe is an electron current, and the negative current indicates that the probe is collecting more ion current than electron current, and/or the probe is emitting electrons. An increased electron emission from the probe, because of an increased heating from the hot emitter, becomes more evident when the probe is located closer to the emitter. The middle part of the probe curve is predominantly prescribed by the thermalized group of electrons as is shown in the semi-log plots (Figure 4).

In the following, the analysis of the probe characteristics obtained with the diode operating in the plasma mode by applying the existing probe theory (Reference 5) is given.

Analysis of Volt-Ampere Curves

Since the probe current I_p is a sum of the electron current I_e arriving at the probe tip, the ion current $-I_i$ contributed by both the plasma ions and surface-generated ions, and the current $-I_b$ by electrons that are emitted back into the emitter from the probe tip, I_p is given by

$$I_p = I_e - I_i - I_b \tag{1}$$

Referring to the electron energy diagram of the diode shown in Figure 5, the current I_b is given by

$$I_b = I_{b0} \exp\ [e(\phi_p - V_p - \phi_E - V_A)/kT_p], \text{ for } \phi_p - V_p \leqslant \phi_E + V_A$$

and

$$I_b = I_{b0}, \text{ for } \phi_p - V_p \geqslant \phi_E + V_A \qquad (2)$$

where I_{b0} is the saturated electron emission from the probe tip at temperature T_p at which its work function is ϕ_p, and V_p is the probe voltage with respect to the collector voltage.

The ion current is saturated for all values of V_p larger than that satisfying the following:

$$-V_p + \phi_p = V_s \qquad (3)$$

where V_s is the potential of the interelectrode space at the probe tip.

The electron current I_e is given by

$$I_e = I_{es} \exp\ [-e(\phi_p - V_p - V_s)/kT_e], \text{ for } \phi_p - V_p \geqslant V_s \qquad (4)$$

where T_e is the electron temperature.

In this equation, a Boltzman distribution that would occur in fully thermalized plasmas is tacitly assumed. The electron saturation current I_{es} was not observable during this measurement because of a local discharge at the probe tip.

In general, then,

$$I_p = I_{es} \exp\ [-e(\phi_p - V_p - V_s)/kT_e] - I_i - I_b, \text{ for } \phi_p - V_p \geqslant V_s \qquad (5)$$

Therefore,

$$I_{es} \exp\ [-e(\phi_p - V_p - V_s)/kT_e] = I_p + I_i + I_b \qquad (6)$$

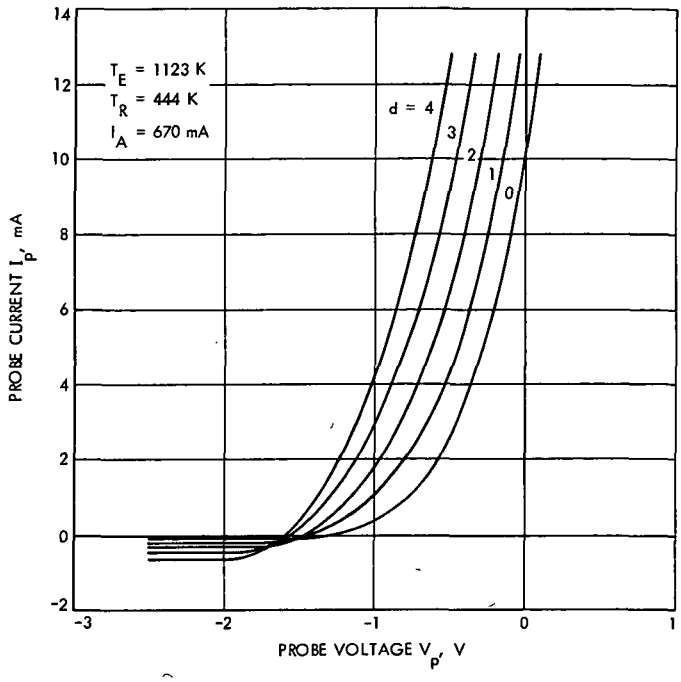

Figure 3. Probe characteristics

Thus, the logarithm of the quantity $I_p + I_i + I_b$, equaling the electron current I_e, should have a linear relationship shown below with the probe voltage V_p:

$$\ln (I_p + I_i + I_b) = \ln (I_e)$$

$$= \left[-\frac{e(\phi_p - V_s)}{kT_e} \right] \left[\frac{eV_p}{kT_e} \right] + \text{constant} \qquad (7)$$

Curves shown in Figure 4 for three different values of T_R with T_E = 1123 K indicate that the logarithm of electron current is linearly dependent upon the probe voltage V_p except for values where the local breakdown or the back emission from the probe disturbs the probe current. From the slope of the curve, which is proportional to e/kT_e, the electron temperature T_e was determined.

The electron temperature T_e was practically independent of distance d (Figure 6) and varied between 17,000 and 3000 K for cesium reservoir temperatures between 404 and 444 K. Observed functional dependence did not agree with other published results (References 1 and 6), which were obtained at higher cesium temperatures or with diodes with smaller gaps.

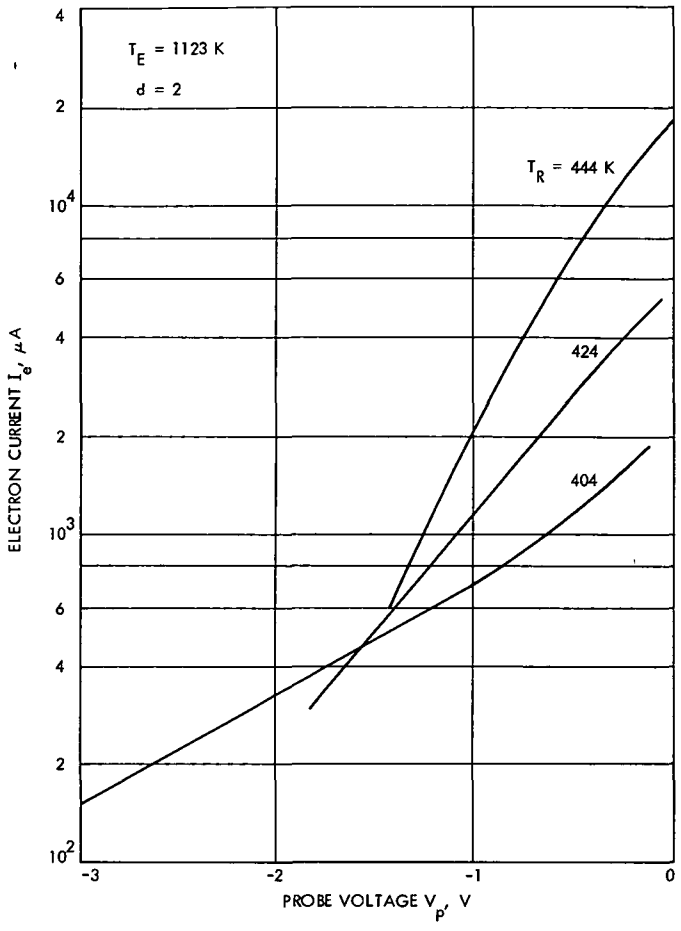

Figure 4. Electron current versus probe voltage

The difference appears to be caused by the fact that the current conduction is drift-dominated in the present work in contrast to the diffusion-dominated conduction in others, in which electrons cool off toward the collector. It may be concluded that the cesium discharge at relatively low pressures and low electrode temperatures is more similar to a glow discharge in inert gases than to a cesium discharge in an ignited thermionic energy converter.

The plasma ion densities were determined from the negative-saturation values of the probe characteristics. In this calculation the probe back-emission I_b was graphically subtracted from the negative saturation to obtain the ion current component I_i. The results obtained at T_E = 1178 K, for the ion density N_i, are shown in Figure 7 in semi-log curves. The ion densities increase toward the emitter (larger d), and it varies exponentially

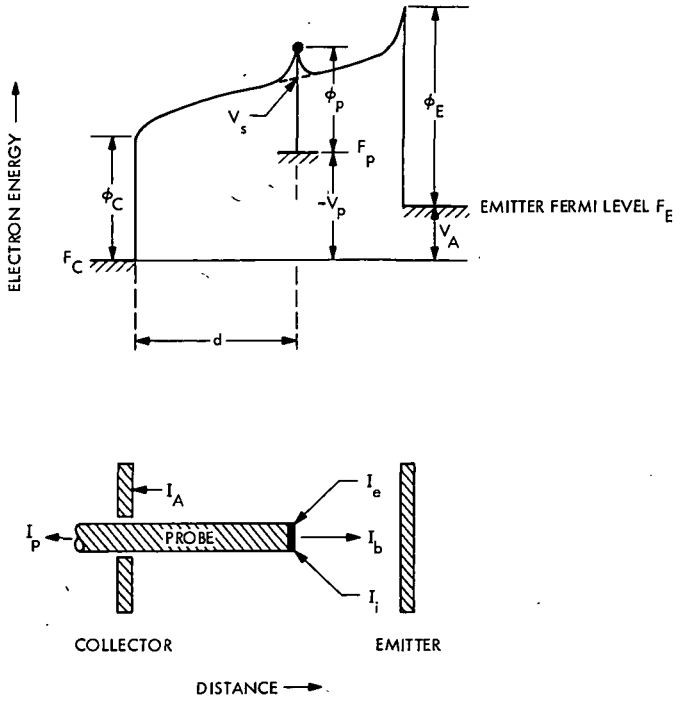

Figure 5. Electron energy diagram

as expected (Reference 7). The ion density, which was of the order of 10% of the cesium gas density, increased with the cesium reservoir temperature T_R.

Lastly, the electric potential profiles in the diode for four different modes of operation will be discussed. The electric potential of the interelectrode space was determined as the probe voltage at which the probe current equaled 1/163 (probe area/collector area) of the diode current. This method was used since the current flow was drift-dominated in this diode in which an LTE (local-thermodynamic-equilibrium) plasma did not exist. The electric potential determined by this method is plotted as a function of distance in Figure 8, after normalizing the potential to zero volts at $d = 0$ (collector). The correction required for this normalization was approximately 0.35 V and is equal to the work function difference between the collector and the probe.

These results show that the negative space potential increases monotonically from the collector toward the emitter, except in the extinguished mode. It should be pointed out that points at the emitter ($d \cong 5$) are the calculated values from $\phi_E - \phi_C + V_A$ (Figure 5) and that the dashed lines between these points and the last measured points at $d = 4.75$ are extrapolations.

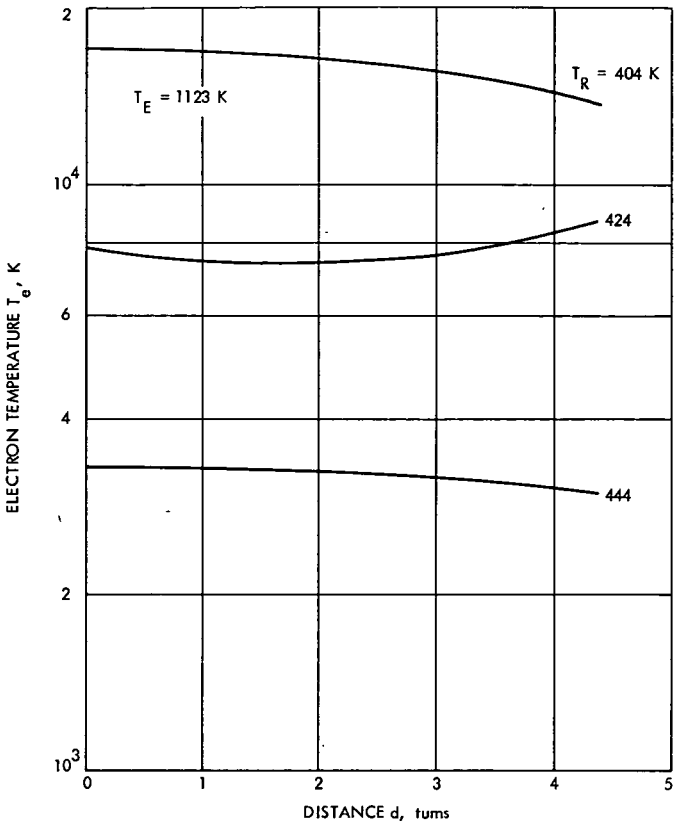

Figure 6. Electron temperature versus probe location

In the extinguished mode the electric potential profile is typical for a negative space-charge-dominated conduction, and the current flow is limited by the negative emitter sheath. As the applied voltage to the collector increases to approximately 5 V, a faint glow appears on the anode indicating a local cesium discharge. In this anode glow the plasma drop is small, as shown in Figure 8 for $d < 1$.

The electric potential profile in a ball-of-fire mode shows a formation of the plasma region being connected to the ion-rich emitter sheath for $4.75 < d < 5.0$. In the plasma mode the profile remains basically the same as that in the ball-of-fire mode since the plasma merely spreads to a larger area from the center of the diode where the probe is located. In both cases the emitter sheath drop is approximately 2 V and the average electric field in the plasma is 4 V/cm.

Conclusions

The probe measurements were made in a simulated thermionic energy converter having an interelectrode spacing of 0.52 cm. The emitter

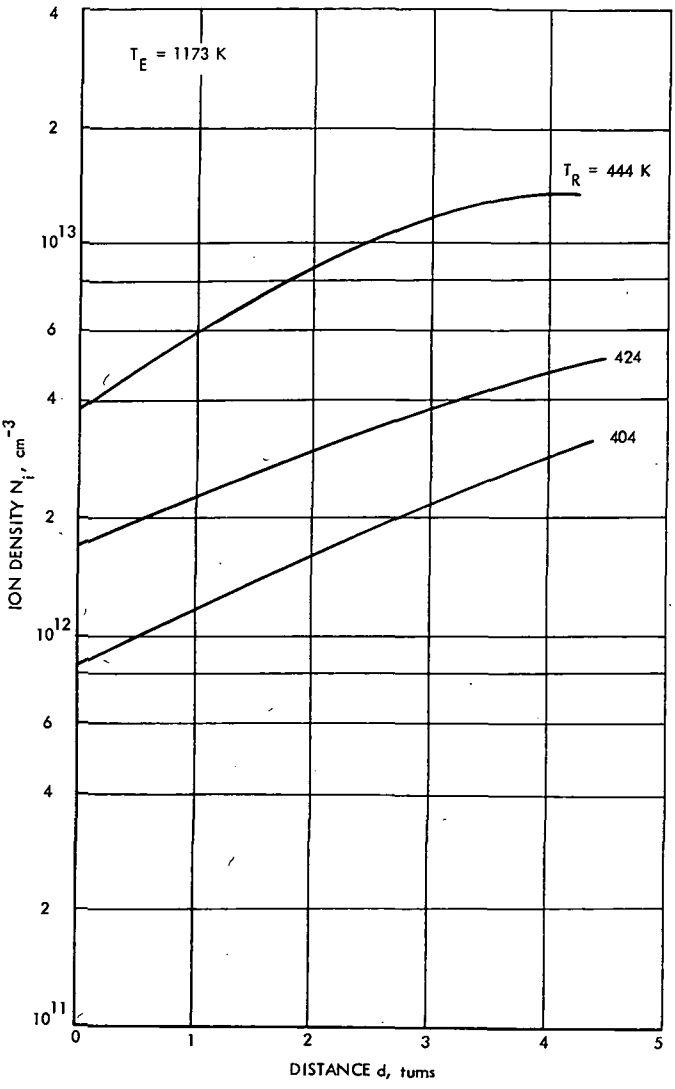

Figure 7. Plasma ion density versus probe location

temperatures were 1123, 1173, and 1223 K, and the cesium reservoir temperatures were 404, 424, and 444 K. The probe, having its active area faced toward the emitter, is axially movable across the entire space between the collector and the emitter. The plasma parameters, including (1) electron temperature, (2) plasma ion densities, and (3) electric potential profiles, were determined in various modes of cesium discharge in the diode.

The electron temperature varied between 17,000 and 3000 K for cesium reservoir temperatures between 404 and 444 K. The higher than expected temperature was a result of low cesium pressure at which the current conduction was drift-dominated.

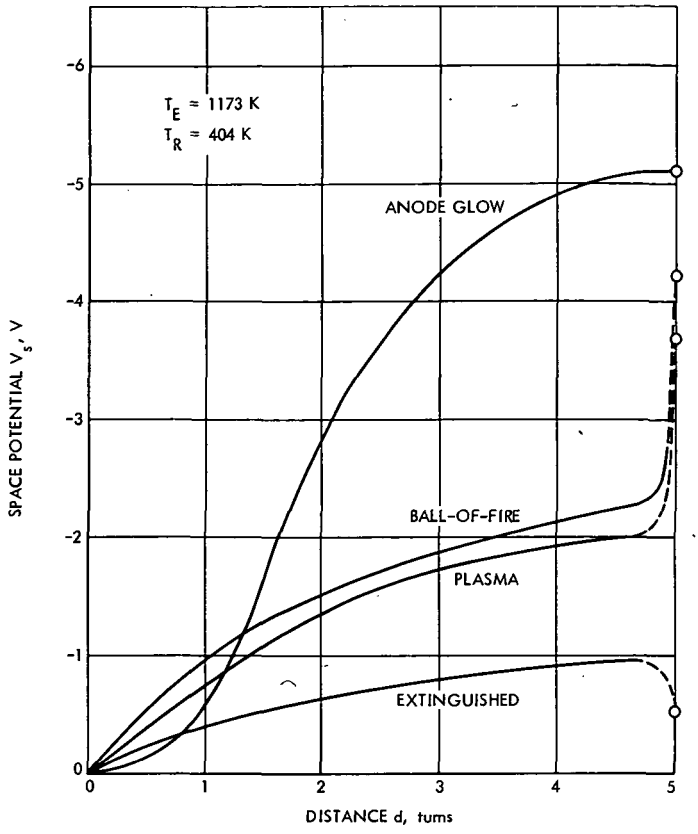

Figure 8. Space electric potential profile

The ion plasma densities were in a range between $10^{13}/cm^3$ and $10^{12}/cm^3$. The magnitude as well as the functional dependence of densities on the location in space was as expected.

The potential profile was obtained in four modes of discharge for the first time in a cesium thermionic diode. The result showed clearly a region of anode glow having a small plasma drop adjacent the collector. The similarity in potential profiles between the ball-of-fire mode and the plasma mode was established; the difference between these two modes mainly lies in the size of the plasma and not the intensity.

The conclusion was extended further to the power performance of practical converters. The maximum output power would be obtained at the transition between the ball-of-fire and the intense plasma mode operation of the converter and the maximum efficiency would be achieved in the unignited mode.

References

1. Bullis, R. H., and Wiegand, W. J., IEEE Report on the Thermionic Conversion Specialist Conference, Cleveland, Ohio, pp. 258–265, Oct. 1964.

2. Johnson, E. O., *RCA Review*, Vol. XVI, pp. 82–108, Mar. 1955.

3. von Engel, A., *Ionized Gases*, p. 195. Oxford University Press, London, 1955.

4. Hansen, L. K., and Warner, C., IEEE Report on the Thermionic Conversion Specialist Conference, Cleveland, Ohio, pp. 310–319, Oct. 1964.

5. Langmuir, L., and Mott-Smith, H. M., *General Electric Review*, Vol. 27, pp. 449, 538, 616, 762, and 810, 1924.

6. Reichelt, W. H., and Kruer, W. L., IEEE Report on the Thermionic Conversion Specialist Conference, San Diego, California, pp. 129–137, Oct. 1965.

7. Shimada, K., "Space-Charge Distribution in a Neutral Plasma," in *Supporting Research and Advanced Development*, Space Programs Summary 37–42, Vol. IV, pp. 56–59. Jet Propulsion Laboratory, Pasadena, Calif., Dec. 31, 1966.

High-Power Microstrip RF Switch

S. D. Choi

Telecommunications Division

A microstrip-type single-pole double-throw (SPDT) switch whose RF and bias portions contain only a metallized alumina substrate and two PIN diodes has been developed. It is superior to electromechanical and currently used circulator-type switches in many aspects of flight-qualified switch characteristics, such as power drain, weight, volume, magnetic cleanliness, cost, and reliability. A technique developed to eliminate the dc blocking capacitors needed for biasing the diodes is described. These capacitors are extra components and could lower the reliability significantly.

An SPDT switch fabricated on a 5.08- × 5.08- × 0.127-cm (2 × 2 × 0.050-in.)[1] substrate has demonstrated an RF power-handling capability greater than 50 W at S-band. The insertion loss is less than 0.25 dB and the input-to-off port isolation is greater than 36 dB over a bandwidth larger than 30 MHz. The input voltage standing-wave ratio is lower than 1.07 over the same bandwidth. Theoretical development of the switch characteristics and experimental results, which are in good agreement with theory, are presented in this article.

Introduction

Future space research will involve not only greater mission distances and durations but also more hostile environments. Successful completion of such missions requires improvement of the state-of-the-art in hardware design of the spacecraft radio system. RF switches, used for switching between antennas and redundant receivers, and transmitters should be extremely reliable and as simple and free from interfering with the rest of the system as possible. Although coaxial-type solid-state RF switches have been previously reported (References 1 and 2), they were not suited for high-power space applications. The PIN diodes used in these switches had inadequate power-handling capability and the coaxial switch circuits were subjected to

[1] Values in customary units are included in parentheses after values in SI (International System) units if the customary units were used in the measurements or calculations.

ionization breakdown at a relatively low power level. Recently, microstrip-compatible diodes with 1000-V reverse breakdown capability have become available. The microstrip-type solid-state diode switch reported here is superior to switch types currently used, such as the circulator and electromechanical types, in such aspects as power drain, weight, volume, magnetic cleanliness, cost, and reliability.

The basic concept of a diode switch is to transmit or reflect the RF power on a transmission line by means of altering the impedance states of one or more solid-state diodes. There are basically two switch types. In one type diodes are placed in shunt across the transmission line, while the other employs series diodes. Schematic drawings for the *on* and *off* modes of the two switch types are shown in Figure 1. For simplicity, the forward-biased switching element is represented with a short circuit and the reverse-biased element with an open circuit.

As is intuitively clear from the figure, the switching element in the series type should be able to handle the entire RF load power through the diode, whereas in the shunt type, the switching element experiences a fraction of the total power because the shunt stub serves as a transformer parallel to the main line. Although the series type is inherently wide band, the shunt type is usually superior to the series type in several important aspects of switch

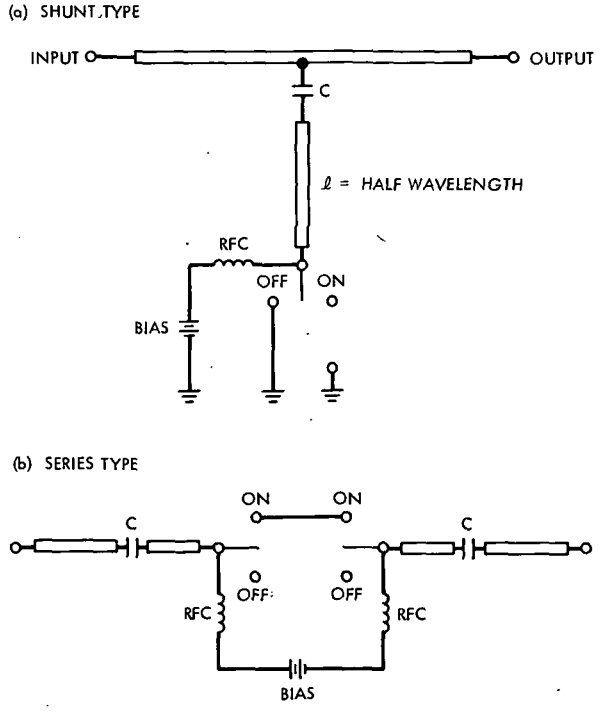

Figure 1. Switch types

characteristics, such as insertion loss, input-to-off port isolation, and power-handling capability.

In the shunt-type switch described in this article, a stub containing a switching diode is placed across a microstrip transmission line. When the switching diode is biased one way, the stub impedance at the main line is high and the RF power is unimpeded. Reversing the direction of the diode bias, the transmission line becomes shorted by a very low impedance presented by the stub. The number of the shunting stubs required in each arm of a switch is dictated primarily by the degree of isolation desired between the input and off port. The length and characteristic impedance of the stub are selected to yield optimum performance of the switch for a given set of diode parameters.

Presentation of the theoretical and measured result is preceded by brief characterizations of the switching element and the microstrip substrate.

PIN Diode and Microstrip Substrate

PIN diodes are exclusively employed as switching elements in solid-state RF switches because of their extremely high impedance under reverse-biased condition. In a PIN diode, highly doped p and n regions are separated by a layer of intrinsic semiconductor as shown in Figure 2. When the diode is forward-biased, carriers are injected into the intrinsic (I) region and it exhibits a very low impedance during the entire RF cycle. When the diode is reverse-biased, all the carriers in the I region are swept out and the I region appears as a low-loss dielectric. Therefore, the reverse-biased diode exhibits a much higher impedance than a reverse-biased ordinary pn junction diode. This is the outstanding feature of the PIN diode as a switching element. Electrical equivalent circuits and typical parameters for the device used are shown in Figure 2 and Table 1, respectively.

The microstrip circuits are fabricated on 1.27-mm (0.050-in.)-thick 99.5% pure alumina substrates with 0.05-μm surface finish on the circuit side and 0.25-μm finish on the ground plane side. Thickness of the gold metallization is 7.62 μm, which is about six times the skin depth at 2295 MHz. Relative permittivity and loss tangent of 99.5% pure alumina at 10 GHz are 9.7 and 0.0001, respectively. The dielectric loss and the conductor loss for 1.27-mm (0.050-in.)-wide transmission line at 2.3 GHz are calculated to be 5.1×10^{-4} dB/cm and 0.02 dB/cm, respectively. The adapter used between the microstrip line and the coaxial line (called the launcher) has an insertion loss of 0.02 dB at 2.3 GHz.

The calculated minimum insertion loss achievable with a 5.08-cm (2-in.)-long 50-Ω transmission line fabricated on this substrate material amounts to 0.15 dB, of which the conductor loss is predominant. A circuitry fabricated on a thicker substrate must have a wider, but not necessarily longer,

Table 1. Typical PIN diode parameters at 2295 MHz

Series resistance R_s	0.6 Ω	At +100 mA
Series inductance L_s	1.2 nH	(lead inductance)
Equivalent series resistance R_{sv}	1.8 Ω	At -200 V
Diode capacitance C_d	0.6 pF	At -200 V

metallization for a system having the same characteristic impedance. Therefore, the conductor loss can be reduced by using a thicker substrate. Further investigation is needed to determine the optimum thickness.

Single-Pole Single-Throw Switches

Schematic diagrams of the shunt stub switch are shown in Figure 3. Figure 3a shows a conventional microstrip switch configuration (Reference 2) in which a dc blocking capacitor is used. In this configuration one end of the diode is RF and dc grounded, which is usually accomplished by drilling a hole through the substrate for a ground post. The dc blocking capacitor is chosen so that, together with its series inductance, it is self-resonant at the band center frequency.

Figure 3b shows a new switch configuration which does not require the dc blocking capacitor or a ground post for the diode. Elimination of one capacitor and one ground post per stub could amount to considerable

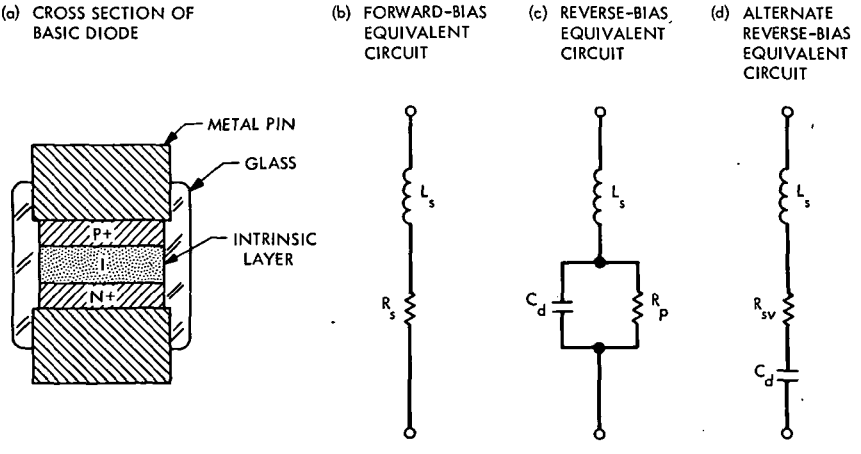

Figure 2. Equivalent circuits for PIN diodes

(a) HALF-WAVE STUB SWITCH WITH DC BLOCKING CAPACITOR

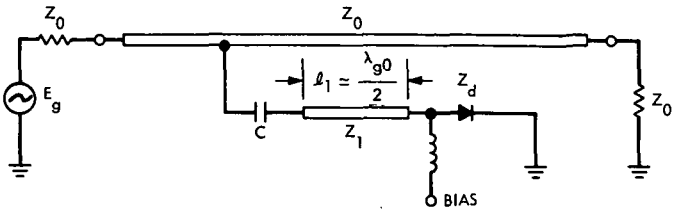

(b) SWITCH WITHOUT DC BLOCKING CAPACITOR

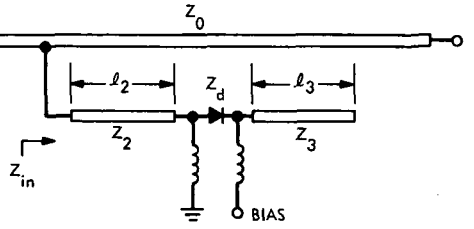

Figure 3. Schematic diagrams of the shunt stub SPST switches

improvement in reliability and ease of manufacturing for multipole switches.

The stub impedance seen by the main line, Z_{in}, is given by

$$Z_{in} = Z_2 \frac{(Z_3 \cos\phi_2 \cos\phi_3 - Z_2 \sin\phi_2 \sin\phi_3) + j(Z_d \cos\phi_2 \sin\phi_3)}{(-Z_d \sin\phi_2 \sin\phi_3) + j(Z_2 \cos\phi_2 \sin\phi_3 + Z_3 \sin\phi_2 \cos\phi_3)} \quad (1)$$

where

$$j = \sqrt{-1}$$

$$\phi_2 = \frac{2\pi}{\lambda_g} \ell_2$$

$$\phi_3 = \frac{2\pi}{\lambda_g} \ell_3$$

$$Z_d = \begin{cases} R_s + jX_L = \text{forward-biased diode impedance} \\ R_{sv} + j(X_L - X_C) = \text{reverse-biased diode impedance} \end{cases}$$

If the diode impedances in the forward- and reverse-biased states were purely real, the lengths of the stub segments, ℓ_2 and ℓ_3 in Figure 3b, should be one-quarter wavelength long at the band center frequency to make Z_{in} maximum for the switch on and Z_{in} minimum for the switch off. However, the impedances of practical diodes are complex as shown in Figure 2. Therefore, the segments are not exactly a quarter-wave long. But for convenience, such stubs are called quarter-wave stubs. For a quarter-wave stub the diode should be forward-biased to turn the switch on, and should be reverse-biased to turn it off.

It is important in a switch that the maximum and minimum stub impedances should occur at the band center frequency f_0, so that the minimum insertion loss and the maximum isolation occur at this frequency. The condition which ensures this is obtained from Equation 1 by setting the imaginary part of the denominator and the real part of the numerator to zero for the switch on and off cases, respectively, and is (for the same characteristic impedances of the stub segments $Z_2 = Z_3$)

$$\left.\begin{aligned} Z_2(\tan\phi_{20} + \tan\phi_{30}) - X_{L0}\tan\phi_{20}\tan\phi_{30} &= 0 \\ Z_2(1 - \tan\phi_{20}\tan\phi_{30}) + (X_{C0} - X_{L0})\tan\phi_{30} &= 0 \end{aligned}\right\} \quad (2)$$

where the subscript zero indicates the corresponding quantities evaluated at the band center frequency f_0.

Solving Equation 2 for the stub lengths yields

$$\left.\begin{aligned} \phi_{20} &= \tan^{-1}\left[\frac{X_{C0}}{2Z_2} \pm \sqrt{\left(\frac{X_{C0}}{2Z_2}\right)^2 - 1}\right] \\ \phi_{30} &= \tan^{-1}\left[\frac{-\left(\frac{X_{C0}}{2Z_2} - \frac{X_{L0}}{Z_2}\right) \mp \sqrt{\left(\frac{X_{C0}}{2Z_2}\right)^2 - 1}}{1 - \frac{X_{C0}X_{L0}}{Z_2^2} + \left(\frac{X_{L0}}{Z_2}\right)^2}\right] \end{aligned}\right\} \quad (3)$$

The stub lengths in terms of quarter wavelength at the band center frequency ($\lambda_{g0}/4$) become

$$\left.\begin{aligned} \ell_2 &= \frac{2\phi_{20}}{\pi}\left(\frac{\lambda_{g0}}{4}\right) \\ \ell_3 &= \begin{cases} \dfrac{2\phi_{30}}{\pi}\left(\dfrac{\lambda_{g0}}{4}\right), & \text{if } \phi_{30} > 0 \\ 2\left(1+\dfrac{\phi_{30}}{\pi}\right)\left(\dfrac{\lambda_{g0}}{4}\right), & \text{if } \phi_{30} < 0 \end{cases} \end{aligned}\right\} \tag{4}$$

For a diode whose parameters are given in Table 1, the lengths become

$$\left.\begin{aligned} [\ell_2, \ell_3] &= \left[0.66\left(\frac{\lambda_{g0}}{4}\right),\ 1.15\left(\frac{\lambda_{g0}}{4}\right)\right] \\ \text{or} \quad [\ell_2, \ell_3] &= \left[0.34\left(\frac{\lambda_{g0}}{4}\right),\ 1.59\left(\frac{\lambda_{g0}}{4}\right)\right] \end{aligned}\right\} \tag{5}$$

for $Z_2 = Z_3 = 50\Omega$. It is clear that the lengths of the stub segments are quite different from a quarter wavelength. The first set of the stub segments in Equation 5 gives a shorter total length and it becomes for $\lambda_{g0}/4 = 1.27$ cm ($f_0 = 2295$ MHz), $[\ell_2, \ell_3] = [0.84$ cm, 1.46 cm]. Stubs are designed according to this formula and adjusted to yield the desired condition. The measured lengths were $[\ell_2, \ell_3] = [0.83$ cm, 1.46 cm], which are in good agreement with the theoretical values.

The insertion loss and isolation of the switch considering only diode impedance are given, respectively, by

$$\left.\begin{aligned} L_{ins} &= 20 \log \left| 1 + \frac{Z_0}{2Z_{in(ON)}} \right| \\ L_{iso} &= 20 \log \left| 1 + \frac{Z_0}{2Z_{in(OFF)}} \right| \end{aligned}\right\} \tag{6}$$

where $Z_{in(ON)}$ and $Z_{in(OFF)}$ are the stub impedances for switch on and off, respectively.

For a quarter-wave stub switch with diode parameters as given in Table 1, these are L_{ins} = 0.039 dB and L_{iso} = 35.08 dB at 2295 MHz. The measured insertion loss was 0.25 dB, which is the sum of losses due to launchers and main line (0.15 dB) and the stub (0.06 dB) and the mismatch loss of the stub (0.04 dB). The measured isolation was 34.2 dB. The theoretical and measured data are plotted in Figure 4 over a frequency range of 2.1 to 2.5 GHz.

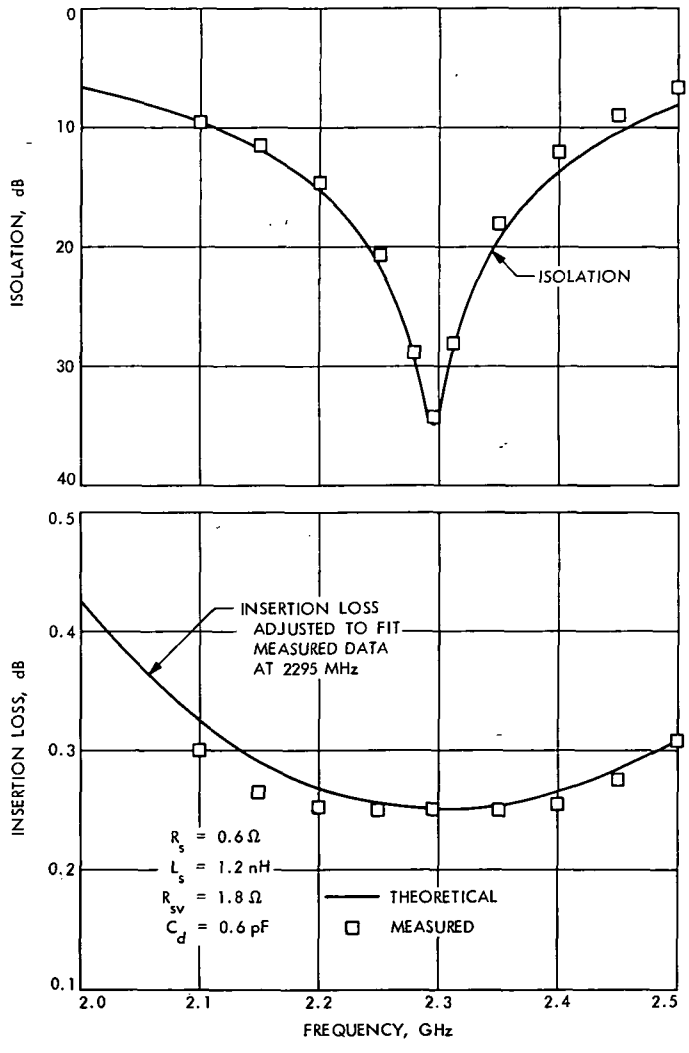

Figure 4. Insertion loss and isolation of SPST quarter-wave stub switch

Another possible configuration for this type of switch employs a stub segment whose length is on the order of one-half wavelength. For this configuration the diode should be reverse-biased to turn the switch on. This is just opposite to the condition for the switch using a quarter-wave stub. This is because a half-wave stub transforms an impedance into itself, whereas a quarter-wave stub transforms an impedance into a reciprocal of the impedance. Choice of one configuration over the other could depend on possible failure modes. For instance, if the failure mode of the diode is a short circuit, a half-wave stub switch will shut off that arm permanently, whereas the arm would be permanently on for a quarter-wave stub. Another important consideration in choosing the configuration is the fact that a half-wave stub switch has inherently narrower bandwidth than a quarter-wave stub switch.

Expressions for the input impedance and length of the stub at the band center frequency are listed in Table 2 for the quarter-wave and half-wave stubs. These equations illustrate which parameters of the diode are important in stub design.

Single-Pole Double-Throw Switch

A single-pole double-throw (SPDT) switch can be formed by combining two single-pole single-throw (SPST) switches. The bias arrangement should

Table 2. Input impedance and length of stubs

Parameter	Quarter-wave stub	Half-wave stub
$Z_{in(ON)}$	$\frac{Z_2 X_{C0}}{R_s \tan \phi_{20}}$	$-\frac{Z_2 X_{C0}}{R_{sv} \tan \phi_{20}}$
$Z_{in(OFF)}$	$\frac{Z_2 R_{sv}}{X_{C0} \tan \phi_{20}}$	$-\frac{Z_2 R_s}{X_{C0} \tan \phi_{20}}$
ϕ_{20}	$\tan^{-1}\left[\frac{X_{C0}}{2Z_2} \pm \sqrt{\left(\frac{X_{C0}}{2Z_2}\right)^2 - 1}\right]$	$\tan^{-1}\left[-\frac{X_{C0}}{2Z_2} \pm \sqrt{\left(\frac{X_{C0}}{2Z_2}\right)^2 - 1}\right]$
ϕ_{30}	$\tan^{-1}\left[\frac{-\left(\frac{X_{C0}}{2Z_2} - \frac{X_{L0}}{Z_2}\right) \mp \sqrt{\left(\frac{X_{L0}}{2Z_2}\right)^2 - 1}}{1 - \frac{X_{C0} X_{L0}}{Z_2} + \left(\frac{X_{L0}}{Z_2}\right)^2}\right]$	

be, of course, such that when one port is on, the other port is off. A photograph of a breadboard version of an SPDT switch is shown in Figure 5.

The insertion loss for the SPDT switch consists of the losses in the ON arm and the OFF arm. The insertion loss due to the forward-biased and reverse-biased diodes is given by

$$L_{ins} = 20 \log \left| 1 + \frac{Z_0}{2Z_{in(ON)}} + \frac{Z_{in(OFF)}}{2Z_0} \right| \tag{7}$$

The remainder of the insertion loss is contributed by the bias networks, the dielectric, and the conductors.

The isolation between the input and the off port for the SPDT switch is 6 dB better than for the SPST switch. This is because in the SPDT switch the incident RF current in the OFF arm is just one-half that in the SPST switch. The isolation is, therefore, given by

$$L_{iso} = 20 \log \left| 4 \left(1 + \frac{Z_0}{2Z_{in(OFF)}} \right) \right| \tag{8}$$

The insertion loss and isolation given by Equations 7 and 8 are plotted in Figure 6.

The measured data is plotted along with the theoretical curves in Figure 6. The insertion loss at the band center frequency was 0.25 dB. The measured data deviates from the theoretical curve less than 0.1 dB at 100 MHz away from the band center frequency. This discrepancy is believed to be due to neglecting the band limiting effect of the bias networks in the theoretical calculations. The measured data for the isolation agrees very well with the theoretical calculation. A summary of the performance of the SPDT switch is listed in Table 3.

Power and Vacuum Test

The SPDT switch shown in Figure 5 was subjected to a power test. The input power was raised in increments of 25 W up to a maximum of 100 W. The switch was allowed sufficient time to thermally stabilize at each power level. The temperature rise of the diode junction was 75°C above the ambient temperature at the 100-W level. According to the manufacturer's specifications, the diode can be safely operated with a junction temperature as high as 150°C.

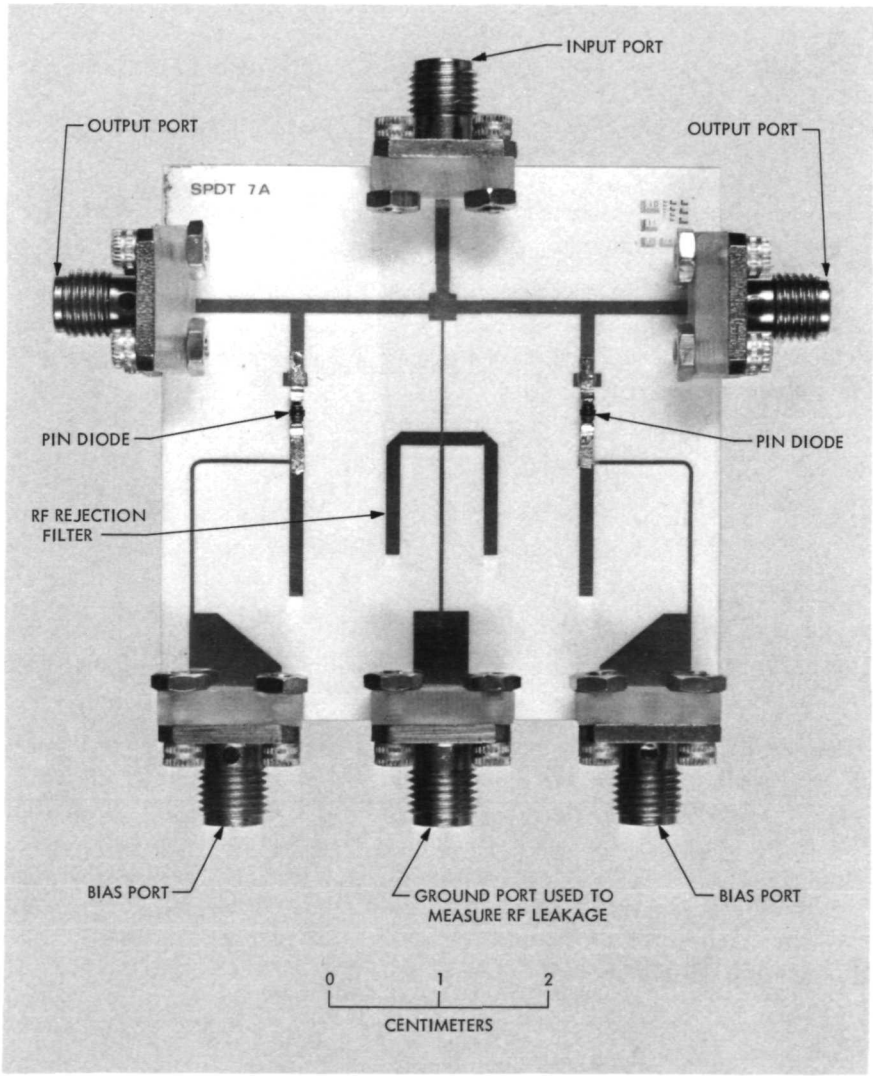

Figure 5. Breadboard SPDT switch

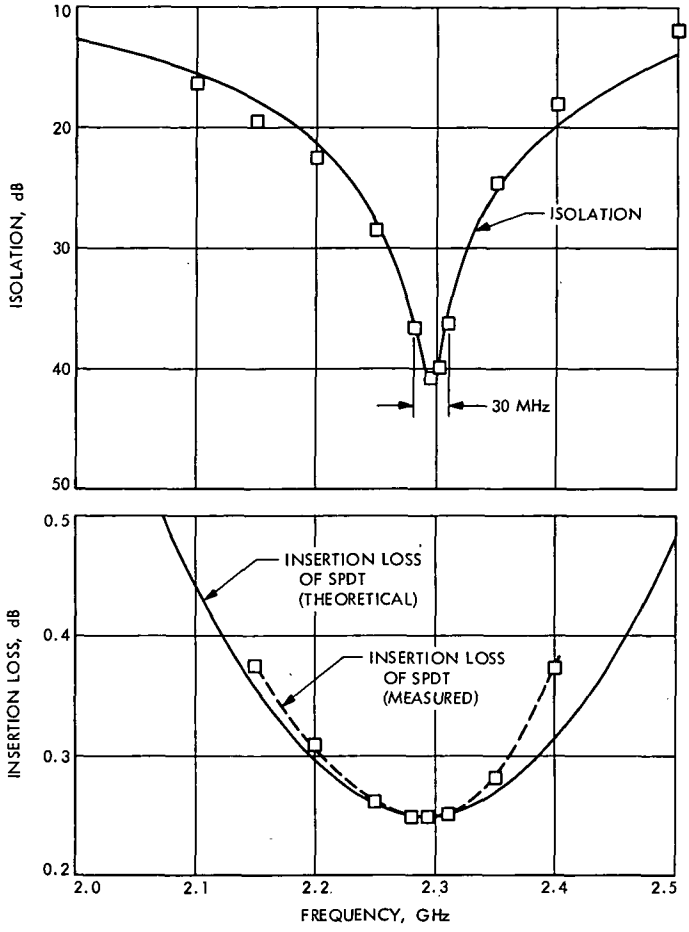

Figure 6. Insertion loss and isolation of SPDT quarter-wave stub switch

Table 3. Performance of SPDT switch

Band center frequency	2295 MHz
Input voltage standing-wave ratio	Lower than 1.07
Insertion loss	0.25 dB over 30 MHz
Isolation (minimum)	36 dB over 30 MHz
Input to bias port isolation	Greater than 45 dB

The power dissipation in the diode, P_D, is given by

$$P_D = \frac{R_s}{Z_0} P_L \tag{9}$$

where P_L is the power input to the switch. The power dissipated in the diode for P_L = 100 W is only 1.2 W. This indicates that the thermal resistance of the diode as mounted on the microstrip circuit is 62.5°C/W. The thermal resistance can be lowered by mounting the substrate on a solid metallic circuit frame and by using beryllium oxide dielectric directly beneath the diode.

The SPDT switch was also subjected to low-pressure tests. When operated at critical pressure [306.6 N/m^2 (2.3 torr)], ionization breakdown occurred at 150 W of RF power. Additional tests were performed at 533.3 × 10^{-5} N/m^2 (4 × 10^{-5} torr) to determine if multipacting breakdown would occur. None was observed for RF power levels as high as 150 W. According to published data (Reference 3), multipacting breakdown should not occur in this switch until 280 W.

Applications

The theory developed here can be easily adapted for the design of switches for many different applications. A few of the switch types which could be used for switching between antennas and redundant receivers and transmitters are illustrated in Figure 7, along with the matrices for the modes of operation and bias conditions. For the sake of simplicity, the stubs and diode bias networks are represented by diodes only.

These switches are combinations of SPST and SPDT switches. Therefore, the work presented in this article is the basic building block for many different switch types.

Summary and Conclusions

A microstrip type RF switch which uses only two PIN diodes on a microstrip substrate has been developed for application in spacecraft radio systems. An SPDT switch fabricated on a 5.08- × 5.08- × 0.127-cm (2- × 2- × 0.05-in.) alumina substrate can easily handle as much as 100 W of RF power. The insertion loss and isolation are better than 0.25 and 36 dB, respectively, over a 30-MHz band centered at 2295 MHz. This microstrip-type switch is superior to the currently used circulator and mechanical switches in terms of reliability, magnetic cleanliness, weight, volume, and power drain. A transfer switch is being made by combining two SPDT switches in parallel.

SWITCH TYPE	SCHEMATIC DIAGRAM	MODE OF OPERATION	DIODE STATE* A B C D
SPST	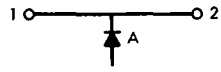	1-2 ON 1-2 OFF	F R
SPDT	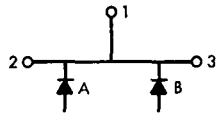	1-2 ON, 1-3 OFF 1-2 OFF, 1-3 ON	F R R F
SP3T	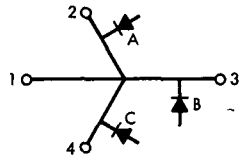	1-2 ON 1-3 ON 1-4 ON	F R R R F R R R F
2P2T	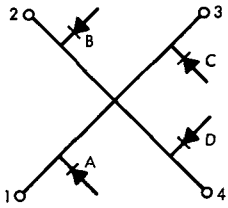	1-3 ON 1-4 ON 2-3 ON 2-4 ON	F R F R F R R F R F F R R F R F
TRANSFER	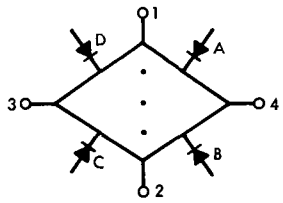	1-3, 2-4 ON 1-4, 2-3 ON	R F R F F R F R

*DIODE STATES ASSUME QUARTER-WAVE STUBS. F AND R DESIGNATE FORWARD AND REVERSE BIASES, RESPECTIVELY.

Figure 7. Application of SPST and SPDT switches to form other switch types

Acknowledgment

The author wishes to express his appreciation to J. F. Boreham for his valuable advice and to J. H. Meysenburg for his contribution to this work.

References

1. White, J. F., and Mortenson, K. E., "Diode SPDT Switching at High Power with Octave Microwave Bandwidth," *IEEE Trans. Microwave Theory and Techniques*, Vol. MTT-16, pp. 30–36, Jan. 1968.
2. Watson, H. A., *Microwave Semiconductor Devices and Their Circuit Applications*, pp. 300–338. McGraw-Hill Book Co., Inc., New York, 1969.
3. Woo, R., *Final Report on RF Voltage Breakdown in Coaxial Transmission Lines*, Technical Report 32-1500. Jet Propulsion Laboratory, Pasadena, Calif., Oct. 1, 1970.

Dynamic Upper Atmospheric Force Model on Stabilized Vehicles for a High-Precision Trajectory Computer Program

A. R. Khatib

Mission Analysis Division

This article summarizes the results of research carried out at JPL for the design and implementation of dynamic upper atmosphere and lift and drag models into the advanced Double-Precision Trajectory Program (DPTRAJ). The upper atmosphere model draws heavily on the behavior of the Earth's upper atmosphere which exhibits cyclic as well as irregular variations in density profile, temperature, pressure, and composition in unison with solar activities as deduced from the more recent land-based and satellite observations.

The lift and drag model is designed specifically for inertially stabilized vehicles of the Mariner class, with possible extension to gravity gradient stabilized vehicles of the GEOS class. The model considers operation in the free molecular flow regimes with large Knudsen numbers. The vehicle is considered a composite structure with basic components having well-defined shapes, each with its own surface characteristics in terms of temperature, reflectivity, and accommodation of free stream molecules. The model takes into account both the calculation of precise aerodynamic force coefficients in terms of expansion of modified Bessel functions in speed ratios and angle of attack, and approximate force coefficients when the speed ratios approach infinity. Other considerations include specular and diffused reflectivity, shielding, and shadow effects.

Introduction

Improvements in the tracking data and orbit determination accuracies at JPL in conjunction with low-altitude orbiter missions having upper atmospheric penetration have resulted in the need for accurate modeling of the aerodynamic forces which influence the trajectories of these vehicles. Accurate lift and drag force models require an accurate, dynamic atmosphere model, as Earth satellite drag analysis have made it obvious that no static model can approximate the atmospheric parameters in the general case. Although modeling complexity is unconstrained in principle when solving equations of motion with special perturbation techniques (i.e., numerical integration), practical limiting factors on the complexity are

determined by computer hardware performance (i.e., precision of the numerical integration) and the accuracy of other trajectory force models. It is also important to design efficient general models which may be used for a wide spectrum of missions in this decade.

The atmospheric model selected draws heavily on the behavior of the Earth's upper atmosphere due to the availability of data obtained in the past decade. Although the amount of factual data on many of the important parameters necessary for the determination of the general variation of atmospheres of other planets is scarce, the mechanisms and inferences implied in the generality of a model based on the behavior of the Earth's upper atmosphere remain valid to the extent of assuming that atmospheric behavior is grossly comparable when projecting dynamic effects to other planets.

The lift and drag force model selected is one that is applicable in a free molecular flow regime, where the atmospheric molecular mean-free-path is larger than the characteristic dimension of the vehicle (i.e., large Knudsen number). For practical considerations, the spacecraft is considered a composite structure of basic well-defined shapes with analytic properties. While ignoring multiple reflections, shielding factors are introduced to approximate the nonlinear interaction between components. The analysis is simplified by ignoring torques and inertia considerations, thus limiting the model to inertially stabilized types of vehicles (e.g., Mariner class) with possible extension to gravity gradient stabilized types (e.g., GEOS class).

Upper Atmosphere

Survey

Instruments and drag analysis methods of investigations revealed the existence of both periodic and irregular variations in the basic parameters of the Earth's upper atmosphere. These variations proved to be in unison with solar activities.

Although the microscopic details of the process of radiation absorption and reradiation are well understood, such processes are generally complicated, especially when evaluating variable solar radiation effects on multicomponent atmospheres.

Several major considerations due to efforts during the past decade can now be stated.

(1) Higher regions of the atmosphere are best represented by a vertical isothermy in a state of diffusion equilibrium. The ratio of the principal constituents is essentially fixed at the beginning of the diffusion level. Heat conduction is the principal transport mode.

(2) The atmosphere is heated by all radiations of the solar spectrum. Principal contributors in terms of the total kinetic energy of a thermospheric column belong to the region 1 to 1700 Å (ultraviolet and soft X-ray). Thermal emission from Coronal condensation clustering above Sun spots is an emitter of radiation (EUV). A single wave length is usually used as an index of solar decimetric flux ($F_{10.7}$). The choice of this index is influenced by its high correlation relative to solar activity and atmospheric temperatures.

(3) Although satisfactory explanations for meridional transport and auroral zone heating due to magnetic storms are not available (Reference 1), satellite drag analysis shows a linear correlation between geomagnetic indices and the upper-atmospheric temperatures with an observed time lag.

(4) The observed variations can be categorized as follows:

   (a) Altitude and latitude position.

   (b) Diurnal (planetary rotation).

   (c) Monthly (27-day solar rotation).

   (d) Semi-annual and seasonal (planetary orbit).

   (e) Solar decimetric radiation (11-yr Sun-spot cycle).

   (f) Magnetic storms (irregular) and auroral activity (high latitudes).

Major approaches used in constructing upper-atmosphere models include: an empirical approach, derived from satellite drag analysis, generally in agreement with physical laws, and a theoretical approach based on conservation laws. The empirical one-dimensional model of Jacchia (Reference 2) is a quasi-static, multiple-component model. The model is based on the assumption of hydrostatic equilibrium, an empirical temperature profile, and a fixed set of boundary conditions for temperature and number densities. Empirical temperature profiles reflecting atmospheric temperature variations due to solar activities are used to compute number densities. Knowledge of thermal diffusion ratios and diffusive equilibrium is assumed. Contrary to observations, a nearly isopycnic layer with a constant density at some level results in models based on the above approach as a consequence of the use of a fixed set of boundary conditions (Reference 3). Another approach taken by Harris and Priester (Reference 4) is in computing the temperature from an energy conservation equation by utilizing all known (and some virtual) heat sources to generate the temperature profile, which is then used simultaneously with number densities assumed in hydrostatic equilibrium. Other more recent models include those by Thomas (Reference 5) and Friedman (Reference 6). The model of Thomas is analytic and one dimensional, where the undimensional conservation equations are transformed to an isobaric frame, thus enabling solution by simple analytic Green functions. Friedman's model utilizes simplified expressions for radiation heating in solution of the conservation

equations. This three-dimensional model allows boundary conditions to vary until agreement with observed data is achieved. This last approach is more physically realistic in that it accounts for horizontal heat conduction and mass diffusion.

General Computer Model

Due to operational flexibility, the empirical model was chosen for the high-precision trajectory program DPTRAJ (Reference 7). The user supplies density and average molecular weight versus height for the full range of exospheric temperatures. The table can be made up of patched set of one-dimensional atmospheres corresponding to given top exospheric temperatures. The range of temperatures extends from the absolute minimum night time to the maximum observed and modeled temperatures. Empirical equations relating variations of exospheric temperature to dynamic causes are evaluated yielding the required temperature at the evaluation epoch. The required parameters at the given height are thus obtained. The empirical form of the temperature equation (Reference 8) is

$$T = (T_{\min} + \Delta T_D) f(\theta), \text{ in kelvins}$$

where

$T_{\min}$ = minimum known temperature

$f(\theta) = 1 + L \cos^M \theta$ = diurnal bulge effect, where the angle θ is measured from the bulge maximum to the considered location, and L and M are constants

ΔT_D = contribution of dynamic effects

$$= (a - T_{\min}) + b\Delta F_{10.7} + \left[c\Delta F'_{10.7} + d(\Delta F'_{10.7})^2\right]$$

$$+ \left[(e + f \sin 2\pi D_1)(\bar{F}_{10.7} \sin 4\pi D_2)\right]$$

$$+ \left[ga_p - h(1 - \exp ka_p)\right]$$

and a, b, c, d, e, f, g, h, and k are constants

$\Delta F_{10.7}$ = decimetric flux less $\bar{F}_{10.7}$, 10^{-22} W-m^{-2} (cps)$^{-1}$ per bandwidth

$\bar{F}_{10.7}$ = average over three solar rotations

$\Delta F'_{10.7}$ = average over one solar rotation less the average over the 11-yr Sun-spot cycle

D_1, (D_2) = days past observed min, (max) seasonal variations

a_p = the 3-h geomagnetic index, properly scaled for atmospheric response time lag, 2×10^{-5} gauss

The dynamic equation terms empirically account for the effects of the solar rotation, solar cycle, semiannual, and magnetic storms, respectively.

Aerodynamic Forces

Survey

At higher altitude, when the ratio of the mean-free-path of free stream molecules to a basic characteristic body dimension (Knudsen number) is large, the rarefied gases do not behave like a continuum. Computation of aerodynamic forces and moments are based on a concept from the kinetic theory of gases known as the free molecular flow regime. The theory takes into account uniform mass motion of gases superimposed upon the thermal motion (Maxwellian distribution) of gas molecules. Ignoring collisions between impinging and re-emitted molecules, the total force on a body is made up of components from surface bombardment by impinging molecules and components due to specular or diffuse re-emission of those molecules. In the specular reflection the normal velocity component is reversed, while the tangential component with shear effects on the surface remains unchanged. In the diffuse reflection, all previous directional history is erased. Molecules leaving the surface have speeds with Maxwellian distribution dependent on re-emitted stream temperature, and direction controlled by the Knudsen cosine law.

The recent methods developed by Heineman (Reference 9), Stalder (Reference 10), and Blick (Reference 11) involve integration of components of the momentum force, imparted to a differential plane area by impinging and reflected molecules, in defined directions. The direction cosines chosen are related to the component of force being computed, which in turn yield the desired aerodynamic coefficients for the type of shape being considered.

The basic equation for the total incident momentum (front and rear sides) per elemental area per unit time is

$$dG_i = \left\{ \frac{\beta^3 mN}{\pi 3/2} \int_{-\infty}^{\infty} \int \left[\int_0^{\infty} c_1 (\mathbf{c} \cdot \hat{\ell}) \exp(-\beta^2 \mathbf{V} \cdot \mathbf{V}) \right.\right.$$

$$\left.\left. - \int_{-\infty}^{0} c_1 (\mathbf{c} \cdot \hat{\ell}) \exp(-\beta^2 \mathbf{V} \cdot \mathbf{V}) \right] dc_1 dc_2 dc_3 \right\} dA$$

where

$\hat{\ell}$ = desired direction of momentum force vector

mN = ρ = number density

β = $1/c$ = reciprocal of most probable molecular speed

$\mathbf{V}$ = thermal velocity

$\mathbf{c}$ = $\mathbf{V} + \mathbf{U}$ = total velocity = sum of thermal and mass velocities

U = Sc = $(\gamma/2)^{1/2} M$ = stream mass speed, and S is the speed ratio, γ is ratio of the specific heats, and M is the Mach number

For example, application of the above equation yields the impinging front side pressure on an elemental area of flat plate along **N** (see Figure 1).

Let

$$\mathbf{U} = U(\sin\theta \hat{\mathbf{N}} - \cos\theta \hat{\mathbf{y}})$$

$$\hat{\ell} = \hat{\mathbf{N}}$$

Therefore,

$$P_i = \frac{\rho U^2}{2} \left\{ \left(\sin^2\theta + \frac{1}{2S^2} \right) [1 + \text{erf}(S \sin\theta)] \right.$$

$$\left. + \frac{\sin\theta}{\sqrt{\pi} S} \exp[-S^2 \sin^2\theta] \right\}$$

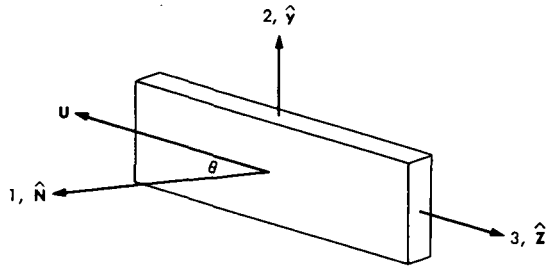

ANGLE OF ATTACK $\alpha = 90 - \theta$

Figure 1. Coordinate system definition

Simplifying assumptions leading to approximate expressions were used by Blick (Reference 11) to obtain aerodynamic coefficients for a larger set of geometric shapes and bodies of revolution. Large speed ratios are assumed (zero kinetic temperature) allowing elimination of error function and exponential terms. As a result, the flow approaches that of an elastic or inelastic Newtonian flow for specular or diffuse reflection, respectively.

General Computer Model

The vehicle is considered a composite structure of components with known aerodynamic properties. The components include: flat plate, sphere, cylinder, and segment of a sphere. For each component, the front and back side surface temperatures, the effective areas, the accommodation coefficients, and the proportions of each type of reflection are assumed known. The orientation of each component relative to slip stream is calculated and the angle of attack is determined. Tables supplying shadow effects in terms of reduction of effective area of each component, based on its orientation relative to the slip stream, are supplied externally.

The total lift and drag forces are then calculated as a vector sum of forces on each component. The fact that this model is designed for inertially stabilized spacecraft simplifies the calculations. Forces are translated and torque considerations are not needed except when the model is utilized in conjunction with GEOS class vehicles. In the case of gravity gradient stabilized GEOS, the restoring gravity torque is needed for the determination of the offset angle created by drag. The total aerodynamic force is then expressed in the proper inertial frame and added to the other perturbative forces in the equations of motion of the spacecraft for numerical integration by DPTRAJ (Reference 7). More complete details of the model and analysis are planned.

References

1. Thomas, G., and Ching, B., *A Study of Atmospheric Heating Applied to the Phenomenon of Geomagnetic Heating*, Aerospace Report TR 0158, 1968.

2. Jacchia, L. G., *Static Diffusion Model of the Upper Atmosphere with Empirical Temperature Profiles*, SAO Special Report 170. Smithsonian Astrophysical Observatory, Cambridge, Mass., 1964.

3. Johnson, W. J., *A Study of the Upper Atmospheric Models*, NASA TM X-53782. National Aeronautics and Space Administration, Washington, 1968.

4. Harris, I., and Priester, W., "The Upper Atmosphere in the Range from 80 to 800 km," *Proposal for CIRA* (Cospar International Reference Atmosphere), 1964.

5. Thomas, G. E., *Analytic Solutions of the Heat Conduction Equation in the Thermosphere*, Air Force Report SAMSO-TR-67-118, 1963.

6. Friedman, M. P., *A Three-Dimensional Model of the Upper Atmosphere*, SAO Special Report 250. Smithsonian Astrophysical Observatory, Cambridge, Mass., 1967.

7. Khatib, A. R., "Double-Precision Trajectory Program: DPTRAJ," in *The Deep Space Network*, Space Programs Summary 37-49, Vol. II, pp. 52–55. Jet Propulsion Laboratory, Pasadena, Calif., Jan. 31, 1968.

8. Khatib, A. R., and Brenkle, J. P., *Consideration of Upper Atmospheric and Aerodynamic Force Models for DPTRAJ*, Technical Memorandum 392-25, 1970 (JPL internal document).

9. Heineman, M., "Theory of Drag in Highly Rarified Gases," *Communication on Pure and Applied Math*, Vol. 1, No. 3, pp. 259–273, 1948.

10. Stalder, J., et al., *Theoretical Aerodynamic Characteristics of Bodies in a Free-Molecular-Flow Field*, NACA TN 2423. National Advisory Committee for Aeronautics, Washington, 1951.

11. Blick, E. F., *Forces on Bodies of Revolution in Free Molecular Flow by the Newtonian-Diffuse Method*, McDonnell Aircraft Corporation Report 6670, 1969.

A Viking Satellite Orbit Trim Strategy

G. R. Hintz

Mission Analysis Division

The Viking Project places a number of interesting and stringent requirements on the control of the satellite orbit to obtain reconnaissance and to prepare for lander release. To satisfy these requirements, different orbit trim maneuver strategies have been developed for two typical Viking missions. This article describes one of these strategies. In addition, a summary of recent numerical results is included to show that this strategy satisfies the mission requirements which have been identified.

Introduction

The Viking Project[1] will send two spacecraft to Mars during the 1975 launch opportunity. Each of these spacecraft will orbit Mars and deploy a soft-lander to the surface of the planet.

The pre-flight navigation analysis for this project has included the analysis of two typical Viking missions. The initial Mission A (launch date August 17, 1975, arrival date June 23, 1976) is a typical candidate for the first spacecraft, while the initial Mission B (launch date September 1, 1975, arrival date August 7, 1976) is a typical candidate for the second spacecraft.

During the Mars orbit trim (MOT) phase of each flight, a sequence of orbit trim spacecraft propulsive maneuvers is performed to remove the effects of orbit-determination and maneuver-execution errors remaining after earlier maneuvers in the flight. The sequence of trim maneuvers is performed according to a pre-determined strategy designed to achieve the mission objectives. This article describes the orbit trim strategy developed for Mission B. A summary of numerical results is included to show that this strategy satisfies the Mission B requirements defined in Reference 1. Reference 2 describes details concerning the analysis of both Missions A and B.

[1] The Viking Project is managed for NASA by the Langley Research Center. Jet Propulsion Laboratory responsibilities in the project include navigation analysis.

Trim Strategy Objectives

The objectives of the orbit trim maneuver strategy for Mission B are:

(1) To satisfy the requirements for landing. The orbit of the spacecraft must be controlled to pass through a prescribed space-time region from which the lander can maneuver to the desired landing site without violating any design constraints. The orbit is specified for that revolution during which the Viking lander separates from the orbiter. The five control parameters are shown in Figure 1 and include the downrange and crossrange error in the landing site latitude relative to the PER point,[2] the orbital period, the periapsis altitude, and the timing error at the periapsis passage immediately following lander touchdown. The current specified tolerances for these five control parameters are given in Table 1.

(2) To provide site reconnaissance at the ninth periapsis passage following the orbit insertion maneuver. This requirement permits the orbiter to execute three site-certification reconnaissance sequences of 3 days each and allows 2 days for the decision to deorbit the lander just prior to the twentieth periapsis passage after Mars orbit insertion (MOI). For a site-certification reconnaissance sequence, Reference 1 specifies that the orbiter remain within an 8-deg central angle and 2000-km slant range of the site for at least 3 min.

(3) To provide adequate orbit determination and command generation time between maneuvers by allowing at least 1½ revolutions between successive maneuvers.

---

[2] The PER point in the satellite orbit occurs at a fixed value of true anomaly for a given entry angle and is the true anomaly of the spacecraft in the nominal orbit when it is directly above the nominal landing site.

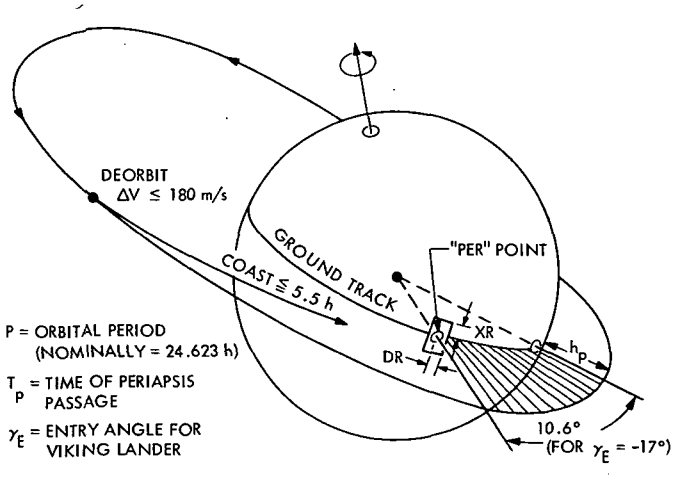

Figure 1. Satellite orbit control for lander deorbit

Table 1. Final control 99% dispersions

Parameter	Reference 1 tolerances	Latest desired tolerances	Final control 99% dispersions
Period, min	±5	±5	-4.9 to +4.6
h_p, km	±300	±150	-148 to +133
Timing, min	±5	±5	-4.9 to +4.9
DR, deg	±1.75	±2	-1.2 to +1.2
XR, deg	±4	±3	-1.6 to +1.6

(4) To satisfy the velocity-magnitude requirement that each trim maneuver be within specified bounds. Each maneuver velocity increment must be larger than 0.25 m/s (determined by a 534-N-s (120 lb-s) minimum impulse constraint) and less than 80 m/s.

(5) To make efficient use of propellant capability. In particular, the velocity increment budget of 175 m/s for all pre-capsule-release orbit trims, together with the variation from the nominal of the MOI maneuver velocity, must not be exceeded.

The orbit trim maneuver strategy is analyzed by means of a Monte Carlo error analysis. If the five objectives above are satisfied for 99% of the Monte Carlo samples, the strategy is acceptable.

MOI Timing Biases

The first facet of the MOT strategy also affects the Mars orbit insertion (MOI) maneuver in the selection of the initial satellite orbit period and timing biases. The initial (nominal) longitude displacement between the landing site and the initial PER point is determined by the selection of a spacecraft arrival time at Mars which permits overlapping two-station coverage by the Deep Space Network (DSN) during MOI command loading and the actual MOI maneuver. This initial longitude displacement is equivalent to an initial timing bias, i.e., the initial longitude offset of the landing site relative to the PER point is equivalent to a certain amount of Mars rotation time east or west of the initial PER point. The initial orbital period bias is determined from this timing bias in the manner discussed below.

A principal feature of the strategy described in this article is the need for time-phasing maneuvers, where an orbital period asynchronous with the rotational period of Mars is used to remove the site longitude offset by the end of a specified number of revolutions. For the initial Mission B, the initial timing bias due to longitude offset of the landing site is −17 h, or about 249 deg west of the initial orbit PER point. The initial period bias is determined

from this timing bias and the number of revolutions to each of the two time-phasing maneuvers MOT_2 and MOT_3.

All of the trim maneuvers are described in the next section. However, at this point in the discussion, it is necessary to know that the second trim maneuver MOT_2 is performed at the fifth periapsis passage P_5, and the third maneuver MOT_3 is performed at the eighth periapsis P_8. (See Figure 2, which indicates the trim maneuver timeline for Mission B.) Given this information, it is possible to select the appropriate initial period bias ΔP_0 relative to the synchronous period (24.623 h). In this selection, the period change introduced by MOT_1 is neglected. If $\Delta P_0 = 17/5 = 3.4$ h, the initial timing bias would be removed in five orbits and the orbiter could synchronize over the landing site via a trim at the fifth periapsis passage P_5, following MOI. If ΔP_0 were selected as $17/8 = 2.1$ h, the initial timing bias would be removed in 8 orbits. In the latter case, a trim at P_5 would only be needed to correct errors and the synchronizing trim could be made at P_8. Any initial period bias between these two extremes would minimize $\Delta V_{MOI} + \Delta V_{MOT_2} + \Delta V_{MOT_3}$ since, in any of these cases, each maneuver reduces the size of the orbit, removing energy from the system. If the initial period were slightly less than 26.7 (24.6 + 2.1) hours, then MOT_2 at P_5 would have to enlarge the orbit, wasting energy. (See Figure 3, which indicates the effect of the initial period bias on the timing offset.) If the initial period were slightly greater than 28.0 (24.6 + 3.4) hours, then MOT_2 would have to move the spacecraft into a subsynchronous (i.e., less than 24.623 h) orbit, causing energy to be wasted. Thus, the ΔV-optimal interval [26.7, 28.0] is determined. A second ΔV-favorable interval [29.8, 32.9] is obtained by waiting until the next Mars revolution. The left- and right-hand endpoints of this second interval are obtained by dividing (17 + 24.6) hours over 8 and 5 orbits, respectively. Succeeding optimizing intervals are indicated in Figure 4. Because of the large anticipated post-MOI period dispersions for Mission B, an initial period in the first interval was rejected. For the analysis given in Reference 2, the second interval was chosen rather than a later interval to reduce the size of the trim maneuvers, and, hence, to reduce the effect of the proportional execution errors. Since the post-MOI period dispersions were expected to be fairly symmetric, the midpoint of this second interval was chosen for the nominal initial period to maximize the probability that the actual spacecraft orbit period would fall inside the optimizing interval. By selecting this biased period, the fan of dispersed paths (cf Figure 2) is pointed downwards for all except about 10% of the low-period dispersed cases to ensure that each maneuver shrinks the size of the orbit.

Several modifications of this strategy for selecting the value of ΔP_0 are possible (cf Figure 4). For example, selecting the initial period so that only 1% of the low-period dispersions are less than 26.7 h would ensure that no energy is wasted for 99% of the samples. However, large post-MOI period dispersions would introduce a large period bias which would require large trim maneuvers. Hence, the effects of execution errors must be considered in such ΔP_0 strategies. Also, note that the intervals in Figure 4 depend on the

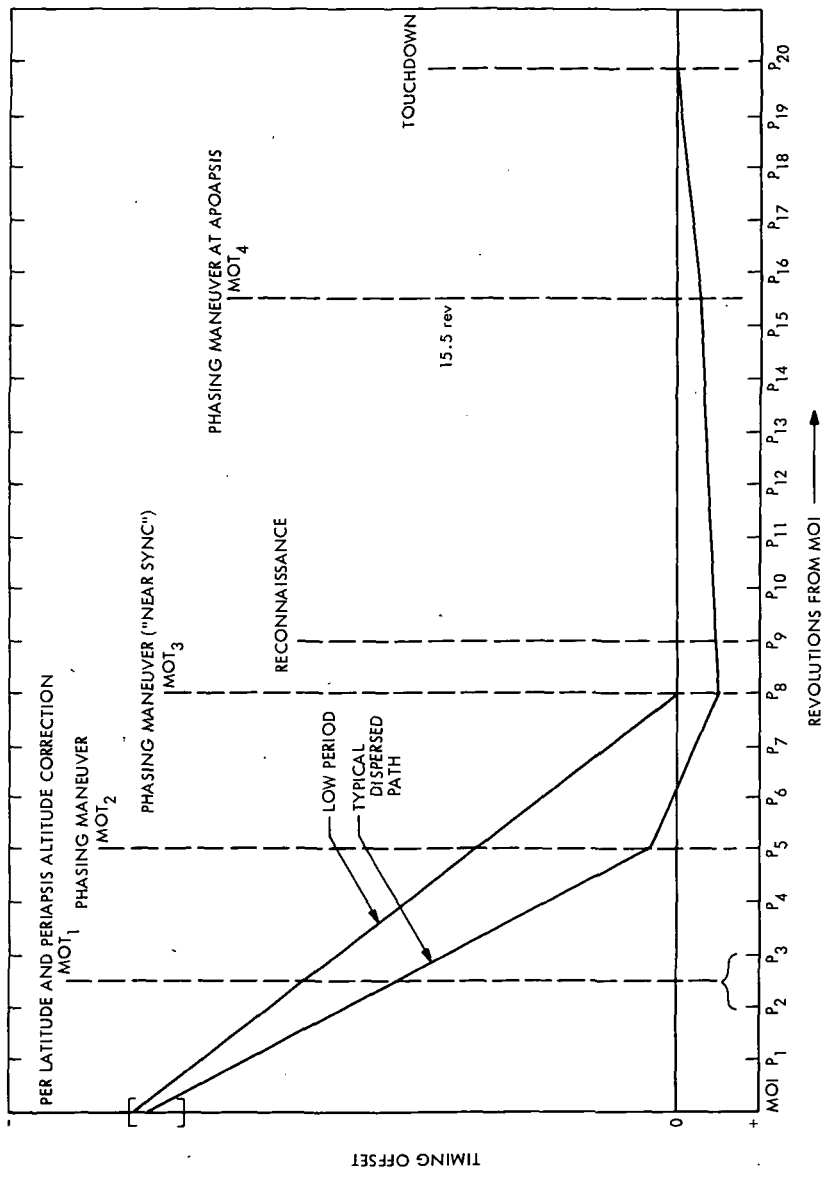

Figure 2. Orbit trim strategy for Mission B

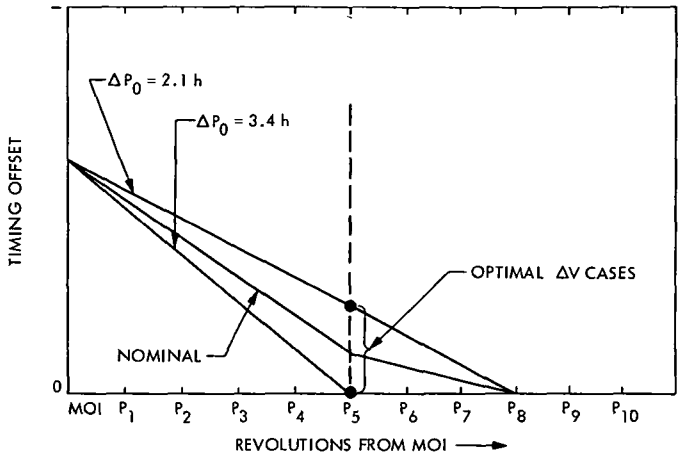

Figure 3. Effect of initial period bias for Mission B

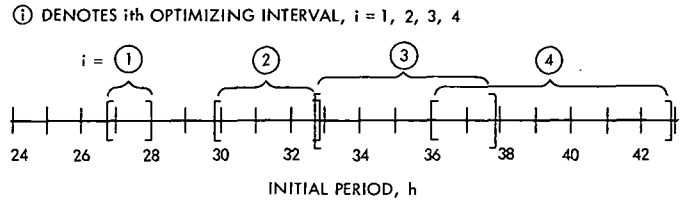

Figure 4. Optimal initial period intervals

initial timing bias. Some of these ΔP_0 strategy modifications are being utilized in current studies.

The MOT Strategy

The first trim maneuver is a three-dimensional maneuver designed to correct the periapsis altitude to the nominal value 1500 km and to place the PER point at the required latitude. The large post-MOI dispersions in periapsis altitude h_p ($\approx \pm 800$ km) dictate that this parameter must be corrected early to provide satisfactory reconnaissance at the ninth periapsis. The h_p correction is combined with an orientation change because it is possible to make this change with very little additional ΔV. Only the latitude of the PER point is corrected in this maneuver since the longitude error can be interpreted as a timing error and corrected very economically in the phasing sequence (MOT_2 and MOT_3) to follow. Thus, the landing site is merely allowed to rotate under the PER point in an orbit having a large period dispersion.

The first maneuver MOT_1 is performed in a ΔV-optimal manner and occurs between the second and third periapsis passage after the orbit

insertion maneuver. The maneuver direction and position in the orbit is determined by a numerical search which minimizes the magnitude of the velocity increment as a function of the eccentric anomaly and the desired change in inclination.

Once the periapsis altitude has been corrected to the desired (nominal) value, except for small errors, it is possible to correct the period and timing errors by changing the height h_a at apoapsis only. These corrections are made in two time-phasing maneuvers performed at periapsis. The maneuver MOT_2 is performed at P_5 to achieve an orbital period such that the site longitude offset is exactly nullified at P_8, where MOT_3 is performed to achieve a near-synchronous orbit. In the absence of errors, these maneuvers would synchronize the PER point to the landing site longitude. However, in order to improve the final timing control of the PER point with respect to the landing site, the third maneuver is actually designed to nullify this final timing error. The maneuver strategy is designed so that this phasing sequence always shrinks the size of the orbit if possible. For those dispersed orbits for which this is not possible at both MOT_2 and MOT_3, MOT_2 is selected to achieve the supersynchronous or subsynchronous post-MOT_2 period which minimizes $\Delta V_{MOT_2} + \Delta V_{MOT_3}$.

The locations of the maneuvers MOT_2 and MOT_3 have been chosen to satisfy Objectives 2 and 3. MOT_3 must be performed before P_9 so the first reconnaissance pass can be made at P_9. Performing the maneuver earlier than P_8 would only allow more time for the timing error to accumulate linearly in time due to period dispersions. Hence, P_8 was chosen for MOT_3. Another consideration in the spacing of these maneuvers is the desirability to maximize the interval between the maneuvers MOT_2 and MOT_3. This maximization reduces the size of MOT_3 to minimize the effect of the proportional execution errors. It also minimizes the amount of velocity that is wasted when it is not possible to shrink the size of the satellite orbit at both MOT_2 and MOT_3.

It should also be noted that performing the maneuvers at periapsis minimizes the velocity increment needed for period changes. It also permits making the maneuvers along the orbiter's velocity vector, which nullifies the first-order effects of maneuver pointing errors. (A description of maneuver execution errors is given in Reference 3.)

The fourth and final pre-capsule release trim maneuver is performed at the sixteenth apoapsis after MOI to achieve accurate timing control of the deorbit orbit. This maneuver removes the timing error which accumulates during the 7½ orbits after MOT_3. Performing MOT_4 at apoapsis reduces the effect of execution errors to about ⅛ that of a maneuver at periapsis. Hence, having neutralized the effects of execution errors, the timing error at touchdown is approximately 4½ times the uncertainty in estimating the orbital period.

The placement of MOT_4 must be properly balanced between P_8 and P_{20}. Location too soon after P_8 permits too much time for timing error growth (which accumulates linearly in time) by P_{20}, violating the 5-min periapsis passage time control requirement of Objective 1. Location too near P_{20} would not allow enough time before P_{20} to correct the accumulated timing error without violating the tight h_p tolerances shown in Table 1. This concern for h_p is introduced by the fact that the maneuver at apoapsis adjusts h_p to change the period in removing the timing error. Selection of the sixteenth apoapsis was determined to achieve the best tradeoff between the two extremes.

Summary of Numerical Results and Conclusions

The orbit trim computer program provides a Monte Carlo error analysis for the selected trim strategy. This program has the capability to target to an input downrange, crossrange (DR × XR) tolerance zone. If the DR × XR error for a particular dispersed orbit is acceptable or can be made acceptable by a longitude change only, the latitude change in MOT_1 is omitted. Such tolerance zones are considered below.

The input parameter values for the orbit trim program were chosen to be compatible with Reference 1 and current hardware capabilities. The performance of the selected strategy relative to each of the five strategy objectives is evaluated next.

When the orbit trim program was targeted for a 1- × 2-deg DR × XR tolerance zone, the 99% dispersions for the five control parameters of the first objective were determined. The values are stated in Table 1, which shows that the control requirements are met.

The requirement for site reconnaissance at the ninth periapsis is satisfied because the timing error at this periapsis is within ±10 min. An error of ±30 min would be acceptable.

The 99% high ΔV values for each of the four trim maneuvers for the 1- × 2-deg target case are given in Table 2, showing that the requirements on the magnitudes of the velocity increments are met.

The total of the velocity increments required for corrective navigation is shown in Figure 5 as a function of the size of the targeted DR × XR tolerance zone. This figure shows that the corrective navigation ΔV budget of 175 m/s is adequate.

The following conclusions may be drawn from the data presented here and are supported by the detailed results of the simulation.

(1) The initial Mission B can be flown satisfying the requirements of Reference 1 and current hardware capabilities. However, if it

Table 2. 99% MOT velocity increment requirements[a]

Trim No.	ΔV, m/s
1	37
2	54
3	45
4	7

[a] These requirements are for Mission B with a 1- × 2-deg target DR × XR tolerance zone.

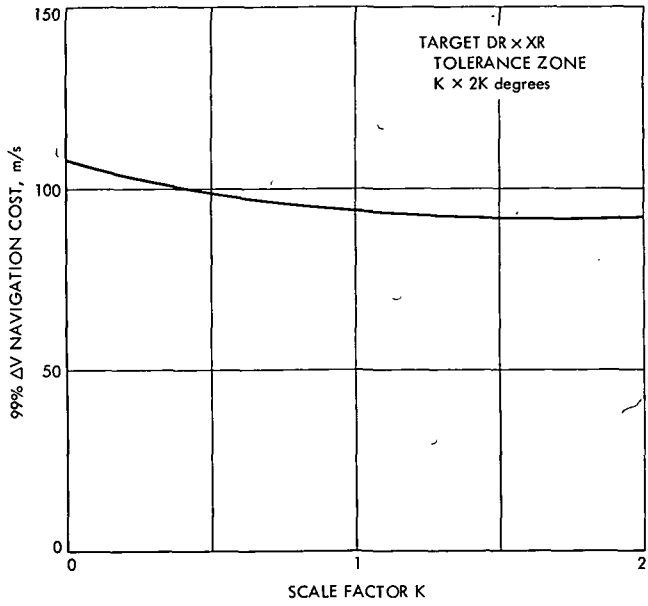

Figure 5. Navigation cost vs targeted DR × XR tolerance zone size

becomes necessary to tighten any of the final control tolerances, it might be necessary to remove some of the conservatism in the current orbit-determination accuracy estimates. For example, to reduce the final timing error, it would be necessary to reduce the error in estimating the orbital period.

(2) For Mission B, very little ΔV is saved by targeting to a non-zero DR × XR tolerance zone. However, the small ΔV savings realized for Mission B by expanding the DR × XR tolerance zone are not repeated for lower-inclination Viking missions. The small savings for Mission B reflect the large post-MOI h_p dispersions and the relatively small post-MOI orientation errors.

References

1. *Viking '75 Project Mission Requirements on System Design*, Appendix A, RS-3703001. Martin-Marietta Corp., Denver, Colo., Mar. 26, 1971.

2. *Viking '75 Project Flight Operations Plan: Vol. VIC. Navigation Plan*, PL-3713003. Edited by C. E. Kohlhase, Jr. Jet Propulsion Laboratory, Pasadena, Calif., July 9, 1971.

3. Gates, C. R., *A Simplified Model of Midcourse Maneuver Execution Errors*, Technical Report 32-504. Jet Propulsion Laboratory, Pasadena, Calif., Oct. 15, 1963.

Bibliography of Current Reporting

Author Index With Abstracts

ABHYANKAR, K. D.

A01 Tables of Auxiliary Functions for the Nonconservative Rayleigh Phase Matrix in Semi-infinite Atmospheres

K. D. Abhyankar and A. L. Fymat

Supplement 195, *Astrophys. J., Suppl. Ser.*, Vol. 23, pp. 35–101, May 1971

Tables of $H^{(1)}(\mu)$, $H^{(2)}(\mu)$, $H_V{}^{(0)}(\mu)$, $H_V{}^{(1)}(\mu)$, and $N(\mu)$ functions appropriate for semi-infinite atmospheres scattering according to the nonconservative Rayleigh phase matrix are given for thirty values of the albedo for single scattering Ω = 0 (0.1) 0.6 (0.05) 0.8 (0.025) 0.9 (0.01) 0.98 (0.005) 0.995 (0.001) 0.999, at intervals of μ = 0 (0.01) 1.0 to six significant figures. They can be used for computing the emergent diffuse radiation field corresponding to an incident illumination in an arbitrary state of polarization.

ANSPAUGH, B. E.

A02 Solar Cell Performance as a Function of Temperature and Illumination Angle of Incidence

B. E. Anspaugh

Technical Memorandum 33-495, September 15, 1971

The response of solar cells to non-normal illumination has been measured. The accurate measurement of this response in the usual solar cell laboratory is quite often complicated by light source difficulties. A solar simulator usually produces a divergent light beam so that rotating a solar cell or a panel of solar cells places a portion of the sample into a more intense beam and another portion into a less intense beam. If the Sun is used as a source, one must take care to block sky radiation from the cells and to continually follow the Sun as it moves across the sky.

A heliostat in the JPL Celestarium was available for performing pre-flight calibrations on the experimental solar panels to be flown on Applications Technology Satellite E (ATS E). The heliostat produced an accurately parallel vertical beam inside a dark room with non-reflecting walls and ceiling. This source proved to be ideal for the required calibration runs, eliminating both light source deficiencies enumerated above. The results of this testing and a comparison with a simple theory are presented in this memorandum.

BACK, L. H.

B01 Laminar Boundary Layers With Large Wall Heating and Flow Acceleration

L. H. Back

AIAA J., Vol. 9, No. 5, pp. 966–969, May 1971

This paper evaluates the effect of large wall heating and flow acceleration on the structure of laminar boundary layers over a range of flow speeds. The heat-transfer parameter was found to increase significantly with the amount of wall heating in flow acceleration regions. This trend suggests taking advantage of heating in flow acceleration regions provided that frictional effects are not important and that the laminar boundary layer is not on the verge of transition to a turbulent boundary layer before the flow is accelerated. Because of flow acceleration, the velocity profiles with wall heating do not have an inflection point in the region near the wall where the velocity increases and therefore would appear to be more stable to small disturbances. This view is supported by other observations on laminarization of turbulent flows through circular tubes, where flow acceleration occurred because of energy transfer from the heated wall.

BAILEY, R. L.

B02 An All-Carbon Radiating Nozzle for Long-Burning Solid Propellant Motors

R. L. Bailey and J. I. Shafer

JPL Quarterly Technical Review, Vol. 1, No. 2, pp. 36–46, July 1971

Three 27-kg solid propellant motors have been static-fired in three tests to demonstrate the feasibility of using nozzles based on all-carbon composite materials for long-burning, high-performance solid rocket propulsion systems suitable for planetary orbit-insertion applications. The successful completion of these firings repre-

sents a significant advancement in long-burning solid propellant motor technology in that: (1) the motor burning times are comparable to those required for space missions; (2) the nozzle weights are about 0.4–0.6 that estimated for equivalent flight-weight ablative nozzles; and (3) unlike the ablative nozzles, the all-carbon radiating nozzles can be reused without, or with only very limited, refurbishment. Additionally, thermal analysis indicates that the nozzle design is acceptable when applied to a scaled-up 355-kg motor with a total burning time of 150 s (the desired time). The all-carbon radiating nozzle design, fabrication, testing, and analysis activities are described in this article.

BARKER, E. S.

B03 High Dispersion Spectroscopic Observations of Venus: VIII. The Carbon Dioxide Band at 10,627 Å

R. A. J. Schorn, L. D. G. Young, and
E. S. Barker (University of Texas)

Icarus: Int. J. Sol. Sys., Vol. 14, No. 1, pp. 21–35, February 1971

For abstract, see Schorn, R. A. J.

BEJCZY, A. K.

B04 Non-orthogonal Redundant Configurations of Single-Axis Strapped-Down Gyros

A. K. Bejczy

JPL Quarterly Technical Review, Vol. 1, No. 2, pp. 107–118, July 1971

The functional reliability of the inertial reference unit of a three-axis stabilized spacecraft for long lifetime missions is of specific concern. Realizing the highly efficient redundancy potential inherent to non-orthogonal emplacements of more than three single-axis strapped-down gyros, and considering practical implementation and performance criteria, 45-deg skew-symmetric six- and four-gyro configurations based on the geometry of a regular octahedron are presented in this article. These configurations result in optimum performance, exhibit unique simplicity in gyro output processing requirements, allow high-density packaging, and require reasonable fabrication and test procedures. The redundancy potential of an octahedron six-array gyro configuration is twice as high as that of six gyros in an orthogonal emplacement. An octahedron-based skew emplacement of four gyros can provide minimum

redundancy for the inertial reference unit, which, for an orthogonal emplacement, could only be obtained by six gyros.

BERGMAN, C. W.

B05 DSN Progress Report for May–June 1971: Doppler Tracking System Mathematical Model

C. W. Bergman

Technical Report 32-1526, Vol. IV, pp. 181–187, August 15, 1971

The mathematical model that can be used to calculate the expected Deep Space Instrumentation Facility doppler tracking system phase noise σ_M is given by

$$\sigma_M = \sqrt{\sigma_R^2 + \sigma_A^2}$$

The rms phase noise σ_R is due to the receiver input noise and is a function of the received signal strength. The strong signal phase noise σ_A is characteristic of station configuration and for practical purposes is independent of signal strength. The value of σ_A is determined experimentally. The test results confirm the validity of the model.

BLANKENHORN, D. H.

B06 Prediction of Lipid Uptake by Prosthetic Heart Valve Poppets From Solubility Parameters

J. Moacanin, D. D. Lawson, H. P. Chin (University of Southern California), E. C. Harrison (University of Southern California), and D. H. Blankenhorn (University of Southern California)

JPL Quarterly Technical Review, Vol. 1, No. 2, pp. 54–60, July 1971

For abstract, see Moacanin, J.

BÖER, K. W.

B07 CdS–Metal Workfunctions at Higher Current-Densities

R. J. Stirn, K. W. Böer (University of Delaware), G. A. Dussel (University of Delaware), and P. Voss (University of Delaware)

Proceedings of the Third International Conference on Photoconductivity, Stanford University, Palo Alto, California, August 12–15, 1969, pp. 389–394

For abstract, see Stirn, R. J.

BREWER, W. A.

B08 Dry-Heat Resistance of Bacterial Spores Recovered From Mariner-Mars 1969 Spacecraft

M. D. Wardle, W. A. Brewer, and M. L. Peterson

Appl. Microbiol., Vol. 21, No. 5, pp. 827–831, May 1971

For abstract, see Wardle, M. D.

BROUCKE, R. A.

B09 Construction of Rational and Negative Powers of a Formal Series

R. A. Broucke (University of California, Los Angeles)

Commun. ACM (Association for Computing Machinery, Inc.), Vol. 14, No. 1, pp. 32–35, January 1971

Some methods are described for the generation of fractional and negative powers of any formal series, such as Poisson series or Chebyshev series. It is shown that, with the use of the three elementary operations of addition, subtraction, and multiplication, all rational (positive and negative) powers of a series can be constructed. There are basically two approaches: the binomial theorem and the iteration methods. Both methods are described, and the relationship between them is pointed out. Some well-known classical formulas are obtained as particular cases, and it is shown how the convergence properties of these formulas can be improved with very little additional computations. Finally, some numerical experiments are described with Chebyshev series and with Fourier series.

BRUNDER, G. J.

B10 DSN Progress Report for May–June 1971: GCF SFOF Communications Terminal Subsystem High-Speed Data Assembly

G. J. Brunder

Technical Report 32-1526, Vol. IV, pp. 144–150, August 15, 1971

New capabilities and equipment have been incorporated into the Ground Communications Facility (GCF) Space Flight Operations Facility (SFOF) Communications Terminal Subsystem high-speed data assembly as a result of the 1970–1971 upgrade in support of the Deep Space Network. The distinct capabilities of the high-speed data assembly are discussed and the new 4800-bps high-speed data circuits and equipment are described on a functional level.

BRUNSTEIN, S. A.

B11 Characteristics of a Cigar Antenna

S. A. Brunstein and R. F. Thomas

JPL Quarterly Technical Review, Vol. 1, No. 2, pp. 87–95, July 1971

Dual-frequency propagation experiments will be performed using the Deep Space Network 64-m antennas and the Mariner Venus–Mercury 1973 and Viking orbiter 1975 spacecraft. For such experiments, the 64-m antennas must be capable of receiving and transmitting at S-band and simultaneously receiving at X-band. One possible configuration involves placing an X-band feed inside the S-band feed horn.

A cigar (metallic-disc-on-rod) antenna was investigated for this application because this type of antenna is physically thin and would have minimal effect on the radiation from the S-band feed horn. A cigar antenna design obtained using new phase velocity data is described in this article. The new phase velocity measurements were required when it was found that the available published data for disc-on-rod structures were in error. The new measurements and the experimental results obtained with the resulting design are also described.

BUECHLER, G.

B12 Lunar Surface Mass Distribution From Dynamical Point-Mass Solution

W. L. Sjogren, P. M. Muller, P. Gottlieb, L. Wong (Aerospace Corporation), G. Buechler (Aerospace Corporation), W. Downs (Aerospace Corporation), and R. Prislin (Aerospace Corporation)

The Moon: Int. J. Lunar Studies, Vol. 2, No. 3, pp. 338–353, February 1971

For abstract, see Sjogren, W. L.

BURKE, E. S.

B13 DSN Progress Report for May–June 1971: DSN Telemetry System

E. S. Burke and C. W. Harris

Technical Report 32-1526, Vol. IV, pp. 4–10, August 15, 1971

The Telemetry System Analysis Group is responsible for analyzing the total performance of the DSN Telemetry System. The group's tasks include both real-time and non-real-time functions. By combining these two functions, the Telemetry System can be analyzed for short- and long-term performance. This can be illustrated by the results of the data that was accumulated during real-time operations for the solar occultation of Pioneer 9, and compiled and analyzed during non-real-time periods.

BURKE, J. D.

B14 Remote Examination of Rock Specimens

J. D. Burke, R. Choate, and R. B. Coryell

JPL Quarterly Technical Review, Vol. 1, No. 2, pp. 131–143, July 1971

In JPL studies of prospects for post-Apollo lunar exploration, methods are being considered for extending the Apollo observations into a more complete understanding of the moon's bulk composition, mode of accretion, and thermal history. Based on Apollo samples to date, it appears that relatively simple remotely controlled methods may be adequate for characterizing lunar materials found along extended surface traverses. To investigate this possibility, studies and experiments have been made to determine (1) what performance can be expected from a minimum rover-borne system with imaging and sample manipulation, and (2) the advantages conferred by desirable additions, such as close-up color imaging, various types of microscopy, and chemical or mineral analysis using X-rays. Laboratory and field experiments reported in this article support the feasibility of this prospect and identify some characteristics of an automated system required to realize this technique.

CAMERON, R. E.

C01 Antarctic Soil Microbial and Ecological Investigations

R. E. Cameron

Research in the Antarctic, pp. 137–189, American Association for the Advancement of Science, Washington, D.C., 1971

During the austral summers of 1966 to 1970, soil microbial and ecological investigations were undertaken in the Antarctic, primarily in the dry valleys of southern Victoria Land, but also on the Antarctic Peninsula and in the Transantarctic Mountains. The primary objective for these investigations was to determine the relationships of edaphic, climatic, microclimatic, topographic, and geographic factors with the habitat, numbers, distribution, kinds, and activities of microorganisms in the cold deserts of Antarctica. In addition to the main objective, subordinate goals were to obtain information on the ecology of cold, polar, temperate, and hot desert areas before searching for possible life on Mars. Although Antarctica does not possess a Martian environment, it can serve as a useful model of ecology for design, testing, and extrapolation. The naturally harsh environmental conditions of the Antarctic provide a valuable testing ground for space exploration and manned bases.

CANNON, W. A.

C02 Adsorption on the Martian Regolith

F. P. Fanale and W. A. Cannon

Nature, Vol. 230, No. 5295, pp. 502–504, April 23, 1971

For abstract, see Fanale, F. P.

CAPEN, C. F.

C03 Martian North Polar Cap, 1962–68

C. F. Capen and V. W. Capen

Icarus: Int. J. Sol. Sys., Vol. 13, No. 1, pp. 100–108, July 1970

A 6-yr observational study of the physical aspects of the Martian arctic region is reported. North Cap regression curves obtained during three Martian spring-summer seasons exhibit seasonal behavior and have similar physical signatures. The cap appears to temporarily halt its retreat when an arctic haze forms over the region during maximum rate of regression just prior to summer

solstice. The arctic climate appeared cooler during the 1966–1967 apparition than during the previous two similar Martian seasons. The peripheral aspects of the North Cap have not basically altered over the past 90 yr.

CAPEN, V. W.

C04 Martian North Polar Cap, 1962–68

C. F. Capen and V. W. Capen

Icarus: Int. J. Sol. Sys., Vol. 13, No. 1, pp. 100–108, July 1970.

For abstract, see Capen, C. F.

CAPODICI, S.

C05 A Design for Thick Film Microcircuit dc-to-dc Converter Electronics

H. M. Wick, Jr., and S. Capodici (General Electric Company)

IEEE Trans. Aerosp. Electron. Sys., Vol. AES-7, No. 3, pp. 528–531, May 1971

For abstract, see Wick, H. M., Jr.

CASSELL, P. L.

C06 Evaluation of Converters Fueled With Uranium Nitride

K. Shimada and P. L. Cassell

Technical Memorandum 33-489, July 30, 1971

For abstract, see Shimada, K.

CAUGHEY, T. K.

C07 Design of Subsystems in Large Structures

T. K. Caughey

Technical Memorandum 33-484, June 30, 1971

A qualitative mathematical analysis is made of various approximate schemes that have been suggested in an attempt to reduce the long and expensive computations which are required in the design of subsystems in large, complex structures. It is shown that the simple scheme of using the known blocked response of the

main structure as the input to the subsystem does not, in general, lead to a convergent iterative process. The theory of the vibration absorber is used to illustrate this point.

A scheme which uses the response of a known system as the input to a new system, which differs only slightly from the known system, is shown to result in a convergent iterative process. It is shown that the first iterate of this process is sufficiently accurate for preliminary design purposes.

CHADWICK, H. D.

C08 The Design of a Low Data Rate MSFK Communication System

H. D. Chadwick and J. C. Springett

IEEE Trans. Commun. Technol., Vol. COM-18, No. 6, pp. 740–750, December 1970

Low data rate communications are of considerable interest for applications in which the received signal-to-noise ratio is very low. At data rates below the neighborhood of 5 bits/s, coherent communication techniques become inefficient, and noncoherent techniques such as m-ary frequency shift keying (MFSK) become attractive. In this paper, the design of an MFSK low data rate communication system is discussed. The problems of synchronization in time and frequency are analyzed, and experimental results of successful laboratory tests of the system are presented.

CHAFIN, R. L.

C09 DSN Progress Report for May–June 1971: DSIF Mariner Mars 1971 TCP Operational Program

R. L. Chafin

Technical Report 32-1526, Vol. IV, pp. 205–212, August 15, 1971

The Deep Space Instrumentation Facility (DSIF) Mariner Mars 1971 Telemetry and Command Processing (TCP) Operational Program provides the software necessary to support the Mariner Mars 1971 mission operations by processing all telemetry data from the spacecraft and providing a means to command the spacecraft from both the Space Flight Operations Facility and the station. The program is designed for use with the multiple-mission telemetry and multiple-mission command hardware. This article describes the organization, operation, and capabilities of this program.

CHIN, H. P.

C10 Prediction of Lipid Uptake by Prosthetic Heart Valve Poppets From Solubility Parameters

J. Moacanin, D. D. Lawson, H. P. Chin (University of Southern California), E. C. Harrison (University of Southern California), and D. H. Blankenhorn (University of Southern California)

JPL Quarterly Technical Review, Vol. 1, No. 2, pp. 54–60, July 1971

For abstract, see Moacanin, J.

CHISHOLM, J. R.

C11 Use of Derived Forcing Functions at Centaur Main Engine Cutoff in Predicting Transient Loads on Mariner Mars '71 and Viking Spacecraft

M. R. Trubert, J. R. Chisholm, and W. H. Gayman

Technical Memorandum 33-486, June 28, 1971

For abstract, see Trubert, M. R.

C12 Use of Centaur Spacecraft Flight Data in the Synthesis of Forcing Functions at Centaur Main Engine Cutoff During Boost of Mariner Mars 1969, OAO-II, and ATS Spacecraft: Analysis and Evaluation

M. R. Trubert, J. R. Chisholm, and W. H. Gayman

Technical Memorandum 33-487, Vol. I, June 21, 1971

For abstract, see Trubert, M. R.

C13 Use of Centaur Spacecraft Flight Data in the Synthesis of Forcing Functions at Centaur Main Engine Cutoff During Boost of Mariner Mars 1969, OAO-II, and ATS Spacecraft: Computer Plots

M. R. Trubert, J. R. Chisholm, and W. H. Gayman

Technical Memorandum 33-487, Vol. II, June 21, 1971

For abstract, see Trubert, M. R.

CHOATE, R.

C14 Remote Examination of Rock Specimens

J. D. Burke, R. Choate, and R. B. Coryell

JPL Quarterly Technical Review, Vol. 1, No. 2, pp. 131–143, July 1971

For abstract, see Burke, J. D.

COFFIN, R. C.

C15 DSN Progress Report for May–June 1971: Computer-Controllable Phase Shifter

R. C. Coffin

Technical Report 32-1526, Vol. IV, pp. 167–169, August 15, 1971

A voltage-variable phase shifter having a linear voltage-to-phase characteristic has been built and tested. The design uses a phase detector in a feedback loop configuration to linearize an RC phase shifter. The phase-shift characteristic is 72 deg/V operable over the range of 0 to 5 V. Linearity is within ±1.5%. The design technique can be applied over frequencies extending from the audio range up to greater than 100 MHz.

COOK, A. F.

C16 Saturn's Rings—A Survey

A. F. Cook (Smithsonian Astrophysical Observatory), F. A. Franklin (Smithsonian Astrophysical Observatory), and F. D. Palluconi

Technical Memorandum 33-488, July 15, 1971

This article surveys Saturn's system of rings with emphasis on the establishment of physically reasonable ring models. The dimensions of the planet and principal ring features are determined from published measurements. Photometry of the A and B rings is reviewed, revising some published results, and commenting on derived parameters in light of recent photometry of snow, ice, and other materials. Models for Rings A, B, and C are presented with supporting discussion; consideration is given to the existence of particles closer to the planet than Ring C and further away than Ring A.

COOPER, M. A.

C17 The Fluorine-19 Nuclear Magnetic Resonance Spectra of Some Fluoroaromatic Compounds. Studies Using Noise Decoupling of Protons

M. A. Cooper, H. E. Weber, and S. L. Manatt

J. Am. Chem. Soc., Vol. 93, No. 10, pp. 2369–2380, May 19, 1971

The ^{19}F nuclear magnetic resonance spectra of a number of fluorobenzenes and other fluoroaromatic molecules have been examined at 94.1 MHz under conditions of complete proton decoupling by noise modulation, which allowed ^{19}F chemical shifts and F . . . F coupling constants to be extracted conveniently without recourse to complete analyses. Details of the digital frequency sweep and the double-tuned probe provisions for a Varian HA-100 spectrometer are given. Where a proton-decoupled spectrum is a single line, the values of $^{1}J_{^{13}C-F}$ and the $^{13}C-^{12}C$ isotope shifts may not always be extracted uniquely from the ^{13}C satellites, although the F . . . F coupling constants can be measured directly. Data on the solvent dependence of F . . . F couplings and ^{19}F chemical shifts in some polar fluorobenzenes are reported. The behavior of $^{3}J_{FF}$ in these systems shows no correlation with solvent dielectric constant, which is interpreted to mean that "reaction field" mechanisms are not important here. However, the smaller variations in $^{4}J_{FF}$ and $^{5}J_{FF}$ are reasonably correlated with the dielectric constant of the solvent, which suggests that the "reaction field" mechanism is more significant here. No simple dependence of the ^{19}F chemical shifts on solvent dielectric constant was found in contrast to some previous results; possible explanations for this are discussed. Accurate values for the long-range F . . . F couplings for a number of difluoronaphthalenes, -biphenyls, and -phenanthrenes are presented for the first time.

CORYELL, R. B.

C18 Remote Examination of Rock Specimens

J. D. Burke, R. Choate, and R. B. Coryell

JPL Quarterly Technical Review, Vol. 1, No. 2, pp. 131–143, July 1971

For abstract, see Burke, J. D.

COSTOGUE, E. N.

C19 Operation of a Lightweight Power Conditioner With a Hollow-Cathode Ion Thruster

E. V. Pawlik, E. N. Costogue, and W. C. Schaefer

J. Spacecraft Rockets, Vol. 8, No. 3, pp. 245–250, March 1971

For abstract, see Pawlik, E. V.

CUDDIHY, E. F.

C20 Solvent-Stress-Cracking and Fatigue Properties of Liquid-Propellant Expulsion Teflon Bladders

E. F. Cuddihy

Technical Report 32-1535, August 1, 1971

Standard laminate Teflon bladders employed as liquid-propellant expulsion devices for the Mariner Mars 1971 spacecraft failed due to formation of tears and cracks near an aluminum seal ring which forms the mouth of the bladder. These failures occurred during flight-acceptance tests in which various solvents were used as referee fuels. From a consideration of the conditions imposed on the bladders during the tests, it was recognized that the neck regions of the bladders were biaxially stressed while at the same time being bathed by the test solvent. A study of the effects of solvent on the biaxial properties of standard laminate materials demonstrated that standard laminate is sensitive to solvent and fails from solvent-stress-cracking at strains less than 6% when biaxially stressed. This characteristic was the prime cause of failure of standard laminate bladders when exposed to solvent during flight-acceptance tests. A new material, designated "codispersion laminate," was found to be insensitive to solvent-stress-cracking and has replaced the standard laminate material used in construction of JPL Teflon bladders.

The solvent sensitivity of standard laminate was also observed in analysis of uniaxial stress-strain data. A correlation could be established between the results from the more detailed and complex biaxial-solvent studies and the simple, more rapid uniaxial technique. This method can be effectively employed as a method for detecting solvent sensitivity in future candidate Teflon materials.

The uniaxial method was applied to a study of the effects of solvents on FEP 120, FEP 9511, and TFE 30, the Teflon components which are used in the construction of the laminate materials. This study revealed that only FEP 120 is significantly solvent-sensitive. This material, not used in codispersion laminate, is a major component of standard laminate and must therefore be labeled as the dominant contributor to the solvent sensitivity of standard laminate. This was further substantiated by the experimental observation that surface crazing which precedes the failure of the standard laminate in solvent occurs in FEP 120.

Finally, a correlation between fatigue and stress-strain behavior of Teflon materials was observed which, together with knowledge of the ultimate breaking stress of the materials, can be used to obtain an estimate of the fatigue properties and permits a rapid assessment of the expected fatigue behavior of candidate materials for

bladders from only a comparison of their ultimate breaking stress. The general principles of this method of fatigue analysis are discussed, emphasis being given to the implication that this technique should have general application for other polymeric materials where stress-strain behavior is comparable to Teflon.

C21 The Effect of an Oxidative–Caustic Environment on Graft Copolymer Membranes

E. F. Cuddihy, J. Moacanin, D. E. Walmsley, and H. Y. Tom

Colloidal and Morphological Behavior of Block and Graft Copolymers, pp. 113–129, Plenum Press, New York, 1971

Separator membranes are required in Ag–Zn batteries to prevent silver ions, dissolved from the silver electrode, from reaching and poisoning the zinc electrode. In addition, the separator membranes are used to prevent physical contact between the electrodes, and must also have the property of allowing ready transport of the charge carrier ions. This paper discusses the results of a study on the long-term effect of the environment in an Ag–Zn battery on a separator material prepared from thin films of crosslinked polyethylene grafted with poly(potassium acrylate), the acrylate content being usually approximately 40 wt %. This type of separator membrane is considered for spacecraft applications because of its relative stability and the ability to withstand heat sterilization at 135°C.

DeMORE, W. B.

D01 Rates and Mechanism of Alkyne Ozonation

W. B. DeMore

Int. J. Chem. Kinet., Vol. III, No. 2, pp. 161–173, March 1971

The rates and products of the reactions of ozone with acetylene, methylacetylene, dimethylacetylene, and ethylacetylene have been studied in a long-path infrared cell at 21 ± 1°C. The gas phase reaction gives products formed by cleavage of the carbon–carbon triple bond. A mechanism is proposed that involves formation of a short-lived acid anhydride intermediate, which is energized by virtue of the reaction exothermicity and undergoes unimolecular decomposition. Formation of an α-dicarbonyl was observed in every case, but there is evidence that a side reaction on the walls accounted for that product. The general relationship between alkyne and alkene ozonation is discussed. The rate measurements showed that, unlike the alkenes, the rate of alkyne ozonation is not

greatly affected by substitution with simple alkyl groups. The rate constant for C_2H_2 agrees with earlier work and thus provides additional support for the previously derived high A-factor for acetylene ozonation relative to alkenes.

DOWNS, G. S.

D02 Use of Pulsar Signals As Clocks

P. E. Reichley, G. S. Downs, and G. Morris

JPL Quarterly Technical Review, Vol. 1, No. 2, pp. 80–86, July 1971

For abstract, see Reichley, P. E.

DOWNS, W.

D03 Lunar Surface Mass Distribution From Dynamical Point-Mass Solution

W. L. Sjogren, P. M. Muller, P. Gottlieb, L. Wong (Aerospace Corporation), G. Buechler (Aerospace Corporation), W. Downs (Aerospace Corporation), and R. Prislin (Aerospace Corporation)

The Moon: Int. J. Lunar Studies, Vol. 2, No. 3, pp. 338–353, February 1971

For abstract, see Sjogren, W. L.

DUSSEL, G. A.

D04 CdS–Metal Workfunctions at Higher Current-Densities

R. J. Stirn, K. W. Böer (University of Delaware), G. A. Dussel (University of Delaware), and P. Voss (University of Delaware)

Proceedings of the Third International Conference on Photoconductivity, Stanford University, Palo Alto, California, August 12–15, 1969, pp. 389–394

For abstract, see Stirn, R. J.

EISENBERGER, I.

E01 Estimating the Parameters of the Chi-Square and Some Related Distributions Using Quantiles

I. Eisenberger

Technical Report 32-1532, July 15, 1971

A two-parameter family of distributions is generated by considering the random variable

$$y_n = \sum_{i=1}^{n} x_i^2,$$

where the x_i are independent and distributed $N(0,\sigma^2)$. For $\sigma^2 = 1$, y_n is said to have the chi-square distribution with n degrees of freedom. This report is concerned with the use of sample quantiles in solving the following estimation problems associated with this distribution:

(1) Estimating σ^2 when n is known.

(2) Estimating n when $\sigma^2 = 1$.

(3) Estimating the product $n\sigma^2$ when neither n nor σ^2 is known.

(4) Estimating both n and σ^2 when neither is known.

(5) Estimating σ for the special cases where $\nu_2 = \sqrt{y_2}$ and $\nu_3 = \sqrt{y_3}$.

Monte Carlo methods are used in applying the various estimators, and the results are listed.

E02 DSN Progress Report for May–June 1971: Detection of Failure Rate Increases

G. Lorden (California Institute of Technology) and
I. Eisenberger

Technical Report 32-1526, Vol. IV, pp. 95–100,
August 15, 1971

For abstract, see Lorden, G.

ESTABROOK, F. B.

E03 Geometric Approach to Invariance Groups and Solution of Partial Differential Systems

B. K. Harrison and F. B. Estabrook

J. Math. Phys. (N.Y.), Vol. 12, No. 4, pp. 653–666,
April 1971

For abstract, see Harrison, B. K.

EVANS, R. H.

E04 DSN Progress Report for May–June 1971: GCF High-Speed Data System Design and Implementation for 1971–1972

R. H. Evans

Technical Report 32-1526, Vol. IV, pp. 133–137, August 15, 1971

The DSN Ground Communications Facility (GCF) high-speed data system capabilities were significantly upgraded to meet the 1971–1972 era requirements. In general, those requirements doubled the data transmission rate to 4800 bps, added block demultiplexing at the remote stations, provided for block synchronous outbound transmission from the Space Flight Operations Facility, and provided positive labeling of error-free blocks. This article discusses the major detail design problems encountered in implementing these requirements.

FANALE, F. P.

F01 Adsorption on the Martian Regolith

F. P. Fanale and W. A. Cannon

Nature, Vol. 230, No. 5295, pp. 502–504, April 23, 1971

The purpose of this study was to measure CO_2 and H_2O adsorption in conditions and on materials likely to be representative of the Martian surface. Based on these data, the significance of adsorption for the history of H_2O and CO_2 on Mars, and for the diurnal phenomena, is considered. Laboratory measurements of the adsorption of CO_2, H_2O, and Kr indicate that pulverized basalt has an extremely high internal surface area. This suggests that the Martian regolith may store an appreciable amount of adsorbed gas, and that the diurnal brightening of Mars may be caused by a fog of ice crystals formed from water molecules desorbed diurnally from the surface.

F02 Potassium–Uranium Systematics of Apollo 11 and Apollo 12 Lunar Samples and of Some Deep Earth Rocks

F. P. Fanale and D. B. Nash

Science, Vol. 172, No. 3988, p. 1167, June 11, 1971

New data on the potassium/uranium ratio in ultramafic rocks presented by Fisher are discussed, and areas of agreement and disagreement with his conclusions are noted. Other new discoveries reported at the Apollo 11 and 12 conferences are interpreted. However, present conclusions concerning the relationship between

the bulk potassium/uranium ratios of terrestrial, lunar, and chondritic material remain unaffected.

FLEISCHER, G. E.

F03 Results of Flexible Spacecraft Attitude Control Studies Utilizing Hybrid Coordinates

P. W. Likins (University of California, Los Angeles) and G. E. Fleischer

J. Spacecraft Rockets, Vol. 8, No. 3, pp. 264–273, March 1971

For abstract, see Likins, P. W.

FOSTER, C. F.

F04 DSN Progress Report for May–June 1971: S-Band Planetary Radar Receiver Development

C. F. Foster

Technical Report 32-1526, Vol. IV, pp. 112–115, August 15, 1971

This article describes the design modification of the DSS 14 (Mars Deep Space Station) bistatic radar receiver. This receiver is basically an open-loop superheterodyne receiver used for development of communication techniques. The modifications include wider bandwidths to support high-speed, high-resolution planetary mapping, and the redistribution of system gain to prevent noise saturation. The redesigned bistatic radar receiver has been installed at DSS 14 and is now being used in the Venus radar mapping experiment.

FRANKLIN, F. A.

F05 Saturn's Rings—A Survey

A. F. Cook (Smithsonian Astrophysical Observatory), F. A. Franklin (Smithsonian Astrophysical Observatory), and F. D. Palluconi

Technical Memorandum 33-488, July 15, 1971

For abstract, see Cook, A. F.

FRAZER, R. E.

F06 **Aluminizing of the 7.01-m Collimating Mirror for the JPL 7.62-m Space Simulator**

E. W. Noller and R. E. Frazer

Technical Memorandum 33-485, July 15, 1971

For abstract, see Noller, E. W.

FREDRICKSEN, H.

F07 **DSN Progress Report for May–June 1971: Generation of the Ford Sequence of Length 2^n, n Large**

H. Fredricksen

Technical Report 32-1526, Vol. IV, pp. 84–85, August 15, 1971

This article presents three algorithms for forming the Ford sequence of length 2^n and compares the storage requirements for each of the three. These sequences are used in checkout of digital communications equipment.

FREY, W.

F08 **DSN Progress Report for May–June 1971: Multiple-Mission Telemetry**

W. Frey, R. Petrie, A. Lai, and R. Greenberg

Technical Report 32-1526, Vol. IV, pp. 160–164, August 15, 1971

This article contains a status update of the Deep Space Instrumentation Facility (DSIF) Multiple-Mission Telemetry (MMT). The equipment covered in this article has been described in detail in earlier DSN Space Programs Summary articles. This article provides information on the changes and new developments to the MMT system. Block diagrams depicting the various DSIF station MMT configurations and telemetry processing equipment added to support the Mariner Mars 1971 flight project are also included.

FYMAT, A. L.

F09 **Tables of Auxiliary Functions for the Nonconservative Rayleigh Phase Matrix in Semi-infinite Atmospheres**

K. D. Abhyankar and A. L. Fymat

Supplement 195, *Astrophys. J., Suppl. Ser.*, Vol. 23, pp. 35–101, May 1971

For abstract, see Abhyankar, K. D.

GAYMAN, W. H.

G01 Use of Derived Forcing Functions at Centaur Main Engine Cutoff in Predicting Transient Loads on Mariner Mars '71 and Viking Spacecraft

M. R. Trubert, J. R. Chisholm, and W. H. Gayman

Technical Memorandum 33-486, June 28, 1971

For abstract, see Trubert, M. R.

G02 Use of Centaur Spacecraft Flight Data in the Synthesis of Forcing Functions at Centaur Main Engine Cutoff During Boost of Mariner Mars 1969, OAO-II, and ATS Spacecraft: Analysis and Evaluation

M. R. Trubert, J. R. Chisholm, and W. H. Gayman

Technical Memorandum 33-487, Vol. I, June 21, 1971

For abstract, see Trubert, M. R.

G03 Use of Centaur Spacecraft Flight Data in the Synthesis of Forcing Functions at Centaur Main Engine Cutoff During Boost of Mariner Mars 1969, OAO-II, and ATS Spacecraft: Computer Plots

M. R. Trubert, J. R. Chisholm, and W. H. Gayman

Technical Memorandum 33-487, Vol. II, June 21, 1971

For abstract, see Trubert, M. R.

GOLDSTEIN, R.

G04 Preliminary Investigations of Ion Thruster Cathodes

R. Goldstein, E. V. Pawlik, and L. C. Wen

Technical Report 32-1536, August 1, 1971

Results of experimental and analytical studies of mercury-vapor-fed hollow cathodes for ion thrusters are presented. These studies have included the thermal and electrical characteristics of the cathodes. It is shown that the primary electron emission mechanism is thermionic when sufficient low work function material is present in the cathode. The cathode temperature is determined by

the current demanded by the external circuit and the work function of the emitting surface. The result is an increase in cathode temperature as the low work function material is depleted. In addition, attempts to reduce cathode temperature by changes in external thermal coupling result only in increasing the power extracted from the discharge. These phenomena affect overall thruster performance.

GOODWIN, P. S.

G05 DSN Progress Report for May–June 1971: Helios Mission Support

P. S. Goodwin

Technical Report 32-1526, Vol. IV, pp. 22–31, August 15, 1971

Project Helios, named after the ancient Greek Goddess of the Sun, is a joint space venture being undertaken by the Federal Republic of West Germany and the United States of America. Two unmanned scientific satellites will be placed into heliocentric orbits: the first during mid-1974, and the second in late 1975. The history of this Project, its mission objectives, and a general description of the spacecraft were given in previous articles. This article presents a description of the spacecraft's radio subsystem and shows the interrelationships between spacecraft design and the planned capabilities of the DSN. Specifically, this article provides a functional description of the Helios Telemetry System.

GORDON, D. L.

G06 Tracking and Data System Support for the Mariner Mars 1969 Mission: Midcourse Maneuver Through End of Nominal Mission

N. A. Renzetti, K. W. Linnes, D. L. Gordon, and T. M. Taylor

Technical Memorandum 33-474, Vol. II, September 1, 1971

For abstract, see Renzetti, N. A.

GOTTLIEB, P.

G07 Lunar Surface Mass Distribution From Dynamical Point-Mass Solution

W. L. Sjogren, P. M. Muller, P. Gottlieb, L. Wong (Aerospace Corporation), G. Buechler (Aerospace

Corporation), W. Downs (Aerospace Corporation), and R. Prislin (Aerospace Corporation)

The Moon: Int. J. Lunar Studies, Vol. 2, No. 3, pp. 338–353, February 1971

For abstract, see Sjogren, W. L.

GRAULING, C. R.

G08 DSN Progress Report for May–June 1971: Data Decoder Assembly

C. R. Grauling

Technical Report 32-1526, Vol. IV, pp. 170–176, August 15, 1971

Future deep space missions (e.g., Pioneer F/G) will be using convolutional coding. The present configuration of the DSN is not suited to perform the decoding of this class of codes. This function (among others) will be performed by the Data Decoder Assembly, which is scheduled for installation in the DSN in September 1971. This article presents a description of the Data Decoder Assembly and its implementation.

GRAY, R. M.

G09 Frequency-Counted Measurements and Phase Locking to Noisy Oscillators

R. M. Gray (Stanford University) and R. C. Tausworthe

IEEE Trans. Commun. Technol., Vol. COM-19, No. 1, pp. 21–30, February 1971

The phase-error variance of a phase-locked loop is dependent on the stability of its voltage-controlled oscillator and that of the source oscillator being tracked. Statistics relative to oscillator stability are commonly gathered by counted-frequency techniques and are so specified in manufacturers' data. Thus, to predict the performance of a loop using such an oscillator, it is necessary to know how to relate counter data to loop error. This paper presents such a method based on a simple but realistic model of oscillator noises and shows that the mean sample variance of the counted-frequency method converges rather curiously and slowly to the actual variance. The model for the flicker component of the noise is physically realistic (finite power) and allows one to find the range of validity for the usual formal calculations for the sample variance of the counted frequency. In addition, insight is gained into the

relation between the sample variance and the actual finite variance of the realistic model.

The effect of oscillator instability on a first-order loop is long-term steady-state phase-error drift and short-term zero-mean fluctuation about this steady state. For the second-order loop, the steady-state drift disappears.

GREENBERG, R.

G10 DSN Progress Report for May–June 1971: Multiple-Mission Telemetry

W. Frey, R. Petrie, A. Lai, and R. Greenberg

Technical Report 32-1526, Vol. IV, pp. 160–164, August 15, 1971

For abstract, see Frey, W.

HADEK, V.

H01 Electron Transfer to Bipyridilium (Paraquat) Salts

A. Rembaum, V. Hadek, and S. P. S. Yen

J. Am. Chem. Soc., Vol. 93, No. 10, pp. 2532–2534, May 19, 1971

For abstract, see Rembaum, A.

HARRIS, C. W.

H02 DSN Progress Report for May–June 1971: DSN Telemetry System

E. S. Burke and C. W. Harris

Technical Report 32-1526, Vol. IV, pp. 4–10, August 15, 1971

For abstract, see Burke, E. S.

HARRISON, B. K.

H03 Geometric Approach to Invariance Groups and Solution of Partial Differential Systems

B. K. Harrison and F. B. Estabrook

J. Math. Phys. (N.Y.), Vol. 12, No. 4, pp. 653-666, April 1971

Methods are discussed for discovery of physically or mathematically special families of exact solutions of systems of partial differential equations. Such systems are described geometrically using equivalent sets of differential forms, and the theory derived for obtaining the generators of their invariance groups—vector fields in the space of forms. These *isovectors* then lead naturally to all the special solutions discussed, and it appears that other special ansätze must similarly be capable of geometric description. Application is made to the one-dimensional heat equation, the vacuum Maxwell equations, the Korteweg-de Vries equation, one-dimensional compressible fluid dynamics, the Lambropoulos equation, and the cylindrically symmetric Einstein-Maxwell equations.

HARRISON, E. C.

H04 Prediction of Lipid Uptake by Prosthetic Heart Valve Poppets From Solubility Parameters

J. Moacanin, D. D. Lawson, H. P. Chin (University of Southern California), E. C. Harrison (University of Southern California), and D. H. Blankenhorn (University of Southern California)

JPL Quarterly Technical Review, Vol. 1, No. 2, pp. 54-60, July 1971

For abstract, see Moacanin, J.

HEER, E.

H05 Optimization of Structures Based on Fracture Mechanics and Reliability Criteria

E. Heer and J.-N. Yang

AIAA J., Vol. 9, No. 4, pp. 621-628, April 1971

Spacecraft structural systems and subsystems are subjected to a number of qualification tests in which the proof loads are chosen at some level above the simulated loads expected during the space mission. Assuming fracture as the prime failure mechanism, and allowing for time effects due to cyclic and sustained loadings, this paper treats an optimization method in which the statistical variability of loads and material properties are taken into account, and in which the proof load level is used as an additional design variable. In the optimization process, the structural weight is the objective function whereas the total expected cost due to coupon

testing for material characterization, caused by failure during proof testing, and due to mission degradation is a constraint. Numerical results indicate that for a given expected cost constraint, substantial weight savings and improvements of reliability can be realized by proof testing.

H06 Reliability of Randomly Excited Structures

J.-N. Yang and E. Heer

AIAA J., Vol. 9, No. 7, pp. 1262–1268, July 1971

For abstract, see Yang, J.-N.

HERRIMAN, A. G.

H07 Mariner Mars 1969 Final Project Report: Scientific Investigations

J. A. Stallkamp, A. G. Herriman, and Mariner Mars 1969 Experimenters

Technical Report 32-1460, Vol. III, September 1, 1961

For abstract, see Stallkamp, J. A.

HOLCOMB, L. B.

H08 Satellite Auxiliary-Propulsion Selection Techniques: Survey of Auxiliary Electric Propulsion Systems

L. B. Holcomb

Technical Report 32-1505, Addendum, July 15, 1971

A review of electric thrusters for satellite auxiliary propulsion was conducted at JPL during the past year. Comparisons of the various thrusters for attitude propulsion and east–west and north–south stationkeeping were made based upon performance, mass, power, and demonstrated life. Reliability and cost are also discussed. The method of electrical acceleration of propellant served to divide the thruster systems into two groups: electrostatic and electromagnetic. Ion and colloid thrusters fall within the electrostatically accelerated group while magnetoplasmadynamic and pulsed plasma thrusters comprise the electromagnetically accelerated group. The survey was confined to research in the United States with accent on flight and flight prototype systems.

HOLMES, J. K.

H09 Digital Command System Second-Order Subcarrier Tracking Performance

J. K. Holmes and C. R. Tegnelia

Technical Report 32-1540, October 1, 1971

Equations are derived for the timing performance of the all-digital, second-order, phase-locked loop proposed for the Viking Orbiter and Thermoelectric Outer-Planet Spacecraft (TOPS) programs. The theory is compared with experimental results and found to agree well over the range of interest.

H10 First Slip Times Versus Static Phase Error Offset for the First- and Passive Second-Order Phase-Locked Loop

J. K. Holmes

IEEE Trans. Commun. Technol., Vol. COM-19, No. 2, pp. 234–235, April 1971

Static phase error offsets occur in first-order and passive second-order phase-locked loops, whenever the rest frequency of the local oscillator and the carrier are different prior to acquisition. The effect of the offset is to degrade performance and in particular to decrease the mean time to first slip. This paper studies first slip times via computer simulation. The mean time to first slip is displayed graphically as a function of signal-to-noise ratio for various static phase error offsets and values of the damping parameter.

HORTON, T. E.

H11 Influence of Differences in Thermochemistry Data Upon High-Temperature Gas Composition

T. E. Horton (University of Mississippi)

AIAA J., Vol. 9, No. 7, pp. 1308–1314, July 1971

In the analysis of propulsion, re-entry, and plasma dynamics problems, one is interested in equilibrium thermodynamic properties and gas composition. For gas dynamic experiments directed at measuring thermochemistry, radiative, or kinetic properties of high-temperature gases, an accurate prediction of chemical equilibrium properties is important in the reduction of data. In this article, a simple analysis is presented which allows the assessment of changes in thermochemistry data in the form of heat of formation, partition functions, specie free-energy, or specie specific heat upon the composition of high-temperature gas mixtures. The anal-

ysis is used to determine the level of sophistication required when treating polyatomic species, diatomic species, and atomic species.

H12 Influence of Water Vapor Upon the Properties of Shocked Air in Thermodynamic Equilibrium

T. E. Horton (University of Mississippi) and W. A. Menard

Phys. Fluids, Vol. 14, No. 7, pp. 1347–1351, July 1971

The role of water, initially mixed with air, upon the properties of shock compressed air has been investigated using a thermodynamic equilibrium computer program. The principal effect of the inclusion of water in the computation of the shock parameters of air is to reduce the temperature of the products. This reduction in temperature results in a reduction in the equilibrium electron concentration by reducing the ionization of NO. The maximum effect occurs at shock velocities of 4.0 to 4.3 km/s. A procedure is presented for estimating the effect of the addition of water.

HU, C.-L.

H13 Flow Dilution Effect on Blood Coagulation in Vivo

C.-L. Hu

Technical Memorandum 33-490, September 15, 1971

Self-regulation is a major characteristic pertaining to in vivo blood coagulation. In vivo coagulation is a set of enzyme reactions that are inhomogeneous in space. The inhomogeneity is maintained by the dilution of the blood flow in vivo. Because of this inhomogeneity, the chemical rate equations should be modified by fluid-dynamic (or flow-dilution) change and diffusion change.

This memorandum proposes a simple model of enzyme reactions and emphasizes the flow-dilution change of the reactions. First, the complex reactions in blood coagulation are discussed and weighed. Second, two controlling chemical reactions, the prothrombin-to-thrombin conversion and the inactivation of thrombin, both of which have significant positive and negative feedbacks, are selected. It is seen then that the reaction rates of both of these reactions will decrease as thrombin concentration is decreased by flow dilution; however, the positive rate decreases more (because of the autocatalyzation of the prothrombin-to-thrombin conversion) than the negative rate. Therefore, when flow dilution increases, the overall reaction direction can be switched from the positive (procoagulative) direction to the negative (anticoagulative) direction; thus, the in vivo coagulation is regulated and confined. This physical picture is analytically investigated by solving the modified Michaelis–Menton's enzyme rate equations. The effect of

varying the antithrombin concentration is also investigated. The background and the physics of this analysis are extensively discussed.

HUNT, R. H.

H14 Lines Intensities of the CO_2 Σ–Σ Bands in the 1.43–1.65 μ Region

R. A. Toth, R. H. Hunt (Florida State University), and E. K. Plyler (Florida State University)

J. Molec. Spectrosc., Vol. 38, No. 1, pp. 107–117, April 1971

For abstract, see Toth, R. A.

ISHIMARU, A.

I01 Fields Excited by an Arbitrarily Oriented Dipole in a Cylindrically Inhomogeneous Plasma

R. Woo and A. Ishimaru (University of Washington)

Radio Sci., Vol. 6, No. 5, pp. 583–592, May 1971

For abstract, see Woo, R.

JACKSON, E. B.

J01 DSN Progress Report for May–June 1971; DSN Research and Technology Support

E. B. Jackson

Technical Report 32-1526, Vol. IV, pp. 110–111, August 15, 1971

Major activities of the Development Support Group at both DSS 13 (Venus Deep Space Station) and the Microwave Test Facility are presented, and accomplishments and progress for each are described. Activities include radio metric observations (20–25 GHz), pulsar observations and planetary radar, precision antenna gain measurement (RASCAL), weak source observations, 100-kW operational clock synchronization transmitter implementation, clock synchronization transmissions, and Deep Space Instrumentation Facility klystron testing.

JAFFE, P.

J02 A Comparison Between Planar and Nonplanar Free-Flight Data

P. Jaffe

JPL Quarterly Technical Review, Vol. 1, No. 2, pp. 1–8, July 1971

Results from the first program designed to explore the difference between the planar and nonplanar dynamic stability coefficient, using the JPL-developed bi-planar wind-tunnel free-flight system, are presented. Two widely different configurations, a blunt 60-deg half-angle cone and a sharp 10-deg half-angle cone, were tested. The overall accuracy of the data was extremely high and firmly demonstrates the capability of the technique. Although no dramatic difference in the coefficients was apparent from the data, which was limited in number, they do suggest that there is a favorable increase in the coefficient as the motion becomes more nonplanar.

J03 Dynamic Stability Tests of Spinning Entry Bodies in the Terminal Regime

P. Jaffe

J. Spacecraft Rockets, Vol. 8, No. 6, pp. 575–579, June 1971

Analytical studies indicate that rolling blunt entry vehicles are susceptible to angle-of-attack divergence in the terminal regime. To investigate this problem, an experimental program was conducted where models were spun up and dropped inside the 500-ft-high Vehicle Assembly Building at Cape Kennedy. The angle-of-attack motion was recorded photographically, and from these data the dynamic stability coefficient was determined. The data confirm the results of the analytic studies and suggest that the dynamic stability coefficient increases, in a favorable way, as the roll rate increases.

JET PROPULSION LABORATORY

J04 A History of the Deep Space Network From Inception to January 1, 1969

Jet Propulsion Laboratory

Technical Report 32-1533, Vol. I, September 1, 1971

The Deep Space Network (DSN) is a precision communications system designed to communicate with and control unmanned spacecraft in the exploration of deep space. The DSN utilizes

large antennas, low-noise phase-lock receiving systems, and high-power transmitters located at stations positioned approximately 120 deg around the Earth. A special world-wide communications system connects these stations to the DSN mission control center in Pasadena, California. It is the policy of the DSN to continuously conduct research and development of new systems, components, and techniques and to incorporate them into the DSN to maintain a state-of-the-art capability. This history, edited by N. A. Renzetti, relates the development and results of this policy through January 1, 1969.

J05 Proceedings of the Fourth Annual Conference on Effects of Lithium Doping on Silicon Solar Cells (Held at the Jet Propulsion Laboratory, Pasadena, California, April 29, 1971)

Jet Propulsion Laboratory

Technical Memorandum 33-491, September 15, 1971

The Fourth Annual Conference on Effects of Lithium Doping on Silicon Solar Cells was sponsored by JPL to provide a forum for an in-depth review and discussion of the results of investigations being carried out by various organizations, under NASA/JPL sponsorship, as part of the Solar Cell Research and Development Program. Participating organizations included cell manufacturers and university and industrial research laboratories. The 15 formal presentations of the conference and a summary are presented in these proceedings, which were edited by P. A. Berman.

JOHNSON, A. C.

J06 DSN Progress Report for May–June 1971: Numerical Evaluation of the Transient Response for a Third-Order Phase-Locked System

A. C. Johnson

Technical Report 32-1526, Vol. IV, pp. 188–199, August 15, 1971

A third-order phase-locked receiver is presently being investigated for possible use in tracking high doppler rates. This article presents additional data pertaining to the transient analysis of a model of a third-order phase-locked receiver. Specifically, the instantaneous response of the system is calculated for an input phase function of the form

$$\theta(t) = \theta_0 + \Omega_0 t + \frac{1}{2}\Lambda_0 t^2$$

where θ_0 is the initial phase offset, Ω_0 the initial frequency offset, and Λ_0 the frequency rate. The results presented may be compared with those of the usual second-order loop.

JOHNSON, J. A.

J07 Quotients in Noetherian Lattice Modules

J. A. Johnson

Proc. Am. Math. Soc., Vol. 28, No. 1, pp. 71–74, April 1971

In this paper we obtain a generalization of the fact that, if M is a maximal (proper) ideal of a Noetherian ring R, then the ring M/MA is a vector space over R/M for all ideals A of the ring R.

JOHNSTON, D. W.

J08 DSN Progress Report for May–June 1971: DSIF Operations Support of Mariner Mars 1971

D. W. Johnston

Technical Report 32-1526, Vol. IV, pp. 200–204, August 15, 1971

This article is an abbreviated description of Deep Space Instrumentation Facility (DSIF) Operations activities in preparation for, and up to and including, Mariner Mars 1971 launches H and I. New DSIF hardware is covered briefly, with more detailed coverage of the DSIF training, testing, operational documentation, and performance aspects of the preparations.

KAWANO, K.

K01 DSN Progress Report for May–June 1971: SFOF Digital Television Hardcopy Equipment

F. L. Singleton and K. Kawano

Technical Report 32-1526, Vol. IV, pp. 123–128, August 15, 1971

For abstract, see Singleton, F. L.

KUO, T.-J.

K02 Comment on "Similarity Rule Estimation Methods for Cone Flow With Variable Gamma"

T.-J. Kuo

AIAA J., Vol. 9, No. 6, p. 1216, June 1971

Comments are made on a paper "Similarity Rule Estimation Methods for Cone Flow With Variable Gamma," by E. F. Blick, R. R. Walters, and C. Von Rosenberg, *AIAA J.*, Vol. 6, No. 5, pp. 959–961, May 1968. It is shown that numerical correlations for conical flows presented by Blick, et al., do not appear to be fully supported for conical bodies flying through high-temperature nuclear blasts or through the atmospheres of the planets.

KURTZ, D. W.

K03 Aerodynamics of Vehicles in Tubes

D. W. Kurtz

JPL Quarterly Technical Review, Vol. 1, No. 2, pp. 9–16, July 1971

Currently many transportation systems are being studied which require vehicles to operate in tunnels under conditions of high blockage. As a consequence, a great deal of interest is being generated in the aerodynamic characteristics of such transportation systems. Model testing should be performed to better understand the aerodynamic aspects of such systems. This article presents a brief description of a facility that was constructed to study these systems and some of the initial results which have been obtained to date.

LAESER, R. P.

L01 DSN Progress Report for May–June 1971: Mariner Mars 1971 Mission Support

R. P. Laeser

Technical Report 32-1526, Vol. IV, pp. 32–39, August 15, 1971

All requirements for DSN capabilities needed to support Mariner Mars 1971 Mars orbital operations have been compiled and reiterated with the implementing organizations. Trade-offs between schedule and capability have been made in some instances. This article describes the resulting configuration by network system.

LAI, A.

L02 DSN Progress Report for May–June 1971: Multiple-Mission Telemetry

W. Frey, R. Petrie, A. Lai, and R. Greenberg

Technical Report 32-1526, Vol. IV, pp. 160–164, August 15, 1971

For abstract, see Frey, W.

LAWSON, C. L.

L03 Applications of Singular Value Analysis

C. L. Lawson

Mathematical Software, pp. 347–356, Academic Press, New York, 1971

The singular value decomposition of a matrix provides quantitative information about a matrix which is very pertinent in a number of situations that arise in scientific computation. In this article, the mathematical concept of the singular value decomposition is reviewed and an example is given of one way in which it can be used to analyze a problem of solving a system of linear equations. Some features are mentioned of the algorithms and subroutines that have been used, and some of the applications which have been made of this type of analysis at JPL are also included.

LAWSON, D. D.

L04 Prediction of Lipid Uptake by Prosthetic Heart Valve Poppets From Solubility Parameters

J. Moacanin, D. D. Lawson, H. P. Chin (University of Southern California), E. C. Harrison (University of Southern California), and D. H. Blankenhorn (University of Southern California)

JPL Quarterly Technical Review, Vol. 1, No. 2, pp. 54–60, July 1971

For abstract, see Moacanin, J.

LEAHEY, C. F.

L05 DSN Progress Report for May–June 1971: Mark IIIA Simulation Center Diagnostic Software

C. F. Leahey

Technical Report 32-1526, Vol. IV, pp. 129–132, August 15, 1971

The expansion and reconfiguration of the DSN simulation center to the Mark IIIA configuration necessitated the modification of existing diagnostic software and the development of new diagnostic and

test programs. This article describes the characteristics of the diagnostics that were developed for the EMR 6050-Univac 1108 interface and the Interactive Alphanumeric Television Display System.

LEVY, R.

L06 Resequencing of the Structural Stiffness Matrix to Improve Computational Efficiency

R. Levy

JPL Quarterly Technical Review, Vol. 1, No. 2, pp. 61–70, July 1971

Improved computational efficiency and reduction in core storage requirements in large-capacity structural-analysis computer programs are achieved by taking advantage of the typical sparseness in the stiffness matrix. In many cases, the favorable effects can be enhanced by resequencing the interconnecting terms of the stiffness matrix. This produces a relatively large empty region that can be bypassed and a relatively small, compact region that is moved into the core for computations.

In the past, the goal of resequencing has been to minimize the stiffness matrix bandwidth. A favorable alternative resequencing procedure that has the goal of reducing the matrix wavefront is described in this article. Comparisons are supplied to show the relative compactness that can be achieved for practical structural models with wavefront sequencing and with bandwidth sequencing. Examples show that wavefront sequencing can produce a savings in the time required for subsequent decomposition of the stiffness matrix.

LIKINS, P. W.

L07 Results of Flexible Spacecraft Attitude Control Studies Utilizing Hybrid Coordinates

P. W. Likins (University of California, Los Angeles) and G. E. Fleischer

J. Spacecraft Rockets, Vol. 8, No. 3, pp. 264–273, March 1971

Explicit analyses are presented in sufficient detail to establish the utility in flexible space vehicle control system design of a hybrid coordinate formulation, employing a combination of discrete and distributed (modal) coordinates. A three-stage process for the design of attitude control systems for flexible vehicles is described:

(1) preliminary design is based on root locus plots for single-axis response of linearized systems with sharply truncated modal coordinate matrices; (2) modifications are imposed as required by eigenvalue analyses of coupled linear systems; and (3) design confirmation is established by complex, nonlinear differential equation simulation using digital computer numerical integration. These procedures are illustrated by application to two vehicle models. A very simple model is used to demonstrate the potentially destabilizing influence of vehicle flexibility, and corresponding results are shown for a realistically complex model of the Thermoelectric Outer-Planet Spacecraft.

LINDSEY, W. C.

L08 Data-Aided Carrier Tracking Loops

W. C. Lindsey (University of Southern California) and
M. K. Simon

IEEE Trans. Commun. Technol., Vol. COM-19, No. 2,
pp. 157–168, April 1971

An innovation that improves the capability and performance of certain types of phase-coherent demodulators is introduced. This innovation has application in the fields of telemetry and tracking, e.g., relay satellite systems, deep-space communications, and military communication systems. The basic idea of the innovation centers around using the power in the composite signal sidebands to enhance the demodulator's effective signal-to-noise ratio (SNR). The vehicle through which this is accomplished employs the principle of decision-directed feedback. In its simplest form it is shown, for the first-order loop, that the maximum improvement in loop SNR relative to a standard phase-locked loop is 10 dB. This paper explores and illustrates the corresponding improvement realized in detection system efficiency. Extension to higher order loops follows directly from the analysis given in this paper.

LINNES, K. W.

L09 DSN Progress Report for May–June 1971: Radio Science Support

K. W. Linnes

Technical Report 32-1526, Vol. IV, pp. 47–48,
August 15, 1971

Since 1967, radio scientists have used the DSN 26- and 64-m antenna stations to investigate pulsars, to study the effects of solar corona on radio signals, and to observe radio emissions of X-ray

sources. Very long baseline interferometry (VLBI) techniques have also been used for high-resolution studies of quasars. Several VLBI observations that were accomplished during the reporting period are summarized.

L10 Tracking and Data System Support for the Mariner Mars 1969 Mission: Midcourse Maneuver Through End of Nominal Mission

N. A. Renzetti, K. W. Linnes, D. L. Gordon, and T. M. Taylor

Technical Memorandum 33-474, Vol. II, September 1, 1971

For abstract, see Renzetti, N. A.

L11 Tracking and Data System Support for the Mariner Mars 1969 Mission: Extended Operations Mission

N. A. Renzetti, K. W. Linnes, and T. M. Taylor

Technical Memorandum 33-474, Vol. III, September 15, 1971

For abstract, see Renzetti, N. A.

LIVINGSTON, F. R.

L12 Planetary Entry Body Heating Rate Measurements in Air and Venus Atmospheric Gas Up to T = 15,000°K

F. R. Livingston and J. W. Williard

AIAA J., Vol. 9, No. 3, pp. 485–492, March 1971

Convective plus radiative shock-tube-model stagnation-point heating rate measurements are presented. Platinum thick-film calorimeter gages, both uncoated and carbon-coated, sensed the heat flux on the external surface of the hemispherical and truncated-cylinder models. This thorough experimental study of total heat flux provides quantitative data necessary to verify existing theoretical radiative flowfield methods. In contrast with past experiments, the radiative flux emanating from a 2π sterad solid angle at all wavelengths is a significant fraction of the total heating measured by the calorimeter. Experimental thermochemical and geometric conditions are systematically changed in order to interpret the results in terms of convective heating, radiative heating, and coupling effects. At temperatures between 12,000 and 15,000°K, the measurements agree with theoretical uncoupled convective heating summed with isothermal radiative flux reduced by a radiative cooling

factor. At lower temperatures, the measured heating was more than expected, especially in air.

LORDEN, G.

L13 DSN Progress Report for May–June 1971: Detection of Failure Rate Increases

G. Lorden (California Institute of Technology) and I. Eisenberger

Technical Report 32-1526, Vol. IV, pp. 95–100, August 15, 1971

The problem of devising systematic policies for replacement of equipment subject to wear-out involves the detection of increases in failure rates. Detection procedures are defined as stopping times N with respect to the observed sequence of random failures. The concepts of "quickness of detection" and "frequency of false reactions" are made precise and a class of procedures is studied which optimizes the former asymptotically as the latter is reduced to zero. Results of Monte Carlo experiments are given which show that efficient quickness of detection is attainable simultaneously for various levels of increase in failure rates.

LUDWIG, A. C.

L14 Near-Field Far-Field Transformations Using Spherical-Wave Expansions

A. C. Ludwig

IEEE Trans. Anten. Prop., Vol. AP-19, No. 2, pp. 214–220, March 1971

Spherical-wave expansions are a well-known technique of expressing electromagnetic field data. However, most previous work has been restricted to idealized cases in which the expansion coefficients are obtained analytically. In this paper spherical-wave expansions are used as a numerical technique for expressing arbitrary fields specified by analytical, experimental, or numerical data. Numerical results on the maximum wave order needed to expand fields arising from a source of a given size are given for two practical cases, and it is found that the generally accepted wave order cutoff value corresponds to 99.9% or more of the power in the input pattern. Near-field patterns computed from far-field data are compared to measured data for the two cases, demonstrating the excellent numerical accuracy of the technique.

LUSHBAUGH, W. A.

L15 DSN Progress Report for May–June 1971: Digital Period Detector Oscilloscope Trigger

W. A. Lushbaugh

Technical Report 32-1526, Vol. IV, pp. 78–83, August 15, 1971

Due to the increased complexity of new digital equipment, there has arisen a need for more sophisticated test equipment. This article describes a piece of equipment for obtaining an optimum trigger for an oscilloscope. This equipment accepts a periodic digital sequence and its associated clock, and outputs a single pulse once per period. This output is intended to be used as the external trigger for an oscilloscope. A digital readout of the numerical value of the period is also provided to enable determination of the correct trigger to be used for a multitrace display.

MACLAY, J. E.

M01 DSN Progress Report for May–June 1971: DSN Monitor System

J. E. Maclay

Technical Report 32-1526, Vol. IV, pp. 11–12, August 15, 1971

The DSN Monitor System is now operational. The system has been significantly changed during the process of moving the IBM 360/75 computers into the Space Flight Operations Facility (SFOF). The display capability is much greater than that available in the previous monitor system design. Additionally, SFOF and Ground Communications Facility monitoring provisions are augmented over the previous design.

MANATT, S. L.

M02 The Fluorine-19 Nuclear Magnetic Resonance Spectra of Some Fluoroaromatic Compounds. Studies Using Noise Decoupling of Protons

M. A. Cooper, H. E. Weber, and S. L. Manatt

J. Am. Chem. Soc., Vol. 93, No. 10, pp. 2369–2380, May 19, 1971

For abstract, see Cooper, M. A.

MARGOLIS, J. S.

M03 Studies of Methane Absorption in the Jovian Atmosphere: III. The Reflecting-Layer Model

J. S. Margolis

Astrophys. J., Vol. 167, No. 3, Pt. 1, pp. 553–558, August 1, 1971

The spectrum of the $3\nu_3$ band of CH_4 in the Jovian spectrum is examined in terms of a model of the atmosphere similar to Trafton's. It is shown that a reflecting-layer model is consistent with the observed temperature, half-width of the absorption lines, and mixing ratio CH_4/H_2 if observations are restricted to the center of the Jovian disk. The failure of the reflecting-layer model of the atmosphere near the edge of the disk is tentatively explained on the basis of a two-layer cloud distribution.

MARINER MARS 1969 EXPERIMENTERS

M04 Mariner Mars 1969 Final Project Report: Scientific Investigations

J. A. Stallkamp, A. G. Herriman, and Mariner Mars 1969 Experimenters

Technical Report 32-1460, Vol. III, September 1, 1961

For abstract, see Stallkamp, J. A.

MARKO, W. J.

M05 Aerobraking of High-Speed Ground Transportation Vehicles

W. J. Marko

JPL Quarterly Technical Review, Vol. 1, No. 2, pp. 17–22, July 1971

A JPL-sponsored aerodynamic testing program has been initiated to perform initial investigations on the effectiveness of a series of aerodynamic brakes on a long cylindrical body. The development of the experimental program is presented in this article and a description of the model and test configuration is given. Preliminary results from a low subsonic wind tunnel test using three standard test techniques are also discussed. A moving-model drop-wire facility has been constructed and initial testing is currently underway. This data, which more correctly simulates the viscous interactions of the model with the ground plane, will be compared with the wind tunnel data and used to develop analytical prediction methods.

MARSH, H. E., JR.

M06 Formulating Propellants for Fully Case-Bonded End-Burning Motors

H. E. Marsh, Jr., and D. E. Udlock

AIAA Preprint 71-654, AIAA/SAE Seventh Propulsion Joint Specialist Conference, Salt Lake City, Utah, June 14–18, 1971

A low-modulus propellant with properties suitable for use in high-performance, fully case-bonded end-burning motors has been developed and demonstrated. This development was achieved by employing a new binder formulating technique based on polymer network theory. High elongation and low modulus were obtained by adjusting the network polymer formation within the propellant binder by means of chain termination. The chain termination was accomplished by the introduction of a monofunctional binder ingredient, which effectively lowers the polymer crosslink concentration, resulting in a highly extensible propellant binder.

The properties of the new binder make possible propellants with controllable physical properties over a wide range. This has allowed the design of a fully case-bonded end-burning motor with a propellant which is elastic enough to withstand the triaxial strains imposed upon it and yet is rigid enough so that it will not deform under its own weight. Preliminary tests with a flight-weight motor containing 360 kg of propellant are successful thus far.

MENARD, W. A.

M07 Influence of Water Vapor Upon the Properties of Shocked Air in Thermodynamic Equilibrium

T. E. Horton (University of Mississippi) and W. A. Menard

Phys. Fluids, Vol. 14, No. 7, pp. 1347–1351, July 1971

For abstract, see Horton, T. E.

MENICHELLI, V. J.

M08 Half-Sine Wave Pulse Firing of Electroexplosive Devices

L. A. Rosenthal (Rutgers University) and V. J. Menichelli

Technical Report 32-1534, July 15, 1971

For abstract, see Rosenthal, L. A.

MO, T. C.

M09 Electromagnetic Wave Propagation in a Uniformly Accelerated Simple Medium

T. C. Mo (California Institute of Technology)

Radio Sci., Vol. 6, No. 6, pp. 673-679, June 1971

The theory of electromagnetic wave propagation in a uniformly accelerated simple medium is generalized to cover the case of an arbitrary initial wave direction. The wave splits into two natural modes relative to the plane of acceleration and the wave vector. The case of high frequency and weak acceleration is solved in detail; to observers at rest with respect to the medium, a drag effect due to apparent gravity is demonstrated, and to inertial observers a drag effect due to medium acceleration is demonstrated. A preferred asymptotic cone of propagation determined by $(\mu\epsilon - 1)^{1/2}$ is found in the accelerated frame. Various drag effects are physically interpreted.

MOACANIN, J.

M10 Prediction of Lipid Uptake by Prosthetic Heart Valve Poppets From Solubility Parameters

J. Moacanin, D. D. Lawson, H. P. Chin (University of Southern California), E. C. Harrison (University of Southern California), and D. H. Blankenhorn (University of Southern California)

JPL Quarterly Technical Review, Vol. 1, No. 2, pp. 54-60, July 1971

Most prosthetic heart valves currently implanted consist of a silicone rubber poppet situated within a metallic cage. Recent reports indicate that gradual deterioration of the poppet can occur and lead to serious valve malfunction. Physical changes (variance) observed in recovered prostheses include discoloration, swelling, and cracking. A major cause of variance is believed to be lipid accumulation. This article presents an assessment of the solubility of lipids in silicone rubber and other commonly used poppet materials. The analysis is based on solubility parameter theory that is based on principles derived from thermodynamic considerations. The results of this analysis predict that highly polar compounds, such as phospholipids or proteins, should not be present in silicone rubber poppets, which is in agreement with observations.

M11 The Effect of an Oxidative–Caustic Environment on Graft Copolymer Membranes

E. F. Cuddihy, J. Moacanin, D. E. Walmsley, and H. Y. Tom

Colloidal and Morphological Behavior of Block and Graft Copolymers, pp. 113–129, Plenum Press, New York, 1971

For abstract, see Cuddihy, E. F.

MORRIS, G.

M12 Use of Pulsar Signals As Clocks

P. E. Reichley, G. S. Downs, and G. Morris

JPL Quarterly Technical Review, Vol. 1, No. 2, pp. 80–86, July 1971

For abstract, see Reichley, P. E.

MOTTINGER, N. A.

M13 DSN Progress Report for May–June 1971: An Examination of the Effects of Station Longitude Errors on Doppler Plus Range and Doppler Only Orbit Determination Solutions With an Emphasis on a Viking Mission Trajectory

V. J. Ondrasik and N. A. Mottinger

Technical Report 32-1526, Vol. IV, pp. 71–77, August 15, 1971

For abstract, see Ondrasik, V. J.

MUDGWAY, D. J.

M14 DSN Progress Report for May–June 1971: Viking Mission Support

D. J. Mudgway

Technical Report 32-1526, Vol. IV, pp. 40–46, August 15, 1971

Previous issues of the DSN Space Programs Summary and the DSN Progress Report devoted attention to management and organization, DSN configurations for telemetry, command, and tracking, and, more recently, to the influence of the DSN in the design of the Viking mission orbiters and landers. Beginning with this issue of the DSN Progress Report, attention will be focused on reporting Viking-related activity in certain specific areas, as the

DSN interface organization progresses from the planning through operational phases of the Viking missions. This article takes up the question of DSN support for Viking navigation and traces progress since the latter part of 1970 through the present time.

MULLER, P. M.

M15 Lunar Surface Mass Distribution From Dynamical Point-Mass Solution

W. L. Sjogren, P. M. Muller, P. Gottlieb, L. Wong (Aerospace Corporation), G. Buechler (Aerospace Corporation), W. Downs (Aerospace Corporation), and R. Prislin (Aerospace Corporation)

The Moon: Int. J. Lunar Studies, Vol. 2, No. 3, pp. 338–353, February 1971

For abstract, see Sjogren, W. L.

NASH, D. B.

N01 Potassium–Uranium Systematics of Apollo 11 and Apollo 12 Lunar Samples and of Some Deep Earth Rocks

F. P Fanale and D. B. Nash

Science, Vol. 172, No. 3988, p. 1167, June 11, 1971

For abstract, see Fanale, F. P.

NEUGEBAUER, M.

N02 Correlated Observations of Electrons and Magnetic Fields at the Earth's Bow Shock

M. Neugebauer, C. T. Russell (University of California, Los Angeles), and J. V. Olson (University of California, Los Angeles)

J. Geophys. Res., Space Phys., Vol. 76, No. 19, pp. 4366–4380, July 1, 1971

The internal structure of the Earth's bow shock has been studied by using simultaneous observations made on board the Orbiting Geophysical Observatory 5 satellite of the magnetic field (0–3 Hz), the ELF magnetic fluctuations (10–1000 Hz), and the suprathermal electrons (100–800 eV). The initial acceleration of electrons from ~10 to 100 eV could not be observed, but electrons with energy ≥100 eV were already present near the foot of the field gradient. These hot electrons were then compressed as they moved up the

field strength gradient. In two of the six shock crossings studied, further acceleration accompanied the compression. The profiles of the flux of electrons with energies >100 eV were similar to the field strength profiles, with the exception that increased fluxes of accelerated electrons were also associated with steep field gradients. For all shock crossings observed, there was a high positive correlation of the flux of both 100- and 200-eV electrons with field strength. Both electron flux and field magnitude reached peak values in the shock front greater than the values found further downstream in the magnetosheath. For the two shock crossings for which directional electron data were available, the solar-oriented instrument observed equal or greater fluxes of accelerated electrons than did the instrument pointing away from the center of the Earth. There was a positive correlation between the fluxes to these two instruments even though they were observing different energy electrons. The ELF magnetic field oscillations started to increase at the same time as the field strength and the flux of accelerated electrons but reached their maximum level upstream of the field strength and electron maximums. The generation of ELF noise coincident with the compression of the electrons is consistent with the unstable growth of waves in cyclotron resonance with the electrons.

NG, E. W.

N03 A General Algorithm for the Solution of Kepler's Equation for Elliptic Orbits

E. W. Ng

Technical Memorandum 33-496, September 1, 1971

An efficient algorithm and subroutine are presented for the solution of Kepler's equation

$$f(E) = E - M - e \sin E = 0$$

where e is the eccentricity, M the mean anomaly, and E the eccentric anomaly. This algorithm is based on simple initial approximations that are cubics of M and an iterative scheme that is a slight generalization of the Newton-Raphson method. Extensive testing involving 20,000 pairs of values of e and M shows that, for single precision ($\sim 10^{-8}$), 42.0% of the cases require one iteration, 57.8% require two iterations, and 0.2% require three iterations. Both single- and double-precision FORTRAN V subroutine listings for the UNIVAC 1108 computer are provided, the double precision listing requiring one additional iteration.

NIGHTINGALE, D.

N04 DSN Progress Report for May–June 1971: High-Speed Data System Performance and Error Statistics at 4800 bps

D. Nightingale

Technical Report 32-1526, Vol. IV, pp. 154–159, August 15, 1971

A survey was conducted from March through June of 1971 to study the performance of the Ground Communications Facility upgraded High-Speed Data System. Operational and other user traffic was used as the basis for the tabulated results. This article describes the conditions under which the data were gathered and draws some conclusions based upon analysis of those data.

NOLLER, E. W.

N05 Aluminizing of the 7.01-m Collimating Mirror for the JPL 7.62-m Space Simulator

E. W. Noller and R. E. Frazer

Technical Memorandum 33-485, July 15, 1971

The modification of the JPL 7.62-m (25-ft) space simulator required the aluminizing of a 7.01-m (23-ft) collimating mirror. The classical aluminizing technique of vaporizing aluminum from tungsten filaments was scaled up from previous experience in aluminizing the JPL 3.05-m (10-ft) collimating mirror. Several techniques were evaluated and discarded in determining the best aluminizing method. From this investigation, a new evaporation system was developed using three electron-beam guns magnetically focused on a single crucible with a second set of coils producing a variable magnetic field to distribute the evaporated aluminum. The mirror was exposed to the aluminum vapor through a large shutter. For thickness control, a crystal microbalance with temperature compensation was used with a digital display.

OLSON, J. V.

O01 Correlated Observations of Electrons and Magnetic Fields at the Earth's Bow Shock

M. Neugebauer, C. T. Russell (University of California, Los Angeles), and J. V. Olson (University of California, Los Angeles)

J. Geophys. Res., Space Phys., Vol. 76, No. 19, pp. 4366–4380, July 1, 1971

For abstract, see Neugebauer, M.

ONDRASIK, V. J.

002 **DSN Progress Report for May–June 1971: Application of Differenced Tracking Data Types to the Zero Declination and Process Noise Problems**

K. H. Rourke and V. J. Ondrasik

Technical Report 32-1526, Vol. IV, pp. 49–60, August 15, 1971

For abstract, see Rourke, K. H.

003 **DSN Progress Report for May–June 1971: An Analytical Study of the Advantages Which Differenced Tracking Data May Offer for Ameliorating the Effects of Unknown Spacecraft Accelerations**

V. J. Ondrasik and K. H. Rourke

Technical Report 32-1526, Vol. IV, pp. 61–70, August 15, 1971

Using the six-parameter representation of the range-rate observable, arguments are presented to show why differenced data may more effectively diminish the effects of unmodelable spacecraft accelerations than the conventional tracking data. For a Viking spacecraft experiencing unknown constant accelerations, the orbit determination solution using differenced data may be two orders of magnitude better than the solution obtained from conventional tracking data.

004 **DSN Progress Report for May–June 1971: An Examination of the Effects of Station Longitude Errors on Doppler Plus Range and Doppler Only Orbit Determination Solutions With an Emphasis on a Viking Mission Trajectory**

V. J. Ondrasik and N. A. Mottinger

Technical Report 32-1526, Vol. IV, pp. 71–77, August 15, 1971

During the early Viking mission accuracy analysis studies, it was discovered that station location errors may degrade the navigation more for doppler plus range solutions than for doppler only solutions. An explanation of this seemingly curious occurrence is given.

PALLUCONI, F. D.

P01 Saturn's Rings—A Survey

A. F. Cook (Smithsonian Astrophysical Observatory), F. A. Franklin (Smithsonian Astrophysical Observatory), and F. D. Palluconi

Technical Memorandum 33-488, July 15, 1971

For abstract, see Cook, A. F.

PAWLIK, E. V.

P02 Preliminary Investigations of Ion Thruster Cathodes

R. Goldstein, E. V. Pawlik, and L. C. Wen

Technical Report 32-1536, August 1, 1971

For abstract, see Goldstein, R.

P03 Operation of a Lightweight Power Conditioner With a Hollow-Cathode Ion Thruster

E. V. Pawlik, E. N. Costogue, and W. C. Schaefer

J. Spacecraft Rockets, Vol. 8, No. 3, pp. 245–250, March 1971

Experimental system studies are under way on solar-electric primary propulsion for deep space probes, using a 20-cm-diam electron-bombardment ion thruster that has a hollow cathode as an electron source and mercury as the propellant. The thruster output power can be varied from 1000 to 2000 W with small penalties in total efficiency. A lightweight power conditioner, originally designed for operation of an ion thruster employing an oxide cathode, has been modified to accommodate the hollow cathode. The thruster and power conditioner redesign, thruster control loops, and recycle procedure to clear sustained arcs are described. Data are presented on operation with the thruster.

PETERSON, M. L.

P04 Dry-Heat Resistance of Bacterial Spores Recovered From Mariner-Mars 1969 Spacecraft

M. D. Wardle, W. A. Brewer, and M. L. Peterson

Appl. Microbiol., Vol. 21, No. 5, pp. 827–831, May 1971

For abstract, see Wardle, M. D.

PETRIE, R.

P05 DSN Progress Report for May–June 1971: Multiple-Mission Telemetry

W. Frey, R. Petrie, A. Lai, and R. Greenberg

Technical Report 32-1526, Vol. IV, pp. 160–164, August 15, 1971

For abstract, see Frey, W.

PLYLER, E. K.

P06 Lines Intensities of the CO_2 Σ–Σ Bands in the 1.43–1.65 μ Region

R. A. Toth, R. H. Hunt (Florida State University), and E. K. Plyler (Florida State University)

J. Molec. Spectrosc., Vol. 38, No. 1, pp. 107–117, April 1971

For abstract, see Toth, R. A.

PRISLIN, R.

P07 Lunar Surface Mass Distribution From Dynamical Point-Mass Solution

W. L. Sjogren, P. M. Muller, P. Gottlieb, L. Wong (Aerospace Corporation), G. Buechler (Aerospace Corporation), W. Downs (Aerospace Corporation), and R. Prislin (Aerospace Corporation)

The Moon: Int. J. Lunar Studies, Vol. 2, No. 3, pp. 338–353, February 1971

For abstract, see Sjogren, W. L.

REICHLEY, P. E.

R01 Use of Pulsar Signals As Clocks

P. E. Reichley, G. S. Downs, and G. Morris

JPL Quarterly Technical Review, Vol. 1, No. 2, pp. 80–86, July 1971

The pulses of energy from pulsars are regarded as ticks from a clock. By comparing this pulsar clock with an earth-based atomic clock, several variations in the pulsar clock's frequency are noted. The major effect is due to the motion of the atomic clock in

relation to the pulsar clock and contains information on the pulsar's position, elements of the earth's orbit, and solar relativistic effects. Another effect is the slowly varying frequency of the pulsar clock and contains information on the physics of the pulsar. In this article, the measurements of these effects and their present and future applications are discussed.

REID, M. S.

R02 DSN Progress Report for May–June 1971: Improved RF Calibration Techniques: System Operating Noise Temperature Calibrations

M. S. Reid

Technical Report 32-1526, Vol. IV, pp. 105–109, August 15, 1971

The system operating noise temperature performance of the low noise research cones at the Goldstone Deep Space Communications Complex is reported for the period February 1 through May 31, 1971. The operating noise temperature calibrations were performed with the ambient termination technique. The cones on which this technique was used during this reporting period were the S-band research operational cone at DSS 13 (Venus Deep Space Station) and the polarization diversity S-band cone at DSS 14 (Mars DSS). The averaged operating noise temperature calibrations for the various cones, and other calibration data, are presented.

REMBAUM, A.

R03 Electron Transfer to Bipyridilium (Paraquat) Salts

A. Rembaum, V. Hadek, and S. P. S. Yen

J. Am. Chem. Soc., Vol. 93, No. 10, pp. 2532–2534, May 19, 1971

Bipyridils quaternized by means of mineral acids and reacted with LiTCNQ exhibit an anomalously high electronic conductivity. This phenomenon is not observed when the quaternization is carried out by means of alkyl halides. Examination of electrical and optical properties of several bipyridilium TCNQ Salts revealed an electron transfer from the radical ion to the paraquat. The postulated mechanism of electron transfer involves the formation of a hydrogen atom and a neutral TCNQ molecule.

R04 Complexes of Heparin With Elastomeric Positive Polyelectrolytes

S. P. S. Yen and A. Rembaum

J. Biomed. Mater. Res. Symposium, Vol. 1, pp. 83–97, 1971

For abstract, see Yen, S. P. S.

RENZETTI, N. A.

R05 DSN Progress Report for May–June 1971: DSN Functions and Facilities

N. A. Renzetti

Technical Report 32-1526, Vol. IV, pp. 1–3, August 15, 1971

The DSN, established by the NASA Office of Tracking and Data Acquisition and under the system management and technical direction of JPL, is designed for two-way communications with unmanned spacecraft traveling approximately 16,000 km (10,000 mi) from earth to planetary distances. The objectives, functions, and organization of the DSN are summarized, and its three facilities—the Deep Space Instrumentation Facility, the Ground Communications Facility, and the Space Flight Operations Facility—are described.

R06 Tracking and Data System Support for the Pioneer Project: Pioneers VI–IX. Extended Missions: July 1, 1969–July 1, 1970

N. A. Renzetti

Technical Memorandum 33-426, Vol. IX, August 15, 1971

The Tracking and Data System supported the deep space phases of the Pioneer 6–9 (Pioneer VI–IX) missions, with two spacecraft in an inward trajectory and two spacecraft in an outward trajectory from the Earth in heliocentric orbits. During the period of this memorandum, scientific instruments aboard each of the spacecraft continued to register information relative to interplanetary particles and fields, and radio metric data generated by the network continued to improve our knowledge of the celestial mechanics of the solar system. In addition to network support activity detail, network performance and special support activities are covered.

R07 Tracking and Data System Support for the Mariner Mars 1969 Mission: Midcourse Maneuver Through End of Nominal Mission

N. A. Renzetti, K. W. Linnes, D. L. Gordon, and T. M. Taylor

Technical Memorandum 33-474, Vol. II, September 1, 1971

The Tracking and Data System support for the Mariner Mars 1969 Project was planned and implemented in close cooperation with the Mission Operations and Spacecraft Systems of the project. The project requirements for tracking, telemetry, command, simulation, mission control, and compatibility testing were reviewed for matching to Deep Space Network (DSN) capabilities. The DSN capabilities to support the project were set forth in an Operations Plan describing the design of the DSN Systems formulated for the support of this particular project. Each of the systems is described. Unusual new features were the Multi-Mission Telemetry System, which eliminated the need for mission-dependent equipment at the tracking stations, and an experimental High-Rate Telemetry System operating at 16,200 bits/s. This unusually high rate, employed for the first time in deep space missions, permitted return of low-resolution pictures in real time and playback of full-resolution pictures from the spacecraft tape recorder in less than 3 h. Normal techniques and rates would have required 7 to 8 days of playback.

The 26-m antenna stations of the DSN provided deep-space-phase support throughout the mission. During the cruise portion of the deep space phase, the DSN 64-m antenna at Goldstone, California provided ranging data to planetary distances; during the planetary encounter, it provided the 16,200-bits/s capability by means of the block-coded High-Rate Telemetry System.

Analysis of the support performance shows that virtually all tracking and telemetry data received on Earth were acquired, processed, and delivered to the project. All commands delivered to the DSN by the project for transmission to the spacecraft were transmitted successfully.

R08 Tracking and Data System Support for the Mariner Mars 1969 Mission: Extended Operations Mission

N. A. Renzetti, K. W. Linnes, and T. M. Taylor

Technical Memorandum 33-474, Vol. III,
September 15, 1971

The Tracking and Data System support for the scientific and engineering experiments of the Mariner Mars 1969 extended operations mission is summarized in this volume. The report covers the period from the end of the original mission on November 1, 1969, to December 31, 1969, and the extended operations mission from January to December 30, 1970. The tracking, telemetry, and command operations of the Deep Space Network with performance evaluations are presented, including the use of the new improved

experimental ranging system, the tricone feed structure, and the experimental 400-kW transmitter at the Mars Deep Space Station at Goldstone, California.

RHEIN, R. A.

R09 Reaction Between Oxygen Difluoride and Diborane: Kinetics and a Proposed Mechanism

R. A. Rhein

AIAA J., Vol. 9, No. 3, pp. 353–357, March 1971

For the reaction between OF_2 and B_2H_6, the initial rates of consumption of OF_2 and B_2H_6 and the initial rate of formation of BF_3 (a reaction product) were experimentally determined over a range of initial partial pressures of 1–30 torr for B_2H_6 and 5–40 torr for OF_2, at 300°K. In addition, the initial consumption rates of OF_2 and B_2H_6 were determined at temperatures ranging from 300 to 330°K. These initial rates were correlated to initial reactant concentrations and to reactor temperature by the expressions

$$\left[\frac{d}{dt}(P_{BF_3})\right]_0 = (2.16 \times 10^{-3})\,[(P_{OF_2})]_0^{1.7}\,[(P_{B_2H_6})]_0^{-0.4} \text{ at } 300°K$$

$$-\left[\frac{d}{dt}(P_{B_2H_6})\right]_0 = (2.82 \times 10^{6})\,[(P_{OF_2})]_0^{2.2}\,[(P_{B_2H_6})]_0^{-0.6} \times \exp(-11{,}000/RT)$$

$$-\left[\frac{d}{dt}(P_{OF_2})\right]_0 = 0.294\,[(P_{OF_2})]_0^{1.6}\,[(P_{B_2H_6})]_0^{0} \exp(-2800/RT)$$

where P is partial pressure in torr at 300°K, t is time in minutes, T is temperature in degrees kelvin, and R is 1.987 cal-mole^{-1}-°K^{-1}.

ROPER, W. D.

R10 Spacecraft Adhesives for Long Life and Extreme Environments

W. D. Roper

Technical Report 32-1537, August 1, 1971

A review of the state-of-the-art of high-performance adhesives was undertaken for the purpose of establishing those newer materials which show potential for future application in spacecraft. Following the state-of-the-art review, several adhesive materials were selected and evaluated in the laboratory. The adhesive materials evaluated included the polyimide, the polybenzimidazole, and the polyquinoxaline polymer systems. In the laboratory work the thermal shock resistance of each material was determined by thermal

cycling through the temperature range of 204 to -73°C. In addition, each adhesive was evaluated for long-term elevated-temperature performance in aging tests conducted at 260°C and 10^{-4} N/cm^2 for 5000 h. The results of this investigation showed that the polyimide adhesive system currently has the greatest potential for use in future spacecraft applications.

ROSENTHAL, L. A.

R11 Half-Sine Wave Pulse Firing of Electroexplosive Devices

L. A. Rosenthal (Rutgers University) and V. J. Menichelli

Technical Report 32-1534, July 15, 1971

An apparatus based on the use of a half-sine wave current pulse for electroexplosive device firing is presented. Energy for adiabatic firing can be readily measured. Theory and equations of energy transfer are developed. The application to measurements on certain insensitive electroexplosive devices is presented as an example of capabilities.

ROTHROCK, C. R.

R12 DSN Progress Report for May–June 1971: GCF Area Communications Terminal Subsystem High-Speed Data Regeneration Assembly

C. R. Rothrock

Technical Report 32-1526, Vol. IV, pp. 151–153, August 15, 1971

The incorporation of a High-Speed Data Regeneration Assembly at the Ground Communications Facility (GCF) Area Communications Terminal located at the Goldstone Deep Space Communications Complex (GDSCC) has provided the necessary interface for high-speed data entering or leaving the complex. The Area Communications Terminal is the trunking and interface center for all operational communications between the Deep Space Stations located at GDSCC and the outside world. The physical as well as electrical characteristics are described.

ROURKE, K. H.

R13 DSN Progress Report for May–June 1971: Application of Differenced Tracking Data Types to the Zero Declination and Process Noise Problems

K. H. Rourke and V. J. Ondrasik

Technical Report 32-1526, Vol. IV, pp. 49–60, August 15, 1971

A preliminary analysis of the information content inherent in differenced doppler and differenced range data [quasi-VLBI (very long baseline interferometry)] is made to illustrate why these data types may be superior to conventional data types, when the spacecraft is at a low declination or is subject to unmodelable accelerations. This simple analysis, based upon a three-parameter model of the range and range-rate observables, shows that in certain circumstances the differenced data types can be expected to improve the accuracy of the orbit determination solution. Some hardware and calibration requirements which will insure that the data will be of sufficient quality are briefly discussed.

R14 DSN Progress Report for May–June 1971: An Analytical Study of the Advantages Which Differenced Tracking Data May Offer for Ameliorating the Effects of Unknown Spacecraft Accelerations

V. J. Ondrasik and K. H. Rourke

Technical Report 32-1526, Vol. IV, pp. 61–70, August 15, 1971

For abstract, see Ondrasik, V. J.

RUPE, J. H.

R15 Nitric Oxide Emission Studies of Internal Combustion Engines

F. H. Shair (California Institute of Technology) and J. H. Rupe

JPL Quarterly Technical Review, Vol. 1, No. 2, pp. 23–35, July 1971

For abstract, see Shair, F. H.

RUSSELL, C. T.

R16 Correlated Observations of Electrons and Magnetic Fields at the Earth's Bow Shock

M. Neugebauer, C. T. Russell (University of California, Los Angeles), and J. V. Olson (University of California, Los Angeles)

J. Geophys. Res., Space Phys., Vol. 76, No. 19, pp. 4366–4380, July 1, 1971

For abstract, see Neugebauer, M.

SCHAEFER, W. C.

S01 Operation of a Lightweight Power Conditioner With a Hollow-Cathode Ion Thruster

E. V. Pawlik, E. N. Costogue, and W. C. Schaefer

J. Spacecraft Rockets, Vol. 8, No. 3, pp. 245–250, March 1971

For abstract, see Pawlik, E. V.

SCHORN, R. A. J.

S02 High Dispersion Spectroscopic Observations of Venus: VIII. The Carbon Dioxide Band at 10,627 Å

R. A. J. Schorn, L. D. G. Young, and E. S. Barker (University of Texas)

Icarus: Int. J. Sol. Sys., Vol. 14, No. 1, pp. 21–35, February 1971

Observations of the 10,627-Å band of carbon dioxide in the spectrum of Venus were made from January 1965 through December 1967. The spectra were obtained at the coudé focus of the Struve reflector at dispersions of 2.8, 3.8, and 5.4 Å/mm. The 17 *best* plates from this period were used to derive rotational temperatures by two methods. In the first method linear least-squares fits to a square-root absorption law were made, and temperatures ranging from 217 to 279°K, with an average temperature of 240 ± 3°K, were derived. The second method also required a linear least-squares fit, this time to the curve of growth. This fit gave slopes from 0.40 to 0.57, corresponding to rotational temperatures of 220 to 228°K, with an average temperature of 241 ± 3°K. Finally, averaging the measurements of 29 plates obtained from the 10,362-, 10,488-, and 10,627-Å bands of carbon dioxide, using the curve-of-growth method of data reduction, gives a rotational temperature of 237 ± 2°K (formal standard deviation). This last value of the temperature should be the most accurate. The values of rotational temperature from this study show no large variations with phase or band considered.

A search was made for spatial and temporal variations in the apparent amount of carbon dioxide in the absorption path. The amount appeared to vary significantly with the phase of Venus, and also with the time of observation. Some spatial variation in the abundance may occur.

S03 The Spectroscopic Search for Water on Mars: A History

R. A. J. Schorn

Proceedings of the International Astronomical Union Symposium on Planetary Atmospheres, Marfa, Texas, October 26–31, 1969, pp. 223–236, 1971

The discovery of water on Mars is similar to the discovery of America; both were done many times by many different people. In both cases, many of the discoveries were either fictitious or difficult to verify. This article traces the history of man's effort in the search of water on Mars since the nineteenth century, and summarizes the evidence of the observations made to date.

SHAFER, J. I.

S04 An All-Carbon Radiating Nozzle for Long-Burning Solid Propellant Motors

R. L. Bailey and J. I. Shafer

JPL Quarterly Technical Review, Vol. 1, No. 2, pp. 36–46, July 1971

For abstract, see Bailey, R. L.

SHAIR, F. H.

S05 Nitric Oxide Emission Studies of Internal Combustion Engines

F. H. Shair (California Institute of Technology) and J. H. Rupe

JPL Quarterly Technical Review, Vol. 1, No. 2, pp. 23–35, July 1971

This article reports on the methods and results of preliminary experiments that have been conducted with an ASME-CFR (American Society of Mechanical Engineers-Committee on Fuel Research) engine in order to determine the effect of fuel composition on the emission characteristics of an internal combustion engine. Initial emphasis was placed upon a comparison of the nitric oxide emissions within the exhaust for various mixtures of natural gas and gasoline. A pneumatically driven atomizer permitted the CFR engine to be operated with gasoline fuel–air ratios down to 0.05. At fuel-air ratios below 0.05, misfiring occurred when either natural gas or gasoline fuels were used. In a natural gas–gasoline fuel mixture, the nitric oxide concentration in the emissions decreased almost linearly with increasing concentration of natural gas, based on a fuel-air ratio near 0.063. It is shown, for the limited conditions investigated, that the concentration of NO_x in the exhaust (on the basis of mass discharged for unit work done) is always less when natural gas is the fuel, except for a limited

range of operation at very lean equivalence ratios where misfiring precluded a direct comparison. However, the emissions were never reduced by more than 1/2, and were limited to approximately 20% over a substantial part of the equivalence ratio range ($1.0 < \phi < 1.3$).

SHIMADA, K.

S06 Performance Evaluations of a Nonfueled and a UO_2-Fueled Cylindrical Thermionic Converter

K. Shimada

Technical Report 32-1539, August 1, 1971

Two cylindrical thermionic energy converters similar to those in a "flashlight" thermionic fuel element were tested electrically at JPL. One converter was not fueled, but the other was fueled with UO_2 imbedded in six pencil-lead-size holes in the emitter, which was made of rhenium. The nonfueled converter was tested primarily for endurance under open-circuit conditions that might occur as a result of a loss of cesium or a broken power lead. The UO_2-fueled converter was tested for fuel-converter compatibility under normal operating conditions with an electric load.

The nonfueled converter showed no change in its performance during 4000 h of testing, whereas the output current of the UO_2-fueled converter degraded 15% during 2400 h of testing at 2000°K. Measurements on the UO_2-fueled converter showed an increase in the collector work function and an increase in the bare emitter work function, which indicate that the degradation was caused primarily by foreign deposits on the collector, probably uranium that effused from the UO_2 fuel through the emitter.

S07 Evaluation of Converters Fueled With Uranium Nitride

K. Shimada and P. L. Cassell

Technical Memorandum 33-489, July 30, 1971

Two thermionic energy converters fueled with uranium nitride were fabricated and subjected to comprehensive tests to evaluate their performance as nuclear thermionic converters. Both converters had plane-parallel electrode geometry to increase the accuracy in making measurements of converter parameters and to simplify the laboratory testing which utilized an electron gun for the emitter heating. Of the two converters, one had a rhenium emitter and the other a tungsten emitter; the collector was niobium in both converters.

The evaluation of fuel-emitter compatibility, which was the major objective of the laboratory tests, was performed by measuring and correlating converter characteristics and electrode work functions.

The first phase of the evaluation, involving parametric testing, was completed. The initial performance of these converters was fully characterized so that any change that might occur during the second phase of the test, the life test, due to fuel-emitter interactions could be readily identified.

SHINOZUKA, M.

S08 Stability Analysis of Complex Structures

J.-N. Yang and M. Shinozuka (Columbia University)

Int. J. Solids Struct., Vol. 7, No. 5, pp. 459–472, May 1971

For abstract, see Yang, J.-N.

S09 Peak Structural Response to Non-stationary Random Excitations

M. Shinozuka and J.-N. Yang

J. Sound Vibr., Vol. 16, No. 4, pp. 505–517, June 22, 1971

Dealing with dynamic responses that can be treated as a non-stationary narrow-band random process, the present paper establishes the distribution function of peak values with a useful frequency interpretation. By a numerical simulation of the peak values, the validity of the distribution function is checked by means of the Monte Carlo method. Under nonstationary random excitations the expected fatigue damage and the asymptotic distribution function of the maximum peak response of structures are also derived.

SHIRLEY, D. L.

S10 Automated Drug Identification for Urban Hospitals

D. L. Shirley

AIAA Preprint 71-532, Urban Technology Conference, New York, New York, May 24–26, 1971

Many urban hospitals are becoming overloaded with drug abuse cases requiring chemical analysis for identification of drugs. In this paper, the requirements for chemical analysis of body fluids for drugs are determined and a system model for automated drug analysis is selected which meets these requirements. The system as modeled would perform chemical preparation of samples, gas-liquid chromatographic separation of drugs in the chemically pre-

pared samples, and infrared spectrophotometric analysis of the drugs, and would utilize automatic data processing and control for drug identification. Requirements of cost, maintainability, reliability, flexibility, and operability are considered.

SHUMKA, A.

S11 Thermal Noise in Space-Charge-Limited Solid-State Diodes With Field-Dependent Mobility and Hot Carriers

A. Shumka

Solid-State Electron., Vol. 14, No. 5, pp. 367–369, May 1971

The analysis performed on thermal noise in space-charge-limited solid-state diodes by solving Langevin's equation is extended to include the effects of a field-dependent mobility and hot carriers. Through analysis, an equivalent noise temperature is derived and the noise spectral intensity is obtained. The ultimate justification of the results is dependent on the validity of the assumption of quasithermodynamic equilibrium.

SIEGMETH, A. J.

S12 DSN Progress Report for May–June 1971: Pioneer Mission Support

A. J. Siegmeth

Technical Report 32-1526, Vol. IV, pp. 13–21, August 15, 1971

The DSN is preparing for the tracking and data acquisition support of Pioneers F and G. The major objective is to produce an effective data return capability from the vicinity of Jupiter. This article describes the spacecraft's internal data flow design and identifies the interfaces between the spacecraft and the DSN data system. This article is a continuation of two previous articles that delineated the mission profiles and spacecraft design.

SIMON, M. K.

S13 An Analysis of the Phase Coherent–Incoherent Output of the Bandpass Limiter

J. C. Springett and M. K. Simon

IEEE Trans. Commun. Technol., Vol. COM-19, No. 1, pp. 42–49, February 1971

For abstract, see Springett, J. C.

S14 Data-Aided Carrier Tracking Loops

W. C. Lindsey (University of Southern California) and M. K. Simon

IEEE Trans. Commun. Technol., Vol. COM-19, No. 2, pp. 157–168, April 1971

For abstract, see Lindsey, W. C.

SINGLETON, F. L.

S15 DSN Progress Report for May–June 1971: SFOF Digital Television Display Subassembly

F. L. Singleton

Technical Report 32-1526, Vol. IV, pp. 116–122, August 15, 1971

This article describes the Space Flight Operations Facility (SFOF) digital television display subassembly, which is a part of the digital television assembly. The subassembly accepts input digital data from the computer subassembly, converts it to video data, stores it, and provides a continuous television-compatible video output that is distributed throughout the SFOF. The display subassembly consists of a system control unit, four display generator units, and various hardcopy generation equipment.

S16 DSN Progress Report for May–June 1971: SFOF Digital Television Hardcopy Equipment

F. L. Singleton and K. Kawano

Technical Report 32-1526, Vol. IV, pp. 123–128, August 15, 1971

The Space Flight Operations Facility (SFOF) digital television display subassembly has a hardcopy generation capability in addition to its display generation capability. The hardcopy capability is discussed in this article. The display subassembly hardcopy equipment consists of a system control unit, 12 copy request units, a display image buffer, and 12 hardcopy printers. The hardcopy equipment can make a print of any digital television display channel upon request.

SJOGREN, W. L.

S17 Lunar Surface Mass Distribution From Dynamical Point-Mass Solution

W. L. Sjogren, P. M. Muller, P. Gottlieb, L. Wong (Aerospace Corporation), G. Buechler (Aerospace Corporation), W. Downs (Aerospace Corporation), and R. Prislin (Aerospace Corporation)

The Moon: Int. J. Lunar Studies, Vol. 2, No. 3, pp. 338–353, February 1971

Combined efforts of JPL and the Aerospace Corporation have provided a front side lunar gravity field using the doppler tracking data from Lunar Orbiters 4 and 5. Data reduction was accomplished with a model which included all dynamical motion due to gravitational perturbations, as well as all tracking geometries. The field is represented as a grid of 580 surface mass points which are contoured and show correlations with various lunar surface features.

SMITH, J. G.

S18 The Information Capacity of Amplitude- and Variance-Constrained Scalar Gaussian Channels

J. G. Smith

Inform. Control, Vol. 18, No. 3, pp. 203–219, April 1971

The amplitude-constrained capacity of a scalar gaussian channel is shown to be achieved by a unique discrete random variable taking on a finite number of values. Necessary and sufficient conditions for the distribution of this random variable are obtained. These conditions permit determination of the random variable and capacity as a function of the constraint value. The capacity of the same gaussian channel subject, additionally, to a nontrivial variance constraint is also shown to be achieved by a unique discrete random variable taking on a finite number of values. Likewise, capacity is determined as a function of both amplitude- and variance-constraint values.

SPRINGETT, J. C.

S19 The Design of a Low Data Rate MSFK Communication System

H. D. Chadwick and J. C. Springett

IEEE Trans. Commun. Technol., Vol. COM-18, No. 6, pp. 740–750, December 1970

For abstract, see Chadwick, H. D.

S20 An Analysis of the Phase Coherent–Incoherent Output of the Bandpass Limiter

J. C. Springett and M. K. Simon

IEEE Trans. Commun. Technol., Vol. COM-19, No. 1, pp. 42–49, February 1971

Many applications of the bandpass limiter (BPL) involve coherent demodulation following the limiter. It is shown that as a result of demodulation, the signal mean and the noise variance are direct functions of the phase angle between the signal component passed by the BPL and the coherent reference. As a result, the relationship between the output and input signal-to-noise ratio may be significantly different than that obtained by Davenport for incoherent limiters. A study is also made of the output noise spectral density, and an approximate expression is derived as a function of the input signal-to-noise ratio, reference phase angle, and the characteristics of the input bandpass filter to the limiter. Also discussed is the first-order signal-plus-noise probability density following coherent demodulation.

STALLKAMP, J. A.

S21 Mariner Mars 1969 Final Project Report: Scientific Investigations

J. A. Stallkamp, A. G. Herriman, and Mariner Mars 1969 Experimenters

Technical Report 32-1460, Vol. III, September 1, 1961

This is the third of three volumes of the Mariner Mars 1969 Final Project Report. It describes the scientific program and lists the initial publications of the investigator teams. Volume I describes preoperational activities, including planning, development and design, manufacture, and testing. Volume II describes the Mariner 6 and 7 mission performance during the launch and space-flight phases.

The scientific mission consisted of the design of the six selected experiments; the construction of four instruments and their incorporation into the spacecraft; the selection of flyby dates and aiming points for the spacecraft and pointing strategy for the instruments; and the acquisition, return, and analysis of data. Due to the excellent performance of the many engineering subsystems,

including several that were first of their kind, enhanced options were carried out that materially increased the amount of scientific data returned. Initial reports have been published; more will follow as the interpretation of the data continues.

STICKFORD, G. H., JR.

S22 A Fiber Optics Slit System Used for Time-Resolved Diagnostics in a Transient Plasma

G. H. Stickford, Jr.

Technical Memorandum 33-492, September 15, 1971

Through the use of fiber optics, a series of very narrow slits has been constructed and placed at the exit plane of a spectrograph. Plasma radiation dispersed by the spectrograph is incident on the slits and is transmitted to separate phototubes via the quartz fibers. With this technique, time-resolved measurements of the spectral shape of the hydrogen Hβ line have been made and used to determine the electron density of a transient plasma. With some knowledge of the pressure or density, the measurements also give the plasma temperature.

Data obtained indicated that the thermodynamic conditions behind the reflected shock in a mixture of 20% H_2–80% He, at incident shock speeds of 12 to 14 km/s and pressures of 66.6 to 133.3 N/m^2 (0.5 to 1.0 mm Hg), correspond to theoretically predicted conditions. Immediately behind the incident shock at speeds of 17 to 24 km/s, the plasma reached equilibrium, then demonstrated a drop in intensity which has been attributed to radiative cooling. At 27 km/s, the data indicated that the plasma did not reach equilibrium, presumably because the plasma cooled within the response time of the phototube intensity measurement.

STINNETT, W. G.

S23 DSN Progress Report for May–June 1971: Operation of the DSN Command System From the Space Flight Operations Facility

W. G. Stinnett

Technical Report 32-1526, Vol. IV, pp. 178–180, August 15, 1971

The Space Flight Operations Facility (SFOF) Mark IIIA Command System has been developed at JPL to meet the requirements of the DSN and Mariner Mars 1971 Flight Project. Although full Mark IIIA requirements have not as yet been realized, operational

experience has shown that one of the key design goals has been accomplished: the control of the use of the DSN Command System from the SFOF. This article describes the operation of the DSN Command System from the SFOF as configured for support of the Mariner Mars 1971 mission. Brief descriptions of functional capabilities, along with the use of these capabilities by DSN and Flight Project personnel, are included.

STIRN, R. J.

S24 CdS–Metal Workfunctions at Higher Current-Densities

R. J. Stirn, K. W. Böer (University of Delaware),
G. A. Dussel (University of Delaware), and
P. Voss (University of Delaware)

Proceedings of the Third International Conference on Photoconductivity, Stanford University, Palo Alto, California, August 12–15, 1969, pp. 389–394

It is shown that the high photocurrents observed in CdS: Ag,Al can only be explained by a marked lowering of the CdS–metal workfunction for slightly blocking contacts, probably due to a change in the dipole part caused by a redistribution of electrons close to the actual boundary. Experimental results on stationary high-field domains, obtained on a vacuum-cleaved CdS crystals with evaporated Au, AG, Cu, Pt, Ni, and Sn contacts, indicated maximum fields well below the fields necessary for tunneling. The kinetics of lowering the barrier height are discussed and indications are given under which conditions the described effect, and under which conditions tunneling through an electrode-barrier, may predominate.

STOCKY, J. F.

S25 Mariner Mars 1971 Orbiter Propulsion Subsystem Type Approval Test Program

J. F. Stocky

JPL Quarterly Technical Review, Vol. 1, No. 2, pp. 47–53, July 1971

A new propulsion subsystem was used on the Mariner Mars 1971 orbiter spacecraft to provide the necessary impulse for trajectory corrections, Mars orbit insertion, and Mars orbit trim maneuvers. The type approval test program that provided the functional, structural, and environmental qualification of this subsystem and demonstrated its performance margin in excess of flight mission

requirements is described. A brief discussion of the problems encountered is included.

TAHERZADEH, M.

T01 Analytically Determined Response of a 300-μm Silicon Detector to a Polyenergetic Beam of Neutrons

M. Taherzadeh

JPL Quarterly Technical Review, Vol. 1, No. 2, pp. 119–130, July 1971

Nuclear radiation from a radioisotope thermoelectric generator used as the prime energy source for electrical power in a space mission could severely affect scientific instruments or detectors on the spacecraft. Therefore, a thorough analysis and evaluation of the types of radiation and their effects on the detectors were necessary.

In this article, the response of a 300-μm silicon detector to an incident polyenergetic neutron beam emitted from a plutonium dioxide fuel power source is determined. The results indicate that the response of the detector is basically due to elastic scattering reactions, and the contribution from other reactions is very small. For neutron energies greater than 4.5 MeV, the (n,p) and (n,α) reactions contribute less than 2% to the total response. The maximum response for this detector is less than 4×10^{-3} counts/neutron within the range of bias energies of 25 to 250 keV. Moreover, this maximum value will decrease if consideration is given to the pulse height defect phenomenon.

T02 Neutron Yield From the (α,n) Reaction in the Isotope Oxygen-18

M. Taherzadeh

Nucl. Sci. Eng., Vol. 44, No. 2, pp. 190–193, May 1971

The problem of evaluating neutron yield from the (α,n) reaction in oxygen has been the subject of much experimental investigation for many years. However, the computational probe has not been extensive, basically due to lack of required data in the literature. Using a computer program, calculations were made to obtain the number of neutrons emitted when α particles from the ^{238}Pu isotope interact with ^{18}O. Neutron yield (n/α) is calculated specifically for each excited state of the recoil ^{21}Ne isotope. The result is in good agreement with the experimental value.

TAUSWORTHE, R. C.

T03 Improvements in Deep-Space Tracking by Use of Third-Order Loops

R. C. Tausworthe

JPL Quarterly Technical Review, Vol. 1, No. 2, pp. 96–106, July 1971

Third-order phase-locked receivers have not yet found wide application in deep-space communications systems because the second-order systems now used have performed adequately on all past spacecraft missions. However, a survey of the doppler profiles for future missions shows that an unaided second-order loop may be unable to perform within reasonable error bounds. This article discusses the characteristics of a simple third-order extension to present second-order systems that will not only extend their doppler-tracking capability, but will widen the pull-in range, decrease pull-in time, lower the voltage-controlled oscillator noise detuning when no signal is present, and lessen the susceptibility to voltage-controlled oscillator drift.

T04 Frequency-Counted Measurements and Phase Locking to Noisy Oscillators

R. M. Gray (Stanford University) and R. C. Tausworthe

IEEE Trans. Commun. Technol., Vol. COM-19, No. 1, pp. 21–30, February 1971

For abstract, see Gray, R. M.

T05 Tracking and Data System Support for the Mariner Mars 1969 Mission: Midcourse Maneuver Through End of Nominal Mission

N. A. Renzetti, K. W. Linnes, D. L. Gordon, and T. M. Taylor

Technical Memorandum 33-474, Vol. II, September 1, 1971

For abstract, see Renzetti, N. A.

T06 Tracking and Data System Support for the Mariner Mars 1969 Mission: Extended Operations Mission

N. A. Renzetti, K. W. Linnes, and T. M. Taylor

Technical Memorandum 33-474, Vol. III, September 15, 1971

For abstract, see Renzetti, N. A.

TEGNELIA, C. R.

T07 Digital Command System Second-Order Subcarrier Tracking Performance

J. K. Holmes and C. R. Tegnelia

Technical Report 32-1540, October 1, 1971

For abstract, see Holmes, J. K.

THOMAS, R. F.

T08 Characteristics of a Cigar Antenna

S. A. Brunstein and R. F. Thomas

JPL Quarterly Technical Review, Vol. 1, No. 2, pp. 87–95, July 1971

For abstract, see Brunstein, S. A.

TOM, H. Y.

T09 The Effect of an Oxidative-Caustic Environment on Graft Copolymer Membranes

E. F. Cuddihy, J. Moacanin, D. E. Walmsley, and H. Y. Tom

Colloidal and Morphological Behavior of Block and Graft Copolymers, pp. 113–129, Plenum Press, New York, 1971

For abstract, see Cuddihy, E. F.

TOTH, R. A.

T10 Lines Intensities of the CO_2 Σ–Σ Bands in the 1.43–1.65 μ Region

R. A. Toth, R. H. Hunt (Florida State University), and E. K. Plyler (Florida State University)

J. Molec. Spectrosc., Vol. 38, No. 1, pp. 107–117, April 1971

The line intensities of the five Σ–Σ bands of CO_2 in the 1.43–1.65-μm region have been measured with relatively low sample pres-

sures and high resolution (0.035–0.06 cm^{-1}). The data are analyzed to obtain the total band intensities and dipole-moment matrix elements. At 296°K the intensity of the $3\nu_3$ band is found to be 3.62×10^{-2} cm^{-2}-atm^{-1}. The intensities of four bands in the Fermi tetrad in order of increasing frequency are 1.15×10^{-3}, 1.14×10^{-2}, 1.12×10^{-2}, and 1.27×10^{-3} cm^{-2}-atm^{-1} at 296°K.

TRUBERT, M. R.

T11 Use of Derived Forcing Functions at Centaur Main Engine Cutoff in Predicting Transient Loads on Mariner Mars '71 and Viking Spacecraft

M. R. Trubert, J. R. Chisholm, and W. H. Gayman

Technical Memorandum 33-486, June 28, 1971

The disturbing forcing functions of the Centaur engines at main engine cutoff derived from acceleration flight data of the Mariner Mars 1969 spacecraft are used to predict acceleration and reaction forces and moments near the base of Mariner Mars 1971 and Viking spacecraft. Mathematical dynamic models of the Mariner Mars 1971 and Viking spacecraft and the Centaur launch vehicle modified for the Viking model are presented. Discussions concerning the method and the accuracy of the results are given.

T12 Use of Centaur Spacecraft Flight Data in the Synthesis of Forcing Functions at Centaur Main Engine Cutoff During Boost of Mariner Mars 1969, OAO-II, and ATS Spacecraft: Analysis and Evaluation

M. R. Trubert, J. R. Chisholm, and W. H. Gayman

Technical Memorandum 33-487, Vol. I, June 21, 1971

Acceleration flight data of Mariner Mars 1969, OAO-II, and ATS spacecraft in the boost phase were used to determine the disturbing forcing function of the Centaur engines at the main engine cutoff event. An inverse solution using the concept of Fourier transform and transfer function is presented. Mathematical dynamic models of the spacecraft and the Centaur launch vehicle were derived and Fourier transforms and time histories of the disturbing forcing function were determined. Analysis to determine the response and reaction forces and moments of another spacecraft using the same Centaur vehicle has been derived.

T13 Use of Centaur Spacecraft Flight Data in the Synthesis of Forcing Functions at Centaur Main Engine Cutoff During Boost of Mariner Mars 1969, OAO-II, and ATS Spacecraft: Computer Plots

M. R. Trubert, J. R. Chisholm, and W. H. Gayman

Technical Memorandum 33-487, Vol. II, June 21, 1971

This volume presents acceleration flight data for five Centaur main engine cutoff events and selected gimbal axis forcing functions. The Centaur gimbal axis forcing functions for the two Mariner Mars 1969 flights (Mariners 6 and 7), derived from the corresponding field joint acceleration flight data, are presented. Selected components of the forcing functions, derived from acceleration flight data for the OAO-II and ATS spacecraft, are also given.

UDLOCK, D. E.

U01 Formulating Propellants for Fully Case-Bonded End-Burning Motors

H. E. Marsh, Jr., and D. E. Udlock

AIAA Preprint 71-654, AIAA/SAE Seventh Propulsion Joint Specialist Conference, Salt Lake City, Utah, June 14–18, 1971

For abstract, see Marsh, H. E., Jr.

VAN TILBORG, H.

V01 DSN Progress Report for May–June 1971: Weights in the Third-Order Reed-Muller Codes

H. van Tilborg

Technical Report 32-1526, Vol. IV, pp. 86–94, August 15, 1971

In order to obtain performance superior to that of the (32,6) first-order Reed-Muller code used on Mariner Mars 1969 and 1971 spacecraft, bandwidth limitations make it necessary to consider Reed-Muller codes of higher orders. In this article, the weights that can actually occur in the third-order Reed-Muller codes of lengths 256 and 512 are investigated. For length 256, the exact set of integers is found that occur as weights. For length 512, the same is done except that it cannot be determined whether 140 and 372 occur as weights or not. It is shown, however, that there are no words of weight 132 or 380, a result which adumbrates an important new theorem on Reed-Muller codes.

VOSS, P.

V02 CdS–Metal Workfunctions at Higher Current-Densities

R. J. Stirn, K. W. Böer (University of Delaware),
G. A. Dussel (University of Delaware), and
P. Voss (University of Delaware)

Proceedings of the Third International Conference on Photoconductivity, Stanford University, Palo Alto, California, August 12–15, 1969, pp. 389–394

For abstract, see Stirn, R. J.

WALMSLEY, D. E.

W01 The Effect of an Oxidative–Caustic Environment on Graft Copolymer Membranes

E. F. Cuddihy, J. Moacanin, D. E. Walmsley, and
H. Y. Tom

Colloidal and Morphological Behavior of Block and Graft Copolymers, pp. 113–129, Plenum Press, New York, 1971

For abstract, see Cuddihy, E. F.

WARDLE, M. D.

W02 Dry-Heat Resistance of Bacterial Spores Recovered From Mariner-Mars 1969 Spacecraft

M. D. Wardle, W. A. Brewer, and M. L. Peterson

Appl. Microbiol., Vol. 21, No. 5, pp. 827–831, May 1971

The dry-heat resistances of 70 bacterial spore isolates recovered from Mariner Mars 1969 spacecraft were determined and expressed as *D* values (decimal reduction times). Fifty per cent of the spore isolates had *D* values of 60 min or less at 125°C. Of organisms with *D* values greater than 60 min, four were selected for a study of the effect of sporulation medium and suspension menstruum on dry-heat resistance. Both sporulation medium and suspension menstruum were found to affect significantly the dry-heat resistance of the bacterial spores tested.

WEBER, H. E.

W03 The Fluorine-19 Nuclear Magnetic Resonance Spectra of Some Fluoroaromatic Compounds. Studies Using Noise Decoupling of Protons

M. A. Cooper, H. E. Weber, and S. L. Manatt

J. Am. Chem. Soc., Vol. 93, No. 10, pp. 2369–2380, May 19, 1971

For abstract, see Cooper, M. A.

WEBER, R.

W04 DSN Progress Report for May–June 1971: MSFN/DSN Integration Program for the DSS 11 26-m Antenna Prototype Station—Addendum

R. Weber

Technical Report 32-1526, Vol. IV, p. 177, August 15, 1971

A plan was proposed in mid-1970 wherein unique DSN equipment would be installed in the 26-m antenna Manned Space Flight Network (MSFN) operations control room and integrated to function with pre-existing MSFN equipment. The details of the integration effort at the Pioneer Deep Space Station (DSS 11) were outlined in Technical Report 32-1526, Vol. III. Additional information is presented here.

WELCH, L. R.

W05 DSN Progress Report for May–June 1971: On the Blizard Decoding Algorithm

L. R. Welch

Technical Report 32-1526, Vol. IV, pp. 101–104, August 15, 1971

This article presents an analysis and modification of the new Blizard decoding algorithm, which promises to give performance superior to any known practical decoding algorithm on the deep space channel. The mathematical foundation given in this article reveals the assumptions needed to derive the algorithms. It is, however, necessary that an investigation be carried out to determine the suitability of these algorithms for specific codes and channels.

WEN, L. C.

W06 Preliminary Investigations of Ion Thruster Cathodes

R. Goldstein, E. V. Pawlik, and L. C. Wen

Technical Report 32-1536, August 1, 1971

For abstract, see Goldstein, R.

WICK, H. M., JR.

W07 A Design for Thick Film Microcircuit dc-to-dc Converter Electronics

H. M. Wick, Jr., and S. Capodici (General Electric Company)

IEEE Trans. Aerosp. Electron. Sys., Vol. AES-7, No. 3, pp. 528–531, May 1971

The design concept for thick film microcircuit dc-to-dc converter electronics used in the power subsystem of the Thermoelectric Outer-Planet Spacecraft is presented. Microcircuits have been used in low power logic circuits for nearly 10 yr, but only recently have these techniques been applied to power subsystem circuits which operate at higher power levels.

Thick film microcircuit techniques have been utilized in a dc-to-dc converter reducing weight by 70%, volume by 80%, and interconnections by 75%. The close piece-part spacing allowed short interconnections and lower dissipation, and reduced noise coupling. The developed microcircuit handled total power levels from 1 to 25 W.

WILCHER, J.

W08 DSN Progress Report for May–June 1971: Multiple-Mission Command System

J. Wilcher and J. Woo

Technical Report 32-1526, Vol. IV, pp. 165–166, August 15, 1971

The Multiple-Mission Command System (MMCS) Project was established in January 1969 to design, test, and install throughout the DSN a command system capable of supporting all foreseeable spacecraft with a single command system. In order to provide support for the Mariner Mars 1971 mission, the equipment was required by early fall of 1970. These objectives have all been met. All DSN stations considered prime for the Mariner Mars 1971

mission have been implemented with the dual MMCS capability, including the pseudonoise sync units required for the Mariner Mars 1971 mission. The DSN stations considered as backup stations for Mariner Mars 1971 have been implemented with dual MMCSs; however, only one pseudonoise sync unit per station was provided.

WILLIARD, J. W.

W09 Planetary Entry Body Heating Rate Measurements in Air and Venus Atmospheric Gas Up to T = 15,000°K

F. R. Livingston and J. W. Williard

AIAA J., Vol. 9, No. 3, pp. 485–492, March 1971

For abstract, see Livingston, F. R.

WILLSON, R. C.

W10 Active Cavity Radiometric Scale, International Pyrheliometric Scale, and Solar Constant

R. C. Willson

J. Geophys. Res., Space Phys., Vol. 76, No. 19, pp. 4325–4340, July 1, 1971

The active cavity radiometer type II, a new and accurate standard detector, has been developed for the absolute measurement of optical radiant flux. The active cavity radiometric scale (ACRS), defined by the active cavity radiometer (ACR), and the international pyrheliometric scale (IPS), defined by a U.S. standard angstrom pyrheliometer, have been compared in recent experiments. Simultaneous measurements of solar irradiance demonstrated an average systematic difference between the two scales of 2.2%, the measurements on the ACRS exceeding those on the IPS. An analytical study of the sensitivity of the ACR to sources of experimental error is presented. The uncertainty in the ACRS is found to be less than ±0.5% at the one solar constant level relative to the absolute scale based on fundamental physical principles. In August 1968 two ACR's measured the solar irradiance at an altitude of 25 km in a balloon-flight experiment. The solar-constant value derived from this measurement was 137.0 mW/cm^2.

WONG, L.

W11 Lunar Surface Mass Distribution From Dynamical Point-Mass Solution

W. L. Sjogren, P. M. Muller, P. Gottlieb,

L. Wong (Aerospace Corporation), G. Buechler (Aerospace Corporation), W. Downs (Aerospace Corporation), and R. Prislin (Aerospace Corporation)

The Moon: Int. J. Lunar Studies, Vol. 2, No. 3, pp. 338–353, February 1971

For abstract, see Sjogren, W. L.

WOO, J.

W12 DSN Progress Report for May–June 1971: Multiple-Mission Command System

J. Wilcher and J. Woo

Technical Report 32-1526, Vol. IV, pp. 165–166, August 15, 1971

For abstract, see Wilcher, J.

WOO, R.

W13 Fields Excited by an Arbitrarily Oriented Dipole in a Cylindrically Inhomogeneous Plasma

R. Woo and A. Ishimaru (University of Washington)

Radio Sci., Vol. 6, No. 5, pp. 583–592, May 1971

In this paper the closed-form solution of the three-dimensional fields excited by an arbitrarily oriented dipole in a cylindrically inhomogeneous isotropic plasma is derived. Geometrical optics is used to represent the fields. The eikonal equation is solved to give the wave fronts from which the rays are obtained. A closed-form representation is obtained for the differential cross section of a three-dimensional tube of rays, thus yielding the amplitude of the wave. Closed-form expressions are also obtained for the normal vector, binormal vector, and torsion along the rays so that polarization is readily determined. For the special case where the antenna is located on axis, the radiation patterns depend only on the on-axis and peak electron densities. The solutions show good agreement with solutions obtained for a cylindrically stratified plasma in an earlier study.

YANG, J.-N.

Y01 On the Statistical Distribution of Spacecraft Maximum Structural Response

J.-N. Yang

JPL Quarterly Technical Review, Vol. 1, No. 2, pp. 71–79, July 1971

In most aerospace engineering applications, the finite number of flight data accumulated in the past is not sufficient to characterize nonstationary random excitations resulting from each flight event, such as booster engine ignition or burnout. In this article, a direct statistical analysis of spacecraft maximum structural response is performed and the spacecraft structural reliability is obtained. It is found that the Gumbel Type I asymptotic distribution of maximum values provides a reasonably good statistical model for spacecraft maximum structural responses. The current approach makes it possible to perform the reliability-based optimum design of spacecraft structures.

Y02 Optimization of Structures Based on Fracture Mechanics and Reliability Criteria

E. Heer and J.-N. Yang

AIAA J., Vol. 9, No. 4, pp. 621–628, April 1971

For abstract, see Heer, E.

Y03 Reliability of Randomly Excited Structures

J.-N. Yang and E. Heer

AIAA J., Vol. 9, No. 7, pp. 1262–1268, July 1971

A method is developed for the prediction of the reliability of narrow-band structures under stationary random excitations. The present approach takes into account the interaction of catastrophic failure modes and fatigue failure modes as well as the statistical variation of the material strength. Fracture mechanics and extreme point processes are employed throughout the formulation. The effect of loading history on the structural reliability is accounted for, which, however, cannot be accomplished using the cumulative damage hypothesis and the Palmgren-Miner rule. It is demonstrated that neglecting the interactions of failure modes, or disregarding the statistical dispersion of the material strength, results in an unconservative reliability estimate. This tends to become more critical as the flaw propagation factor or the dispersion of the material strength increases.

Y04 Stability Analysis of Complex Structures

J.-N. Yang and M. Shinozuka (Columbia University)

Int. J. Solids Struct., Vol. 7, No. 5, pp. 459–472, May 1971

A systematic approach is presented for the stability analysis of rigid frames and trusses, including the effect of bending moments and shear forces in structures before buckling. The linear graph theory and the transfer matrix technique are employed throughout; the former is perfectly suited for the stability analysis of complex structures, since it automatically takes the geometrical configuration of the "entire" structure into consideration. This permits a derivation of the determining characteristic equation in a general and straightforward fashion. Also, the application of the linear graph theory permits a convenient use of a high-speed digital computer for the numerical computation involved. The present formulation for the stability analysis degenerates into that of the structural analysis in which the effect of axial force on flexure mode is neglected.

Y05 Peak Structural Response to Non-stationary Random Excitations

M. Shinozuka and J.-N. Yang

J. Sound Vibr., Vol. 16, No. 4, pp. 505–517, June 22, 1971

For abstract, see Shinozuka, M.

YEN, S. P. S.

Y06 Electron Transfer to Bipyridilium (Paraquat) Salts

A. Rembaum, V. Hadek, and S. P. S. Yen

J. Am. Chem. Soc., Vol. 93, No. 10, pp. 2532–2534, May 19, 1971

For abstract, see Rembaum, A.

Y07 Complexes of Heparin With Elastomeric Positive Polyelectrolytes

S. P. S. Yen and A. Rembaum

J. Biomed. Mater. Res. Symposium, Vol. 1, pp. 83–97, 1971

A new elastomeric heparin complex containing from 7 to 16% of heparin was synthesized from commercially available polyether diisocyanates. Chemical analysis and solubility measurements of intermediates as well of the final product showed beyond doubt that an ionic bond was formed between heparin and the quaternized polyether polyurethane. The solubility of the heparin complex in specific solvents systems permitted to cast films or form coatings on commercial plastics. The films and the coatings were

found to be non-thrombogenic and whole human blood could be stored in 1/8- or 3/16-in.-ID coated tubing for at least 24 h without occurrence of clotting. The values of tensile strength, elongation at break and of the shear modulus as a function of temperature showed that the heparinized complexes were endowed with desirable mechanical properties under ambient conditions.

YINGER, E. L.

Y08 DSN Progress Report for May–June 1971: GCF DSS Communications Equipment Subsystem High-Speed Data Assembly

E. L. Yinger

Technical Report 32-1526, Vol. IV, pp. 138–143, August 15, 1971

This article describes the functional operation of the Ground Communications Facility (GCF)-developed and -supplied high-speed data assembly now in use at each Deep Space Station (DSS), except DSS 13 (Venus DSS), and CTA 21 (JPL Compatibility Test Area at Pasadena). The article discusses the subassemblies used, including those developed and incorporated during the latest reconfiguration, to fulfill the GCF High-Speed Data System requirements for the 1971–1972 period. The assembly is used to convert all high-speed data leaving the DSS to a form suitable for transmission to the Space Flight Operations Facility and converts all high-speed data entering the DSS to a form suitable for use by the on-station computers.

YOUNG, A. T.

Y09 Use of Photomultiplier Tubes for Photon Counting

A. T. Young

Appl. Opt., Vol. 10, No. 7, pp. 1681–1683, July 1971

A recent paper by R. Foord, et al., *Appl. Opt.*, Vol. 8, p. 1975, 1969, on "The Use of Photomultiplier Tubes for Photon Counting" is believed to contain several errors regarding pulse height distribution, signal/noise ratio, and electron collection efficiency. Extensive correspondence with the authors has led to agreement on a few points but several major differences remain to be resolved. In this article, arguments are presented showing the areas of disagreement and the probable cause for the anomalies.

YOUNG, L. D. G.

Y10 Effective Pressure for Line Formation in the Atmosphere of Venus

L. D. G. Young

Icarus: Int. J. Sol. Sys., Vol. 13, No. 3, pp. 449–458, November 1970

The effective pressure of line formation is derived from spectra of Venus taken at the McDonald Observatory. Two models are used to determine the change of effective pressure for line formation with Venus phase angle. The effective pressure is seen to decrease as the phase angle is increased from 26 to 164 deg. For a fixed phase angle the effective pressure generally decreases with increasing line strength. For example, the very strong bands at 1.2 μm are formed at an effective pressure 2 to 3 times less than the pressure for the bands at 1.0 μm.

Y11 High Dispersion Spectroscopic Observations of Venus: VIII. The Carbon Dioxide Band at 10,627 Å

R. A. J. Schorn, L. D. G. Young, and E. S. Barker (University of Texas)

Icarus: Int. J. Sol. Sys., Vol. 14, No. 1, pp. 21–35, February 1971

For abstract, see Schorn, R. A. J.

Y12 Interpretation of High Resolution Spectra of Mars: III. Calculations of CO Abundance and Rotational Temperature

L. D. G. Young

J. Quant. Spectrosc. Radiat. Transfer, Vol. 11, No. 4, pp. 385–390, April 1971

High-resolution spectra for the whole disk of Mars have been reanalyzed to obtain a mean rotational temperature of 205 ± 7°K (standard deviation) using four distributions for the collision-broadened line half-width. A line-by-line calculation using Voigt line profiles has been performed to fit the measured equivalent widths for a range of Martian surface pressures. This fit indicates that a carbon-monoxide abundance of over 40, but less than 47 cm-atm is in the total path for a surface pressure of greater than 5, but less than 6 mb if a constant line width is assumed. If a 25% error has been made in measuring the equivalent widths, the carbon-monoxide abundance is 47 +32,–24 cm-atm for a surface pressure of 5 mb. Depending upon the distribution of line widths assumed, for line widths that vary throughout the band, the carbon-monoxide

abundance is greater than 27, but less than 57 cm-atm in the total path for a surface pressure of greater than 5, but less than 6 mb.

ZOHAR, S.

Z01 High Precision Moments for the Fourier Coefficients of Arbitrary Functions

S. Zohar

Technical Memorandum 33-460, October 1, 1971

Evaluation of the integrals

$$\int_0^{\pi/2} \xi^n \begin{matrix}\sin\\ \cos\end{matrix} k\xi \, d\xi$$

where n and k are positive integers, is considered in detail. The difficulties in their direct evaluation are analyzed and overcome using a method capable of very high precision. A detailed error analysis yields a reliable error bound for the results obtained this way.

The method has been applied in computing a table of parameters allowing the evaluation of the above integrals for

$$n = 2,3,\cdots,201$$
$$k = 1,2,\cdots,200$$

with a relative error of 2^{-132} ($\approx 2 \times 10^{-40}$). Two types of tests indicate that the actual errors are well below this upper bound.

At the other extreme, very simple coarse estimates of the integrals are also obtained and their error bounds established. The computed parameters are also shown to be related to the (high order) derivatives of band-limited functions and to the incomplete gamma function.

Subject Index

Subject Categories

Subjects

Publication Index

Technical Reports

DSN Progress Report for May—June 1971 (Technical Report 32-1526, Vol. IV)

Technical Memorandums

Number	Entry
33-426, Vol. IX	R06
33-460	Z01
33-474, Vol. II	R07
33-474, Vol. III	R08
33-484	C07

JPL Quarterly Technical Review, Vol. 1, No. 2

Open Literature Reporting

Proceedings of the Third International Conference on Photoconductivity, Stanford University, Palo Alto, California, August 12–15, 1969 **Entry**

pp. 389–394 ..... S24

Proc. Am. Math. Soc. **Entry**

Vol. 28, No. 1, pp. 71–74 ..... J07

Radio Sci. **Entry**

Vol. 6, No. 5, pp. 583–592 ..... W13

Vol. 6, No. 6, pp. 673–679 ..... M09

Research in the Antarctic **Entry**

pp. 137–189 ..... C01

Science **Entry**

Vol. 172, No. 3988, p. 1167 ..... F02

Solid-State Electron. **Entry**

Vol. 14, No. 5, pp. 367–369 ..... S11

The Moon: Int. J. Lunar Studies **Entry**

Vol. 2, No. 3, pp. 338–353 ..... S17

Urban Technology Conference, New York, New York, May 24–26, 1971 **Entry**

AIAA Preprint 71-532 ..... S10

NASA — JPL — Coml., L.A., Calif.